Water Interfaces as a Source and Sink of Reactive Trace Gases in the Atmosphere

By

Gordon A. Novak

A dissertation submitted in partial fulfillment of the requirements for the degree of

Doctor of Philosophy

(Chemistry)

at the

UNIVERSITY OF WISCONSIN-MADISON

2020

Date of final oral examination: March 23rd, 2020

The dissertation is approved by the following members of the Final Oral Committee:

Timothy H. Bertram, Professor, Chemistry

Gilbert M. Nathanson, Professor, Chemistry

Etienne Garand, Associate Professor, Chemistry

Ankur A. Desai, Professor, Atmospheric and Oceanic Science

Abstract

The ocean surface serves as a source and sink for a diverse set of reactive trace gases in the atmosphere, including volatile organic compounds (VOC), reactive halogens, and oxidized and reduced nitrogen compounds. The exchange of reactive trace gases between the atmosphere and ocean has been shown to alter atmospheric oxidant concentrations and drive particle nucleation and growth. Uncertainties in cloud radiative forcing and aerosol-cloud interactions are among the largest uncertainties in current global climate models. Climate models are particularly sensitive to cloud cover over the remote ocean due to large changes in albedo between the ocean surface and cloud tops. Oceanic emissions contribute to cloud condensation nuclei concentrations, either through the direct emission of particles during wave breaking, or through the formation of secondary aerosol particles following the emission of reactive gas-phase compounds. Despite generally small and diffuse oceanic emission rates for reactive trace gases, it has been shown that oxidant and particle number concentrations are acutely sensitive to air-sea trace gas exchange rates and the chemical composition of emitted species. To date, *field* measurements of air-sea reactive gas exchange have focused primarily on the emission of gases of biological origin, such as dimethyl sulfide (DMS). While DMS emissions are relatively well constrained, the gas-phase oxidation that connects DMS to sulfate aerosol is less well understood. Recent *laboratory* measurements suggest that heterogeneous and photochemical reactions occurring at the air-sea interface can also lead to the production and emission of a wide array of reactive VOC. When laboratory-based measurements are used to derive global scale emissions, the calculated sea-to-air fluxes of reactive VOC generated from heterogeneous and photochemical processes are comparable or larger in magnitude to the sea-to-air flux of DMS. It is not yet clear how the mechanisms proposed in these laboratory experiments translate to atmospheric conditions. The proposed abiotic emissions are also a potential source of VOC in regions of low biological activity which carries important implications for regional and global modeling.

This thesis presents work to directly constrain the magnitude and speciation of biotic and abiotic ocean-atmosphere VOC exchange and subsequent processing in the atmosphere. Chapter 1 details direct eddy covariance flux measurements of O_3 deposition to the coastal ocean from a deployment to Scripps Pier La Jolla, CA in 2018. The rate of O_3 deposition to the ocean is important as both a sink of O_3 which is an air pollutant and greenhouse gas, and also because it controls the magnitude

of potential abiotic emissions from heterogeneous chemistry at the ocean atmosphere interface. Chapter 2 presents the first broad survey of VOC air-sea exchange by eddy covariance flux at the coastal Scripps Pier site. This study directly targeted biotic and abiotic VOC emission fluxes and included coincident measurements of solar irradiance, O_3 mixing ratios, and ocean biochemical parameters. In Chapter 3 I describe the use of eddy covariance flux measurements from an airborne platform on the NASA Atmospheric Tomography mission (ATom) as a probe of cloud processing and uptake in the marine boundary layer. Cloud uptake can act as a terminal sink of low volatility species in the boundary layer, affecting VOC, HO_x, and NO_x budgets in cloud capped boundary layers. Chapters 4 and 5 describe the characterization of new chemical ionization mass spectrometry methods which enable the high sensitivity and precision measurements necessary for the eddy covariance technique. Chapter 4 presents detailed calibrations of benzene cluster cation reagent ions for the detection of isoprene, monoterpenes, and sesquiterpenes. Chapter 5 is a detailed characterization of oxygen anion reagent ion chemistry (Ox-CIMS) which enables extremely high sensitivity detection of O_3 necessary for measurements of O_3 deposition to the ocean. Together this thesis describes new tools for and new observations of the air-sea exchange of reactive trace gases.

Dedication

This work was funded by the National Science Foundation through Grant GEO AGS 1829667.

I would like to thank all of the people I have worked with who made the day to day success of my work possible. Every member of the Bertram Group has had a hand in shaping my research and in making grad school a continuously exciting and enjoyable experience. In particular, Steve Schill and Katy Zimmerman were my first mentors as an undergrad in the group and set the groundwork for all my success as a researcher since. James Brady was essential for providing practical advice on lab issues and for keeping me company as the first people in the group in Madison. Michelle Kim set the groundwork for the CIMS and flux techniques I used which are the core of this thesis. Sean Staudt, Chris Jernigan, Delaney Kilgour, Rachel Bergin, and Joe Gord have all been a joy to work with and I am sure I will look back fondly on our chats every day at lunch wherever I end up. I have had the privilege to mentor a number of undergraduate students who made research endlessly rewarding and who taught me far more about research than I taught them. In particular, working with Cristina Bahaveolos and Jake O'Hearn has been one of the most enjoyable parts of my time in graduate school and I excited to see all the great work they will do from here. Finally, Michael Vermeuel has been involved in essentially all of the work presented in this thesis but more importantly has been a great friend.

Thank you to Tim for being an unceasingly supportive mentor who allowed me to follow my interests across various projects and who was patient and supportive during my struggles and the base of all of my growth as a scientist.

Most of all thank you to my parents and my brothers Kevin and Ryan for their continuous encouragement and support.

"*Because I know that time is always time*

And place is always and only place

And what is actual is actual only for one time

And only for one place"

T.S. Elliott - Ash Wednesday

Coauthors and Contributors

The Introduction chapter is in part, a reprint of material currently in review at Accounts of Chemical Research. Gordon A. Novak and Timothy H. Bertram (2020), Reactive VOC production from photochemical and heterogeneous reactions occurring at the air-ocean interface. The dissertation author was the primary author of this paper.

Chapter 1: Contributing authors; Gordon A. Novak, Michael P. Vermeuel, and Timothy H. Bertram.

Chapter 2: Contributing authors; Gordon A. Novak, Michael P. Vermeuel, Delaney Kilgour, Chris M. Jernigan, and Timothy H. Bertram.
Additional thanks to: Sarah Amiri, Jon Sauer, Alexia Moore, Mathew Pendergraft, Mitchell Santander and Kimberly Prather.

Chapter 3 presents publicly available data collected during the NASA Atmospheric Tomography (ATom) and Student Airborne Research Project (SARP) projects. We thank all researchers involved in those projects for use of their data. Specifically, we thank Patrick Veres, and Andy Neuman for facilitating access to their observations of HPMTF which are the central component of this work. We thank Glenn Wolfe for providing guidance on airborne flux analysis and for making a Matlab based wavelet EC flux toolbox publicly available which was used in the analysis in this work. We also thank Ian Faloona for valuable discussions on cloud processing and entrainment rates. Finally, we thank Chris Jernigan for discussion of HPMTF production and solubility.

Chapter 4, in full, is a reprint of the material as it appears in Atmospheric Measurement Techniques. Gordon A. Novak, Michael P. Vermeuel, and Timothy H. Bertram (2019), Simultaneous Detection of Ozone and Nitrogen Dioxide by Oxygen Anion Chemical Ionization Mass Spectrometry: A Fast Time Response Sensor Suitable for Eddy Covariance Measurements, AMT., 2019, doi: https://doi.org/10.5194/amt-2019-445, with minor formatting edits. The dissertation author was the primary investigator and author of this paper.

Chapter 5, in full, is a reprint of the material as it appears in Atmospheric Measurement Techniques. Avi Lavi, Michael P. Vermeuel, Gordon A. Novak, and Timothy H. Bertram (2018), The sensitivity of benzene cluster cation chemical ionization mass spectrometry to select biogenic terpenes. AMT., 2018, doi: 10.5194/amt-11-3251-2018, with minor formatting edits. The dissertation author was an equal contributing author of this paper.

TABLE OF CONTENTS

TABLE OF FIGURES

TABLE OF TABLES

Thesis Introduction

I.1 Ocean-Atmosphere Trace Gas Exchange

Interactions at the ocean-atmosphere interface have a profound impact on climate and chemistry in the atmosphere. The exchange of mass and energy across the air-sea interface influences local and regional temperatures and global hydrological cycles. Further, the air-sea exchange of oxygen (O_2) and the greenhouse gas carbon dioxide (CO_2) have been extensively studied given their impacts on climate and ocean biogeochemistry, with the ocean acting as a CO_2 sink. A wide suite of lower concentration reactive trace gases also exchange across the air-sea interface with diverse impacts on atmospheric composition, aerosol and cloud formation, and the oxidative capacity of the atmosphere. Included among these are volatile organic compounds (VOCs), which participate in the catalytic production of ozone (O_3) in the atmosphere, contribute to aerosol particle formation and growth, and are linked to cloud condensation nuclei (CCN) activity and cloud formation.

The air-water flux (F) of a gas is typically parameterized in the two-layer framework of Liss and Slater (1974)[1] as described in Equation 1. C_w and C_g are the concentrations of the compound in the water and air respectively, H is the Henry's law solubility (here in dimensionless gas over liquid units), and K_t is a total transfer velocity for the molecule.

$$F = -K_t(C_g - HC_w) \quad \text{E1}$$

The flux of a molecule can be conceptualized as movement towards an equilibrium concentration in the gas and liquid phases, which is controlled by the concentration gradient of C_w and C_g, and the solubility of the molecule (H). K_t then describes how quickly the compound is moving towards equilibrium. This transfer velocity is affected by all processes that contribute to the resistance to transfer, including turbulent mixing in the atmospheric boundary layer, diffusion

across the laminar sublayer on both sides of the air-water interface, and other waterside processes including surface reactivity. K_t does not have any dependence on the direction or magnitude of the concentration gradient and can instead be conceptualized as a resistance to transfer. A variety of parameterizations exist for determination of K_t which treat the various physical and chemical terms involved in gas transfer[1–4]. Gases in the atmosphere and ocean have H spanning many orders of magnitude, resulting in species being both sub- and supersaturated in the ocean. If the ocean is supersaturated for a given compound it will drive an emission flux to the atmosphere and *vice versa*. For highly soluble molecules that are supersaturated in the atmosphere (such as nitric acid (HNO_3) or dinitrogen pentoxide (N_2O_5)), uptake into water is fast once a molecule reaches the air-water interface. Transfer is then limited by the rate of turbulent mixing and diffusion in the gas phase and the molecule is considered to be air-side limited in its transfer. Conversely for a poorly soluble molecule that is supersaturated in the atmosphere (such as CO_2 or dimethyl sulfide (DMS)), transfer in the atmosphere to the interface is fast relative to the rate of transfer into water and the transfer rate is considered water-side limited. The applicability of this framework is less clear for a hypothetical gas that is formed immediately at the ocean-atmosphere interface, as the molecule may not feel one or more of the laminar and turbulent layers of the ocean or atmosphere.

Air-sea transfer velocities of specific species such as CO_2, O_2, and DMS have been extensively studied and parameterized. However, the exchange of lower abundance reactive trace gasses are comparatively poorly studied. To date, direct flux observations exist for only a small number of reactive trace gases, including N_2O_5 and nitryl chloride ($ClNO_2$)[5], sulfur dioxide (SO_2)[6], glyoxal[7], isoprene and monoterpenes[8], acetaldehyde, methanol, and acetone[9] and O_3[10,11]. A primary aim of this thesis work is to expand the coverage of air-sea reactive trace gas exchange

measurements and assess their potential impact on the oxidative capacity of the troposphere and their contribution to aerosol formation and growth.

I.2 Biological production and sea-to-air transfer of reactive VOC

Emissions of volatile organic compounds (VOC) from the ocean surface have been shown to impact oxidant loadings and secondary aerosol formation in the marine atmosphere.[12–16] To date, marine VOC research has primarily focused on the seawater production and emission of dimethyl sulfide (DMS) and its links to cloud formation, the foundation for the CLAW hypothesis[17] which proposed a self-regulating climate feedback loop between DMS, cloud cover and surface temperatures. While supporting evidence for the complete feedback loop is mixed,[18,19] there are many lines of evidence which demonstrate the impact of DMS emissions on aerosol, clouds, and oxidative capacity of the marine atmosphere. Comparatively less work has focused on other marine biogenic VOC (BVOC) sources including isoprene and monoterpenes. Monoterpene and isoprene emissions are known to be considerably smaller than DMS but may still have significant impacts on aerosol formation due to their high secondary organic aerosol (SOA) yields[20] and ability to produce extremely low volatility oxidation products.[21] In addition, isoprene and monoterpenes also have substantially faster biomolecular reaction rate constants for reaction with ozone and hydroxyl (OH) radicals compared to DMS.

DMS is produced in the surface ocean from the cleavage of dimethylsulfoniopropionate (DMSP), a metabolite found in a wide range of macro- and micro-algae. Extensive global data sets of dissolved DMS concentrations and DMS emission fluxes has been collected over much of the global oceans. This database of global surface seawater DMS measurements and detailed studies of DMS air-sea transfer rates have led to the development of well constrained DMS emissions inventories, where the global, annual average DMS emission rate is estimated to be between 14.7

to 21.1 Tg C yr^{-1}.[22–25] While there remain uncertainties in elements of the DMSP and DMS production and conversion pathways, the spatiotemporal distribution of DMS waterside concentrations and emissions flux observations are generally well described in global models. For a comprehensive review of DMS production, chemistry, and air-sea exchange see Carpenter et al. (2012).[26]

Once emitted into the atmosphere, DMS is oxidized by OH and halogen radicals (Cl and BrO) to form lower volatility products, which can contribute to new particle formation after further oxidation to sulfate (SO_4^{2-}), or particle growth following oxidation to methyl sulfonic acid (MSA). The lifetime of DMS to oxidation by OH is roughly 1.2 days for an OH concentration of 2×10^6 molecules cm^{-3}. The OH-oxidation of DMS proceeds by either OH addition (primarily forming MSA) or hydrogen abstraction (primarily forming SO_2), where the branching fraction is a strong function of temperature.[27] Reported yields of SO_2 from DMS oxidation vary significantly from ~30-100%.[28] Much of this uncertainty in SO_2 yield can be linked to an incomplete understanding of the intermediate oxidation steps following reaction with OH and uncertainties in halogen and multiphase chemistry.[27] Recent laboratory and field observations have shown the significance of a previously unknown DMS oxidation pathway leading to the formation of a stable intermediate ($C_2H_4O_3S$; hydroperoxy methylthioformate; HPMTF) which is not included in any current global chemistry models. HPMTF is formed in the OH initiated H-abstraction pathway, following two intramolecular H-shift reactions, which outpace biomolecular reactions at low NO_x.[29,30] Ambient observations over wide regions of the global marine boundary layer on the NASA Atmospheric Tomography (ATom) campaign confirmed that HPMTF is ubiquitous in the remote marine atmosphere and suggest that *ca.* 40% of emitted DMS goes on to form HPMTF.[31] Determination of the atmospheric fate of HPMTF is an active area of research,[30] as this chemistry may necessitate

significant updates to our understanding of sulfur processing in the marine atmosphere. These observations highlight the important gaps in current understanding for even the most well studied marine VOC.

In addition to DMS, laboratory monoculture studies have demonstrated that marine phytoplankton can efficiently produce isoprene and select monoterpenes, with production rates dependent on phytoplankton speciation, solar radiation, temperature , and nutrient loadings.[32] Surface seawater isoprene concentrations have been reported in the range of 0.1-100 pM, with higher concentrations often, but not always,[33] correlated with chlorophyll *a*.[32] Phytoplankton monoculture studies indicate that isoprene production rates are an order of magnitude larger than total monoterpene production rates.[34] Marine gas-phase isoprene mixing ratios have been observed as high as 375 ppt during a phytoplankton bloom.[35] Average MBL monoterpene mixing ratios from that study were 125 ppt (phytoplankton bloom) and 5 ppt (non-bloom) in the southern Atlantic Ocean. A review of non-bloom measurements shows gas-phase isoprene mixing ratios are typically less than 20 ppt.[32] Speciated monoterpenes measurements over several cruises in the Atlantic and Arctic showed average concentrations form 0.5 to 2.9 pM, with no clear correlation to biological productivity.[36]

Estimates of isoprene emissions, parameterized from dissolved concentrations (bottom-up) and remote sensing products (top-down) result in emission estimates from 0.1 to 12 Tg C yr^{-1} respectively.[37,38] Marine monoterpene emissions are even more uncertain, with estimated global flux ranging between 0.01 and 29.5 Tg C yr^{-1} from bottom-up and top-down methods respectively.[39] Modeled global monoterpene emissions of 0.16 Tg C yr^{-1} were determined by incorporating extensive observations of dissolved monoterpenes from a wide spatial area in the Atlantic and Arctic.[36]

Our group reported the first simultaneous, eddy covariance measurements of DMS, isoprene, and monoterpene air-sea fluxes as part of the High Wind Gas Exchange Study (HiWinGS) over the Northern Atlantic Ocean during fall.[8] Average isoprene and monoterpene emission fluxes were small, consistent with prior calculations, with campaign averages of 5.0×10^7 and 2.6×10^7 molecules cm^{-2} s^{-1}, respectively. For the campaign mean, the sum of isoprene and monoterpene fluxes were significantly lower than the average DMS flux (1.04×10^9 molecules cm^{-2} s^{-1}). However, in localized hotspots during an upwelling event, the maximum monoterpene flux (1.62×10^9 molecules cm^{-2} s^{-1}) was larger than coincident DMS emissions, highlighting the importance of local biological variability on BVOC emissions. The frequency of these high monoterpene emitting bloom events are not well constrained but appear to be linked to upwelling events that redistribute nutrients to the surface, stimulating phytoplankton blooms. Scaling the observed emission fluxes during this study to the global oceans results in annual emissions of 4.71, 0.57, and 0.60 Tg C yr^{-1} for DMS, isoprene, and monoterpenes, respectively. Those emissions weighted by OH reactivity and normalized to DMS are 1, 1.02, and 0.28 for DMS, isoprene, and monoterpenes respectively, highlighting the significance of terpenes on atmospheric oxidative capacity despite smaller mass emissions. An overview of DMS, monoterpene, and isoprene emissions are presented in **Figure I.1.** This brief review of select reactive biogenic emissions highlights the known importance of DMS, isoprene, and monoterpene emissions on the marine atmosphere and provides a calibration point for the scale of marine reactive carbon emissions and their potential impacts on SOA and oxidant loadings.

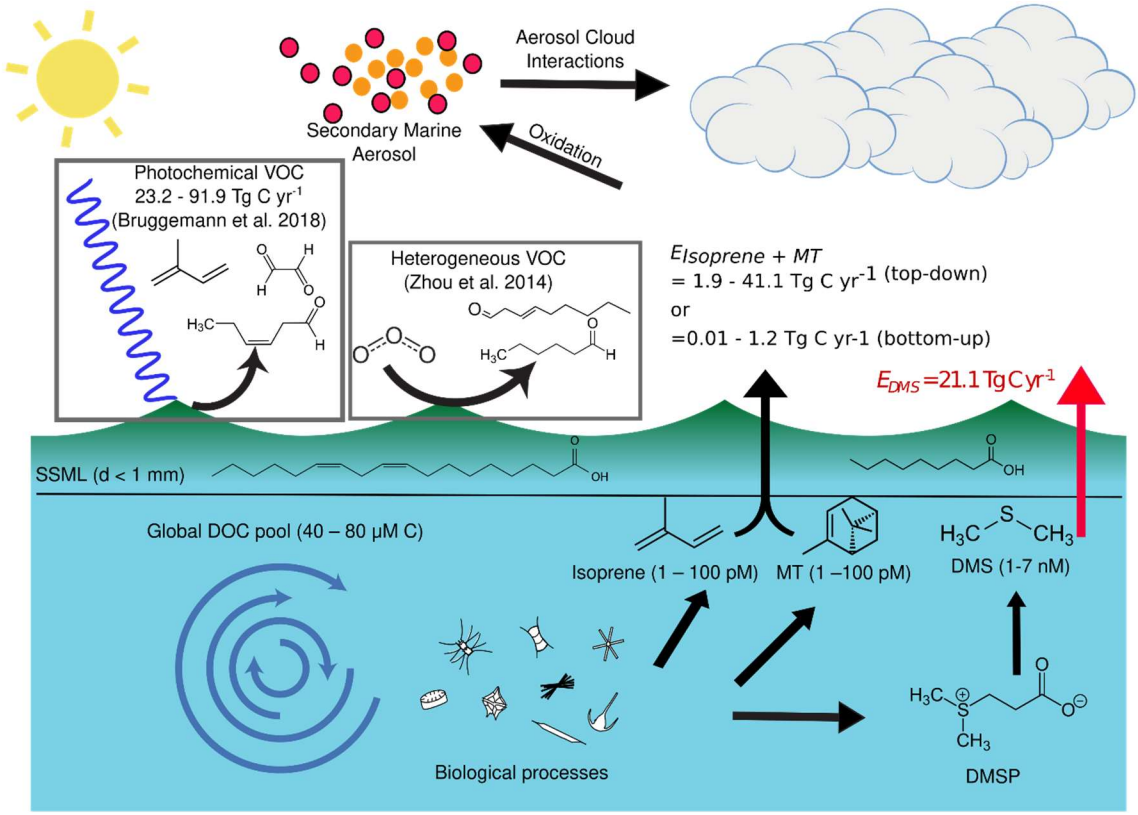

Figure I.1. Overview of marine biotic (DMS, monoterpenes (MT), and isoprene) and abiotic (photochemical[40] and heterogeneous[41]) ocean VOC emission sources. Quoted DMS emissions are from the Lana et al. (2011) climatology.22 MT and isoprene emission estimates are separated into top-down[39,42] and bottom-up[32,39,43] methodologies.

I.3 Known photochemical production of VOC at the ocean surface

To date, study of marine VOC production mechanisms and emission rates have focused primarily on biochemical processes with a particular focus on DMS. However, photochemical emissions of a small number of species including alkyl nitrates[33], acetone[34–36], and acetaldehyde[36,37] have previously been investigated. Alkyl nitrates have a well-established photochemical production pathway, where photochemically produced RO_2 and NO_2 react in the surface waters to form RO_2NO_2 species. [39] Alkyl nitrates also have direct biological production sources with an unclear distribution between the two production mechnaisms[33,38]. Alkyl nitrate emissions are significant as a source of NO_x to the remote marine atmosphere, where O_3 production is severely NO_x limited[39]. Acetone air-sea exchange is bidirectional with a net sink term in the Northern

Hemisphere oceans and a net source in the tropical oceans.[35] Globally, dissolved acetone in the ocean is in near equilibrium with the gaseous acetone in the atmosphere, acting as net sink of 2-7.5 Tg yr^{-1}.[34,35] Ocean acetone production has been shown from both photochemical and biological pathways[36], with *in situ* gross production rates from a transect of the Atlantic show 48-100% of waterside acetone production is from photochemical sources.[36] Acetone SOA yields are likely negligible and it reacts slowly with OH ($k = 2.2 \times 10^{-13}$ cm^3 $molecules^{-1}$ s^{-1}). However, acetone photolysis also produces OH, influencing the HO_x budget.[40] Acetaldehyde photoproduction is well supported, with multiple studies showing production from photolysis of colored dissolved organic matter (CDOM)[41] and measurements of near surface dissolved concentrations showing a diel cycle peaking in midday.[37] Gross production measurements showed that photochemical production accounted for up to 68% of the total source.[36] Net global marine acetaldehyde emissions have been modeled to be from 19 to 31 Tg C yr^{-1}.[42,43] Acetaldehyde does not contribute to SOA production but has a fast bimolecular rate constant with OH ($k = 1.62 \times 10^{-11}$ cm^3 $molecules^{-1}$ s^{-1}) and thus is an important term in the marine OH budget. Photoproduction of alkyl nitrates, acetone, and acetaldehyde all occur in bulk seawater, identified by enhanced concentrations throughout the photic zone.[36] These photoproduction sources also have relatively well studied global emission climatologies which allows for inclusion in chemistry models.

I.4 Photochemical production of VOC at the ocean surface

Recently, a series of laboratory experiments have suggested that photochemical and heterogeneous reactions occurring at the ocean-atmosphere interface could be a significant source of reactive VOC. VOC formed through abiotic mechanisms encompass a wide range of oxygenated and unsaturated molecules distinct from those discussed previously, with potential impacts on the marine HO_x and SOA budget. A schematic diagram of biotic and abiotic emission sources and

estimates of their magnitudes is presented in **Figure I.1**. Measurements of the chemical composition of the sea-surface microlayer (SSML) have indicated that it is strongly enriched in dissolved organic matter with chromophoric functional groups,[57] which could react with OH and O_3 or undergo photochemical reactions, all of which can lead to VOC production. For example, photolysis of both a proxy SSML (nonanoic acid, NA) as well as authentic SSML samples with added humic acid (HA) as a photosensitizer both showed photoenhanced isoprene production.[58] Scaling these laboratory results to ocean conditions suggested that photochemical isoprene fluxes could be as large as $0.8 – 1.7 \times 10^9$ molecules cm^{-2} s^{-1}, which is comparable in magnitude to DMS emission rates and higher than the expected isoprene emissions from bulk biogenically produced isoprene.[8,58] Additional laboratory photochemical studies of proxy and authentic SSML samples have demonstrated prompt formation of a variety of reactive species including saturated and unsaturated aldehydes.[58–64] Emissions from these studies generally show a wide array of products with lower emission fluxes than those described above for isoprene. For example, Bruggemann et al.[63] reported photoenhanced emissions of 1.1×10^8, 4.4×10^8, and 71×10^8 molecules cm^{-2} s^{-1} for octanal, isoprene, and acetone respectively, along with many other products, from irradiance of biofilms scaled to an ambient mean solar flux of 92 Wm^{-2}. These photochemical production studies have generally included the addition of a photosensitizing agent to the SSML sample, typically 4-benzoylbenzoic acid (BBA) or commercial HA. A comparison of photochemical production from NA with BBA, HA, and authentic marine dissolved organic matter (m-DOM) as photosensitizing agents showed that authentic m-DOM did not result in enhanced photochemical VOC production, while the BBA and HA samples showed photochemical emissions consistent with prior studies.[65] This raises questions as to appropriate proxies of photosensitizers and SSML constituents to use in laboratory studies. However, Rossignol et al.[64] demonstrated photoenhanced VOC production

from concentrated NA with no added photosensitizers. While aqueous NA at the solubility limit does not absorb in the UV-visible spectral range of actinic flux at Earth's surface (>280 nm), the authors demonstrated that concentrated interfacial NA does show weak absorption in the actinic flux wavelengths. They propose this absorbance is driven by the presence of a weakly absorbing reactive state of NA which is enhanced at the interface, allowing photochemistry in the absence of traditional photosensitizing groups. While these studies have provided new molecular insight into photochemical VOC production mechanisms, it is not yet clear how representative these studies are of the significantly more dilute and chemically complex SSML. Future laboratory studies should focus on measuring VOC production and emission from multicomponent systems representative of the authentic SSML.

I.5 Production of VOC from heterogeneous reactions occurring at the ocean surface

Heterogeneous reactions of ozone (O_3) with model and authentic SSML samples also efficiently produce reactive VOC including alkanals and alkenals in laboratory studies.[41,66] Ozone is known to react efficiently with both iodide and a variety of DOC compounds at the ocean interface, representing an important global loss term for O_3.[67] Interfacial marine reactions of O_3 are a central driver of reactive halogen emissions to the atmosphere, contributing up to 75% of the observed iodine oxide levels over the tropical Atlantic.[68] Laboratory exposure of a proxy SSML containing linoleic acid to O_3 resulted in emission of carbonyls at near 100% total molecular yield.[41] Exposure of authentic SSML samples also showed prompt production of a wider set of gas phase carbonyl products.[41] Heterogeneous reactions of O_3 with the SSML generated by a laboratory grown phytoplankton culture produced C7-C10 carbonyls and also drove new aerosol particle formation and growth.[66] These studies provide intriguing evidence that heterogeneous reactions of O_3 at the ocean surface may be an important abiotic heterogeneous source of reactive VOCs in the marine

atmosphere. An overview of proposed photochemical and heterogeneous reaction mechanisms discussed here are presented in **Figure I.2**.

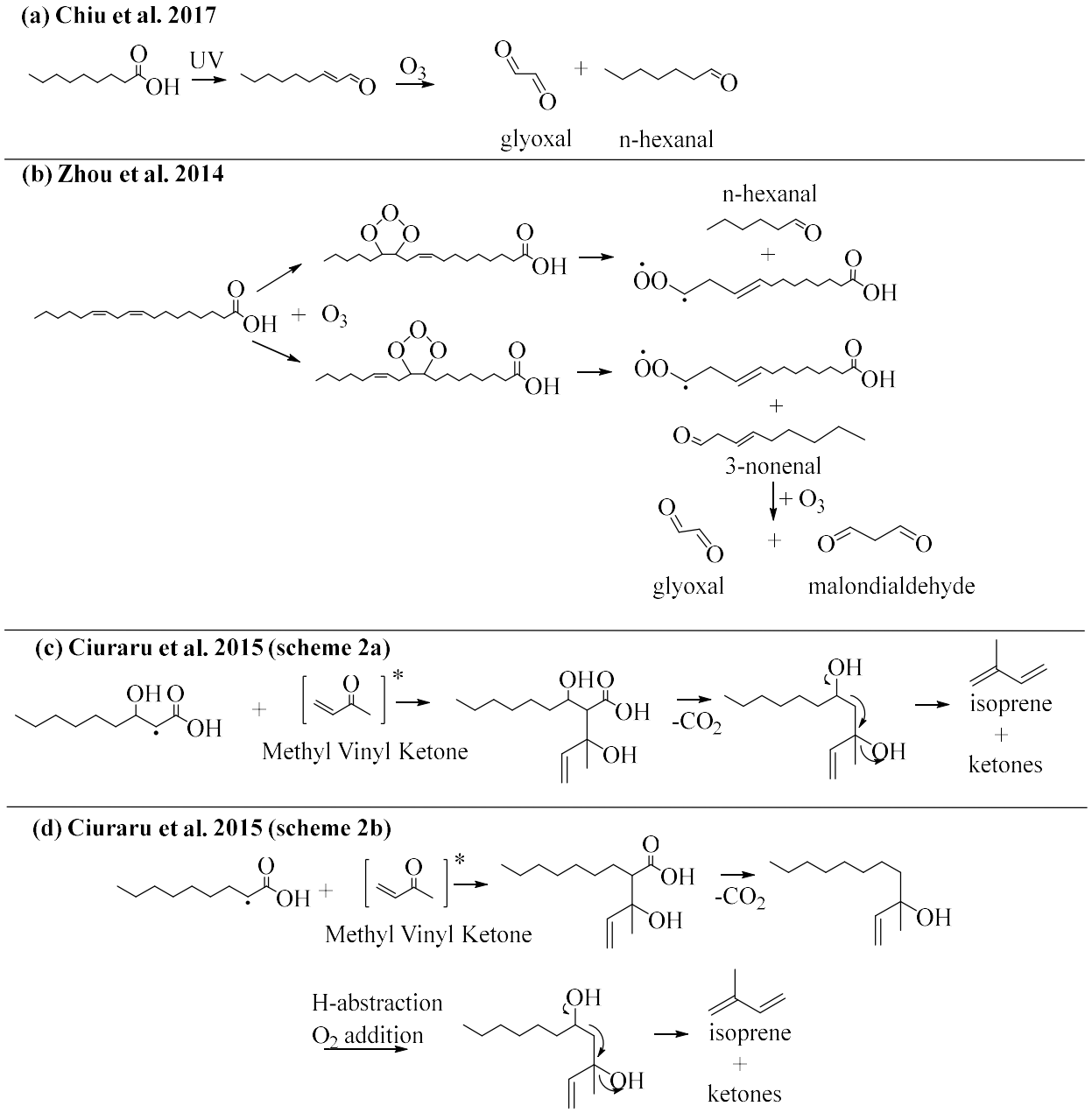

Figure I.2. Overview of proposed abiotic VOC formation pathways from photochemical and heterogeneous mechanisms. Panels (a), (c), and (d) are photochemical mechanisms.[58,59] Panel (b) is a heterogeneous reaction of O_3 at the marine interface.[41]

I.6 Models of interfacial abiotic VOC emission magnitudes

Enrichment of organic molecules in the SSML has been suggested to be ubiquitous across the global ocean when wind speeds are moderate (<13 m s^{-1}), suggesting abiotic emission sources may be viable over a broad spatiotemporal distribution.[69] The SSML is enhanced in organic material by factors of 2-4 over bulk surface water (bulk DOC = 40-80 mM C), which is still significantly less than compact monolayer coverage used in laboratory studies. [69,70] SSML enrichment factors are similar across regions of high and low biological productivity, suggesting abiotic emissions, if present, could be viable even in regions removed from local biological productivity.[69] A global modeling study applying laboratory derived photochemical emission factors and SSML coverage parameterized to windspeed proposed a total photochemical emission source of 23.2–91.9 Tg C yr^{-1}.[40] This emission term is competitive with global DMS emissions (21.1 Tg C yr^{-1}) even at the lower range of the estimate.[22]

To the best of our knowledge, there are no global modeling studies of O_3 driven VOC emissions. To estimate the magnitude of the VOC source stemming from O_3 deposition, we conducted a simple model calculation constrained by measured O_3 deposition velocities and laboratory-derived VOC yields. Reported ozone deposition velocities to the ocean surface are typically from 0.01 to 0.05 cm s^{-1}.[10,67] Taking a representative deposition velocity of 0.02 cm s^{-1} and an O_3 concentration of 30 ppbv results in an O_3 deposition flux of 1.5×10^{10} molecules cm^{-2} s^{-1}. Assigning effective VOC yields of 10 or 50% from O_3 deposition corresponds to emissions of 1.5×10^9 and 7.2×10^9 molecules cm^{-2} s^{-1} respectively. Crudely scaling this emission across the global ocean and assigning an average VOC structure containing 5 carbons results in an emission source of 17.5 to 87.3 Tg C yr^{-1}, comparable to DMS emissions of 21.1 Tg C yr^{-1}.[22] Clearly there are several large uncertainties in this exercise, with the effective VOC yield and molecular structures being almost

entirely unconstrained. Further, ozone deposition is known to be dominated by reactions with iodide at the ocean surface, meaning a 50% VOC yield is likely an upper limit.[67] The lower bound of 10% used in the calculation is arbitrary and only used for illustration, the yield from the actual ocean interface may be orders of magnitude lower. This exercise is intended to emphasize that significant further constraints on VOC emissions from O_3 deposition are necessary and is not intended to be a rigorous prediction of the emissions from heterogeneous production of O_3 at the ocean interface. Still, within the currently available laboratory and field study constraints, this heterogenous VOC production mechanism could be significant,[41,66] but relies heavily on the ratio of the reaction rates between O_3 and iodide compared with O_3 and DOM.

These laboratory measurements and modeling studies provide strong motivation for the field measurement community to determine the extent to which heterogeneous and photochemical reactions at the air-ocean interface impact gas and aerosol concentrations in the marine boundary layer. At present, it is not clear how laboratory measurements, conducted on quiescent surface films with model surfactant systems represent the heterogeneous, chemically complex, and significantly more dilute SSML interface.

I.7 Field measurements of interfacial marine abiotic VOC emission sources

There are several lines of evidence from field observations that provide insight on the extent to which emissions from SSML interfacial chemistry may or may not be important for reactive VOC budgets: 1) Observations of strong (>20x) enrichment in low molecular weight carbonyls in the SSML, relative to the subsurface waters, with a diel cycle peaking in the afternoon suggesting carbonyl production in the SSML may be driven by photochemistry.[48] 2) *In situ* and remote sensing instruments have shown elevated concentrations of glyoxal in the MBL, and nighttime emission flux of glyoxal from the ocean surface,[71] which cannot be accounted for by gas-phase oxidation of

biogenic VOC alone, suggesting a role for SSML chemistry[71–73] 3) Direct measurements of isoprene ocean emission fluxes *via* eddy covariance were shown to be independent of shortwave radiation intensity. [8] 4) Observations of elevated formic acid concentrations over the Arctic Ocean during periods of low wind speed and high solar irradiance have been attributed to a photochemical SSML ocean source.[74] The combined effect of these results and others make clear that our understanding of emissions to the marine atmosphere is incomplete and that abiotic sources need to be constrained.

Recent results from the NASA Atmospheric Tomography study (ATom) have provided an extensive chemically detailed dataset over large regions of the global remote oceans. ATom was a series of flights from 2016-2018 sampling the remote marine atmosphere with the goal of improving understanding of trace gases and short lived greenhouse gases throughout the global remote atmosphere. [75] A key finding from the ATom campaign was the observation of a persistent missing source of acetaldehyde in the boundary layer and free troposphere.[76] Inclusion of an interfacial ocean acetaldehyde source of 34 Tg yr^{-1} improved model to measurement agreement in the boundary layer, but given the short atmospheric lifetime of acetaldehyde (<4 hr) it was not sufficient to explain the enhanced acetaldehyde observed at higher altitudes. This enhanced acetaldehyde acts as a missing sink of hydroxyl (OH) radicals in the marine atmosphere which is not accounted for in current chemistry models. Despite the missing acetaldehyde source, analyses conducted using the GEOS-Chem chemical transport model were able to successfully simulate OH radical magnitudes and vertical profiles within the combined uncertainties of the measurement and model.[56] Notably, the global modeling analysis of Travis et al. (2020)[56] incorporated photochemical abiotic emissions following Bruggemann et al. (2018),[40] which together with an enhanced biogenic emission scheme increased modeled OH reactivity (OHR) over the ocean by

10%. Additionally, a chemical box model simulation using Master Chemical Mechanism v3.3.1 (MCM) chemistry was consistent with observations for OH and hydroperoxyl (HO_2) radicals within the measurement uncertainty.[77] These results suggest that oxidant loadings in the remote marine atmosphere are generally consistent with currently understood emissions and chemistry. In slight contrast, direct measurements of OHR during ATom were larger than the cumulative OHR of the trace gases measured and of OHR in the GEOS-Chem modeling study which suggests a missing OHR on the order of 0.5 s^{-1} in the marine boundary layer.[56,78] The authors suggest a missing sea surface VOC emission source of unknown composition may be responsible for the missing OHR term. Any missing species added to account for the missing OHR would also have to efficiently recycle OH in order to remain consistent with the measured OH and HO_2 concentrations and could not contribute to PAN formation to remain consistent with observed PAN.[56] Given those requirements and the wide suite of VOCs measured during ATom, it is challenging to invoke a large missing VOC that is consistent with all of measured constraints.[56] Together these results suggest that oxidative capacity during ATom was generally well captured in the remote marine troposphere, but that a persistent missing source of acetaldehyde and possibly OHR is present.

I.8 Impact of marine reactive VOC emissions on SOA production

The extent to which marine trace gases impact particle number and mass concentrations following oxidation to low vapor pressure compounds is a complex function of trace gas emission rates, oxidation kinetics and mechanisms, and meteorology. Model determinations of the global ocean contribution to the organic fraction of marine aerosol (OC) vary significantly, ranging from a cumulative primary and SOA source of 8 Tg C yr^{-1} to 25-40 Tg C yr^{-1} considering only SOA.[79,80] Additional modeling work suggests that the global aerosol burden from marine isoprene emissions

is less than 0.05 Tg C yr^{-1}.[42,81] Our group measured VOC fluxes during HiWinGS to estimate the range in secondary organic aerosol production rates (P_{SOA}) from measured isoprene and monoterpene emissions. Using an organic aerosol yield of 0.05, P_{SOA} was calculated to be 0.2 ng m^{-3} d^{-1} and 25 ng m^{-3} d^{-1} for mean and maximum monoterpene fluxes observed during HiWinGS, which roughly scales to 0.016 and 1.97 Tg yr^{-1}.[8] A general version of this calculation is presented in **Figure I.3** for global P_{SOA} from VOC emissions of generic composition as a function of SOA yield. Taking E_{VOC} of 1×10^{10} and 1×10^{11} molecules cm^{-2} s^{-1} and SOA yields of 1% drives total annual SOA production of 6.1 and 40.8 Tg yr^{-1} respectively, which cover the range of model determinations of total marine SOA. Bruggemann et al.[40] calculated that their proposed interfacial photochemistry source would contribute SOA mass of 0.48 – 0.60 Tg yr^{-1}, which corresponds to 1.5-7.5% of the estimated total SOA source described above. Given the paucity of field observations, direct measurements of air-sea flux magnitudes and speciation will be critical to quantitative assessments of the impact of air-sea gas exchange on aerosol particle composition, where the modeling approach of Kim et al. (2017)[8] provides a framework for assessing the impact of observed air-sea emissions of other VOCs on aerosol particle number and mass concentrations.

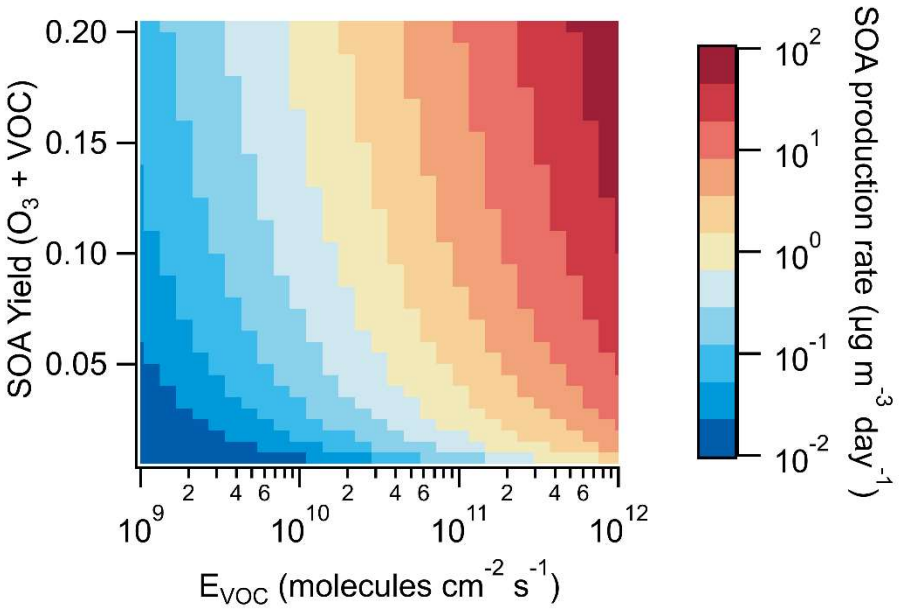

Figure I.3. Modeled secondary organic aerosol production rate (P_{SOA}) as a function of ocean VOC emission flux (E_{VOC}) and condensable SOA product yield. Figure generated following all details of the modeling approach of Kim et al. (2017)[8] extended out to larger E_{VOC} rates.

I.9 Impact of marine reactive VOC emissions on atmospheric oxidative capacity

Air-sea gas exchange can also impact oxidant concentrations by altering OHR and/or oxidant production rates following photolysis (e.g., acetone). Results from the ATom campaign provide constraints on the contribution of non-methane hydrocarbons (NMHC) to OHR in the remote marine boundary layer. Modeled OHR is highly sensitive to VOC emission and speciation. To make this point, we constructed a 0-D VOC emissions box model with the Framework for 0-Dimensional Atmospheric Modeling (F0AM)[82] using MCM chemistry to assess impacts of VOC emissions (E_{VOC}) on OHR (**Figure I.4a**). Emissions are mixed into an 800 m boundary layer height with a 1-day lifetime to dilution. The model is constrained by mean ATom 3 marine boundary layer meteorology and the mixing ratios of all major inorganic species and methane. A baseline OHR of 0.8 s^{-1} is set by reactions with inorganic species and methane. Model runs of different VOC speciation and E_{VOC} rates were run for three days to allow all secondary products that may also contribute to OHR to stabilize, with the day three noontime OHR values reported. The ATom

3 reported 25th-75th percentile range of measured boundary layer OHR were 1.2-2.4 s^{-1}. The largest E_{VOC} consistent with observed OHR is *ca.* 1.1 × 10^{11} molecules cm^{-2} s^{-1} for acetaldehyde. The minimum VOC emission rates consistent with the ATom observations are less clear but are likely to be at least 1× 10^{9} molecules cm^{-2} s^{-1}, which is a typical baseline emission rate of DMS.[8] This model framework provides a method to assess sensitivity of OHR to changes in prescribed VOC air-sea fluxes as new E_{VOC} source terms are developed.

Total OH concentration ([OH]) also serves as a constraint on the potential E_{VOC} term.[12] Donahue and Prinn (1990)[12] used a box-modeling approach to calculate [OH] as a function of E_{VOC} and to determine the range of E_{VOC} consistent with observations in the marine boundary layer, constrained by observed speciated NMHC as well as CO and CH_4. They found that E_{VOC} from 1 × 10^{10} to 2 × 10^{11} molecules cm^{-2} s^{-1} were consistent with observations, with the range driven either by uncertainty in measurements or true atmospheric variability. An adapted version of these results are shown in **Figure I.4b**. A model run for E_{VOC} of 5.4 × 10^{10} molecules cm^{-2} s^{-1} yielded diel average [OH] = 8.4 × 10^{5} molecules cm^{-3} which is in line with [OH] derived from inversions of methyl chloroform mixing ratios. Other box modelling work showed that isoprene emissions of 0.1 – 6 × 10^{9} molecules cm^{-2} s^{-1} suppressed OH and HO_2 radical concentrations by as much as 26 and 13% respectively. The measurements and modelling of OHR and [OH] made during ATom suggest that [OH] is well captured with currently known chemistry in the marine boundary layer but that OHR is underpredicted. It is unclear what speciation and magnitude of interfacial abiotic VOC emissions would be consistent with those observations. The net impact of an interfacial abiotic E_{VOC} of 1 × 10^{10} molecules cm^{-2} s^{-1} with SOA yield of 1% and a reactivity with OH equivalent to acetaldehyde would result in a P_{SOA} of 6.1 Tg yr^{-1} and an increase in ROH of nearly

0.1 s^{-1}. Both of those terms would have important impacts on chemistry of the remote marine atmosphere which need to be further constrained.

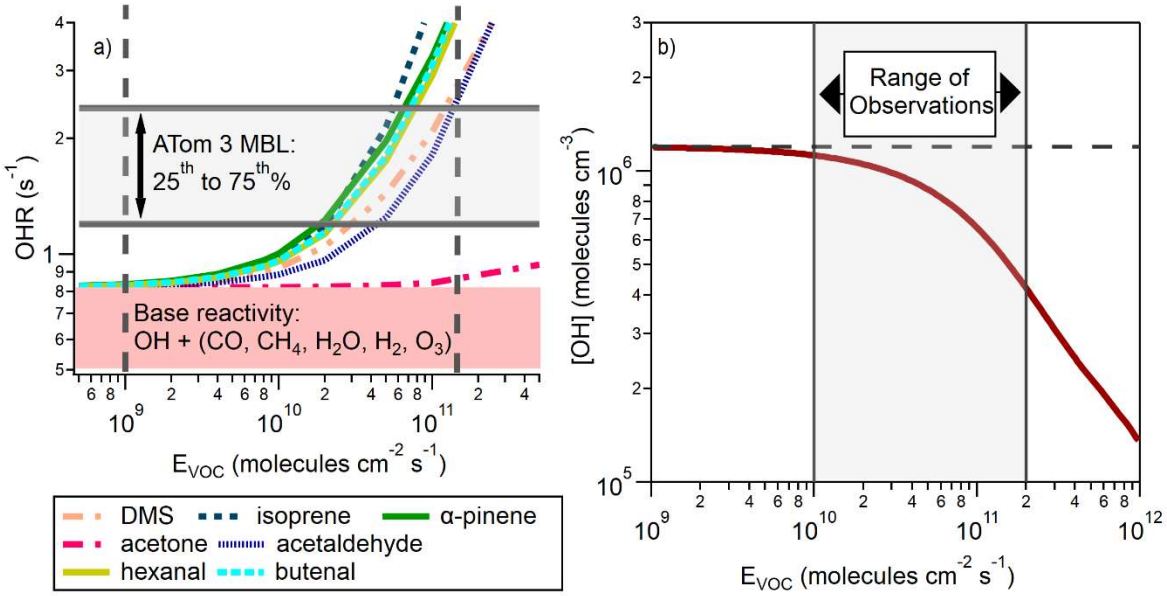

Figure I.4. a) Modeled OH reactivity (OHR) as a function of VOC emission rates (E_{VOC}) for various VOC speciation. Horizontal solid lines are the 25th to 75th percentile range of R_{OH} observations made during ATom 3. Dashed vertical lines are the corresponding minimum and maximum E_{VOC} consistent with the observed ATom OHR. b) Modeled dependence of diel average [OH] on E_{VOC}. The shaded region represents the range in calculated E_{VOC} flux constrained by NMHC gas observations in the marine boundary layer (adapted from Donahue and Prinn (1990)[12]).

I.10 O_3 deposition and surface reactions

The deposition of tropospheric ozone (O_3) to water surfaces is a significant but poorly constrained component of the global tropospheric O_3 budget [83]. O_3 deposition is significant as both a sink of tropospheric O_3 and as a source of VOCs to the marine atmosphere *via* heterogeneous reactions at the ocean interface as described in previous sections. Overall there are few direct observations of O_3 deposition to water surfaces, with measured values of O_3 deposition velocities ($v_d(O_3)$) spanning from 0.01 to 0.15 cm s^{-1} for seawater and 0.01 to 0.1 cm s^{-1} for freshwater [10,84–87].

O_3 is a sparingly soluble molecule ($H = 1 \times 10^{-2}$ M atm^{-1}) and surface reactivity of O_3 is known to significantly enhance O_3 deposition rates.[88] The primary surface reactants driving O_3 deposition to

the ocean are iodide (I^-) and dissolved organic carbon (DOC) species as shown in R1 and R2 respectively [67,84]. DOC is a complex and poorly understood mixture of saturated and unsaturated organic molecules which is ubiquitous in surface waters of oceans and lakes [89,90].

$$O_3 + I^- \xrightarrow[k_{I^-}]{} IO_3^- \qquad \text{R1}$$

$$O_3 + \text{DOC} \xrightarrow[k_{DOC}]{} \text{Products} \qquad \text{R2}$$

The relative contribution of these two reaction pathways on controlling O_3 deposition rates are poorly known and have significant differences between modelling approaches, with some models treating DOC reactions as negligible and others showing reactivity with DOC and I^- contributing roughly equally to O_3 deposition.[67,84,91] The relative reactivity of O_3 with DOC vs I^- is of fundamental importance in setting the potential for O_3 heterogeneous reactions to emit VOCs, as only reactions with DOC are expected to drive VOC emissions. Chapter 1 describes EC flux observations of O_3 deposition to a coastal ocean site where I^- and DOC are both present and to a eutrophic lake where DOC is high (>400 μM) but I^- is negligible as a way to assess the relative significance of these terms in controlling O_3 deposition.

I.11 Chemical Ionization Mass Spectrometry

Measurements of reactive trace gases in the ambient atmosphere pose substantial analytical and instrumental challenges. Detection of trace gases present at part per trillion mixing ratios necessitates both high sensitivity and high selectivity to avoid interferences in complex sampling environments. Instruments must also be field deployable (relatively small and low power consumption) and stable over wide ranges of humidity, temperature, and trace gas loadings. In recent years chemical ionization mass spectrometry (CIMS) techniques have emerged as powerful tools for measurements of a wide array of reactive trace gases from various sampling platforms.[92]

In CIMS methods, the analyte gas is ionized by an intentionally introduced reagent ion before detection in the mass spectrometer. Choice of the reagent ion determines the class of analyte molecules that can be detected, introducing a selectivity in the detection. To date, a variety of reagent ions have been successfully applied for atmospheric trace gas measurements, including proton transfer from H_3O^+ for detection of unsaturated and moderately oxidized molecules,[93] acetate anions for detection of strong acids which can transfer a proton to the acetate anion,[94] iodide anions (I^-) for detection of a diverse set of oxygenated molecules which can form stable adducts with I^-[95], and several other reagent ion schemes.[96–99] Development and characterization of new reagent ion chemistry methods allows for the sensitive and precise detection of other atmospheric trace gases *via* CIMS. An overview of CIMS methods used in this work is presented in **Table I.1**. This thesis describes the characterization of benzene cluster cation chemistry for detection of isoprene and monoterpenes (Chapter 5), and the development and characterization of oxygen anion chemistry for the detection of O_3 and NO_2 (Chapter 4).

Reagent Ion	**Sensitive to**	**Ionization Modes**	**Thesis Chapter**
$O_2^-, O_2^-(H_2O)_n$	O_3, NO_2, CH_3OOH,SO_2	X^- (charge transfer) $O_2 \bullet X^-$ (adduct formation)	1 & 4
H_3O^+	Low oxidation VOCs	HX^+ (proton-transfer	2
I^-, $I^-(H_2O)_n$	OVOCs	$I \bullet X^-$ (adduct formation)	3
$(C_6H_6)^+_n$	BVOCs (DMS, isoprene, MT)	X^+ (charge transfer) $C_6H_6 \bullet X^+$ (adduct formation)	5

Table I.1. Overview of chemical ionization mass spectrometery reagent ion techniques used in this thesis work.

In recent years commercially available time-of-flight (ToF) mass analyzers suitable for field deployment and atmospheric sampling have become commercially available. These include

compact ToF (cToF) mass analyzers with resolving power on the order of 1000 *m/Δm* and high-resolution (HToF) mass analyzers with resolution of *ca.* 5000 *m/Δm*. The cToF mass analyzers are capable of unit mass resolution for the masses of volatile compounds present in the atmosphere (typically <500 *m/Q*). The HToF mass analyzers allow better than unit mass analysis allowing for separation of ions at the same nominal mass, increasing confidence and specificity of quantified peaks. The larger general advantage of cToF and HToF instruments over quadrupole mass analyzers is the collection of the full mass spectra simultaneously at high time resolution (>1Hz). This has proven tremendously useful in atmospheric sampling, enabling larger data coverage and high resolution sampling necessary for mobile platform sampling and eddy covariance techniques.[100–102] The work described in this thesis utilizes both cToF and HToF mass analyzers.

I.12 Eddy Covariance Flux

The vertical flux (*F*) of a trace gas can be measured with the well-established eddy covariance (EC) technique where flux is calculated as the time average of the instantaneous covariances from the mean of vertical wind (*w*) and the scalar magnitude (*x*) shown in Eq. 2. Overbars are means and primes are the instantaneous variance from the mean. Here *N* is the total number of data points during the minute flux averaging period (typically 10-30 minutes). This technique exploits the turbulent mixing typically present in the boundary layer (~lowest 1 km) of the Earth's atmosphere, where three-dimensional turbulent eddies of various length scales carry compounds to and from interface.

$$F = \frac{1}{N}\sum_{i=1}^{N}(w_i - \bar{w})\,(x_i - \overline{x_3}) = \langle w' x_3' \rangle \qquad \text{E2}$$

EC sampling imposes stringent sensor requirements which has limited its suitability for measurements of many atmospheric constituents of interest. Sensors suitable for EC measurements must be capable of high time response measurements (>1Hz) in order to capture the smaller scale

turbulent eddies. The sensor must also have high short-term precision in order to resolve small fluctuations in analyte signal driven by true vertical flux from the instrument noise. Finally, the sensor must have long term stability over the length of the flux averaging period (~30 minutes) in order to minimize uncertainty in the calculated flux. CIMS methods have proven particularly well suited for EC measurements from a variety of sampling platforms, including stationary ground sites[5], underway research vessels[8], and aircraft[102].

I.13 Thesis Overview

Recent laboratory and field observations have challenged the assumption that ocean biochemical processes are the primary driver of marine trace gas emissions and SOA chemistry. Laboratory studies have highlighted the potential for heterogenous and photochemical reactions at the ocean interface as new sources of VOCs in the marine atmosphere, which may have very different spatial and temporal distributions compared to biogenic emissions. In addition, large scale field campaigns suggest a large missing source of acetaldehyde and possibly OH reactivity in the remote marine atmosphere. However there remains significant uncertainty in scaling laboratory observations of interfacial VOC production to the ambient atmosphere which provides a clear motivation for targeted research to close the gap between laboratory model system studies and large-scale atmospheric concentration measurements.

This thesis describes work to address these open questions in ocean-atmosphere trace gas exchange. This includes development of a CIMS method enabling EC flux measurements of O_3 deposition to water surfaces (Chapter 4), which was applied for O_3 deposition studies to the coastal Pacific Ocean and a freshwater eutrophic lake (Lake Mendota, Madison WI) as discussed in Chapter 1. These observations allow constraints on O_3 deposition rates and the potential role of heterogeneous O_3 reactions as a source of abiotic VOCs in the marine atmosphere. Chapter 2

describes direct EC flux observations of a broad survey of VOCs detectable by proton-transfer-reaction (PTR) CIMS, with the goal of constraining the relative significance of biotic and abiotic VOC emissions. In Chapter 3, the application of airborne EC flux vertical profiles are explored as a probe of cloud uptake and processing in the marine boundary layer. Detailed laboratory characterizations of benzene cluster cation reagent ion chemistry for the detection of isoprene, monoterpenes, and sesquiterpenes is presented in Chapter 5. This method was previously used for the only EC measurements of ocean isoprene and monoterpene emission fluxes[8] and will be useful in interpreting those results and in future field deployments utilizing benzene cluster cations.

References

(1) Liss, P. S.; Slater, P. G. Flux of Gases across the Air-Sea Interface. *Nature* **1974**, *247* (5438), 181–184. https://doi.org/10.1038/247181a0.

(2) Fairall, C. W.; Bradley, E. F.; Rogers, D. P.; Edson, J. B.; Young, G. S. Bulk Parameterization of Air-Sea Fluxes for TOGA COARE. *J. Geophys. Res.* **1996**, *101*, 3747–3764. https://doi.org/10.4236/ica.2011.23023.

(3) Fairaill, C. W.; Hare, J. E.; Edson, J. B.; McGillis, W.; Fairall, C. W.; Hare, J. E.; Edson, J. B.; McGillis, W. Parameterization and Micrometeorological Measurement of Air–Sea Gas Transfer. *Boundary-Layer Meteorol.* **1999**, *96* (1), 63–105. https://doi.org/10.1023/A:1002662826020.

(4) Johnson, M. T. A Numerical Scheme to Calculate Temperature and Salinity Dependent Air-Water Transfer Velocities for Any Gas. *Ocean Sci.* **2010**, *6* (4), 913–932. https://doi.org/10.5194/os-6-913-2010.

(5) Kim, M. J.; Farmer, D. K.; Bertram, T. H. A Controlling Role for the Air-Sea Interface in the Chemical Processing of Reactive Nitrogen in the Coastal Marine Boundary Layer. *Proc. Natl. Acad. Sci. U. S. A.* **2014**, *111* (11), 3943–3948. https://doi.org/10.1073/pnas.1318694111.

(6) Porter, J. G.; De Bruyn, W.; Saltzman, E. S. Eddy Flux Measurements of Sulfur Dioxide Deposition to the Sea Surface. *Atmos. Chem. Phys.* **2018**, *18* (20), 15291–15305. https://doi.org/10.5194/acp-18-15291-2018.

(7) Coburn, S.; Ortega, I.; Thalman, R.; Blomquist, B.; Fairall, C. W.; Volkamer, R. Measurements of Diurnal Variations and Eddy Covariance (EC) Fluxes of Glyoxal in the

Tropical Marine Boundary Layer: Description of the Fast LED-CE-DOAS Instrument. *Atmos. Meas. Tech.* **2014**, *7* (10), 3579–3595. https://doi.org/10.5194/amt-7-3579-2014.

(8) Kim, M. J.; Novak, G. A.; Zoerb, M. C.; Yang, M.; Blomquist, B. W.; Huebert, B. J.; Cappa, C. D.; Bertram, T. H. Air-Sea Exchange of Biogenic Volatile Organic Compounds and the Impact on Aerosol Particle Size Distributions. *Geophys. Res. Lett.* **2017**, *44* (8), 3887–3896. https://doi.org/10.1002/2017GL072975.

(9) Yang, M.; Beale, R.; Smyth, T.; Blomquist, B. Vertical Fluxes and Atmospheric Cycling of Methanol, Acetaldehyde, and Acetone in a Coastal Environment. *Atmos. Chem. Phys. Discuss.* **2013**, *13* (3), 8101–8152. https://doi.org/10.5194/acpd-13-8101-2013.

(10) Helmig, D.; Lang, E. K.; Bariteau, L.; Boylan, P.; Fairall, C. W.; Ganzeveld, L.; Hare, J.; Huebert, B. J.; Pallandt, M. Atmosphere-Ocean Ozone Fluxes during the TexAQS 2006, STRATUS 2006, GOMECC 2007, GasEx 2008, and AMMA 2008 Cruises. *J. Geophys. Res. Atmos.* **2012**, *117* (D4). https://doi.org/10.1029/2011JD015955.

(11) Lenschow, D. H.; Pearson, R.; Stankov, B. B. Estimating the Ozone Budget in the Boundary Layer by Use of Aircraft Measurements of Ozone Eddy Flux and Mean Concentration. *J. Geophys. Res.* **1981**, *86* (C8), 7291. https://doi.org/10.1029/JC086iC08p07291.

(12) Donahue, N. M.; Prinn, R. G.; Prinn, G.; Prinn, R. G. Nonmethane Hydrocarbon Chemistry in the Remote Marine Boundary Layer. *J. Geophys. Res.* **1990**, *95* (D11), 18387–18411. https://doi.org/10.1029/JD095iD11p18387.

(13) Liakakou, E.; Vrekoussis, M.; Bonsang, B.; Donousis, C.; Kanakidou, M.; Mihalopoulos, N. Isoprene above the Eastern Mediterranean: Seasonal Variation and Contribution to the Oxidation Capacity of the Atmosphere. *Atmos. Environ.* **2007**, *41* (5), 1002–1010. https://doi.org/10.1016/j.atmosenv.2006.09.034.

(14) Palmer, P. I.; Shaw, S. L. Quantifying Global Marine Isoprene Fluxes Using MODIS Chlorophyll Observations. *Geophys. Res. Lett.* **2005**, *32* (9), 1–5. https://doi.org/10.1029/2005GL022592.

(15) Gantt, B.; Johnson, M. S.; Meskhidze, N.; Sciare, J.; Ovadnevaite, J.; Ceburnis, D.; O'Dowd, C. D. Model Evaluation of Marine Primary Organic Aerosol Emission Schemes. *Atmos. Chem. Phys.* **2012**, *12* (18), 8553–8566. https://doi.org/10.5194/acp-12-8553-2012.

(16) Meskhidze, N.; Xu, J.; Gantt, B.; Zhang, Y.; Nenes, A.; Ghan, S. J.; Liu, X.; Easter, R.; Zaveri, R. Global Distribution and Climate Forcing of Marine Organic Aerosol: 1. Model Improvements and Evaluation. *Atmos. Chem. Phys.* **2011**, *11* (22), 11689–11705. https://doi.org/10.5194/acp-11-11689-2011.

(17) Charlson, R. J.; Lovelock, J. E.; Andreaei, M. O.; Warren, S. G. Oceanic Phytoplankton, Atmospheric Sulphur, Cloud. *Nature* **1987**, *330*, 1987.

(18) Quinn, P. K.; Bates, T. S. The Case against Climate Regulation via Oceanic Phytoplankton Sulphur Emissions. *Nature* **2011**, *480* (7375), 51–56. https://doi.org/10.1038/nature10580.

(19) Grandey, B. S.; Wang, C. Enhanced Marine Sulphur Emissions Offset Global Warming and Impact Rainfall. *Sci. Rep.* **2015**, *5*, 1–7. https://doi.org/10.1038/srep13055.

(20) Griffin, R. J.; Cocker, D. R.; Flagan, R. C.; Seinfeld, J. H. Organic Aerosol Formation from the Oxidation of Biogenic Hydrocarbons. *J. Geophys. Res. Atmos.* **1999**, *104* (D3), 3555–3567. https://doi.org/10.1029/1998JD100049.

(21) Ehn, M.; Thornton, J. A.; Kleist, E.; Sipila, M.; Junninen, H.; Pullinen, I.; Springer, M.; Rubach, F.; Tillmann, R.; Lee, B.; et al. A Large Source of Low-Volatility Secondary Organic Aerosol. *Nature* **2014**, *506* (7489), 476–479. https://doi.org/10.1038/nature13032.

(22) Lana, A.; Bell, T. G.; Simó, R.; Vallina, S. M.; Ballabrera-Poy, J.; Kettle, A. J.; Dachs, J.; Bopp, L.; Saltzman, E. S.; Stefels, J.; et al. An Updated Climatology of Surface Dimethlysulfide Concentrations and Emission Fluxes in the Global Ocean. *Global Biogeochem. Cycles* **2011**, *25* (1), 1–17. https://doi.org/10.1029/2010GB003850.

(23) Galí, M.; Levasseur, M.; Devred, E.; Simó, R.; Babin, M. Sea-Surface Dimethylsulfide (DMS) Concentration from Satellite Data at Global and Regional Scales. *Biogeosciences* **2018**, *15* (11), 3497–3519. https://doi.org/10.5194/bg-15-3497-2018.

(24) Kloster, S.; Feichter, J.; Maier-Reimer, E.; Six, K. D.; Stier, P.; Wetzel, P. DMS Cycle in the Marine Ocean-Atmosphere System - A Global Model Study. *Biogeosciences* **2006**, *3* (1), 29–51. https://doi.org/10.5194/bg-3-29-2006.

(25) Land, P. E.; Shutler, J. D.; Bell, T. G.; Yang, M. Exploiting Satellite Earth Observation to Quantify Current Global Oceanic DMS Flux and Its Future Climate Sensitivity. *J. Geophys. Res. Ocean.* **2014**. https://doi.org/10.1002/2014JC010104.

(26) Carpenter, L. J.; Archer, S. D.; Beale, R. Ocean-Atmosphere Trace Gas Exchange. *Chem. Soc. Rev.* **2012**, *41* (19), 6473–6506. https://doi.org/10.1039/c2cs35121h.

(27) Hoffmann, E. H.; Tilgner, A.; Schrödner, R.; Bräuer, P.; Wolke, R.; Herrmann, H. An Advanced Modeling Study on the Impacts and Atmospheric Implications of Multiphase Dimethyl Sulfide Chemistry. *Proc. Natl. Acad. Sci.* **2016**, *113* (42), 11776–11781. https://doi.org/10.1073/pnas.1606320113.

(28) Faloona, I. Sulfur Processing in the Marine Atmospheric Boundary Layer: A Review and Critical Assessment of Modeling Uncertainties. *Atmos. Environ.* **2009**, *43* (18), 2841–2854. https://doi.org/10.1016/j.atmosenv.2009.02.043.

(29) Wu, R.; Wang, S.; Wang, L. New Mechanism for the Atmospheric Oxidation of Dimethyl Sulfide. The Importance of Intramolecular Hydrogen Shift in a CH3SCH2OO Radical. *J. Phys. Chem. A* **2015**, *119* (1), 112–117. https://doi.org/10.1021/jp511616j.

(30) Berndt, T.; Scholz, W.; Mentler, B.; Fischer, L.; Hoffmann, E. H.; Tilgner, A.; Hyttinen, N.; Prisle, N. L.; Hansel, A.; Herrmann, H. Fast Peroxy Radical Isomerization and OH Recycling in the Reaction of OH Radicals with Dimethyl Sulfide. *J. Phys. Chem. Lett.* **2019**, 6478–6483. https://doi.org/10.1021/acs.jpclett.9b02567.

(31) Veres, P. R.; Neuman, J. A.; Bertram, T. H.; Assaf, E.; Wolfe, G. M.; Williamson, C. J.; Weinzierl, B.; Tilmes, S.; Thompson, C. R.; Thames, A. B.; et al. Global Airborne Sampling Reveals a Previously Unobserved Dimethyl Sulfide Oxidation Mechanism in the Marine Atmosphere. *Proc. Natl. Acad. Sci.* **2020**, 201919344. https://doi.org/10.1073/pnas.1919344117.

(32) Shaw, S. L.; Gantt, B.; Meskhidze, N. Production and Emissions of Marine Isoprene and Monoterpenes: A Review. *Adv. Meteorol.* **2010**, *2010* (1), 1–24. https://doi.org/10.1155/2010/408696.

(33) Zindler, C., C. A. Marandino, H. W. B.; F. Schütte, and E. S. S. Nutrients Determine DMS and Isoprene Distribution in Atlantic Ocean. *Geophys. Res. Lett.* **2014**, *41* (9), 3181–3188. https://doi.org/https://doi.org/10.1002/2014GL059547.

(34) Meskhidze, N.; Sabolis, A.; Reed, R.; Kamykowski, D. Quantifying Environmental Stress-Induced Emissions of Algal Isoprene and Monoterpenes Using Laboratory Measurements. *Biogeosciences* **2015**, *12* (3), 637–651. https://doi.org/10.5194/bg-12-637-2015.

(35) Yassaa, N.; Peeken, I.; Zllner, E.; Bluhm, K.; Arnold, S.; Spracklen, D.; Williams, J. Evidence for Marine Production of Monoterpenes. *Environ. Chem.* **2008**, *5* (6), 391–401. https://doi.org/10.1071/EN08047.

(36) Hackenberg, S. C.; Andrews, S. J.; Airs, R. L.; Arnold, S. R.; Bouman, H. A.; Cummings, D.; Lewis, A. C.; Minaeian, J. K.; Reifel, K. M.; Small, A.; et al. Basin-Scale Observations of Monoterpenes in the Arctic and Atlantic Oceans. *Environ. Sci. Technol.* **2017**, *51* (18), 10449–10458. https://doi.org/10.1021/acs.est.7b02240.

(37) Matsunaga, S.; Mochida, M.; Saito, T.; Kawamura, K. In Situ Measurement of Isoprene in the Marine Air and Surface Seawater from the Western North Pacific. *Atmos. Environ.* **2002**, *36* (39–40), 6051–6057. https://doi.org/10.1016/S1352-2310(02)00657-X.

(38) Broadgate, W. J.; Liss, P. S.; Penkett, A.; June, M. Seasonal Emissions of Isoprene and Other Reactive Hydrocarbon Gases from the Ocean. *Geophys. Res. Lett.* **1997**, *24* (21), 2675–2678. https://doi.org/https://doi.org/10.1029/97GL02736.

(39) Luo, G.; Yu, F. A Numerical Evaluation of Global Oceanic Emissions of Alpha-Pinene and Isoprene. *Atmos. Chem. Phys.* **2010**, *10* (4), 2007–2015. https://doi.org/doi:10.5194/acp-10-2007-2010.

(40) Brüggemann, M.; Hayeck, N.; George, C. Interfacial Photochemistry at the Ocean Surface

Is a Global Source of Organic Vapors and Aerosols. *Nat. Commun.* **2018**, *9* (1), 1–19. https://doi.org/10.1038/s41467-018-04528-7.

(41) Zhou, S.; Gonzalez, L.; Leithead, A.; Finewax, Z.; Thalman, R.; Vlasenko, A.; Vagle, S.; Miller, L. A.; Li, S. M.; Bureekul, S.; et al. Formation of Gas-Phase Carbonyls from Heterogeneous Oxidation of Polyunsaturated Fatty Acids at the Air-Water Interface and of the Sea Surface Microlayer. *Atmos. Chem. Phys.* **2014**. https://doi.org/10.5194/acp-14-1371-2014.

(42) Arnold, S. R.; Spracklen, D. V.; Williams, J.; Yassaa, N.; Sciare, J.; Bonsang, B.; Gros, V.; Peeken, I.; Lewis, A. C.; Alvain, S.; et al. Evaluation of the Global Oceanic Isoprene Source and Its Impacts on Marine Organic Carbon Aerosol. *Atmos. Chem. Phys. Discuss.* **2008**, *8* (4), 16445–16471. https://doi.org/10.5194/acpd-8-16445-2008.

(43) Hackenberg, S. C.; Andrews, S. J.; Airs, R.; Arnold, S. R.; Bouman, H. A.; Brewin, R. J. W.; Chance, R. J.; Cummings, D.; Dall'Olmo, G.; Lewis, A. C.; et al. Potential Controls of Isoprene in the Surface Ocean. *Global Biogeochem. Cycles* **2017**, *31* (4), 644–662. https://doi.org/10.1002/2016GB005531.

(44) Dahl, E. E.; Saltzman, E. S. Alkyl Nitrate Photochemical Production Rates in North Pacific Seawater. *Mar. Chem.* **2008**, *112* (3–4), 137–141. https://doi.org/10.1016/j.marchem.2008.10.002.

(45) Yang, M.; Beale, R.; Liss, P.; Johnson, M.; Blomquist, B.; Nightingale, P. Air–Sea Fluxes of Oxygenated Volatile Organic Compounds across the Atlantic Ocean. *Atmos. Chem. Phys.* **2014**, *14* (14), 7499–7517. https://doi.org/10.5194/acp-14-7499-2014.

(46) Fischer, E. V; Jacob, D. J.; Millet, D. B.; Yantosca, R. M.; Mao, J. The Role of the Ocean in the Global Atmospheric Budget of Acetone. *Geophys. Res. Lett.* **2012**, *39* (1), n/a-n/a. https://doi.org/10.1029/2011gl050086.

(47) Dixon, J. L.; Beale, R.; Nightingale, P. D. Production of Methanol, Acetaldehyde, and Acetone in the Atlantic Ocean. *Geophys. Res. Lett.* **2013**, *40* (17), 4700–4705. https://doi.org/10.1002/grl.50922.

(48) Zhou, X.; Mopper, K. Photochemical Production of Low-Molecular-Weight Carbonyl Compounds in Seawater and Surface Microlayer and Their Air-Sea Exchange. *Mar. Chem.* **1997**, *56*, 201–213. https://doi.org/10.1016/S0304-4203(96)00076-X.

(49) Kim, M. J.; Michaud, J. M.; Williams, R.; Sherwood, B. P.; Pomeroy, R.; Azam, F.; Burkart, M.; Bertram, T. H. Bacteria-Driven Production of Alkyl Nitrates in Seawater. *Geophys. Res. Lett.* **2015**, *42* (2), 597–604. https://doi.org/10.1002/2014gl062865.

(50) Neu, J. L.; Lawler, M. J.; Prather, M. J.; Saltzman, E. S. Oceanic Alkyl Nitrates as a Natural Source of Tropospheric Ozone. *Geophys. Res. Lett.* **2008**, *35* (13).

https://doi.org/10.1029/2008gl034189.

(51) Ge, S.; Xu, Y.; Jia, L. Effects of Inorganic Seeds on Secondary Organic Aerosol Formation from Photochemical Oxidation of Acetone in a Chamber. *Atmos. Environ.* **2017**, *170*, 205–215. https://doi.org/10.1016/j.atmosenv.2017.09.036.

(52) McKeen, S. A.; Gierczak, T.; Burkholder, J. B.; Wennberg, P. O.; Hanisco, T. F.; Keim, E. R.; Gao, R. S.; Liu, S. C.; Ravishankara, A. R.; Fahey, D. W. The Photochemistry of Acetone in the Upper Troposphere: A Source of Odd-Hydrogen Radicals. *Geophys. Res. Lett.* **1997**, *24* (24), 3177–3180. https://doi.org/10.1029/97gl03349.

(53) Mopper, K.; Stahovec, W. L. Sources and Sinks of Low Molecular Weight Organic Carbonyl Compounds in Seawater. *Mar. Chem.* **1986**. https://doi.org/10.1016/0304-4203(86)90052-6.

(54) Wang, S.; Hornbrook, R. S.; Hills, A.; Emmons, L. K.; Tilmes, S.; Lamarque, J. F.; Jimenez, J. L.; Campuzano-Jost, P.; Nault, B. A.; Crounse, J. D.; et al. Atmospheric Acetaldehyde: Importance of Air-Sea Exchange and a Missing Source in the Remote Troposphere. *Geophys. Res. Lett.* **2019**, *46* (10), 5601–5613. https://doi.org/10.1029/2019GL082034.

(55) Millet, D. B.; Guenther, A.; Siegel, D. A.; Nelson, N. B.; Singh, H. B.; de Gouw, J. A.; Warneke, C.; Williams, J.; Eerdekens, G.; Sinha, V.; et al. Global Atmospheric Budget of Acetaldehyde: 3-D Model Analysis and Constraints from in-Situ and Satellite Observations. *Atmos. Chem. Phys. Discuss.* **2010**, *10*, 3405–3425. https://doi.org/10.5194/acp-10-3405-2010.

(56) Travis, K.; Heald, C.; Allen, H.; Apel, E.; Arnold, S.; Blake, D.; Brune, W.; Chen, X.; Commane, R.; Crounse, J.; et al. Constraining Remote Oxidation Capacity with ATom Observations. *Atmos. Chem. Phys. Discuss.* **2020**, 1–41. https://doi.org/https://doi.org/10.5194/acp-2019-931.

(57) Donaldson, D. J.; Vaida, V. The Influence of Organic Films at the Air-Aqueous Boundary on Atmospheric Processes. *Chem. Rev.* **2006**, *106* (4), 1445–1461. https://doi.org/10.1021/cr040367c.

(58) Ciuraru, R.; Fine, L.; Pinxteren, M. Van; D'Anna, B.; Herrmann, H.; George, C. Unravelling New Processes at Interfaces: Photochemical Isoprene Production at the Sea Surface. *Environ. Sci. Technol.* **2015**, *49* (22), 13199–13205. https://doi.org/10.1021/acs.est.5b02388.

(59) Ciuraru, R.; Fine, L.; Van Pinxteren, M.; D'Anna, B.; Herrmann, H.; George, C. Photosensitized Production of Functionalized and Unsaturated Organic Compounds at the Air-Sea Interface. *Sci. Rep.* **2015**, *5* (March), 1–10. https://doi.org/10.1038/srep12741.

(60) Fu, H.; Ciuraru, R.; Dupart, Y.; Passananti, M.; Tinel, L.; Rossignol, S.; Perrier, S.;

Donaldson, D. J.; Chen, J.; George, C. Photosensitized Production of Atmospherically Reactive Organic Compounds at the Air/Aqueous Interface. *J. Am. Chem. Soc.* **2015**, *137* (26), 8348–8351. https://doi.org/10.1021/jacs.5b04051.

(61) Chiu, R.; Tinel, L.; Gonzalez, L.; Ciuraru, R.; Bernard, F.; George, C.; Volkamer, R. UV Photochemistry of Carboxylic Acids at the Air-Sea Boundary: A Relevant Source of Glyoxal and Other Oxygenated VOC in the Marine Atmosphere. *Geophys. Res. Lett.* **2017**, *44* (2), 1079–1087. https://doi.org/10.1002/2016GL071240.

(62) Tinel, L.; Rossignol, S.; Bianco, A.; Passananti, M.; Perrier, S.; Wang, X.; Brigante, M.; Donaldson, D. J.; George, C. Mechanistic Insights on the Photosensitized Chemistry of a Fatty Acid at the Air/Water Interface. *Environ. Sci. Technol.* **2016**, *50* (20), 11041–11048. https://doi.org/10.1021/acs.est.6b03165.

(63) Brüggemann, M.; Hayeck, N.; Bonnineau, C.; Pesce, S.; Alpert, P. A.; Perrier, S.; Zuth, C.; Hoffmann, T.; Chen, J.; George, C. Interfacial Photochemistry of Biogenic Surfactants: A Major Source of Abiotic Volatile Organic Compounds. *Faraday Discuss.* **2017**, *200*, 59–74. https://doi.org/10.1039/c7fd00022g.

(64) Rossignol, S.; Tinel, L.; Bianco, A.; Passananti, M.; Brigante, M.; Donaldson, D. J.; George, C.; Lyon, U.; Claude, U.; Lyon, B. Atmospheric Photochemistry at a Fatty Acid–Coated Air-Water Interface. *Science (80-.).* **2016**, *353* (6300), 699–702. https://doi.org/10.1126/science.aaf3617.

(65) Trueblood, J. V; Alves, M. R.; Power, D.; Santander, M. V; Cochran, R. E.; Prather, K. A.; Grassian, V. H. Shedding Light on Photosensitized Reactions within Marine-Relevant Organic Thin Films. *ACS Earth Sp. Chem.* **2019**, *3*, 1614–1623. https://doi.org/10.1021/acsearthspacechem.9b00066.

(66) Schneider, S. R.; Collins, D. B.; Lim, C. Y.; Zhu, L.; Abbatt, J. P. D. Formation of Secondary Organic Aerosol from the Heterogeneous Oxidation by Ozone of a Phytoplankton Culture. *ACS Earth Sp. Chem.* **2019**, *3*, 0–8. https://doi.org/10.1021/acsearthspacechem.9b00201.

(67) Chang, W.; Heikes, B. G.; Lee, M. Ozone Deposition to the Sea Surface: Chemical Enhancement and Wind Speed Dependence. *Atmos. Environ.* **2004**, *38* (7), 1053–1059. https://doi.org/10.1016/j.atmosenv.2003.10.050.

(68) Carpenter, L. J.; MacDonald, S. M.; Shaw, M. D.; Kumar, R.; Saunders, R. W.; Parthipan, R.; Wilson, J.; Plane, J. M. C. C. Atmospheric Iodine Levels Influenced by Sea Surface Emissions of Inorganic Iodine. *Nat. Geosci.* **2013**, *6* (2), 108–111. https://doi.org/10.1038/ngeo1687.

(69) Wurl, O.; Wurl, E.; Miller, L.; Johnson, K.; Vagle, S. Formation and Global Distribution of Sea-Surface Microlayers. **2011**, 121–135. https://doi.org/10.5194/bg-8-121-2011.

(70) Carlson, C. A.; Hansell, D. A. *DOM Sources, Sinks, Reactivity, and Budgets*; 2014. https://doi.org/10.1016/B978-0-12-405940-5.00003-0.

(71) Coburn, S.; Ortega, I.; Thalman, R.; Blomquist, B.; Fairall, C. W.; Volkamer, R. Measurements of Diurnal Variations and Eddy Covariance (EC) Fluxes of Glyoxal in the Tropical Marine Boundary Layer: Description of the Fast LED-CE-DOAS Instrument. *Atmos. Meas. Tech.* **2014**, *7* (10), 3579–3595. https://doi.org/10.5194/amt-7-3579-2014.

(72) Wittrock, F.; Richter, A.; Oetjen, H.; Burrows, J. P.; Kanakidou, M.; Myriokefalitakis, S.; Volkamer, R.; Beirle, S.; Platt, U.; Wagner, T. Simultaneous Global Observations of Glyoxal and Formaldehyde from Space. *Geophys. Res. Lett.* **2006**, *33* (16), 1–5. https://doi.org/10.1029/2006GL026310.

(73) Fu, T. M.; Jacob, D. J.; Wittrock, F.; Burrows, J. P.; Vrekoussis, M.; Henze, D. K. Global Budgets of Atmospheric Glyoxal and Methylglyoxal, and Implications for Formation of Secondary Organic Aerosols. *J. Geophys. Res. Atmos.* **2008**, *113* (15). https://doi.org/10.1029/2007JD009505.

(74) Mungall, E. L.; Abbatt, J. P. D.; Wentzell, J. J. B.; Lee, A. K. Y.; Thomas, J. L.; Blais, M.; Gosselin, M.; Miller, L. A.; Papakyriakou, T.; Willis, M. D.; et al. Microlayer Source of Oxygenated Volatile Organic Compounds in the Summertime Marine Arctic Boundary Layer. *Proc. Natl. Acad. Sci. U. S. A.* **2017**, *114* (24), 6203–6208. https://doi.org/10.1073/pnas.1620571114.

(75) Wofsy, S. C.; Afshar, S.; Allen, H. M.; Apel, E.; Asher, E. C.; Barletta, B.; Bent, J.; Bian, H.; Biggs, B. C.; Blake, D. R.; et al. Merged Data from the Atmospheric Tomography Mission. ORNL DAAC, Oak Ridge, Tennessee, USA 2018. https://doi.org/https://doi.org/10.3334/ORNLDAAC/1581.

(76) Wang, S.; Hornbrook, R. S.; Hills, A.; Emmons, L. K.; Tilmes, S.; Lamarque, J. F.; Jimenez, J. L.; Campuzano-Jost, P.; Nault, B. A.; Crounse, J. D.; et al. Atmospheric Acetaldehyde: Importance of Air-Sea Exchange and a Missing Source in the Remote Troposphere. *Geophys. Res. Lett.* **2019**, *46* (10), 5601–5613. https://doi.org/10.1029/2019GL082034.

(77) Brune, W. H.; Miller, D. O.; Thames, A. B.; Allen, H. M.; Apel, E. C.; Blake, D. R. Exploring Oxidation in the Remote Free Troposphere : Insights from Atmospheric Tomography (ATom). **2019**. https://doi.org/10.1029/2019JD031685.

(78) Thames, A. B.; Brune, W. H.; Miller, D. O.; Allen, H. M.; Apel, E. C.; Blake, R.; Bui, T. P.; Commane, R.; Crounse, J. D.; Daube, B. C.; et al. Missing OH Reactivity in the Global Marine Boundary Layer. **2019**, No. October, 1–29.

(79) Spracklen, D. V.; Arnold, S. R.; Sciare, J.; Carslaw, K. S.; Pio, C. Globally Significant Oceanic Source of Organic Carbon Aerosol. *Geophys. Res. Lett.* **2008**, *35* (12), 1–5. https://doi.org/10.1029/2008GL033359.

(80) Roelofs, G. J. A GCM Study of Organic Matter in Marine Aerosol and Its Potential Contribution to Cloud Drop Activation. *Atmos. Chem. Phys.* **2008**, *8* (3), 709–719. https://doi.org/10.5194/acp-8-709-2008.

(81) Gantt, B.; Meskhidze, N.; Kamykowski, D. A New Physically-Based Quantification of Marine Isoprene and Primary Organic Aerosol Emissions. *Atmos. Chem. Phys.* **2009**, *9* (14), 4915–4927. https://doi.org/10.5194/acp-9-4915-2009.

(82) Wolfe, G. M.; Marvin, M. R.; Roberts, S. J.; Travis, K. R.; Liao, J. The Framework for 0-D Atmospheric Modeling (F0AM) v3.1. *Geosci. Model Dev.* **2016**, *9* (9), 3309–3319. https://doi.org/10.5194/gmd-9-3309-2016.

(83) Galbally, I. E.; Roy, C. R. Destruction of Ozone at the Earth's Surface. *Q. J. R. Meteorol. Soc.* **1980**, *106* (449), 599–620. https://doi.org/10.1002/qj.49710644915.

(84) Ganzeveld, L.; Helmig, D.; Fairall, C. W.; Hare, J.; Pozzer, A. Atmosphere-Ocean Ozone Exchange: A Global Modeling Study of Biogeochemical, Atmospheric, and Waterside Turbulence Dependencies. *Global Biogeochem. Cycles* **2009**, *23* (4), 1–16. https://doi.org/10.1029/2008GB003301.

(85) Lenschow, D. H.; Pearson, R. J.; Stankov, B. B. Measurements of Ozone Vertical Flux to Ocean and Forest. *J. Geophys. Res.* **1982**, *87* (C11), 8833–8837. https://doi.org/10.1029/JC087iC11p08833.

(86) Kawa, S. R.; Pearson, R. Ozone Budgets from the Dynamics and Chemistry of Marine Stratocumulus Experiment. *J. Geophys. Res.* **1989**, *94* (D7), 9809–9817. https://doi.org/10.1029/JD094iD07p09809.

(87) Wesely, M. L.; Hicks, B. B. A Review of the Current Status of Knowledge on Dry Deposition. *Atmospheric Environment*. 2000. https://doi.org/10.1016/S1352-2310(99)00467-7.

(88) Schwartz, S. E. Factors Governing Dry Deposition of Gases to Surface Water. In *Precipitation Scavenging and Atmosphere-Surface Exchange*; Schwartz, S., Slinn, W. G. N., Eds.; Hemisphere Publ: Washington D.C., 1992; pp 789–801.

(89) Hansell, D. A.; Carlson, C. A.; Repeta, D. J.; Schlitzer, R. Dissolved Organic Matter in the Ocean a Controversy Stim Ulates New Insights. *Oceanography* **2009**, *22* (SPL.ISS. 4), 202–211. https://doi.org/10.5670/oceanog.2009.109.

(90) Sobek, S.; Tranvik, L. J.; Prairie, Y. T.; Kortelainen, P.; Cole, J. J. Patterns and Regulation of Dissolved Organic Carbon: An Analysis of 7,500 Widely Distributed Lakes. *Limnol. Oceanogr.* **2007**, *52* (3), 1208–1219. https://doi.org/10.4319/lo.2007.52.3.1208.

(91) Luhar, A. K.; Woodhouse, M. T.; Galbally, I. E. A Revised Global Ozone Dry Deposition Estimate Based on a New Two-Layer Parameterisation for Air-Sea Exchange and the Multi-

Year MACC Composition Reanalysis. *Atmos. Chem. Phys.* **2018**, *18* (6), 4329–4348. https://doi.org/10.5194/acp-18-4329-2018.

(92) Huey, L. G. Measurement of Trace Atmospheric Species by Chemical Ionization Mass Spectrometry: Speciation of Reactive Nitrogen and Future Directions. *Mass Spectrom Rev* **2007**, *26* (2), 166–184. https://doi.org/10.1002/mas.20118.

(93) de Gouw, J. A.; Goldan, P. D.; Warneke, C.; Kuster, W. C.; Roberts, J. M.; Marchewka, M.; Bertman, S. B.; Pszenny, A. A. P.; Keene, W. C. Validation of Proton Transfer Reaction-Mass Spectrometry (PTR-MS) Measurements of Gas-Phase Organic Compounds in the Atmosphere during the New England Air Quality Study (NEAQS) in 2002. *J. Geophys. Res. Atmos.* **2003**, *108* (D21), 1–18. https://doi.org/10.1029/2003JD003863.

(94) Veres, P.; Roberts, J. M.; Warneke, C.; Welsh-Bon, D.; Zahniser, M.; Herndon, S.; Fall, R.; de Gouw, J. Development of Negative-Ion Proton-Transfer Chemical-Ionization Mass Spectrometry (NI-PT-CIMS) for the Measurement of Gas-Phase Organic Acids in the Atmosphere. *Int. J. Mass Spectrom.* **2008**, *274* (1–3), 48–55. https://doi.org/10.1016/j.ijms.2008.04.032.

(95) Lee, B. H.; Lopez-Hilfiker, F. D.; Mohr, C.; Kurtén, T.; Worsnop, D. R.; Thornton, J. A. An Iodide-Adduct High-Resolution Time-of-Flight Chemical-Ionization Mass Spectrometer: Application to Atmospheric Inorganic and Organic Compounds. *Environ. Sci. Technol.* **2014**, *48* (11), 6309–6317. https://doi.org/10.1021/es500362a.

(96) Crounse, J. D.; McKinney, K. A.; Kwan, A. J.; Wennberg, P. O. Measurement of Gas-Phase Hydroperoxides by Chemical Ionization Mass Spectrometry. *Anal. Chem.* **2006**, *78* (19), 6726–6732. https://doi.org/10.1021/ac0604235.

(97) Leibrock, E.; Huey, L. G. Ion Chemistry for the Detection of Isoprene and Other Volatile Organic Compounds in Ambient Air. *Geophys. Res. Lett.* **2000**, *27* (12), 1719–1722. https://doi.org/10.1029/1999GL010804.

(98) Kim, M. J.; Zoerb, M. C.; Campbell, N. R.; Zimmermann, K. J.; Blomquist, B. W.; Huebert, B. J.; Bertram, T. H. Revisiting Benzene Cluster Cations for the Chemical Ionization of Dimethyl Sulfide and Select Volatile Organic Compounds. *Atmos. Meas. Tech. Discuss.* **2015**, *8* (10), 10121–10157. https://doi.org/10.5194/amtd-8-10121-2015.

(99) Huey, L. G.; Hanson, D. R.; Howard, C. J. Reactions of SF6- and I- with Atmospheric Trace Gases. *J. Phys. Chem.* **1995**, *99* (14), 5001–5008. https://doi.org/10.1021/j100014a021.

(100) Lee, B. H.; Lopez-Hilfiker, F. D.; Mohr, C.; Kurtén, T.; Worsnop, D. R.; Thornton, J. A. An Iodide-Adduct High-Resolution Time-of-Flight Chemical-Ionization Mass Spectrometer: Application to Atmospheric Inorganic and Organic Compounds. *Environ. Sci. Technol.* **2014**, *48* (11), 6309–6317. https://doi.org/10.1021/es500362a.

(101) Bertram, T. H.; Kimmel, J. R.; Crisp, T. A.; Ryder, O. S.; Yatavelli, R. L. N.; Thornton, J. A.; Cubison, M. J.; Gonin, M.; Worsnop, D. R. A Field-Deployable, Chemical Ionization Time-of-Flight Mass Spectrometer. *Atmos. Meas. Tech.* **2011**, *4* (7), 1471–1479. https://doi.org/10.5194/amt-4-1471-2011.

(102) Wolfe, G. M.; Hanisco, T. F.; Arkinson, H. L.; Bui, T. P.; Crounse, J. D.; Dean-Day, J.; Goldstein, A.; Guenther, A.; Hall, S. R.; Huey, G.; et al. Quantifying Sources and Sinks of Reactive Gases in the Lower Atmosphere Using Airborne Flux Observations. *Geophys. Res. Lett.* **2015**. https://doi.org/10.1002/2015GL065839.

Chapter 1. Ozone Dry Deposition to Coastal Ocean and Eutrophic Lake Surfaces

Abstract

The deposition of tropospheric ozone (O_3) to water surfaces is a significant but poorly constrained component of the global O_3 budget. The deposition velocity of O_3 ($v_d(O_3)$) is a complex function of turbulent mixing and reactivity at the water surface, primarily with iodide and dissolved organic carbon (DOC). We present direct measurements of $v_d(O_3)$ via eddy covariance to the coastal mid-latitude Pacific Ocean and a eutrophic freshwater lake. The mean ocean and lake $v_d(O_3)$ were 0.013 and 0.038 cm s^{-1} respectively. The lake $v_d(O_3)$ is likely controlled solely by reactions of O_3 with DOC which are poorly captured in models of O_3 deposition, as lake iodide concentrations are low (<5 nM). Ocean $v_d(O_3)$ showed no significant relationship with wind speed or sea-surface temperature which is compared against the COARE air-sea flux algorithm. Observed $v_d(O_3)$ is used to constrain potential volatile organic carbon (VOC) emissions driven by heterogeneous reactions of O_3 with DOC. Calculated emissions are up to 11.8 to 58 Tg C yr^{-1} but are subject to considerable

1.1 Introduction

Ozone plays a central role in tropospheric oxidative chemistry,[1] is a regulated air pollutant,[2] human and vegetative health hazard,[3] and a potent greenhouse gas.[4] The deposition of tropospheric ozone (O_3) to water surfaces is a significant but poorly constrained component of the global tropospheric O_3 budget.[5] Many common chemical transport models (CTM) assign a fixed O_3 dry deposition rate to water surfaces on the order of 0.01 to 0.05 cm s^{-1}, based on the resistance framework of Wesely, (1989)[6], as summarized by Luhar et al., (2017).[7] In models that explicitly treat O_3 deposition and surface chemistry, there remains significant disagreement in the magnitude of total annual global O_3 deposition to water surfaces, ranging from 95 Tg yr^{-1} to 360 Tg yr^{-1}.[8,9] Overall there is a paucity of observations of O_3 deposition to water surfaces, with measured values of O_3

deposition velocities ($v_d(O_3)$**)** spanning from 0.01 to 0.15 cm s^{-1} for seawater and 0.01 to 0.1 cm s^{-1} for freshwater.[8,10–13] Notably there is only one prior direct eddy covariance (EC) measurement of $v_d(O_3)$ to a lake surface.[14] Helmig et al. (2012)[10] presented the most comprehensive set of observations of $v_d(O_3)$ to the ocean, reporting $v_d(O_3)$ from 0.009 – 0.034 cm s^{-1} across five research cruises with broad coverage of the global oceans. This dataset spans a large range of wind speeds (U_{10}; 0-18 m s^{-1}) and sea-surface temperatures (SST; ~3-33°C) which has been essential for constraining O_3 deposition models.[7,9] Detailed characterization of ocean/lake chemical, physical, and biological properties, necessary for further developing model parameterization of $v_d(O_3)$, are largely absent form current field datasets of ozone deposition.

The rate and direction of air-water trace gas flux (*F)* is a function of the gas-phase (C_a) and aqueous (C_w) concentrations, solubility (K_H, in dimensionless gas over liquid units), and a transfer velocity parameter (K_T) which accounts for all processes that contribute to the resistance to transfer including surface reactivity, as shown in E1.[15] For species with negligible solubility and water side concentrations like O_3, F is controlled by K_t and C_a, and the C_w and K_H terms can be eliminated to reformulate E1 as a deposition velocity ($v_d(O_3)$) as shown in E2.

$$F = K_t(K_H C_w - C_a) \quad \text{E1}$$

$$v_d(O_3) = F/C_a \quad \text{E2}$$

O_3 deposition is primarily controlled by waterside resistance, with turbulent transfer and diffusion in the gas phase having minor significance (see Section S1.1 for a more comprehensive description of factors influencing air-sea exchange rates). O_3 is a relatively insoluble molecule ($K_H = 1 \times 10^{-2}$ M atm^{-1}) and surface reactivity enhances $v_d(O_3)$ by up to a factor of 40 compared to the case considering only solubility.[16]

The primary surface reactants driving O_3 deposition to the ocean are iodide (I^-) and dissolved organic carbon (DOC) species as shown in R1 and R2 respectively.[8,17] DOC is a complex mixture of saturated and unsaturated organic molecules which are ubiquitous in both the ocean and freshwater lakes.[18,19]

$$O_3 + I^- \xrightarrow{k_{I^-}} IO_3^- \quad \text{(R1)}$$

$$O_3 + DOC \xrightarrow{k_{DOC}} Products \quad \text{(R2)}$$

The rates of reactions R1 and R2 vary by orders of magnitude with k_{I^-}= 2.4 x 10^9 M^{-1} s^{-1} at 293 K,[20] and k_{DOC} from 1.8 x 10^5 (C_2H_4) [21] to 8.6 x 10^8 M^{-1} s^{-1} (DMS)[22] depending on the DOC species used as a proxy. The only existing literature report of k_{DOC} with authentic marine DOC was 2.6 × 10^7 M^{-1} s^{-1}.[23] The limited observations of k_{DOC} for proxy species and authentic DOC, and the unknown temperature dependence of k_{DOC} drives considerable uncertainty in determining an appropriate overall k_{DOC} for implementation in O_3 deposition models.

There is considerable disagreement as to the relative importance of I^- and DOC in controlling $v_d(O_3)$. The modeling study of Chang et al., (2004)[17] found that reaction with I^- (R1) was sufficient to explain observed $v_d(O_3)$ and speciated reactions with DOC were too slow to be significant. This is in contrast to the modeling of Ganzeveld et al. (2009)[8], which found approximately equal impact of DOC and I^- due to the incorporation of reactions of O_3 with chlorophyll, based on reaction rates determined in laboratory studies.[24] The discrepancy between models is partially from the inclusion of different DOC molecules and bimolecular rate constants. Additional laboratory studies of O_3 deposition to solutions containing I^- and authentic marine or riverine DOC showed that DOC and I^- had roughly equal contributions to $v_d(O_3)$.[23,25] Recently, Luhar et al. (2018)[9] developed the most thorough physical modeling framework for O_3 deposition, which uses a two-layer water

framework to account for both surface and bulk reactions of O_3 with I^-, showed good general with the observations of Helmig et al. (2012).[10] In that model, the authors elected not to include reactions with DOC (R2) in their framework as it degraded model agreement with observed trends of $v_d(O_3)$ with SST. It is clear from laboratory studies that reactions of O_3 with authentic and proxy DOC species can be significant. However, a unified deposition parameterization accounting for surface reactions with both R1 and R2 has been elusive due in part to the lack of observational constraints on $v_d(O_3)$ and on near surface chemical concentrations and the lack of appropriate k_{DOC} rate constants.

A simple model calculation of $v_d(O_3)$ from a surface layer reactivity model following Garland et al. (1980) is presented in **Figure. 1.1** as a function of [DOC], [I^-] and k_{DOC}. The model calculation describes that the relative contribution of I^- and DOC to $v_d(O_3)$ in various concentration regimes. Additional model details are presented in Section S1.1. We calculate $v_d(O_3)$ over the typical ranges of [I^-] and [DOC] in global ocean and in freshwater lakes, shown as the red and grey shaded regions respectively on the axis labels. A k_{DOC} of 2×10^6 M^{-1} s^{-1} calculated in panel (a) is taken as conservative lower estimate from the limited set of speciated DOC rates which have been measured. The k_{DOC} of 1.5 x 10^7 M^{-1} s^{-1} is the implied reaction rate needed to match the observed $v_d(O_3)$ Lake Mendota in Madison, WI as discussed further in Section 1.3. The calculation applies a fixed friction velocity of 0.2 m s^{-1} and a water surface temperature of 292 K for parameterization transfer in the gas phase turbulent and diffusive sublayers as described in Section S1.1. A fixed bimolecular rate constant (k_{I^-} = 2×10^9 M^{-1} s^{-1}) is used for R2. This model exercise is intended to show the sensitivity of $v_d(O_3)$ to k_{DOC} and the need constrain k_{DOC} for both for ocean and freshwater lake systems. For representative ocean [DOC] = 60 μM and [I^-] = 100 nM, we use k_{DOC} = 1.5×10^7 M^{-1} s^{-1}, which nearly doubles $v_d(O_3)$ compared to the base case k_{DOC} of 2×10^6 M^{-1} s^{-1} ($v_d(O_3)$

= 0.017 and 0.031 cm s^{-1} respectively). Notably, fast $v_d(O_3)$ (>0.01 cm s^{-1}) can be sustained exclusively by reactions with DOC for k_{DOC} values well within known speciated k_{DOC} values (1.8 × 10^5 M^{-1} s^{-1} for C_2H_4 to 8.6 × 10^8 M^{-1} s^{-1} for DMS).

Deposition of O_3 to the ocean through R1 and R2 has also been suggested to play an important role in the emissions of reactive halogens (R1)[23,27] and VOCs to the atmosphere (R2).[28,29] Reaction R1 of O_3 is proposed to be the primary source of iodine to the atmosphere.[23] Laboratory experiments showed that heterogeneous reactions of O_3 with proxy and authentic sea-surface microlayer (SML) efficinetly emittied reactive VOCs, including aldehydes and glyxoal, with net gas phase yields on the order of 100%. These results provide additional motivation for improving our understanding of O_3 deposition rates and the relative roles of I^- and DOC reactivity, both for their controlling roles in global O_3 mixing ratios but also as potentially significant sources of reactive VOC and halogen species to the marine atmosphere.

Here we present direct measurements of O_3 concentration and vertical fluxes and calculations of O_3 dry deposition rates from a coastal ocean site at Scripps Pier in La Jolla, CA and from the shoreline of an urban eutrophic lake (Lake Mendota, Madison WI). These data allow for comparison to parameterizations of deposition velocity to U_{10} and SST for the coastal dataset and to assess the relative role of DOC and I^- by comparing the lake (high [DOC], low/no [I^-]) and ocean (low/moderate [DOC], high [I^-]) observations. We use the observed lake $v_d(O_3)$ to calculate the implied k_{DOC} necessary to explain our observation of fast DOC driven deposition ($v_d(O_3)$ = 0.038 cm s^{-1}). We also present a series of calculations to assess the potential magnitude of VOC emissions from surface O_3 reactions, constrained by our observed O_3 deposition rates, highlighting the need for further constraints on VOC yield from heterogeneous reactions with O_3.

1.2 Measurements of O_3 Deposition Velocity

1.2.1 Eddy Covariance Flux

Air-water vertical fluxes (F) of O_3 were determined *via* the eddy covariance (EC) method, where F is computed as the mean product of the instantaneous variances of the 10 Hz measurements of ambient O_3 mixing ratios and vertical wind velocity (w) as shown in Eq. 3. Where $C_{a,O3}{}'$ and w' are the instantaneous deviation of C_a and w from the mean value, and the overbar denotes the average over the flux period, here ca. 27 min $v_d(O_3)$ is calculated from F according to Eq. 2, where $C_{a,O3}$ is the mean ambient mixing ratio during the flux averaging period.

$$F = \overline{w' C_{a,O3}{}'} \qquad \text{E3}$$

Ozone mixing ratios were measured at 10 Hz with a chemical ionization time-of-flight mass spectrometer (CI-ToFMS, Aerodyne Research Inc., TOFWERK AG) utilizing a newly developed oxygen anion reagent ion chemistry (Ox-CIMS) method which is fully described in Novak et al., (2019)[30] with additional relevant details in the Section S1.2. The Ox-CIMS measurement was collocated with a Gil Sonic HS-50 sonic anemometer (Sonic HS-50, Gil Instruments) measuring three-dimensional wind speed at 10 Hz for use in the eddy covariance flux calculation, described in Eq. 3. Full details of field sampling conditions and EC flux data processing and quality control are presented in Novak et al., (2019) and Section S1.3.

1.2.2 Scripps Pier Flux Site

Scripps pier is a 330 m long research pier located at the Scripps Institution of Oceanography (SIO) in La Jolla, CA. Continuous buoy measurements show that this site experiences characteristic onshore winds from the west during the daytime for June-September, with windspeeds from 0-6 m s^{-1} observed during the study period. The sampling site at the end of the pier is located 100 m

beyond the wave breaking zone, with an inlet height of 13 m above mean lower low tide level. Ozone vertical flux was measured with the Ox-CIMS from the pier for a total of 37 days during July and August 2018, as described fully in Novak et al. (2019).[30] This site has been successfully used for previous EC air–sea exchange studies,[31,32] including a study by our group utilizing the same CI-ToFMS instrument used here operating in a different reagent ion chemistry mode.[33]

During the study period, SST at SIO Pier ranged from 17–26 °C, with the lower temperatures observed during rapid (<12 hr) turnover events in the near shore water column. Continuous measurements of SST and chlorophyll are collected at a 1-minute time resolution from the end of the pier by an automated shore station operated by the Southern California Coastal Ocean Observing System.[34] *In-situ* chlorophyll data is not available for the full study period due to biofouling on the sensor.

1.2.3 Lake Mendota Flux Site

Eddy covariance flux measurements were made from the roof of the University of Wisconsin Madison Hasler Laboratory of Limnology on the shore of Lake Mendota in May 2018 for seven days of continuous measurement. Instrument operating conditions were generally identical to the SIO Pier deployment with all changes discussed in Section S1.2. The Ox-CIMS inlet manifold and sonic anemometer mount extended 2 m beyond the edge of the building directly over the lake surface. The inlet measurement height was approximately 12 m above the mean water level. This site has been used previously for long running eddy covariance flux measurements of air-lake CO_2

exchange.[35] This site is non-ideal for EC flux measurements and requires careful data filtering to remove periods of recirculating flow as described in S1.3.2.

1.3. Ozone Deposition Rates

A histogram of observed $v_d(O_3)$ to the coastal ocean from Scripps Pier and to the freshwater Lake Mendota are shown in **Figure 1.2**. The observed 20-80th percentile range at Scripps Pier was -0.0011 to 0.027 cm s^{-1} with a mean of 0.013 cm s^{-1} and a campaign ensemble limit of detection (LOD) of 0.0024 cm s^{-1} from a total of 246 individual 27-minute flux measurement periods. The observed 20-80th percentile range for the Lake Mendota observations were -0.067 to 0.11 with a mean of 0.038 over 85 quality-controlled flux measurement periods.

The observed mean $v_d(O_3)$ from Scripps Pier of 0.013 cm s^{-1} is at the lower range of previous observations of ocean O_3 deposition (0.01 – 0.05 cm s^{-1}).[8,10] Observed $v_d(O_3)$ as a function of U_{10} and SST are shown in **Figure 1.3** and are compared to modelled $v_d(O_3)$ from the NOAA COARE v3.6 bulk gas flux algorithm (additional details below and in S1.5).[36] The observed mean $v_d(O_3)$ of 0.013 cm s^{-1} was in good agreement with the COARE algorithm predicted value of 0.015 cm s^{-1}. Observed $v_d(O_3)$ was found to have no statistically significant trend with either wind speed or SST. The lack of a relationship with U_{10} is consistent with the model results for the low to moderate wind speed range sampled (0-6 m s^{-1}), where molecular gas transfer is expected to dominate.[17] Luhar et al., (2018),[9] suggested that $v_d(O_3)$ should increase with SST due to a combination of a parameterized increase of [I$^-$] with SST and an increase in k_{I^-} with SST. This trend was not statistically resolvable in our observations. The parameterization of [I$^-$] against SST follows MacDonald et al. (2014)[37] and is also plotted as the upper x-axis on **Figure 1.3b**. The literature parameterizations of [I$^-$] against SST are generated from global data sets which show higher [I$^-$] in warmer tropical waters and lower values near the poles.[37–39] It is not clear if this

global mean trend of SST with [I^-] is a suitable model for capturing short term changes in [I^-] at a fixed sampling site. Diel sampling of [I^-] across three sites in the tropical Atlantic found no diel trend and literature values of net iodide production are small (0.27 to 0.55 nM day^{-1}) which further supports that a trend of $v_d(O_3)$ with SST may not be present at a fixed sampling site.[38] Luhar et al., (2018)[9] also use the temperature dependent k_{I^-} of Magi et al., (1997)[20] which showed a strong positive increase with temperature, but as noted by Macdonald et al., (2014)[37] the reported Arrhenius equation (k_{I^-} = 1.44 × 10^{22} exp(-73080/RT) M^{-1} s^{-1}) in that work includes a pre-exponential factor 10 orders of magnitude larger than the diffusion limited reaction rate and thus appears unphysical. A temperature independent k_{I^-} may be more appropriate until further confirmation of its temperature dependence becomes available.[37] Variability in $v_d(O_3)$ larger than the flux LOD was observed over the narrow SST range from 22 to 24°C which implies the potential presence of other controlling variables. The NOAA COARE v3.6 gas transfer algorithm follows the temperature dependent [I^-] and k_{I^-} parameterizations of Luhar et al., (2018)[9] and includes a two-layer reactivity model which incorporates reactivity of O_3 with I^- in both the surface molecular sublayer and the turbulently mixed waterside bulk. Implementation of the NOAA COARE v3.6 algorithm is described further in Section S1.5 The sensitivity of the NOAA COARE v3.6 default configuration to variations in the parameterization of [I^-], molecular sublayer thickness, and the inclusion of DOC are shown in Fig S1.1 and S1.2.

The mean observed $v_d(O_3)$ from Lake Mendota was 0.038 cm s^{-1}. To our knowledge the only prior EC measurement of $v_d(O_3)$ to freshwater was from Wesely et al., (1981)[14] who reported a $v_d(O_3)$ of 0.01 cm s^{-1} to Lake Michigan. Galbally & Roy, (1980)[5] reported lake water $v_d(O_3)$ determined by enclosure loss rate studies from 0.015 to 0.1 cm s^{-1}. The observed mean Lake Mendota $v_d(O_3)$ is at the upper end of observed range to the ocean of 0.01 – 0.05 cm s^{-1}.[8,10] The

limited duration of $v_d(O_3)$ measurements made at Lake Mendota (1 week, with limited periods of winds from the lake) makes meaningful parameterization of lake $v_d(O_3)$ against meteorological parameters challenging. However, the comparable mean magnitude of $v_d(O_3)$ to a freshwater surface compared to the coastal ocean observations is still informative, as deposition to Lake Mendota is likely driven exclusively by reactions with DOC. DOC in Lake Mendota is routinely measured with a Shimadzu TOC-VCSH Total Organic Carbon Analyzer as part of the North Temperate Lakes Long Term Ecological Research Network.[40] Mean DOC for May- June 2018 encompassing our full observation period was 425 μM. Iodide or total iodine have not been measured in Lake Mendota to our knowledge, but surface concentrations in fresh water lakes are typically from 0-10 nM with most lakes below 4 nM.[41,42] We select a value of 2 nM for Lake Mendota for use in subsequent calculations.

In a global survey of 7,514 lakes the median near-surface DOC was 476 μM (mean 632 μM), with 87% of lakes between 80 and 1667 μM, suggesting that Lake Mendota is generally representative of median global lake DOC. The large range in lake DOC also implies $v_d(O_3)$ may vary significantly between individual lakes if our hypothesis of DOC controlled deposition is true. The median lake DOC of 476 μM is larger than the observed range in the surface ocean (40 -80 μM).[18,19] From our observations, O_3 deposition rates to Lake Mendota are larger than the sole literature EC $v_d(O_3)$ measurement to a freshwater lake of 0.01 cm s^{-1}, measured at Lake Michigan with wind speeds from 3.0 to 6.5 m s^{-1}.[14] This result is qualitatively consistent with the lower [DOC] in Lake Michigan (100 to 200 μM) compared to Lake Mendota (425 μM).[43,44]

The implied k_{DOC} reaction rate constant needed to sustain the observed Lake Mendota $v_d(O_3)$ of 0.038 cm s^{-1} is 1.6×10^7 M^{-1} s^{-1} given a measured [DOC] of 425 μM, an estimated [I^-] of 2 nM, and a U_* of 0.2 cm s^{-1}, calculated using a surface reactivity model following Garland et al.,

(1980)[26] and described further in Section S1.1 This implied k_{DOC} represents a net bimolecular rate constant for O_3 with all surface DOC species. This implied k_{DOC} is in general agreement with the only available measurement of k_{DOC} of 2.6×10^7 M^{-1} s^{-1}, measured on authentic marine DOC.[45] Martino et al., (2012)[25] made laboratory measurements of $v_d(O_3)$ as a function of I^- and authentic DOC which showed that that I^- and DOC contribute roughly equally under ocean conditions ($[I^-]$ = 150 nM, [DOC] = 80μM) but did not directly present the bimolecular rate constant k_{DOC}. Coleman et al., (2012)[46] applied the laboratory measurements of Martino et al., (2012) in a model calculation to determine $k_{DOC} = 3.44 \times 10^6$ M^{-1} s^{-1}. The inferred k_{DOC} for Lake Mendota is near the middle of the range reported for speciated O_3 water surface reaction rate constants of 1.8×10^5 M^{-1} s^{-1} for C_2H_4 to 8.6×10^8 M^{-1} s^{-1} for DMS. It is also important to note that DOC concentrations in the surface microlayer (top 50 μm) are likely enhanced by 2-5 times relative to the near surface DOC concentrations of 425 μM used in this calculation.[47] Due to this surface DOC enhancement, our inferred k_{DOC} is likely to be higher results from laboratory studies that do not account for surface enactment. While our observations are for a specific eutrophic freshwater lake, they suggest that O_3 surface reactions with total DOC are sufficiently fast to drive a large $v_d(O_3)$ and should be considered for inclusion in chemical transport models used for predicting O_3 concentrations in coastal environments. O_3 transport over water bodies has been the focus of several field recent field studies which would benefit from improved parameterization of $v_d(O_3)$.[48,49]

To assess the relative contribution of I^- and DOC to our observed $v_d(O_3)$ at Scripps Pier we use a similar modeling approach as described above. Taking a mean near surface $[I^-]$ = 80 nm and an estimated coastal [DOC] = 70 μM [18] we calculate $v_d(O_3)$ using our previously described surface reactivity model for various values of k_{DOC} and k_{I^-} and compare them to the mean observed Scripps

Pier $v_d(O_3)$ of 0.013 cm s^{-1}. For the case of k_{DOC} = 0 M^{-1} s^{-1} and k_{I^-} = 2 × 10^9 M^{-1} s^{-1}, the calculated $v_d(O_3)$ is 0.014 cm s^{-1}. Conversely, taking k_{DOC} = 1.5 × 10^7 M^{-1} s^{-1} (the implied rate from the Lake Mendota observations) and k_{I^-} = 0 M^{-1} s^{-1}, the calculated $v_d(O_3)$ is 0.030 cm s^{-1} which is outside the uncertainty of our observed Scripps Pier value. Taking a more conservative k_{DOC} = 2 × 10^6 M^{-1} s^{-1} with k_{I^-} = 0 M^{-1} s^{-1} yields $v_d(O_3)$ is 0.011 cm s^{-1}. Finally, taking the case of k_{DOC} = 2 × 10^6 M^{-1} s^{-1} and k_{I^-} = 2 × 10^9 M^{-1} s^{-1} results in $v_d(O_3)$ of 0.018 cm s^{-1}. From this exercise it is clear that the implied Lake Mendota k_{DOC} of 1.5 × 10^7 M^{-1} s^{-1} when scaled to the ocean case results in a calculated $v_d(O_3)$ that is too large compared to the Scripps pier observations. The cases with a more conservative k_{DOC} = 2 × 10^6 M^{-1} s^{-1} (with or without iodide) and the case with only k_{I^-} = 2 × 10^9 M^{-1} s^{-1} (0 DOC) were all consistent with the SIO observations within the uncertainty. This suggests that there is within currently available constraints on k_{DOC} there is potential for either DOC or I^- to contribute to ocean $v_d(O_3)$ depending on model assumptions made. Additional laboratory work is needed to constrain a representative k_{DOC} for the ocean using authentic marine DOC at concentrations consistent with the ocean interface.

1.4. Constraining VOC Emissions from Heterogeneous Reactions with O_3

The reaction of O_3 on water surfaces has been proposed as a potentially significant source of VOCs and reactive halogen species to the atmosphere.[28] Here we use observed O_3 deposition rates from SIO Pier and Lake Mendota as a constraint on the potential magnitude of O_3-driven VOC emissions. The VOC emission flux (E_{VOC}) is calculated as a function of $v_d(O_3)$ and converted to a flux in molecules cm^{-2} s^{-1} by applying a fixed [O_3] = 30ppbv and scaling to a gas phase VOC yield (Φ_{VOC}) from 0-100% as shown in **Figure 1.4**. At the mean measured ocean $v_d(O_3)$ of 0.013 cm s^{-1}, [O_3] of 30 ppbv and Φ_{VOC} of 10 or 50%, E_{VOC} is 9.8 ×10^8 and 4.9 × 10^9 molecules cm^{-2} s^{-1}, respectively. Importantly, this calculation assumes that every depositing O_3 molecule reacts with

DOC and is therefore an estimate of the maximum possible O_3 driven emission rate. The competitive reactions of O_3 with dissolved halogens including I^- would suppress VOC yields in authentic seawater making even 50% yield a likely upper limit. However, recent studies have suggested that Br^- can enhance O_3 reactive uptake and VOC emissions, suggesting possible catalytic effects for reactions with VOC.[50] It is also known that a fraction of O_3 reactions happen in the bulk ocean and not the interface, meaning any highly soluble oxidized molecule formed is likely not transferred to the gas phase efficiently. This effect would further reduce effective Φ_{VOC}. Zhou et al. (2014) reported a net gas phase Φ_{VOC} of 105-110% relative to O_3 consumption for reaction on a linoleic acid monolayer surface, with specific yields of 78%, 29%, 4% and <1% for n-hexanal, 3-nonenal, malondialdehyde and glyoxal respectively. While this study was performed in the laboratory on highly concentrated quiescent film and is the likely not directly translatable to the ambient ocean, these values are the only available direct constraint on potential Φ_{VOC}. Scaling the calculated E_{VOC} from the mean coastal ocean $v_d(O_3)$ of 0.013 at Φ_{VOC} of 10 and 50% to the global ocean surface area yields a mean annual VOC flux of 11.8 - 59 Tg C yr^{-1} (assuming 5 carbons per molecule). This E_{VOC} source is of the same approximate magnitude as literature estimates of global DMS emissions of 21.1 Tg C yr^{-1} (28.1 Tg S yr^{-1}).[51–53] For the mean observed Lake Mendota $v_d(O_3)$ of 0.038 cm s^{-1} and a 10% VOC yield, the calculated E_{VOC} is 2.85 x 10^9 molecules cm^{-2} s^{-1}, or 0.28 Tg C yr^{-1} if scaled to the global lake surface area of 4.2 × 10^6 km^2 .[54] This potential lake VOC source has not been considered previously and while small compared to other terrestrial sources, it could be a significant VOC source in some pristine regions. Steinke et al., (2018) highlighted the importance of lake BVOC emissions in the arctic where there is significant lake coverage and competing terrestrial VOC sources are small. Clearly, there is significant uncertainty in this model calculation with appropriate VOC yields from heterogeneous

reactions of O_3 being almost entirely unconstrained. We present this analysis to motivate that E_{VOC} from heterogeneous reactions with O_3 could be significant, and that further constraints are necessary to determine the magnitude of this potential VOC source. The calculated marine E_{VOC} range from 11.8 - 59 Tg C yr^{-1} is not intended as a rigorous estimate of global emissions suitable for use in CTM.

1.5. Outlook

The paired observations of $v_d(O_3)$ to the ocean at Scripps Pier and the freshwater Lake Mendota suggest that DOC may play an important role in setting O_3 deposition rates. The net impact of this reactivity is highly uncertain due to a general lack of constraints from field observations and laboratory measurements of DOC reaction rates. Deposition to Lake Mendota is likely driven exclusively by reactions with DOC, with an implied rate constant for the surface reaction of O_3 with DOC of 1.5 x 10^7 M^{-1} s^{-1} as calculated from a simple surface reactivity model. It is not clear how this implied reaction rate scales to the global ocean, but it suggests the role of DOC in controlling $v_d(O_3)$ should be further investigated. Current global chemical models typically use fixed $v_d(O_3)$, while models specifically investigating O_3 dry deposition to water show significant differences and do not always account for reactions with DOC. Accurate treatment of O_3 surface reactions on natural waters are also needed to capture emission fluxes of reactive halogen and VOC species.[23,28] A simple calculation constrained by our observed O_3 deposition flux rates suggest that VOC emissions from heterogeneous reactions of O_3 at the ocean surface could be on the order of 11.8 – 59 Tg C yr^{-1} which is comparable with global DMS emissions of 21.1 Tg C yr^{-1} but significant further constrains are needed before this emission source could be included in global models.[52]

Supplement

S1.1 Ozone surface reactivity and deposition model

As described in E2 in the main text, the deposition velocity (v_d) is calculated from flux (F) and gas phase concentration (C_a). v_d can be further parameterized into a series of resistance to transfer in the framework of Wesely, (1989)[2] as shown in Equation S1. Where r_a is resistance to turbulent mixing in the atmospheric surface layer, r_b is resistance to diffusion through the atmospheric surface sublayer, and r_c is the resistance to uptake to the liquid surface which includes solubility and reactivity. The terms r_a, r_b, and r_c can then be individually parameterized for calculation in models following the one layer reactivity scheme of Garland et al. (1980)[22] as shown in equations ES2-5 in order to calculate the contribution of each resistance term. Here κ is the Von Karman constant (taken to be 0.4), u_* is friction velocity, z is the measurement height (13 m), z_o is the roughness height, S_c is the Schmidt number, D is the diffusion constant in water, k_i is the rate constant of a dissolved species with O_3, and C_i is the concentration of that dissolved species.

$$v_d = (r_a + r_b + r_c)^{-1} \quad \text{ES1}$$

$$r_a = \frac{1}{\kappa u_*} ln\left(\frac{z}{z_o}\right) \quad \text{ES2}$$

$$r_b = \frac{5}{u_*} Sc^{\frac{2}{3}} \quad \text{ES3}$$

$$r_c = \frac{K_H}{\sqrt{\lambda D}} \quad \text{ES4}$$

$$\lambda = \sum_i k_i C_i \quad \text{ES5}$$

The deposition rate of ozone is dominated by the liquid surface (r_c) term due to its low solubility and relatively slow reaction rates [13]. Further r_c is controlled by the reactivity term λ, which enhances v_d by a factor of 40 compared to the case where r_c is only controlled by solubility. As discussed in

the main text the reactions with iodide (I^-) and dissolved organic carbon (DOC) as in R1 and R2 are the major reaction pathways for O_3, and are the only reactions considered in this work.

This parameterization of r_c follows the surface reactivity framework of Garland et al., (1980)[22] where all reactions happen in a single surface layer of homogeneous composition. Luhar et al., (2018)[5] has developed an alternative two-layer reactivity model where some O_3 is turbulently mixed into the bulk layer and allowed to react there. That model implementation only included reactivity with I^-. The importance of the turbulent mixing term is in part set by the total O_3 reactivity, with higher reactivities reducing the importance of turbulent mixing. Our modelling exercise is intended to capture the relative influence of I^- and DOC on $v_d(O_3)$ and therefore elect to use the one-layer reactivity approach.

Dissolved iodide concentrations ($[I^-]$) are commonly parameterized against sea-surface temperature (SST) based on regressions from global datasets. The parameterization used in the Luhar et al. (2018)[5] and NOAA COARE v3.6 models follows the parameterization of MacDonald et al. (2014) as shown in Equation ES6. We also apply the MacDonald et al. (2014)[33] parameterization for calculation of $[I^-]$ as a function of SST as plotted in **Figure 1.3**.

$$[I^-] = 1.46 \times 10^6 \, e^{\left(\frac{-913}{SST}\right)} \qquad \text{ES6}$$

Calculation of v_d throughout the text and in **Figure 1.1** was made using the one-layer reactivity model as a function of $[I^-]$ and [DOC] following equations ES1-ES5 with the following default values: $\kappa = 0.4$, $u_* = 0.2$ m s^{-1}, $K_H = 4.06$ (O_3 dimensionless gas over liquid solubility), $z_0 = 6.12 \times 10^{-5}$ m (calculated from the Charnock relation given in Equation S7, where a_c is the Charnock parameter taken as 0.015, and g is gravitational acceleration taken as 9.8 m^2 s^{-2})[49], $S_c = 1.11$, and

$D = 1.59 \times 10^{-9}$ cm^2 s^{-1}. A fixed $k_I = 2 \times 10^9$ M^{-1} s^{-1} was used for all calculations unless otherwise noted.

$$z_0 = a_c \frac{u_*^2}{g} \quad \text{ES7}$$

S1.2 Instrument and field deployment sampling configuration

S1.2.1 Oxygen anion chemical ionization time-of-flight mass spectrometer

A complete description of the chemical ionization time-of-flight mass spectrometer instrument used is available in Bertram et al., (2011).[50] Full details of the use oxygen anion reagent ion chemistry with the chemical ionization time-of-flight mass spectrometer (Ox-CIMS) used for detection of O_3, including laboratory characterization and field deployment for eddy covariance sampling from Scripps Pier is presented in Novak et al., (2019).[26] Here we provide a brief overview of the general instrument and use of oxygen anion reagent ion chemistry and refer the reader to the above texts for additional detail.

The Ox-CIMS samples ambient air directly into an ion molecule reaction region (IMR) held at 95 mbar, where a subset of ambient species react with the oxygen anion (O_2^-) reagent ions. The O_2^- reagent ion is generated by passing a 200:2200 volumetric blend of O_2:N_2 through a polonium-210 alpha particle source which is subsampled into the IMR by a critical orifice. Ambient O_3 quickly undergoes a charge transfer reaction with O_2^- to form O_3^- (R1) which then reacts with ambient CO_2 to form the stable detected CO_3^- (R2). Charge transfer from O_2^- is expected to proceed for any analyte with an electron affinity (E.A.) greater than O_2 (E.A. 0.45 eV) which includes O_3 (E.A. 2.1 eV). Absolute sensitivity to O_3 is 180 cps pptv^{-1} with a limit of detection of 13 pptv for 1Hz sample averaging. There is no dependence of instrument sensitivity to O_3 on ambient specific humidity over the range 8-16 g kg^{-1} typical of the marine boundary layer.

Mass resolution of the instrument (at -m/Q 60, the mass of the CO_3^- detection product of O_3) is 950 $m/\Delta m$. We analyze all data at unit mass resolution. Full mass spectra were collected for a mass range of 27 to 327 -m/Q and were recorded at 10 Hz for analysis.

$$O_3 + O_2(H_2O)_n^- \rightarrow O_3^- + O_2 + nH_2O \quad \text{(RS1)}$$

$$O_3^- + CO_2 \rightarrow CO_3^- + O_2 \quad \text{(RS2)}$$

S1.2.2 Field Sampling Calibration and Backgrounds

Full details of the Scripps Pier EC flux deployment are described in Novak et al. (2019).[26] All details of the sampling configuration at Lake Mendota were the same as the Scripps Pier deployment, expect for the addition of 10 m of length to the PFA tubing to the sampling inlet line. Briefly, the Ox-CIMS sampled from a 20m long (30 m for Lake Mendota), 0.64 cm i.d, perfluoroalkoxy alkane (PFA) inlet manifold with the intake point co-located with a sonic anemometer recording 3-dimensional winds at 10Hz (Gill Instruments HS-50). The inlet sample line was held at 40 °C and pumped at 18-23 slpm (Reynolds number 3860-4940) by a dry scroll pump (SH-110, Agilent) to ensure a fast time response (<2 s) and maintain turbulent flow. The Ox-CIMS subsampled 1.5 slpm from this inlet manifold through a critical orifice into the IMR. The Ox-CIMS subsampling block and IMR were held at 35°C. This sampling configuration maintained fast time responses and minimized wall interactions. Relative humidity and temperature were also recorded in-line downstream of the subsampling point.

Instrument backgrounds were determined by periodically (approximately every 30 minutes) overflowing the sampling manifold with dry ultra-high purity nitrogen (UHP N_2). As described in detail in Novak et al., (2019)[26], instrument backgrounds were corrected to account for

the change in O_3 product distribution when sampling in in dry UHP N_2 compared to ambient air containing CO_2. Typical background O_3 signal was 1.3 ppbv.

Instrument sensitivity was assessed in the Scripps Pier deployment by the standard addition of a C-13 isotopically labelled formic acid standard for 3 minutes every 35 minutes. For the Scripps Pier deployment, O_3 mixing ratios were determined by scaling the humidity dependent sensitivity of ozone from pre- and post-campaign calibrations to the field calibrations of C-13 formic acid. For the Lake Mendota deployment O_3 mixing ratios were determined by directly applying laboratory determined specific humidity dependent calibration factors for O_3 determined immediately prior to the deployment, to the ambient observations.

S1.3 Eddy Covariance Flux data processing and quality control

S1.3.1 General data treatment

Full details of the Scripps Pier flux data processing and quality control are given in Novak et al. (2019).[26] Generally data processing for the Lake Mendota was the same except as noted in Section S1.3.2. Briefly, the following data processing steps were applied: 1.) Three dimensional winds were coordinate rotated using a planar fit method to remove unintentional tilts in the sonic mounting and account for local flow distortion. 2.) The O_3 timeseries was detrended with a linear function prior to the flux calculation. 3.) The O_3 and vertical wind data were despiked using a mean absolute deviation filter before the eddy covariance flux calculation following Mauder et al., (2013). 4.) Winds were filtered by wind sector so that only periods of onshore flow were considered. 5.) A friction velocity threshold was applied to reject periods of low shear driven turbulence for the Scripps Pier dataset. For the Scripps Pier data, periods were rejected if their measured friction velocity was more than 50% different from the friction velocity calculated by the NOAA COARE v3.6 algorithm. 6.) A fixed lag time was applied to align the signal of O_3 and

w. A delay in O_3 relative to *w* is driven by the volumetric residence time of O_3 in the inlet tubing. For Scripps Pier a lag time of 0.9 s was used and for Lake Mendota a lag time of 1.7 s was used. 7.) Ambient sampling periods were divided into 27-minute long flux averaging periods. Analysis of the ogives showed this to be sufficiently long to sample the largest scale turbulent eddies. 8.) Non-stationary flux periods were rejected using a 40% stationarity threshold following Foken and Wichura (1996)[51] 9.) Outliers in the calculated $v_d(O_3)$ were determined and removed for points three scaled median absolute deviations from the median.

S1.3.2 Lake Mendota specific data treatment

The Lake Mendota flux sampling site is a non-ideal flux site due to heterogeneous terrain around the sensor and the influence of the building itself on local flows as described by Reed et al. (2018).[31] In particular a immediately behind the sensor location was seen to drive nighttime drainage flows towards the sensor and the lake. A data filtering approach directly following Reed et al. (2018)[31] was applied which includes a flux footprint filter to remove non-lake data periods, and screening out data within 10° orthogonal to the sonic anemometer to account for a vertical velocity bias from flow distortion by the building. Sonic anemometer coordinate rotation, stationarity filtering, despiking, detrending, and lag time determination were all applied to the Lake Mendota data set as noted in Section S1.3.1.

S1.4 Estimating Lake Mendota Iodide

Iodide concentrations have not been measured at Lake Mendota to our knowledge. Snyder & Fehn, (2004) reported total iodine in a large number of lakes to typically be from 1-10 μg L^{-1} with most values below 5 μg L^{-1}. Observations of iodine and iodide in Lake Constance and its tributeries were consistent with that range, with total iodine from 1-10 μg L^{-1} with speciated iodide typically being 0-10% of total iodine (0-1.3 μg L^{-1}).[38] Taking iodide as being 10% of total iodine gives a

typical represenative range 0.1-1 μg L^{-1} or 0.8 to 8 nM. We elect to use a iodide concentration of 2 nM for Lake Mendota and note that all presented calculations are fairly insensitive to calculations of $v_d(O_3)$ are fairly insensitive to iodide over the range of 0.8 to 8 nM.

S1.5. NOAA COARE Algorithm Implementation

The NOAA Coupled Ocean–Atmosphere Response Experiment (COARE v3.6) bulk algorithm was used as a comparison for the observed wind-speed and SST dependent O_3 deposition velocities observed in the SIO observations.[5,35,52] The COARE algorithms are a physically based meteorological and gas transfer bulk flux parametrization. Specific alterations of the COARE v3.6 algorithm were made by Fairall et al. to better capture O_3 deposition following the approach of.[5] In particular, this included the implementation of a two-layer waterside model which treats a diffusive surface layer and turbulent mixing in the bulk. The relative importance of O_3 reactivity is set by the thickness of the surface diffusive layer (δ_m) and the total reactivity of O_3.[5] COARE v3.6 explicitly parameterizes the reaction of O_3 with I^-, incorporating the SST dependent parameterization of iodide concentrations (Equation S6)[33] and the temperature dependent bimolecular rate constant of Magi et al., (1997).[16] The base implementation of COARE v3.6 does not include reactions of O_3 with DOC.

In our implementation of the COARE v3.6 algorithm, observed meteorology and chemical parameters were used as inputs for each individual flux measurement period. These observed inputs included: wind speed, air temperature, sea-surface temperature, static pressure, relative humidity, latitude, and gas phase O_3 mixing ratios. Fixed values of downward shortwave = 150 W m^{-2}, longwave radiation = 370 W m^{-2}, salinity = 35 PSU, observation height of all parameters = 12 m, and boundary layer height = 400 m. All other algorithm inputs used the included default parameterizations. The fixed marine boundary layer height (BLH) of 400 m was used taken

approximate mean daytime BLH from the NOAA HRRR Stability product retrieved from the READY web server for July 2018. The default microlayer thickness of 3 μM was used in all calculations. Additional sensitivity tests of COARE v3.6 algorithm determination of $v_d(O_3)$ to changes in iodide reactivity, surface layer thickness, inclusion of waterside turbulent mixing, and inclusion of DOC reactivity are shown in Figure S1.1 and S1.2.

NOAA COARE v3.6 was run in Matlab using the codes publicly available at: ftp://ftp1.esrl.noaa.gov/BLO/Air-Sea/bulkalg/cor3_6/. (codes used by the authors are available upon request if the above link becomes unavailable)

Acknowledgements

This work was supported by National Science Foundation (NSF) Grant GEO AGS 1829667.

The authors thank the staff at Scripps Pier, Scripps Institute of Oceanography and at the UW—Madison Department of Limnology for support in instrument deployments, with particular thanks to Jeff Bowman for facilitating access to Scripps Pier.

Glenn M. Wolfe is gratefully acknowledged for publicly providing (archived on GitHub) a Matlab based FluxToolbox of analysis scripts, potions of which were altered for use in this analysis.

This research was performed using the computing resources and assistance of the UW-Madison Center for High Throughput Computing (CHTC) in the Department of Computer Sciences. The CHTC is supported by UW-Madison, the Advanced Computing Initiative, the Wisconsin Alumni Research Foundation, the Wisconsin Institutes for Discovery, and the National Science Foundation, and is an active member of the Open Science Grid, which is supported by the National Science Foundation and the U.S. Department of Energy's Office of Science.

References

(1) Finlayson-Pitts, B. J.; Pitts, J. N. Global Tropospheric Chemistry and Climate Change. In *Chemistry of the Upper and Lower Atmosphere*; 2000. https://doi.org/10.1016/b978-012257060-5/50016-2.

(2) World Health Organization. *Air Quality Guidelines. Global Update 2005*; 2006. https://doi.org/10.1007/BF02986808.

(3) Avnery, S.; Mauzerall, D. L.; Liu, J.; Horowitz, L. W. Global Crop Yield Reductions Due to Surface Ozone Exposure: 1. Year 2000 Crop Production Losses and Economic Damage. *Atmos. Environ.* **2011**, *45* (13), 2284–2296. https://doi.org/10.1016/j.atmosenv.2010.11.045.

(4) IPCC. *Climate Change 2014: Synthesis Report. Contribution of Working Groups I, II and III to the Fifth Assessment Report of the Intergovernmental Panel on Climate Change*;

Geneva, Sqitzerland, 2014.

(5) Galbally, I. E.; Roy, C. R. Destruction of Ozone at the Earth's Surface. *Q. J. R. Meteorol. Soc.* **1980**, *106* (449), 599–620. https://doi.org/10.1002/qj.49710644915.

(6) Wesely, M. L. Parameterization of Surface Resistances to Gaseous Dry Deposition in Regional-Scale Numerical Model. *Atmos. Environ.* **1989**, *23* (6), 1293–1304. https://doi.org/https://doi.org/10.1016/0004-6981(89)90153-4.

(7) Luhar, A. K.; Galbally, I. E.; Woodhouse, M. T.; Thatcher, M. An Improved Parameterisation of Ozone Dry Deposition to the Ocean and Its Impact in a Global Climate-Chemistry Model. *Atmos. Chem. Phys.* **2017**, *17* (5), 3749–3767. https://doi.org/10.5194/acp-17-3749-2017.

(8) Ganzeveld, L.; Helmig, D.; Fairall, C. W.; Hare, J.; Pozzer, A. Atmosphere-Ocean Ozone Exchange: A Global Modeling Study of Biogeochemical, Atmospheric, and Waterside Turbulence Dependencies. *Global Biogeochem. Cycles* **2009**, *23* (4), 1–16. https://doi.org/10.1029/2008GB003301.

(9) Luhar, A. K.; Woodhouse, M. T.; Galbally, I. E. A Revised Global Ozone Dry Deposition Estimate Based on a New Two-Layer Parameterisation for Air-Sea Exchange and the Multi-Year MACC Composition Reanalysis. *Atmos. Chem. Phys.* **2018**, *18* (6), 4329–4348. https://doi.org/10.5194/acp-18-4329-2018.

(10) Helmig, D.; Lang, E. K.; Bariteau, L.; Boylan, P.; Fairall, C. W.; Ganzeveld, L.; Hare, J.; Huebert, B. J.; Pallandt, M. Atmosphere-Ocean Ozone Fluxes during the TexAQS 2006, STRATUS 2006, GOMECC 2007, GasEx 2008, and AMMA 2008 Cruises. *J. Geophys. Res. Atmos.* **2012**, *117* (D4). https://doi.org/10.1029/2011JD015955.

(11) Lenschow, D. H.; Pearson, R. J.; Stankov, B. B. Measurements of Ozone Vertical Flux to Ocean and Forest. *J. Geophys. Res.* **1982**, *87* (C11), 8833–8837. https://doi.org/10.1029/JC087iC11p08833.

(12) Kawa, S. R.; Pearson, R. Ozone Budgets from the Dynamics and Chemistry of Marine Stratocumulus Experiment. *J. Geophys. Res.* **1989**, *94* (D7), 9809–9817. https://doi.org/10.1029/JD094iD07p09809.

(13) Wesely, M. L.; Hicks, B. B. A Review of the Current Status of Knowledge on Dry Deposition. *Atmospheric Environment*. 2000. https://doi.org/10.1016/S1352-2310(99)00467-7.

(14) Wesely, M. L.; Cook, D. R.; Williams, R. M. Field Measurement of Small Ozone Fluxes to Snow, Wet Bare Soil, and Lake Water. *Boundary-Layer Meteorol.* **1981**, *20* (4), 459–471. https://doi.org/10.1007/BF00122295.

(15) Liss, P. S.; Slater, P. G. Flux of Gases across the Air-Sea Interface. *Nature* **1974**, *247* (5438),

181–184. https://doi.org/10.1038/247181a0.

(16) Schwartz, S. E. Factors Governing Dry Deposition of Gases to Surface Water. In *Precipitation Scavenging and Atmosphere-Surface Exchange*; Schwartz, S., Slinn, W. G. N., Eds.; Hemisphere Publ: Washington D.C., 1992; pp 789–801.

(17) Chang, W.; Heikes, B. G.; Lee, M. Ozone Deposition to the Sea Surface: Chemical Enhancement and Wind Speed Dependence. *Atmos. Environ.* **2004**, *38* (7), 1053–1059. https://doi.org/10.1016/j.atmosenv.2003.10.050.

(18) Hansell, D. A.; Carlson, C. A.; Repeta, D. J.; Schlitzer, R. Dissolved Organic Matter in the Ocean a Controversy Stim Ulates New Insights. *Oceanography* **2009**, *22* (SPL.ISS. 4), 202–211. https://doi.org/10.5670/oceanog.2009.109.

(19) Sobek, S.; Tranvik, L. J.; Prairie, Y. T.; Kortelainen, P.; Cole, J. J. Patterns and Regulation of Dissolved Organic Carbon: An Analysis of 7,500 Widely Distributed Lakes. *Limnol. Oceanogr.* **2007**, *52* (3), 1208–1219. https://doi.org/10.4319/lo.2007.52.3.1208.

(20) Magi, L.; Schweitzer, F.; Pallares, C.; Cherif, S.; Mirabel, P.; George, C. Investigation of the Uptake Rate of Ozone and Methyl Hydroperoxide by Water Surfaces. *J. Phys. Chem. A* **1997**, *101* (27), 4943–4949. https://doi.org/10.1021/jp970646m.

(21) Dowideit, P.; Von Sonntag, C. Reaction of Ozone with Ethene and Its Methyl- and Chlorine-Substituted Derivatives in Aqueous Solution. *Environ. Sci. Technol.* **1998**, *32* (8), 1112–1119. https://doi.org/10.1021/es971044j.

(22) Gershenzon, M.; Davidovits, P.; Jayne, J. T.; Kolb, C. E.; Worsnop, D. R. Simultaneous Uptake of DMS and Ozone on Water. *J. Phys. Chem. A* **2001**, *105* (29), 7031–7036. https://doi.org/10.1021/jp010696y.

(23) Carpenter, L. J.; MacDonald, S. M.; Shaw, M. D.; Kumar, R.; Saunders, R. W.; Parthipan, R.; Wilson, J.; Plane, J. M. C. C. Atmospheric Iodine Levels Influenced by Sea Surface Emissions of Inorganic Iodine. *Nat. Geosci.* **2013**, *6* (2), 108–111. https://doi.org/10.1038/ngeo1687.

(24) Clifford, D.; Donaldson, D. J.; Brigante, M.; D'Anna, B.; George, C. Reactive Uptake of Ozone by Chlorophyll at Aqueous Surfaces. *Environ. Sci. Technol.* **2008**, *42* (4), 1138–1143. https://doi.org/10.1021/es0718220.

(25) Martino, M.; Lézé, B.; Baker, A. R.; Liss, P. S. Chemical Controls on Ozone Deposition to Water. *Geophys. Res. Lett.* **2012**, *39* (5), 39–43. https://doi.org/10.1029/2011GL050282.

(26) Garland, J. A.; Elzerman, A. W.; Penkett, S. A. The Mechanism for Dry Deposition of Ozone to Seawater Surface. *J. Geophys. Res.* **1980**, *85* (C12), 7488–7492. https://doi.org/10.1029/JC085iC12p07488.

(27) Martino, M.; Mills, G. P.; Woeltjen, J.; Liss, P. S. A New Source of Volatile Organoiodine Compounds in Surface Seawater. *Geophys. Res. Lett.* **2009**, *36* (1), 2–6. https://doi.org/10.1029/2008GL036334.

(28) Zhou, S.; Gonzalez, L.; Leithead, A.; Finewax, Z.; Thalman, R.; Vlasenko, A.; Vagle, S.; Miller, L. A.; Li, S. M.; Bureekul, S.; et al. Formation of Gas-Phase Carbonyls from Heterogeneous Oxidation of Polyunsaturated Fatty Acids at the Air-Water Interface and of the Sea Surface Microlayer. *Atmos. Chem. Phys.* **2014**. https://doi.org/10.5194/acp-14-1371-2014.

(29) Schneider, S. R.; Collins, D. B.; Lim, C. Y.; Zhu, L.; Abbatt, J. P. D. Formation of Secondary Organic Aerosol from the Heterogeneous Oxidation by Ozone of a Phytoplankton Culture. *ACS Earth Sp. Chem.* **2019**, *3*, 0–8. https://doi.org/10.1021/acsearthspacechem.9b00201.

(30) Novak, G.; Vermeuel, M.; Bertram, T. Simultaneous Detection of Ozone and Nitrogen Dioxide by Oxygen Anion Chemical Ionization Mass Spectrometry: A Fast Time Response Sensor Suitable for Eddy Covariance Measurements. *Atmos. Meas. Tech. Discuss.* **2019**. https://doi.org/10.5194/amt-2019-445.

(31) Porter, J. G.; De Bruyn, W.; Saltzman, E. S. Eddy Flux Measurements of Sulfur Dioxide Deposition to the Sea Surface. *Atmos. Chem. Phys.* **2018**, *18* (20), 15291–15305. https://doi.org/10.5194/acp-18-15291-2018.

(32) Ikawa, H.; Oechel, W. C. Temporal Variations in Air-Sea CO2 Exchange near Large Kelp Beds near San Diego, California. *J. Geophys. Res. Ocean.* **2015**, *120* (1), 50–63. https://doi.org/10.1002/2014JC010229.

(33) Kim, M. J.; Farmer, D. K.; Bertram, T. H. A Controlling Role for the Air-Sea Interface in the Chemical Processing of Reactive Nitrogen in the Coastal Marine Boundary Layer. *Proc Natl Acad Sci U S A* **2014**, *111* (11), 3943–3948. https://doi.org/10.1073/pnas.1318694111.

(34) Wright, D. Oceanographic Data Collected from Station Scripps Pier in the Coastal Waters of California by Southern California Coastal Ocean Observing System (SCCOOS) at Scripps Institution of Oceanography (SIO) and Assembled by Southern California Coastal Ocean Obser. NOAA National Centers for Environmental Information 2016.

(35) Reed, D. E.; Dugan, H. A.; Flannery, A. L.; Desai, A. R. Carbon Sink and Source Dynamics of a Eutrophic Deep Lake Using Multiple Flux Observations over Multiple Years. *Limnol. Oceanogr. Lett.* **2018**, *18*, 285–292. https://doi.org/10.1002/lol2.10075.

(36) Chance, R.; Baker, A. R.; Carpenter, L.; Jickells, T. D. The Distribution of Iodide at the Sea Surface. *Environ. Sci. Process. Impacts* **2014**, *16* (8), 1841–1859. https://doi.org/10.1039/c4em00139g.

(37) Macdonald, S. M.; Gómez Martín, J. C.; Chance, R.; Warriner, S.; Saiz-Lopez, A.; Carpenter, L. J.; Plane, J. M. C. A Laboratory Characterisation of Inorganic Iodine Emissions from the Sea Surface: Dependence on Oceanic Variables and Parameterisation for Global Modelling. *Atmos. Chem. Phys.* **2014**, *14* (11), 5841–5852. https://doi.org/10.5194/acp-14-5841-2014.

(38) Sherwen, T.; Chance, R. J.; Tinel, L.; Ellis, D.; Evans, M. J.; Carpenter, L. J. A Machine-Learning-Based Global Sea-Surface Iodide Distribution. *Earth Syst. Sci. Data* **2019**, *11* (3), 1239–1262. https://doi.org/10.5194/essd-11-1239-2019.

(39) Fairall, C. W.; Helmig, D.; Ganzeveld, L.; Hare, J. Water-Side Turbulence Enhancement of Ozone Deposition to the Ocean. *Atmos. Chem. Phys.* **2007**, *7* (2), 443–451. https://doi.org/10.5194/acp-7-443-2007.

(40) Center for Limnology NTL LTER. North Temperate Lakes LTER: Chemical Limnology of Primary Study Lakes: Nutrients, PH and Carbon 1981 - Current. Environmental Data Initiative 2012. https://doi.org/10.6073/pasta/cc6f0e4d317d29200234c7243471472a.

(41) Snyder, G.; Fehn, U. Global Distribution of 129I in Rivers and Lakes: Implications for Iodine Cycling in Surface Reservoirs. *Nucl. Instruments Methods Phys. Res. Sect. B Beam Interact. with Mater. Atoms* **2004**, *223–224*, 579–586. https://doi.org/10.1016/j.nimb.2004.04.107.

(42) Gilfedder, B. S.; Petri, M.; Wessels, M.; Biester, H. An Iodine Mass-Balance for Lake Constance, Germany: Insights into Iodine Speciation Changes and Fluxes. *Geochim. Cosmochim. Acta* **2010**, *74* (11), 3090–3111. https://doi.org/10.1016/j.gca.2010.03.008.

(43) Zhou, Z.; Guo, L.; Minor, E. C. Characterization of Bulk and Chromophoric Dissolved Organic Matter in the Laurentian Great Lakes during Summer 2013. *J. Great Lakes Res.* **2016**, *42* (4), 789–801. https://doi.org/10.1016/j.jglr.2016.04.006.

(44) Biddanda, B. A.; Cotner, J. B. Enhancement of Dissolved Organic Matter Bioavailability by Sunlight and Its Role in the Carbon Cycle of Lakes Superior and Michigan. *J. Great Lakes Res.* **2003**, *29* (2), 228–241. https://doi.org/10.1016/S0380-1330(03)70429-8.

(45) Shaw, M. D.; Carpenter, L. J. Modification of Ozone Deposition and I2 Emissions at the Air-Aqueous Interface by Dissolved Organic Carbon of Marine Origin. *Environ. Sci. Technol.* **2013**, *47* (19), 10947–10954. https://doi.org/10.1021/es4011459.

(46) Coleman, L.; McVeigh, P.; Berresheim, H.; Martino, M.; O'Dowd, C. D. Photochemical Impact on Ozone Fluxes in Coastal Waters. *Adv. Meteorol.* **2012**, *2012*. https://doi.org/10.1155/2012/943785.

(47) Wurl, O.; Wurl, E.; Miller, L.; Johnson, K.; Vagle, S. Formation and Global Distribution of Sea-Surface Microlayers. *Biogeosciences* **2011**, *8* (1), 121–135. https://doi.org/10.5194/bg-

8-121-2011.

(48) Sullivan, J. T.; Berkoff, T.; Gronoff, G.; Knepp, T.; Pippin, M.; Allen, D.; Twigg, L.; Swap, R.; Tzortziou, M.; Thompson, A. M.; et al. The Ozone Water-Land Environmental Transition Study: An Innovative Strategy for Understanding Chesapeake Bay Pollution Events. *Bull. Am. Meteorol. Soc.* **2019**, *100* (2), 291–306. https://doi.org/10.1175/BAMS-D-18-0025.1.

(49) Qin, M.; Yu, H.; Hu, Y.; Russell, A. G.; Odman, M. T.; Doty, K.; Pour-Biazar, A.; McNider, R. T.; Knipping, E. Improving Ozone Simulations in the Great Lakes Region: The Role of Emissions, Chemistry, and Dry Deposition. *Atmos. Environ.* **2019**, *202* (January), 167–179. https://doi.org/10.1016/j.atmosenv.2019.01.025.

(50) Mekic, M.; Loisel, G.; Zhou, W.; Jiang, B.; Vione, D.; Gligorovski, S. Ionic-Strength Effects on the Reactive Uptake of Ozone on Aqueous Pyruvic Acid: Implications for Air-Sea Ozone Deposition. *Environ. Sci. Technol.* **2018**, *52* (21), 12306–12315. https://doi.org/10.1021/acs.est.8b03196.

(51) Kloster, S.; Feichter, J.; Maier-Reimer, E.; Six, K. D.; Stier, P.; Wetzel, P. DMS Cycle in the Marine Ocean-Atmosphere System - A Global Model Study. *Biogeosciences* **2006**, *3* (1), 29–51. https://doi.org/10.5194/bg-3-29-2006.

(52) Lana, A.; Bell, T. G.; Simó, R.; Vallina, S. M.; Ballabrera-Poy, J.; Kettle, A. J.; Dachs, J.; Bopp, L.; Saltzman, E. S.; Stefels, J.; et al. An Updated Climatology of Surface Dimethlysulfide Concentrations and Emission Fluxes in the Global Ocean. *Global Biogeochem. Cycles* **2011**, *25* (1), 1–17. https://doi.org/10.1029/2010GB003850.

(53) Land, P. E.; Shutler, J. D.; Bell, T. G.; Yang, M. Exploiting Satellite Earth Observation to Quantify Current Global Oceanic DMS Flux and Its Future Climate Sensitivity. *J. Geophys. Res. Ocean.* **2014**. https://doi.org/10.1002/2014JC010104.

(54) Downing, J. A.; Duarte, C. M. Abundance and Size Distribution of Lakes, Ponds and Impoundments. *Encycl. Inl. Waters* **2009**, *51* (5), 469–478. https://doi.org/10.1016/B978-012370626-3.00025-9.

(55) Steinke, M.; Hodapp, B.; Subhan, R.; Bell, T. G.; Martin-Creuzburg, D. Flux of the Biogenic Volatiles Isoprene and Dimethyl Sulfide from an Oligotrophic Lake. *Sci. Rep.* **2018**, *8* (1), 1–10. https://doi.org/10.1038/s41598-017-18923-5.

(56) Stull, R. B. An Introduction to Boundary Layer Meteorology. *An Introd. to Bound. layer Meteorol.* **1988**. https://doi.org/10.1007/978-94-009-3027-8.

(57) Bertram, T. H.; Kimmel, J. R.; Crisp, T. A.; Ryder, O. S.; Yatavelli, R. L. N.; Thornton, J. A.; Cubison, M. J.; Gonin, M.; Worsnop, D. R. A Field-Deployable, Chemical Ionization Time-of-Flight Mass Spectrometer. *Atmos. Meas. Tech.* **2011**, *4* (7), 1471–1479.

https://doi.org/10.5194/amt-4-1471-2011.

(58) Foken, T.; Wichura, B. Tools for Quality Assessment of Surface-Based Flux Measurements. *Agric. For. Meteorol.* **1996**, *78* (1–2), 83–105. https://doi.org/10.1016/0168-1923(95)02248-1.

(59) Fairall, C. W.; Yang, M.; Bariteau, L.; Edson, J. B.; Helmig, D.; McGillis, W.; Pezoa, S.; Hare, J. E.; Huebert, B.; Blomquist, B. Implementation of the Coupled Ocean-Atmosphere Response Experiment Flux Algorithm with CO2, Dimethyl Sulfide, and O3. *J. Geophys. Res. Ocean.* **2011**, *116* (10). https://doi.org/10.1029/2010JC006884.

Figures

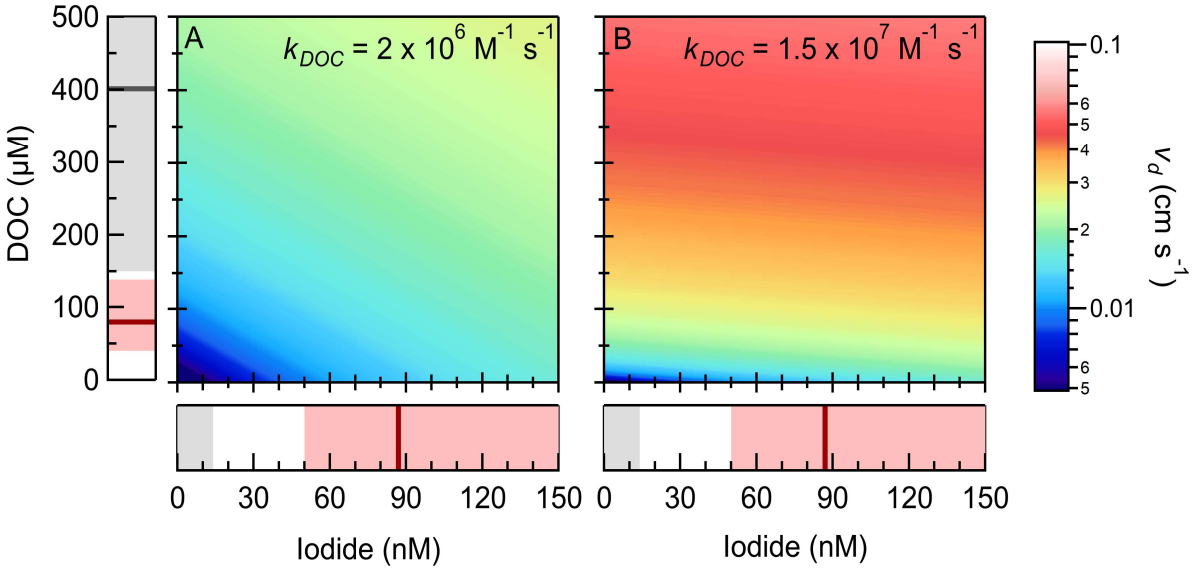

Figure 1.1. Calculated $v_d(O_3)$ as a function of water DOC and iodide concentrations for k_{DOC} of (a) 2 x 10^6 M^{-1} s^{-1} and (b) 1.5 x 10^7 M^{-1} s^{-1}. The red and grey shaded regions on the x- and y-axis represent typical surface concentrations of I^- and DOC for mid-latitude ocean and freshwater lakes respectively. The solid red and grey lines are the approximate mean values for the SIO and Lake Mendota O_3 deposition studies.

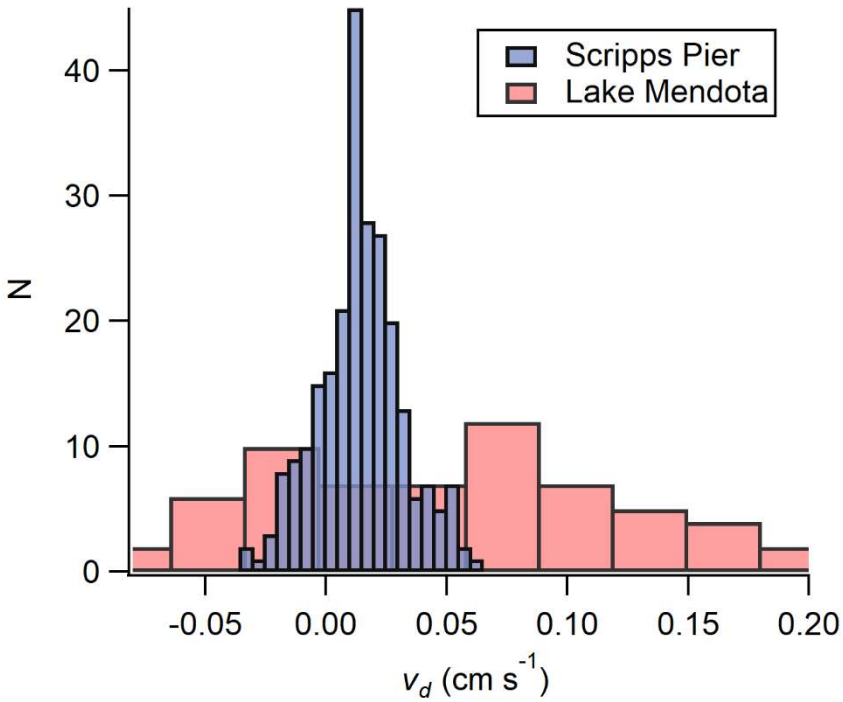

Figure 1.2. Observed $v_d(O_3)$ to the coastal ocean from Scripps Pier and to the eutrophic freshwater Lake Mendota. Mean measured $v_d(O_3)$ to the coastal ocean and Lake Mendota were 0.013 cm s^{-1} and 0.038 cm s^{-1} respectively.

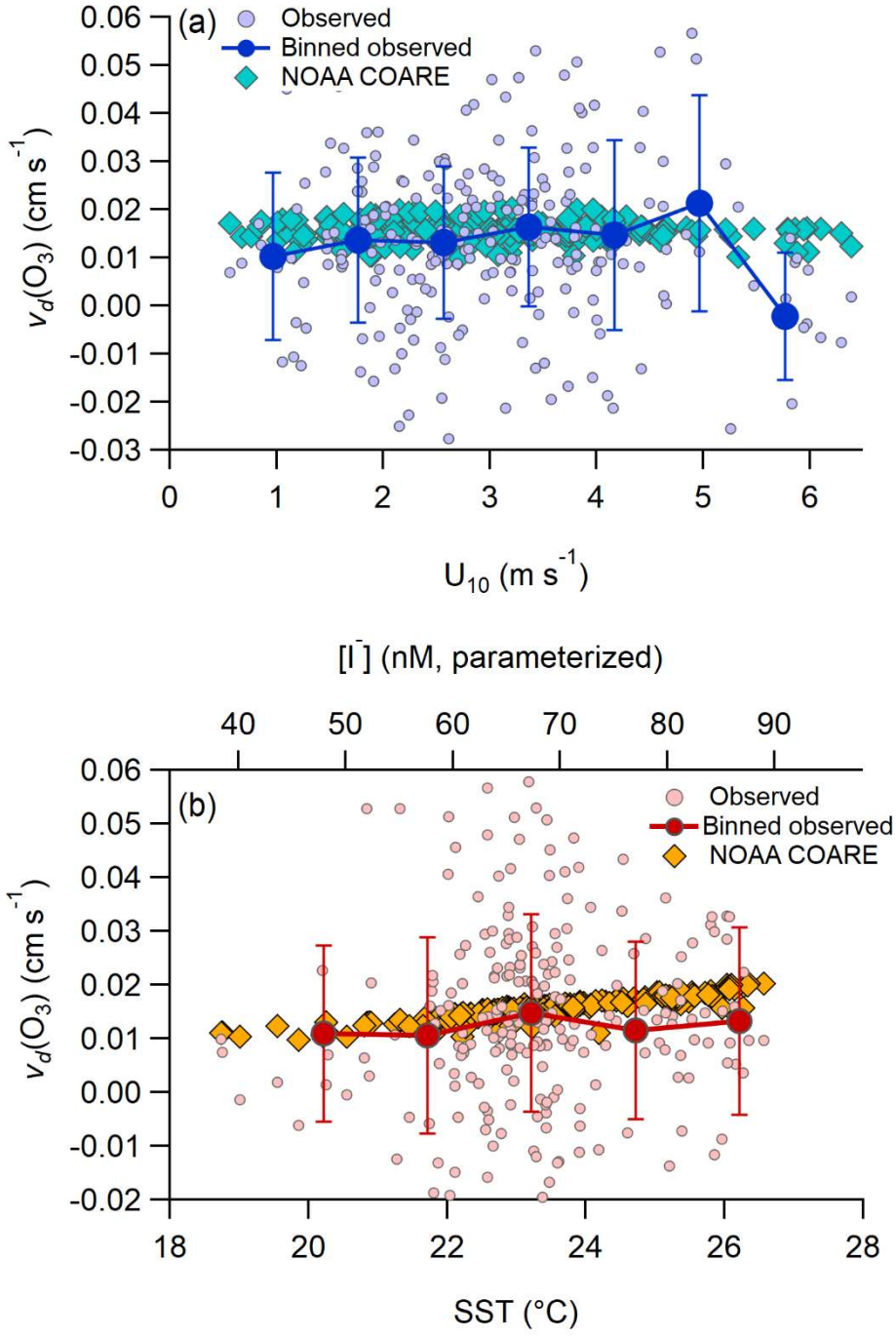

Figure 1.3. Observed relationship of O_3 v_d with (a) horizontal wind speed (U_{10}) and (b) sea-surface temperature (SST), as measured from Scripps Pier. NOAA COARE traces on (a) and (b) are the calculated $v_d(O_3)$ from the NOAA COARE v3.6 algorithm and the observed meteorology for each flux measurement period.

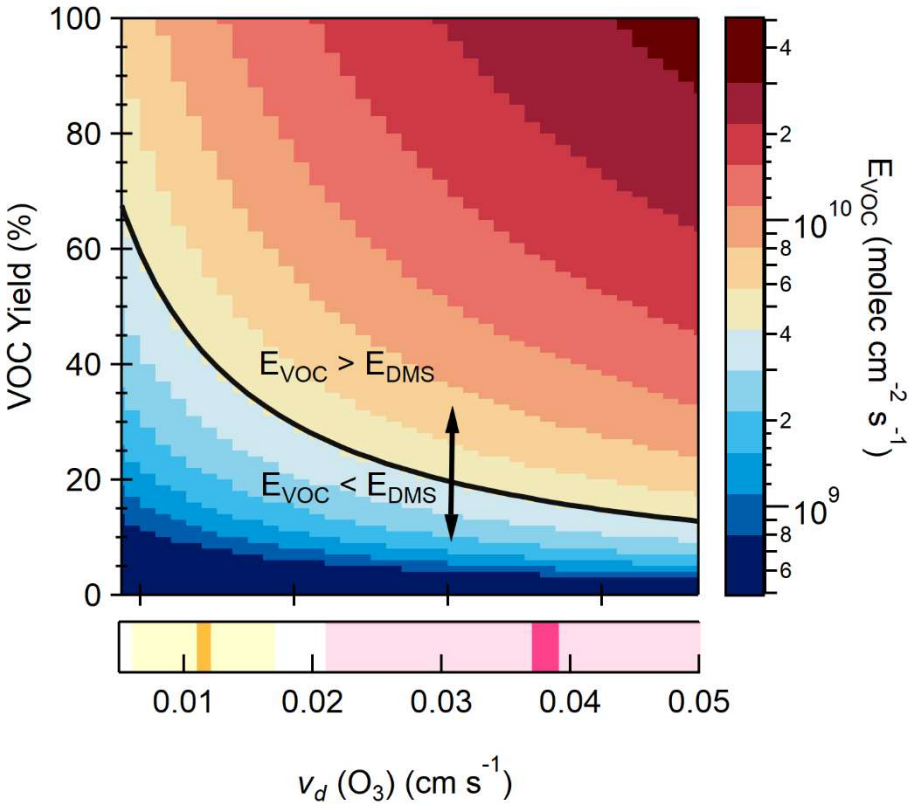

Figure 1.4. Calculated VOC emission flux (E_{voc}) as a function of O_3 deposition velocities and VOC yield. The O_3 mixing ratio is 30 ppbv and the deposition of O_3 is assumed to be the rate limiting step. The solid black line is the contour where scaled E_{VOC} is equal to global mean E_{DMS} from Lana et al. (2011). The yellow and pink shaded regions on the x-axis are the interquartile range of observed $v_d(O_3)$ for the SIO and Lake Mendota measurements respectively. The solid yellow and pink lines are the mean values of the observations.

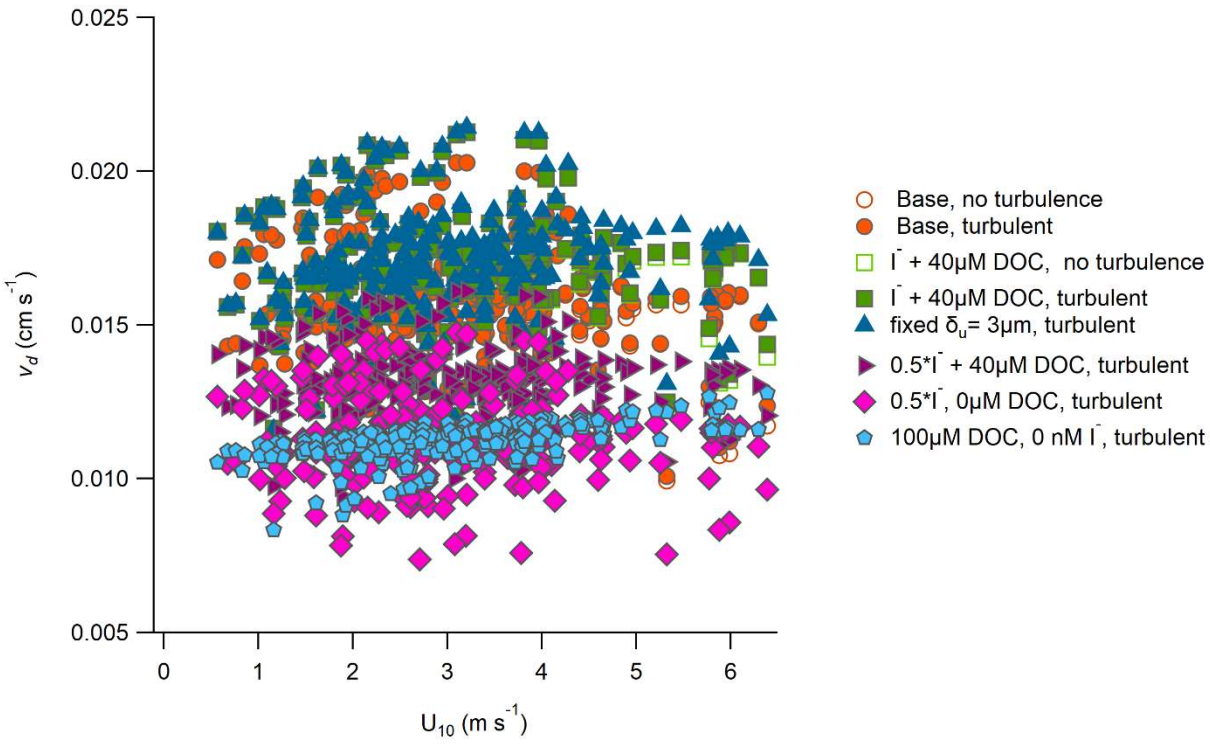

Figure 1.S1. Calculated $v_d(O_3)$ as a function of wind speed from the NOAA COARE v3.6 algorithm using observed meteorology for each Scripps Pier flux measurement period under various model parameterizations. Notation "turbulent" and "no turbulence" indicate whether the two-layer model waterside model with bulk ocean turbulent mixing was turned on or off respectively. Iodide concentrations are parameterized from SST following MacDonald et al. (2014).

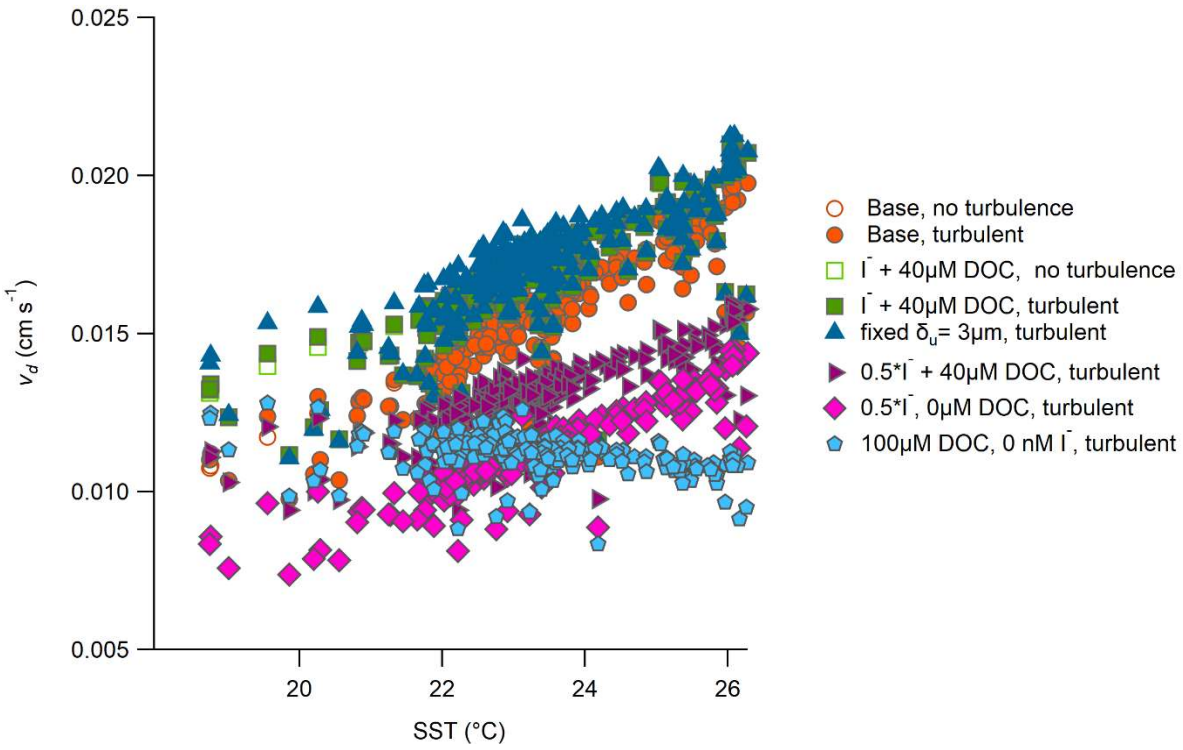

Figure 1.S2. Calculated $v_d(O_3)$ as a function of sea-surface temperature (SST) from the NOAA COARE v3.6 algorithm using observed meteorology for each Scripps Pier flux measurement period under various model parameterizations. Notation "turbulent" and "no turbulence" indicate whether the two-layer model waterside model with bulk ocean turbulent mixing was turned on or off respectively. Iodide concentrations are parameterized from SST following MacDonald et al. (2014).

Chapter 2. Air-sea exchange of volatile organic compounds at a coastal ocean site

Abstract

The ocean surface serves as a source and sink for a diverse set of reactive trace gases in the atmosphere, including non-methane volatile organic compounds (NMVOC). To date, direct observations of air-sea exchange of NMVOCs has been limited to a small set of atmospheric constituents and estimates of ocean emissions for many NMVOC are incomplete. The exchange of reactive trace gases between the atmosphere and ocean has been shown to alter atmospheric oxidant concentrations and drive particle nucleation and growth. Here we present eddy-covariance (EC) flux observations from one month of ambient sampling from Scripps Pier at the Scripps Institution of Oceanography, La Jolla CA, in September 2019. EC flux observations were made with a latest generation high sensitivity (>2 cps ppt^{-1}) and mass resolution ($m/\Delta m$ >4500) Vocus proton transfer reaction time-of-flight mass spectrometer, enabling a broad survey of marine NMVOC exchange. A total of 44 species were found to have statistically significant air-sea flux (at an 80% confidence level). Dimethyl sulfide was found to account for 40% of net NMVOC carbon mass emission flux, with 11 ions capturing 90% of total carbon mass emissions. Acetone, acetic acid, acetaldehyde and methanol were observed to be the primary depositing NMVOCs accounting for 40, 29, 13, and 6% of carbon mass deposition flux respectively. Laboratory studies have suggested that photochemistry occurring at the ocean surface could contribute significantly to NMVOC emissions. In this study, we do not observe a strong correlation between VOC flux with either ozone or solar irradiance, in contrast with previous laboratory studies. Observed NMVOC emission fluxes were observed to best correlated with horizontal wind-speed consistent with existing parameterizations of bulk air-sea trace gas exchange. Results from this study demonstrate the utility of performing broad, untargeted studies of air-sea trace gas exchange. Future studies following this framework over wider spatiotemporal coverage of the remote ocean

will be essential to fully constrain the relative roles of biotic and abiotic marine NMVOC exchange.

2.1 Introduction

Emissions of non-methane volatile organic compounds (NMVOC) from the ocean surface have been shown to impact oxidant loadings and secondary aerosol (SOA) formation in the marine atmosphere.[1–5] To date, marine NMVOC research has primarily focused on the seawater production and emission of dimethyl sulfide (DMS). Total annual estimates of DMS emissions range between 14.7 to 21.1 Tg C yr^{-1}.[6–9] Comparatively less work has focused on other marine biogenic NMVOC sources including isoprene and monoterpenes (MT). Isoprene and MT are known to be efficiently produced by some species of marine phytoplankton.[10] Surface seawater isoprene concentrations have been reported in the range of 0.1-100 pM, with higher concentrations often correlated with chlorophyll *a*.[10,11] Speciated dissolved MT concentrations ranged from 0.5 to 2.9 pM over several cruises in the Atlantic and Arctic with no clear correlation to biological productivity.[12] Marine gas-phase isoprene mixing ratios have been observed as high as 375 ppt during a phytoplankton bloom,[13] but are typically less than 20 ppt in non-bloom conditions.[10] MT mixing ratios were 125 ppt (phytoplankton bloom) and 5 ppt (non-bloom) in the southern Atlantic Ocean.[13] The only eddy covariance (EC) flux observations of isoprene and MT air-sea fluxes in the literature were measured during High Wind Gas Exchange Study (HiWinGS) over the Northern Atlantic Ocean during fall, with campaign mean emission fluxes of 5.0×10^7 molecules cm^{-2} s^{-1} for isoprene, 2.6×10^7 molecules cm^{-2} s^{-1} for MT, and 1.04×10^9 molecules cm^{-2} s^{-1} for DMS.[14] However, in a localized biological hotspot during an upwelling event, the maximum monoterpene flux (1.62×10^9 molecules cm^{-2} s^{-1}) was larger than coincident DMS emissions, highlighting the importance of local biological variability on biogenic NMVOC emissions. Observed DMS,

isoprene, and MT fluxes from that study scaled to the global ocean gives estimated annual emissions of 4.71, 0.57, and 0.60 Tg C yr^{-1} for DMS, isoprene, and monoterpenes, respectively. Those annual emissions weighted by OH reactivity and normalized to DMS are 1, 1.02, and 0.28 for DMS, isoprene, and monoterpenes respectively, highlighting the significance of terpenes on atmospheric oxidative capacity despite smaller mass emissions. Total marine isoprene emissions parameterized from dissolved concentrations (bottom-up) and remote sensing products (top-down) result in emission estimates from 0.1 to 12 Tg C yr^{-1} respectively.[15,16] Marine monoterpene emissions are also highly uncertain, with estimated global emissions of 0.01 and 29.5 Tg C yr^{-1} from bottom-up and top-down methods respectively.[17] While monoterpene and isoprene emissions are known to be considerably smaller than DMS they may still have significant impacts on aerosol formation due to their high SOA yields[18] and ability to produce extremely low volatility oxidation products.[19] In addition, isoprene and monoterpenes also have substantially faster biomolecular reaction rate constants for reaction with ozone and hydroxyl (OH) radicals compared to DMS.

In addition to biogenic NMVOC, abiotic photochemical production of a small number of NMVOC in ocean surface waters have previously been investigated, including alkyl nitrates,[20] acetone,[21–23] and acetaldehyde.[23,24] These photoproduction sources all have relatively well-studied global emission climatologies which allows for inclusion in chemistry models. Additional laboratory experiments have suggested that photochemical and heterogeneous reactions occurring at the ocean-atmosphere interface (sea-surface microlayer, SML) could also be a significant source of a wide suite of reactive NMVOC to the marine atmosphere.[25–33] NMVOC formed through abiotic mechanisms encompass a wide range of oxygenated and unsaturated molecules distinct from those discussed previously, with potential impacts on the marine HO_x and SOA budget. For example, Bruggemann et al.[30] reported photoenhanced emissions of 1.1×10^8, 4.4×10^8, and 71×10^8

molecules cm^{-2} s^{-1} for octanal, isoprene, and acetone respectively, along with many other products, from irradiance of biofilms scaled to an ambient mean solar flux of 92 Wm^{-2}. Laboratory exposure of a proxy SML containing linoleic acid to O_3 resulted in emission of carbonyls at near 100% total molecular yield.[32] Exposure of authentic SML samples also showed prompt production of a wider set of gas phase carbonyl products.[32] While these studies have provided new molecular insight into marine photochemical and heterogeneous NMVOC production mechanisms in the laboratory, it is not yet clear how representative these studies are of the significantly more dilute and chemically complex ambient SML. To date no ambient studies directly targeting these potential interfacial abiotic NMVOC emission sources have been conducted.

EC flux experiments in terrestrial ecosystems including temperate forests,[34–37] citrus groves,[38,39] tropical rainforests,[40] and urban landscapes[41,42] have demonstrated the utility of broad surveys of bidirectional NMVOC exchange in constraining reactive carbon budgets. To date, EC flux studies in the marine atmosphere have been limited to targeted studies of select NMVOCs, targeted molecules such as methanol, acetone, and acetaldehyde;[21,43] DMS, MT, and isoprene;[14] and glyoxal;[44] in addition to numerous studies of only DMS flux.[45–48] These experiments have provided important constraints on specific components of the marine NMVOC budget. A transect of the Atlantic showed that the ocean acts as a persistent sink of methanol, which extrapolated to a net global atmospheric sink of 42 Tg yr^{-1} which was in contrast to some modelling studies which suggested bidirectional ocean flux.[43,49] Observations of acetone air-sea exchange by EC show that acetone flux is bidirectional, acting as a net source in subtropical regions and a net sink at higher latitudes,[50] consistent with global climatologies.[22,51] Acetaldehyde emissions from EC flux measurements on an Atlantic transect extrapolated to a net emission of 3 Tg yr^{-1} which is smaller than most model estimates of 34-57 Tg yr^{-1}. These direct marine EC flux experiments have

provided essential constraints for model NMVOC budgets and motivate the need for a more complete survey of NMVOC ocean-atmosphere exchange analogous to those performed in the terrestrial environment.

Here we describe results from an EC flux experiment at a coastal ocean site using a latest generation high sensitivity Vocus PTR-TOF for NMVOC detection.[52] We present an untargeted survey of air-sea NMVOC flux, where EC flux of all detectable ions was calculated, resulting in a total of 44 ions which showed statistically significant EC flux. We also present correlations of observed flux with O_3 and solar irradiance in order to resolve potential signatures of abiotic NMVOC emission sources. Results from this study provide the first dataset for the bidirectional air-sea exchange of a broad suite of biogenic and abiotic NMVOC and provide a framework for future air-sea NMVOC exchange studies.

2.2 Experimental Methods

2.2.1 Scrips Pier Flux Experiment Overview

Measurements of NMVOC gas phase mixing ratios and EC flux were made continuously from the end of the Ellen Browning Scripps Pier Memorial Pier (hereon SIO Pier) at the Scripps Institution of Oceanography during September 2019. The full ambient study period ran from September 3rd to September 30st, but all results presented in this work are from September 19th to September 30th when instrument configuration and calibration procedures were optimized and consistent. Analysis of the pre-September 19th data period is ongoing. The SIO pier is 330 m long and extends at least 100 m beyond the wave breaking zone. The SIO Pier site has been used regularly for EC studies of ocean-atmosphere trace gas exchange.[53–56] Scripps Pier experiences a characteristic sea-breeze circulation pattern where winds are from the ocean at moderate windspeeds (0-6 m s^{-1}) during daytime and are from land at night. In this study, NMVOC measurements were performed with a

latest generation Vocus PTR-TOF (Vocus) instrument (TOFWERK, Aerodyne),[52] with an HTOF mass analyzer (resolution *ca* 5000 $m/\Delta m$) allowing for separation of isobaric compounds. The primary advantage of the Vocus is the improved sensitivity of 1-2 orders of magnitude compared to prior generation instruments.[52] Mean sensitivity to DMS and isoprene over the campaign were 4.1 and 2.2 cps ppt^{-1} respectively, discussed further in Section 2.2.3. This high instrument sensitivity is essential for resolving the EC flux of species with low flux magnitudes. The Vocus sampling at 10 Hz time resolution but was down averaged to 1 Hz during post-processing for the data presented in the work. The recorded mass range was from m/Q 19 to 500. The Vocus was operated at a reduced back segmented-quadrupole (BSQ) amplitude of 215 V to improve the mass transmission of low mass (<40 m/Q) ions, as discussed in Krechmer et al. (2018).[52] The Vocus was housed in a temperature-controlled trailer at the end of the pier and sampled through a 19 m long PFA inlet (0.625 cm i.d.). The inlet was pumped at 20 slpm in order to maintain turbulent flow in the sampling line (Reynolds number 4280) and to maintain a fast inlet time response (calculated volumetric evacuation time 1.7 s). The full inlet line was held at 40°C which was always above ambient temperatures in order to prevent condensation of water vapor on inlet surfaces. The Vocus subsampled from the main inlet at 100 sccm, through a PFA tee located immediately in front of the Vocus capillary inlet into the instrument drift tube. In addition to the main inlet line, all surfaces in contact with the ambient sample flow, including unions and valves, were composed of PFA except for one stainless-steel union at the Vocus subsampling point. The inlet ambient sampling point was collocated with a sonic anemometer recording three-dimensional winds at 10 Hz (Gil HS-50). The sonic anemometer and Vocus inlet were mounted on a 6.1 m long boom extended beyond the end of the pier to minimize flow distortions from the pier. The inlet was mounted on the boom at a height of 13 m above the mean lower low tide level. The Vocus

inlet was mounted approximately 8 cm below the sonic, with no horizontal displacement. Ocean depth below the pier sampling point was *ca.* 6 m.

Additional ancillary measurements made continuously from the pier included ozone (O_3) mixing ratios, temperature, relative humidity, and incoming solar irradiance. O_3 mixing ratios were measured at 1-minute time resolution (POM, 2B Technologies) in line with the Vocus with a subsampling point immediately downstream of the Vocus subsampling point. Temperature and RH (Vaisala HMP110) were also measured inline downstream of the Vocus subsampling point at 1 Hz time resolution. Incoming total solar irradiance at 1 Hz time resolution (Licor LI-200R) was measured via a sensor mounted on top of the trailer housing the Vocus. The campaign mean diel profiles of wind speed, wind direction, O_3 mixing ratios, and solar irradiance are presented in **Figure 2.1.**

2.2.2 Ocean water biochemistry sampling

Continuous measurements of sea-surface temperature (SST), salinity, and chlorophyll are collected at a 1-minute time resolution from the end of the pier by an automated shore station operated by the Southern California Coastal Ocean Observing System.[57] Additional daily discrete ocean water samples were collected from the end of the pier at depths of 0 and 5 m with a Niskin sampler for analysis of biochemical parameters including: temperature, pH, nutrient concentrations, iodide and iodine concentrations, dissolved organic carbon (DOC) concentration, UV-VIS absorption and fluorescence for quantification of colored dissolved organic matter (CDOM) abundance, and phytoplankton and bacteria abundance and speciation. Processing and analysis of data products from the discrete water samples is ongoing.

2.2.3. Vocus data processing

NMVOC data from the Vocus was recorded at 10 Hz and down averaged in post-processing to 1 Hz for the analysis presented here. Peak fitting and integration were performed with the Tofware software package. A total of 1446 ion peaks were fit and integrated. Of these approximately 800 had a signal to noise ratio (S/N) greater than 3 and were used in subsequent EC flux analysis.

2.2.3 Vocus calibrations and backgrounds

Instrument sensitivities were determined during ambient sampling by standard addition of a NMVOC gas standard at two mixing ratios to the full sampling inlet every 2.5-4 hours. Components of the NMVOC gas standard are listed in **Table 2.1.** For all ions that were not directly calibrated for, we apply the mean calibration factor determined from all components of the NMVOC gas standard. For the campaign this mean calibration factor was from 2.0 to 3.5 cps $pptv^{-1}$. Instrument backgrounds were determined by overflowing the full inlet line with dry UHP N_2 at the tip of the ambient sampling point. An example timeseries of background determination and calibration during the Scripps Pier deployment and resulting calibration curves for DMS and xylene are shown in **Figure 2.2.** Ambient sampling periods were subdivided into 30-minute blocks and were matched to the nearest temporal calibration and background determination point. Background signal were subtracted from each 30-minute block and were then multiplied by their calibration factor to convert from cps to mixing ratio.

Dry N_2 overflow periods were also used to determine the Vocus instrument response time (τ_r), defined as the time required for the signal to fall to 1/e of its initial value. An example response time calculated from the 10 Hz DMS decay during an N_2 overflow period fit to an exponential decay is shown in **Figure 2.3**. The instrument response time for DMS was calculated to be 0.2 s. The cutoff frequency (f_{cut}) of the Vocus is defined as the frequency where the signal is attenuated by a factor of $1/\sqrt{2}$, which can be calculated from τ_r according to Eq. 1.[58]

$$f_{cut} = \frac{1}{2\pi\ \tau_r} \quad \text{E1}$$

The calculated f_{cut} from the measured DMS τ_r was 0.8 Hz. This value suggests that there should be minimal attenuation in the flux signal (cospectra) at frequencies lower than 0.8 Hz if the instrument response time is the controlling factor in high frequency attenuation, which is discussed further in Section 2.2.5.5.

2.2.4 EC Flux method Data Processing and quality control

The transfer of trace gases across the air-sea interface is a complex function of both atmospheric and oceanic physical and chemical processes, where gas exchange is controlled by turbulence in the atmospheric and water boundary layers, molecular diffusion in the interfacial regions surrounding the air−water interface, and the solubility and chemical reactivity of the gas in the liquid molecular sublayer.[59,60] The flux (F) of trace gas across the interface is described by Eq. 2, as a function of both the gas-phase (C_g) and liquid phase (C_l) concentrations and the dimensionless gas over liquid Henry's law constant (H), where K_t, the total transfer velocity for the gas (with units cm s^{-1}), encompasses all of the chemical and physical processes that govern air−sea gas exchange.

$$F = -K_t\left(C_g - HC_l\right) \quad \text{E2}$$

Trace gas flux (F) can be measured in the turbulent planetary boundary layer with the well-established eddy covariance (EC) technique where F is calculated as the time average of the instantaneous covariances from the mean of vertical wind (w) and the NMVOC scalar magnitude (x) as shown in Eq. 3. Overbars are means and primes are the instantaneous variance from the mean. Here N is the total number data points during the flux averaging period. Ambient data was subdivided into 30-minute flux averaging periods prior to the EC flux calculation.

$$F_x = \frac{1}{N}\sum_{i=1}^{N}(w_i - \overline{w})\,(x_i - \overline{x_3}) = \langle w' x_3' \rangle \quad \text{E3}$$

2.2.5 EC Flux Data Processing and quality control

Several standard EC data processing steps, data filters, and quality control checks were applied during flux analysis including: 1) filtering by wind direction for periods of onshore winds (true wind direction 200-360°), 2) coordinate rotation of three-dimensional wind components by the planar fit method to remove unintentional tilts in the sonic mounting and account for local flow distortions,[61] 3) application of a friction velocity (U_*) threshold of 0.05 cm s^{-1} to reject periods of low shear driven turbulence, 4) despiking of NMVOC data using a mean absolute deviation filter before the EC flux calculation following Mauder et al., (2013),[62] 5) linear detrending of NMVOC and *w* was applied for mean removal for the EC calculation, and 6) NMVOC flux stationarity was assessed following Foken et al., (1996),[63] with flux periods rejected if they were non-stationary at a 30% threshold.

2.2.5.2 Lag time determination

The EC flux calculation involves the instantaneous variance of *w'* and *x'* which is complicated if there are time lags between the two data sources. Lag times between measurements of *w* and NMVOC data (*x*) were determined by analysis of the cross-covariance of *w* and DMS scalar data. Because the internal clocks of the computers logging data from the Vocus and the sonic anemometer were not perfectly synchronized during the campaign, there was an observed lag time between *w* and NMVOC data. Even if the computer clocks were perfectly synchronized, a time lag between NMVOC data and *w* would exist due to the transit time of ambient air through the inlet volume, with expected inlet gas evacuation time of approximately 1.7 s. An example cross-covariance lag time determination for DMS from an individual flux period is shown in **Figure 2.3a.** The optimum lag time for this period taken as the maximum of the cross-covariance was -13

seconds. A step-change in the lag time of the cross-covariance maximum was observed corresponding to an instrument shutdown period during a planned power outage. Lag times before the instrument shutdown were on the order of 15 s and after the shutdown were on the order 32 s as shown in **Figure 2.3b**, labelled as Periods 1 and 2 respectively. No abrupt changes in lag time determined during continuous sampling periods were observed. All other flux diagnostics were consistent between the periods, suggesting the change in lag time was due to clock differences between the data recording devices during the power outage and not a change in the flow rate through the sampling inlet. A histogram of optimum lag times determined for DMS taken as the absolute maximum (MAX), or the maximum of a 10-point moving median function (MOV) of the DMS cross covariance function from each flux calculation period is shown in **Figure 2.3c.** The peaks of the bimodal distribution correspond to lag times determined for periods before and after the instrument shutdown period. The agreement in lag times determined by the MAX and MOV lag methods suggests that a clear peak in the cross-correlation was present for most DMS flux periods.[64]

For ions with lower flux signal to noise (S/N), a clear peak in the cross-correlation is not always present, complicating the lag time determination. To resolve this, we took the mean lag time determined by the MAX lag method for DMS, MeSH, and acetone for each flux averaging period as the lag time used for all ions (Iterative lag method). A histogram of lag times for isoprene determined by the MAX, MOV, and Iterative methods are shown in **Figure 2.4.** There is a broad distribution in determined lag times by the MAX and MOV for isoprene due to the lower flux S/N, while the Iterative lag times follow a clear bimodal distribution. The Iterative lag method uses only ions with high flux S/N resulting in a narrow distribution of determined lag times, that are taken to be closer to the true lag time and was used for all EC flux calculations.

2.2.5.3 Flux LOD determination

The error in each flux averaging period (LOD) for each ion was be determined by analysis of the root mean squared error (RMSE) of the cross-covariance between vertical wind speed and mass spectrometer signal at lag times significantly longer than the calculated true lag time [64–66]. The random flux error is determined using lag windows of -150 to -180 and 150 to 180 s, which are significantly larger than the determined optimum lag times discussed in Section 2.2.5.3 of 15-40 s. The selection of the -150 to -180 and 150 to 180 s lag windows is somewhat arbitrary and may still capture organized atmospheric structure that persists over long time periods. Use determination of LOD by the RMSE (LOD_{RMSE}) captures variance in the cross-covariance at long lag times but also accounts for long term offsets from zero in the cross-covariance, providing a more conservative determination of the LOD compared to simply determining the standard deviation.[64] The final flux LOD_{RMSE} was determined for each ion during each flux averaging period by multiplying the LOD_{RMSE} error by 1.96 to give the flux LOD at the 95% confidence level.

2.2.5.4 Flux LOD filtering

Ions were considered to have statistically significant flux if their campaign mean absolute flux was larger than 60% of the campaign mean flux LOD_{RMSE}, which is equivalent to an 80% confidence level. This method follows the approach of Park et al. (2013) for determination of bidirectional NMVOC flux, with a reduced LOD_{RMSE} threshold used (80% confidence level here vs 99.7% used by Park et al. (2013)). NMVOC air-sea flux magnitudes are generally much smaller than flux in terrestrial environments and use of a S/N = 3 threshold as in Park et al. (2013)[39] would reject all but 6 ions. We instead elect to use a lower confidence threshold while acknowledge the corresponding increase in uncertainty for these smaller magnitude exchanging ions. Application

of the 80% confidence level threshold results in 44 total ions with statistically significant flux. All ions with statistically significant flux are listed in **Table 2.2** with their exact mass, assigned molecular composition, assigned structural identification if one was made, campaign mean EC flux, and bimolecular rate constants with OH.

2.2.5.5 Flux spectral analysis

Spectral analysis provides a means to evaluate experimental performance in capturing low- and high-frequency flux signals. Here we describe the flux spectra for DMS and sensible heat (SH) compared against the idealized Kaimal et al. (1972)[67] spectral response. Comparison of observed frequency weighted cospectra shape of DMS and SH against the idealized Kaimal cospectra is useful to validate that the observed signal was not significantly attenuated at low or high frequencies. SH flux is calculated using air temperature measured directly by the sonic anemometer and should have no flux attenuation. Cospectral averaging is performed by binning frequency into 50 evenly log spaced bins and normalizing the integrated cospectra to 1. The area under the unnormalized cospectra curve is the equivalent to the flux for that observation period. Cospectra of DMS and SH from an individual flux averaging period of windspeed 4.3 m s^{-1} is shown in **Figure 2.6a**. The shift of the DMS cospectral curve relative to the SH and Kaimal curves at high frequencies (>0.1 Hz) is indicative of potential high frequency attenuation during sampling of DMS. Ogives of DMS,SH, and Kaimal from the same flux period are shown in **Figure 2.6b**. The ogive is the normalized cumulative distribution of the cospectra, which is used to validate both that no high-frequency attenuation is present and that the flux averaging time is sufficiently long that all frequencies contributing for the flux is captured. The apparent plateau in the ogive at low frequencies for DMS and SH validates that the selected 30-minute flux averaging time is sufficiently long to capture the largest eddies contributing to the flux. The ogive of DMS shows a

generally similar spectral shape compared to the SH and Kaimal ogives, especially at frequencies below 0.1 Hz. At frequencies above 0.1 Hz the ogive of DMS is flatter than SH or the Kaimal curve, indicative of attenuation at these high frequencies. High pumping rates in sampling line were used to ensure that turbulent flow was always maintained in the sampling line, which reduces the effects of high frequency attenuation.[68]

To assess the degree of expected frequency attenuation we applied the flux attenuation model of Horst, (1997) shown in Equation. 4. For our determined instrument response time (τ_c) for DMS of 0.2 s (described in Section 2.2.3), and a wind speed of 4.3 m s^{-1} we calculate this flux attenuation to be on the order of 4%.

$$\frac{F_m}{F_x} = \frac{1}{1+(2\pi n_m \tau_c U/z)^{\alpha}} \qquad \text{E4}$$

Where F_m/F_x is the ratio of the measured flux to the unattenuated flux, U is wind speed, z is measurement height, and n_m and α are scaling factors for an unstable boundary layer taken as 0.085 and 7/8 respectively. A more direct determination of the Vocus flux attenuation by comparing the the ratio of the DMS and SH cospectral shapes for each period is in progress.

2.3 Results and Discussion

2.3.1 Meteorology Overview

Observed meteorology and ocean biochemical parameters showed minimal variance over the sampling period presented here. Sea-surface temperatures during the campaign 23.3°C (21.6 to 24.7°C interquartile range). Air temperatures and relative humidity means were 22°C (19.5 to 23.6°C interquartile range) and 79.9% (72.3 to 88.3% interquartile range) respectively. Chlorophyll concentrations suggest moderate biological productivity with an observed campaign mean of 1.86 μg L^{-1} (1.5 to 2.0 μg L^{-1} interquartile range). O_3 mixing ratios showed a clear diel

pattern peaking in midafternoon (as shown in **Figure 2.1**), with a campaign mean of 32.6 ppbv (27.6 to 38.9 ppbv interquartile range). Wind speeds during onshore wind periods were from 0 to 6 m s^{-1}, typically peaking in late afternoon with a campaign mean of 2.8 m s^{-1}. Clear sky conditions were observed for all afternoons during the study period, with solar irradiance peaked near noon at *ca.* 1000 W m^{-2}. Morning and late evening periods showed occasional presence of marine stratocumulus clouds which drove day-to-day variability in solar irradiance during those times.

2.3.2 Major NMVOC flux and mixing ratios

Analysis of the flux magnitudes, diel profiles, and relationships with horizontal wind speed for several known major exchanging compounds included DMS, isoprene, MT, methanethiol (MeSH), methanol (MeOH), and acetone provides insight on the factors controlling flux magnitudes at the Scripps pier site. Mean diel profiles of mixing ratios and flux magnitudes of DMS and acetone are shown in **Figure 2.7**. DMS hourly mean mixing ratios ranged from 60 to 120 pptv, peaking at night when oxidation by OH is slow. DMS flux shows a clear peak in mid-afternoon, reaching a maximum of 1.3 pptv m s^{-1} at hour 15 (PDT). Acetone mixing ratios show a growth in at night reaching a peak of 2 ppbv just before sunrise, and a minimum during the day of 1.1 ppbv. This pattern is likely driven by the characteristic sea-breeze circulation pattern at this site, where winds are from the open ocean during the day and are from the land during the night, generally coming from central San Diego towards the south-east. Urban influenced NMVOC therefore builds up at night in the shallow marine boundary layer (MBL) and dissipates during the day when winds come from cleaner marine regions. These high acetone gas phase mixing ratios at night and into the morning drive a supersaturation in the atmosphere and deposition to the ocean. This is observed in the diel flux profile of acetone, where deposition flux is strong during the mid-morning to early afternoon, peaking at -1.2 pptv m s^{-1} at 14 PDT. Similar nighttime buildups of NMVOC mixing

ratios were observed for many anthropogenically influenced NMVOCs including benzene, toluene, methanol, and acetaldehyde. Of those, methanol and acetaldehyde had statistically significant EC flux and showed deposition profiles similar to acetone. Flux analysis from hour of day 23 to 7 PDT was not possible as winds during those times were persistently from land.

The flux magnitudes of DMS, MeSH, MeOH, and acetone all showed an increase with windspeed as shown in **Figure 2.8**, with DMS and MeSH showing net emission fluxes, and MeOH and acetone with net deposition. This increase in flux magnitude with windspeed is consistent with expectations for species where exchange is air-side limited.[60] Wind speeds were low in early morning (<1.5 m s^{-1}) and peaked in the afternoon (as shown in **Figure 2.1**) which drives the observed peak in flux in the afternoon for DMS and other species.

2.3.3 DMS flux regressions

The regression of the flux of DMS against other NMVOC such as MeSH, isoprene, and acetone provides insights about potential shared source or sink terms. The emission flux of DMS and MeSH show a strong correlation (R^2 = 0.78) as shown in **Figure 2.9a**, which implies a common emission source, which is consistent prior flux observations and known ocean biological production mechanisms.[70,71]Conversely, DMS and isoprene both show net emission fluxes and have known marine biological production sources but their emission flux is poorly correlated (R^2 = 0.04) as shown in **Figure 2.9c**, suggesting distinct marine biological sources. The correlation of DMS emission flux and acetone deposition is also poor (R^2 = 0.06) as shown in **Figure 2.9b**, which is likely in part driven by the enhanced gas phase mixing ratios and deposition flux of acetone during the morning due to anthropogenic influence described in Section 2.3.2. Finally, the emission flux of isoprene and MT are reasonably well correlated (R^2 = 0.2) as shown in **Figure 2.9d**, which implies some common sources but that biological variability may be significant.

Further analysis of these regressions as a function of marine biological speciation and abundance will be made once analysis of the discreet water samples are completed.

2.3.4 Total NMVOC flux

In addition to analysis of specific NMVOCs of interest, we also determined the contribution of all observed exchanging ions to the net emitting and depositing carbon mass flux as shown in **Figure 3.10**. This analysis shows the contribution to the cumulative NMVOC carbon mass flux as a function of the number of molecules considered. For NMVOC emission fluxes, consideration of only one ion (DMS) accounts for 40% of the observed NMVOC carbon mass emissions, and consideration of 11 ions accounts for 90%. For NMVOC carbon mass deposition, consideration of one ion (acetone) accounts for 40% of the cumulative total and consideration of five ions accounts for 90% of the cumulative deposition. Similar analysis in a terrestrial forest showed that 45 ions needed to be considered to capture 90% of observed NMVOC carbon mass deposition flux, and five ions were needed to capture 90% of emissions.[34] This implies that in the marine environment carbon mass emissions are spread amongst more species, while deposition is controlled by significantly fewer species as compared to a terrestrial forest. The speciated breakdown of the percent contribution to the cumulative carbon mass flux is shown in **Figure 3.11.** The three largest individual emitting NMVOC by carbon mass were DMS, isoprene, and MT at 40%, 12%, and MT at 6% respectively. Siloxanes were also shown to be a significant in the carbon mass emission budget, contributing 20% to the total. Siloxanes are volatile compounds which are present in personal care products, which are washed away in wastewater streams at high abundance.[72,73] Siloxanes once in the atmosphere have a long lifetime to oxidation by OH (>10 days),[74] and their impacts on oxidative cycling in the marine atmosphere are likely limited. However, siloxanes have been shown to be a useful general tracer of personal care product NMVOC emissions.[73] Deposition

flux was dominated by acetone, C_2H_2O (a likely acetic acid fragment), acetaldehyde, and methanol contributing 40%, 29%, 13%, and 6% respectively to cumulative NMVOC carbon mass deposition. Theses species are all atmospheric oxidation products with diel patterns indicative of urban influence at night driving high gas phase mixing ratio in the morning and deposition fluxes.

The mean diel profile of the net carbon mass flux and its individual speciated components are shown in **Figure 3.12.** The net carbon mass flux shows a diel profile, with net deposition from hours 9 to 16 PST, and net emission from 17 to 23 PST. The net cumulative carbon mass flux over the full day is an emission of 3.6 μg m^{-2} day^{-1}. This suggests that in an urban coastal environment carbon source and sink terms are closely matched, resulting in a small net contribution to the total carbon mass budget. As a relative scale, net cumulative NMVOC carbon mass flux in a citrus grove was measured to be 139 μg m^{-2} hr^{-1}, using a similar EC flux methodology.[38] Also plotted on **Figure 3.12**, are the mean diel profiles of windspeed and acetone gas phase mixing ratios. The speciated NMVOC emission terms all show a profile that tracks with windspeed, peaking in the mid-afternoon and falling off in both morning and evening when windspeeds are lower. Notably, there is not a clear peak in NMVOC emissions centered at noon which would be expected for photochemical abiotic emission sources. The term driving the peak in siloxane emissions in the late afternoon and evening (hours 16-23 PST) when windspeeds are declining is not clear, but may be related to runoff of personal care products which has a bimodal distribution with peaks in the early morning and late afternoon.[73] The speciated deposition magnitudes appear to be a combined function of windspeed and gas phase mixing ratios, which results in a net carbon mass deposition in the morning when NMVOC mixing ratios are high, driven by nighttime anthropogenic influence, and a peak in the speciated deposition flux in early afternoon when windspeeds are higher and before gas phase mixing ratios reach their minimum.

2.3.5 OH reactivity flux

Weighting of observed NMVOC by its reactivity with OH allows for quantification of air-sea exchange on the oxidative budget in the MBL. The diel profile of total OH reactivity for all exchanging NMVOC is shown in **Figure 3.13**. Observed mean hourly OH reactivity ranged from 5 to 8 s^{-1} peaking at night due to accumulation of urban influenced air and reaching a minimum in late afternoon when winds were from onshore. For all ions where a molecular identification was made, we use literature values for its bimolecular rate constants with OH. For all ions where a molecular identification was not made we used the 50th percentile OH reactivity from Park et al. (2013)[38] of 1.82×10^{-11} cm^3 $molecules^{-1}$ s^{-1}. The speciated NMVOC contribution to the cumulative emission flux weighted by OH bimolecular rate constant is shown in **Figure 3.14**. Isoprene was found to be the dominant contributor to OH reactivity weighted marine NMVOC emission flux, accounting for 52% of the total. Additional major contributors to OH weighted emission flux were DMS at 21%, MeSH at 5%, MT at 2%, and siloxanes at 7%. Consideration of only the four most abundant observed marine BVOCs (DMS, MeSH, isoprene, and MT) accounts for 80% of the total OH reactivity weighted emission flux. This exercise highlights the both significance of isoprene compared to DMS in influencing marine oxidative capacity, and the controlling role of known marine BVOC on total OH reactivity weighted emissions. To date, direct constraints on marine isoprene emission flux is extremely limited with only one prior EC flux study reported in the literature.[14] In remote marine regions removed from immediate urban influence, we expect ocean emissions of siloxanes to be negligible which would further enhance the contribution of BVOCs in OH reactivity weighted NMVOC emissions. Notably absent are strong contributions from aldehyde emissions which have been suggested to have abiotic marine emission sources and have fast reaction rate constants with OH (k_{OH} on the order of 1×10^{11} cm^3 $molecules^{-1}$ s^{-1}).[32,75]

2.3.6 Limited evidence for photochemical isoprene production

Laboratory studies have suggested that photochemical reactions in the SML could act as a significant source of isoprene to the marine atmosphere.[28,75] Photolysis of both a proxy SML surface of a nonanoic acid monolayer as well as an authentic SML sample with added humic acid (HA) as a photosensitizer both showed photoenhanced isoprene production.[28] Scaling these laboratory results to ocean conditions suggested that photochemical isoprene fluxes could be as large as 0.8 to 1.7 × 10^9 molecules cm^{-2} s^{-1}. Laboratory studies of irradiance of a biofilm also showed photochemical isoprene flux, albeit at lower magnitudes, of 4.4 × 10^8 when scaled to an ambient mean solar flux of 92 Wm^{-2}. As shown in **Figure 2.15**, the observed isoprene flux appears to be independent of solar irradiance. Also plotted are the isoprene photoemission rates from Ciuraru et al. (2015), using the values corrected for surface enrichment (SE=1) and scaled linearly to solar irradiance. The photoenhanced isoprene production reported in that study does not appear to be consistent with our ambient flux observations. Analysis of the other 42 statistically significant exchanging NMVOCs also did not show a clear relationship with either solar irradiance or O_3 mixing ratios which would be expected if large abiotic NMVOC emission sources were active. While the results of this study do not support abiotic isoprene or NMVOC emission sources, further study in more pristine marine regions is warranted as anthropogenic NMVOC influence at this near-urban coastal site may complicate the analysis of abiotic emission sources for some species.

2.4 Conclusions

We present EC flux results for the ocean-atmosphere exchange of 44 NMVOC species which represents a substantial increase in the number of simultaneously studied compounds (typically 1-3) from prior studies. These results allow for analysis of the cumulative contribution of emitting

and depositing NMVOC to carbon mass and OH reactivity budgets. We find that consideration of only four commonly measured BVOCs accounts for 59% of carbon mass emission flux, and 80% of the OH reactivity weighted emission flux. DMS was the dominate emitting NMVOC in carbon mass units contributing 40% to the cumulative total. Isoprene was the largest term in the OH reactivity weighted emissions contributing 52%. Deposition flux was found to be dominated by acetone, a likely acetic acid fragment ion, acetaldehyde, and methanol, contributing 40%, 29%, 13%, and 6% respectively to the cumulative carbon mass deposition flux. Mixing ratios of depositing species where enhanced at night due to persistent winds from urban areas, resulting in supersaturation in the gas phase and net deposition. The cumulative daily carbon mass flux was calculated to be 3.6 μg m^{-2} day^{-1} indicating that emissions and depositions were nearly equal at this coastal site. Notably, no strong evidence for abiotic NMVOC by either photochemical or heterogeneous reaction sources was observed. Regressions of emission fluxes showed weak to no correlation with solar irradiance and O_3 mixing ratio for all observed emitting species. In particular isoprene emissions were found to have no dependence on solar irradiance, in contrast with recent laboratory experiments. These results from a coastal site are the first broad EC survey of air-sea NMVOC exchange. Extension of the methods presented here to remote marine regions with broad spatiotemporal coverage will be essential to resolve open questions on the role of air-sea NMVOC exchange on atmospheric oxidative capacity and SOA budgets.

References

(1) Donahue, N. M.; Prinn, R. G.; Prinn, G.; Prinn, R. G. Nonmethane Hydrocarbon Chemistry in the Remote Marine Boundary Layer. *J. Geophys. Res.* **1990**, *95* (D11), 18387–18411. https://doi.org/10.1029/JD095iD11p18387.

(2) Liakakou, E.; Vrekoussis, M.; Bonsang, B.; Donousis, C.; Kanakidou, M.; Mihalopoulos, N. Isoprene above the Eastern Mediterranean: Seasonal Variation and Contribution to the Oxidation Capacity of the Atmosphere. *Atmos. Environ.* **2007**, *41* (5), 1002–1010.

https://doi.org/10.1016/j.atmosenv.2006.09.034.

(3) Palmer, P. I.; Shaw, S. L. Quantifying Global Marine Isoprene Fluxes Using MODIS Chlorophyll Observations. *Geophys. Res. Lett.* **2005**, *32* (9), 1–5. https://doi.org/10.1029/2005GL022592.

(4) Gantt, B.; Johnson, M. S.; Meskhidze, N.; Sciare, J.; Ovadnevaite, J.; Ceburnis, D.; O'Dowd, C. D. Model Evaluation of Marine Primary Organic Aerosol Emission Schemes. *Atmos. Chem. Phys.* **2012**, *12* (18), 8553–8566. https://doi.org/10.5194/acp-12-8553-2012.

(5) Meskhidze, N.; Xu, J.; Gantt, B.; Zhang, Y.; Nenes, A.; Ghan, S. J.; Liu, X.; Easter, R.; Zaveri, R. Global Distribution and Climate Forcing of Marine Organic Aerosol: 1. Model Improvements and Evaluation. *Atmos. Chem. Phys.* **2011**, *11* (22), 11689–11705. https://doi.org/10.5194/acp-11-11689-2011.

(6) Lana, A.; Bell, T. G.; Simó, R.; Vallina, S. M.; Ballabrera-Poy, J.; Kettle, A. J.; Dachs, J.; Bopp, L.; Saltzman, E. S.; Stefels, J.; et al. An Updated Climatology of Surface Dimethlysulfide Concentrations and Emission Fluxes in the Global Ocean. *Global Biogeochem. Cycles* **2011**, *25* (1), 1–17. https://doi.org/10.1029/2010GB003850.

(7) Galí, M.; Levasseur, M.; Devred, E.; Simó, R.; Babin, M. Sea-Surface Dimethylsulfide (DMS) Concentration from Satellite Data at Global and Regional Scales. *Biogeosciences* **2018**, *15* (11), 3497–3519. https://doi.org/10.5194/bg-15-3497-2018.

(8) Kloster, S.; Feichter, J.; Maier-Reimer, E.; Six, K. D.; Stier, P.; Wetzel, P. DMS Cycle in the Marine Ocean-Atmosphere System - A Global Model Study. *Biogeosciences* **2006**, *3* (1), 29–51. https://doi.org/10.5194/bg-3-29-2006.

(9) Land, P. E.; Shutler, J. D.; Bell, T. G.; Yang, M. Exploiting Satellite Earth Observation to Quantify Current Global Oceanic DMS Flux and Its Future Climate Sensitivity. *J. Geophys. Res. Ocean.* **2014**. https://doi.org/10.1002/2014JC010104.

(10) Shaw, S. L.; Gantt, B.; Meskhidze, N. Production and Emissions of Marine Isoprene and Monoterpenes: A Review. *Adv. Meteorol.* **2010**, *2010* (1), 1–24. https://doi.org/10.1155/2010/408696.

(11) Zindler, C., C. A. Marandino, H. W. B.; F. Schütte, and E. S. S. Nutrients Determine DMS and Isoprene Distribution in Atlantic Ocean. *Geophys. Res. Lett.* **2014**, *41* (9), 3181–3188. https://doi.org/https://doi.org/10.1002/2014GL059547.

(12) Hackenberg, S. C.; Andrews, S. J.; Airs, R. L.; Arnold, S. R.; Bouman, H. A.; Cummings, D.; Lewis, A. C.; Minaeian, J. K.; Reifel, K. M.; Small, A.; et al. Basin-Scale Observations of Monoterpenes in the Arctic and Atlantic Oceans. *Environ. Sci. Technol.* **2017**, *51* (18), 10449–10458. https://doi.org/10.1021/acs.est.7b02240.

(13) Yassaa, N.; Peeken, I.; Zllner, E.; Bluhm, K.; Arnold, S.; Spracklen, D.; Williams, J.

Evidence for Marine Production of Monoterpenes. *Environ. Chem.* **2008**, *5* (6), 391–401. https://doi.org/10.1071/EN08047.

(14) Kim, M. J.; Novak, G. A.; Zoerb, M. C.; Yang, M.; Blomquist, B. W.; Huebert, B. J.; Cappa, C. D.; Bertram, T. H. Air-Sea Exchange of Biogenic Volatile Organic Compounds and the Impact on Aerosol Particle Size Distributions. *Geophys. Res. Lett.* **2017**, *44* (8), 3887–3896. https://doi.org/10.1002/2017GL072975.

(15) Matsunaga, S.; Mochida, M.; Saito, T.; Kawamura, K. In Situ Measurement of Isoprene in the Marine Air and Surface Seawater from the Western North Pacific. *Atmos. Environ.* **2002**, *36* (39–40), 6051–6057. https://doi.org/10.1016/S1352-2310(02)00657-X.

(16) Broadgate, W. J.; Liss, P. S.; Penkett, A.; June, M. Seasonal Emissions of Isoprene and Other Reactive Hydrocarbon Gases from the Ocean. *Geophys. Res. Lett.* **1997**, *24* (21), 2675–2678. https://doi.org/https://doi.org/10.1029/97GL02736.

(17) Luo, G.; Yu, F. A Numerical Evaluation of Global Oceanic Emissions of Alpha-Pinene and Isoprene. *Atmos. Chem. Phys.* **2010**, *10* (4), 2007–2015. https://doi.org/doi:10.5194/acp-10-2007-2010.

(18) Griffin, R. J.; Cocker, D. R.; Flagan, R. C.; Seinfeld, J. H. Organic Aerosol Formation from the Oxidation of Biogenic Hydrocarbons. *J. Geophys. Res. Atmos.* **1999**, *104* (D3), 3555–3567. https://doi.org/10.1029/1998JD100049.

(19) Ehn, M.; Thornton, J. A.; Kleist, E.; Sipila, M.; Junninen, H.; Pullinen, I.; Springer, M.; Rubach, F.; Tillmann, R.; Lee, B.; et al. A Large Source of Low-Volatility Secondary Organic Aerosol. *Nature* **2014**, *506* (7489), 476–479. https://doi.org/10.1038/nature13032.

(20) Dahl, E. E.; Saltzman, E. S. Alkyl Nitrate Photochemical Production Rates in North Pacific Seawater. *Mar. Chem.* **2008**, *112* (3–4), 137–141. https://doi.org/10.1016/j.marchem.2008.10.002.

(21) Yang, M.; Beale, R.; Liss, P.; Johnson, M.; Blomquist, B.; Nightingale, P. Air–Sea Fluxes of Oxygenated Volatile Organic Compounds across the Atlantic Ocean. *Atmos. Chem. Phys.* **2014**, *14* (14), 7499–7517. https://doi.org/10.5194/acp-14-7499-2014.

(22) Fischer, E. V; Jacob, D. J.; Millet, D. B.; Yantosca, R. M.; Mao, J. The Role of the Ocean in the Global Atmospheric Budget of Acetone. *Geophys. Res. Lett.* **2012**, *39* (1), n/a-n/a. https://doi.org/10.1029/2011gl050086.

(23) Dixon, J. L.; Beale, R.; Nightingale, P. D. Production of Methanol, Acetaldehyde, and Acetone in the Atlantic Ocean. *Geophys. Res. Lett.* **2013**, *40* (17), 4700–4705. https://doi.org/10.1002/grl.50922.

(24) Zhou, X.; Mopper, K. Photochemical Production of Low-Molecular-Weight Carbonyl Compounds in Seawater and Surface Microlayer and Their Air-Sea Exchange. *Mar. Chem.*

1997, *56*, 201–213. https://doi.org/10.1016/S0304-4203(96)00076-X.

(25) Ciuraru, R.; Fine, L.; Van Pinxteren, M.; D'Anna, B.; Herrmann, H.; George, C. Photosensitized Production of Functionalized and Unsaturated Organic Compounds at the Air-Sea Interface. *Sci. Rep.* **2015**, *5* (March), 1–10. https://doi.org/10.1038/srep12741.

(26) Fu, H.; Ciuraru, R.; Dupart, Y.; Passananti, M.; Tinel, L.; Rossignol, S.; Perrier, S.; Donaldson, D. J.; Chen, J.; George, C. Photosensitized Production of Atmospherically Reactive Organic Compounds at the Air/Aqueous Interface. *J. Am. Chem. Soc.* **2015**, *137* (26), 8348–8351. https://doi.org/10.1021/jacs.5b04051.

(27) Chiu, R.; Tinel, L.; Gonzalez, L.; Ciuraru, R.; Bernard, F.; George, C.; Volkamer, R. UV Photochemistry of Carboxylic Acids at the Air-Sea Boundary: A Relevant Source of Glyoxal and Other Oxygenated VOC in the Marine Atmosphere. *Geophys. Res. Lett.* **2017**, *44* (2), 1079–1087. https://doi.org/10.1002/2016GL071240.

(28) Ciuraru, R.; Fine, L.; Pinxteren, M. Van; D'Anna, B.; Herrmann, H.; George, C. Unravelling New Processes at Interfaces: Photochemical Isoprene Production at the Sea Surface. *Environ. Sci. Technol.* **2015**, *49* (22), 13199–13205. https://doi.org/10.1021/acs.est.5b02388.

(29) Tinel, L.; Rossignol, S.; Bianco, A.; Passananti, M.; Perrier, S.; Wang, X.; Brigante, M.; Donaldson, D. J.; George, C. Mechanistic Insights on the Photosensitized Chemistry of a Fatty Acid at the Air/Water Interface. *Environ. Sci. Technol.* **2016**, *50* (20), 11041–11048. https://doi.org/10.1021/acs.est.6b03165.

(30) Brüggemann, M.; Hayeck, N.; Bonnineau, C.; Pesce, S.; Alpert, P. A.; Perrier, S.; Zuth, C.; Hoffmann, T.; Chen, J.; George, C. Interfacial Photochemistry of Biogenic Surfactants: A Major Source of Abiotic Volatile Organic Compounds. *Faraday Discuss.* **2017**, *200*, 59–74. https://doi.org/10.1039/c7fd00022g.

(31) Rossignol, S.; Tinel, L.; Bianco, A.; Passananti, M.; Brigante, M.; Donaldson, D. J.; George, C.; Lyon, U.; Claude, U.; Lyon, B. Atmospheric Photochemistry at a Fatty Acid–Coated Air-Water Interface. *Science (80-.).* **2016**, *353* (6300), 699–702. https://doi.org/10.1126/science.aaf3617.

(32) Zhou, S.; Gonzalez, L.; Leithead, A.; Finewax, Z.; Thalman, R.; Vlasenko, A.; Vagle, S.; Miller, L. A.; Li, S. M.; Bureekul, S.; et al. Formation of Gas-Phase Carbonyls from Heterogeneous Oxidation of Polyunsaturated Fatty Acids at the Air-Water Interface and of the Sea Surface Microlayer. *Atmos. Chem. Phys.* **2014**. https://doi.org/10.5194/acp-14-1371-2014.

(33) Schneider, S. R.; Collins, D. B.; Lim, C. Y.; Zhu, L.; Abbatt, J. P. D. Formation of Secondary Organic Aerosol from the Heterogeneous Oxidation by Ozone of a Phytoplankton Culture. *ACS Earth Sp. Chem.* **2019**, *3*, 0–8.

https://doi.org/10.1021/acsearthspacechem.9b00201.

(34) Millet, D. B.; Alwe, H. D.; Chen, X.; Deventer, M. J.; Griffis, T. J.; Holzinger, R.; Bertman, S. B.; Rickly, P. S.; Stevens, P. S.; Léonardis, T.; et al. Bidirectional Ecosystem-Atmosphere Fluxes of Volatile Organic Compounds Across the Mass Spectrum: How Many Matter? *ACS Earth Sp. Chem.* **2018**, *2* (8), 764–777. https://doi.org/10.1021/acsearthspacechem.8b00061.

(35) Alwe, H. D.; Millet, D. B.; Chen, X.; Raff, J. D.; Payne, Z. C.; Fledderman, K. Oxidation of Volatile Organic Compounds as the Major Source of Formic Acid in a Mixed Forest Canopy. *Geophys. Res. Lett.* **2019**, *46* (5), 2940–2948. https://doi.org/10.1029/2018GL081526.

(36) Nguyen, T. B.; Crounse, J. D.; Teng, A. P.; St. Clair, J. M.; Paulot, F.; Wolfe, G. M.; Wennberg, P. O. Rapid Deposition of Oxidized Biogenic Compounds to a Temperate Forest. *Proc. Natl. Acad. Sci.* **2015**, *112* (5), E392–E401. https://doi.org/10.1073/pnas.1418702112.

(37) Wolfe, G. M.; Hanisco, T. F.; Arkinson, H. L.; Bui, T. P.; Crounse, J. D.; Dean-Day, J.; Goldstein, A.; Guenther, A.; Hall, S. R.; Huey, G.; et al. Quantifying Sources and Sinks of Reactive Gases in the Lower Atmosphere Using Airborne Flux Observations. *Geophys. Res. Lett.* **2015**. https://doi.org/10.1002/2015GL065839.

(38) Park, J. H.; Goldstein, A. H.; Timkovsky, J.; Fares, S.; Weber, R.; Karlik, J.; Holzinger, R. Active Atmosphere-Ecosystem Exchange of the Vast Majority of Detected Volatile Organic Compounds. *Science (80-.).* **2013**, *341* (6146), 643–647. https://doi.org/10.1126/science.1235053.

(39) Park, J. H.; Goldstein, A. H.; Timkovsky, J.; Fares, S.; Weber, R.; Karlik, J.; Holzinger, R. Eddy Covariance Emission and Deposition Flux Measurements Using Proton Transfer Reaction – Time of Flight – Mass Spectrometry (PTR-TOF-MS): Comparison with PTR-MS Measured Vertical Gradients and Fluxes. *Atmos. Chem. Phys.* **2013**, *13* (3), 1439–1456. https://doi.org/10.5194/acp-13-1439-2013.

(40) Karl, T.; Potosnak, M.; Guenther, A.; Clark, D.; Walker, J.; Herrick, J. D.; Geron, C. Exchange Processes of Volatile Organic Compounds above a Tropical Rain Forest: Implications for Modeling Tropospheric Chemistry above Dense Vegetation. *J. Geophys. Res. Atmos.* **2004**, *109* (18). https://doi.org/10.1029/2004JD004738.

(41) Karl, T.; Apell, E.; Hodzic, A.; Riemer, D. D.; Blake, D. R.; Wiedinmyer, C. Emissions of Volatile Organic Compounds Inferred from Airborne Flux Measurements over a Megacity. *Atmos. Chem. Phys.* **2009**, *9* (1), 271–285. https://doi.org/10.5194/acp-9-271-2009.

(42) Karl, T.; Striednig, M.; Graus, M.; Hammerle, A.; Wohlfahrt, G. Urban Flux Measurements Reveal a Large Pool of Oxygenated Volatile Organic Compound Emissions. *Proc. Natl.*

Acad. Sci. U. S. A. **2018**, *115* (6), 1186–1191. https://doi.org/10.1073/pnas.1714715115.

(43) Yang, M.; Nightingale, P. D.; Beale, R.; Liss, P. S.; Blomquist, B.; Fairall, C. Atmospheric Deposition of Methanol over the Atlantic Ocean. *Proc Natl Acad Sci U S A* **2013**, *110* (50), 20034–20039. https://doi.org/10.1073/pnas.1317840110.

(44) Coburn, S.; Ortega, I.; Thalman, R.; Blomquist, B.; Fairall, C. W.; Volkamer, R. Measurements of Diurnal Variations and Eddy Covariance (EC) Fluxes of Glyoxal in the Tropical Marine Boundary Layer: Description of the Fast LED-CE-DOAS Instrument. *Atmos. Meas. Tech.* **2014**, *7* (10), 3579–3595. https://doi.org/10.5194/amt-7-3579-2014.

(45) Huebert, B. J.; Blomquist, B. W.; Hare, J. E.; Fairall, C. W.; Johnson, J. E.; Bates, T. S. Measurement of the Sea-Air DMS Flux and Transfer Velocity Using Eddy Correlation. *Geophys. Res. Lett.* **2004**, *31* (23). https://doi.org/10.1029/2004gl021567.

(46) Blomquist, B. W.; Huebert, B. J.; Fairall, C. W.; Faloona, I. C. Determining the Sea-Air Flux of Dimethylsulfide by Eddy Correlation Using Mass Spectrometry. *Atmos. Meas. Tech.* **2010**, *3* (1), 1–20. https://doi.org/10.5194/amt-3-1-2010.

(47) Yang, M.; Huebert, B. J.; Blomquist, B. W.; Howell, S. G.; Shank, L. M.; McNaughton, C. S.; Clarke, A. D.; Hawkins, L. N.; Russell, L. M.; Covert, D. S.; et al. Atmospheric Sulfur Cycling in the Southeastern Pacific-Longitudinal Distribution, Vertical Profile, and Diel Variability Observed during VOCALS-REx. *Atmos. Chem. Phys.* **2011**, *11* (10), 5079–5097. https://doi.org/10.5194/acp-11-5079-2011.

(48) Bell, T. G.; De Bruyn, W.; Miller, S. D.; Ward, B.; Christensen, K.; Saltzman, E. S. Air–Sea Dimethylsulfide (DMS) Gas Transfer in the North Atlantic: Evidence for Limited Interfacial Gas Exchange at High Wind Speed. *Atmos. Chem. Phys.* **2013**, *13* (21), 11073–11087. https://doi.org/10.5194/acp-13-11073-2013.

(49) Millet, D. B.; Jacob, D. J.; Custer, T. G.; De Gouw, J. A.; Goldstein, A. H.; Karl, T.; Singh, H. B.; Sive, B. C.; Talbot, R. W.; Warneke, C.; et al. New Constraints on Terrestrial and Oceanic Sources of Atmospheric Methanol. *Atmos. Chem. Phys.* **2008**, *8* (23), 6887–6905. https://doi.org/10.5194/acp-8-6887-2008.

(50) Yang, M.; Beale, R.; Liss, P.; Johnson, M.; Blomquist, B.; Nightingale, P. Air-Sea Fluxes of Oxygenated Volatile Organic Compounds across the Atlantic Ocean. *Atmos. Chem. Phys.* **2014**, *14* (14), 7499–7517. https://doi.org/10.5194/acp-14-7499-2014.

(51) Brewer, J. F.; Bishop, M.; Kelp, M.; Keller, C. A.; Ravishankara, A. R.; Fischer, E. V. A Sensitivity Analysis of Key Natural Factors in the Modeled Global Acetone Budget. *J. Geophys. Res.* **2017**, *122* (3), 2043–2058. https://doi.org/10.1002/2016JD025935.

(52) Krechmer, J.; Lopez-Hilfiker, F.; Koss, A.; Hutterli, M.; Stoermer, C.; Deming, B.; Kimmel, J.; Warneke, C.; Holzinger, R.; Jayne, J.; et al. Evaluation of a New Reagent-Ion Source

and Focusing Ion-Molecule Reactor for Use in Proton-Transfer-Reaction Mass Spectrometry. *Anal. Chem.* **2018**, *90* (20), 12011–12018. https://doi.org/10.1021/acs.analchem.8b02641.

(53) Kim, M. J.; Farmer, D. K.; Bertram, T. H. A Controlling Role for the Air-Sea Interface in the Chemical Processing of Reactive Nitrogen in the Coastal Marine Boundary Layer. *Proc. Natl. Acad. Sci. U. S. A.* **2014**, *111* (11), 3943–3948. https://doi.org/10.1073/pnas.1318694111.

(54) Porter, J. G.; De Bruyn, W.; Saltzman, E. S. Eddy Flux Measurements of Sulfur Dioxide Deposition to the Sea Surface. *Atmos. Chem. Phys.* **2018**, *18* (20), 15291–15305. https://doi.org/10.5194/acp-18-15291-2018.

(55) Ikawa, H.; Oechel, W. C. Temporal Variations in Air-Sea CO2 Exchange near Large Kelp Beds near San Diego, California. *J. Geophys. Res. Ocean.* **2015**, *120* (1), 50–63. https://doi.org/10.1002/2014JC010229.

(56) Novak, G.; Vermeuel, M.; Bertram, T. Simultaneous Detection of Ozone and Nitrogen Dioxide by Oxygen Anion Chemical Ionization Mass Spectrometry: A Fast Time Response Sensor Suitable for Eddy Covariance Measurements. *Atmos. Meas. Tech. Discuss.* **2019**. https://doi.org/10.5194/amt-2019-445.

(57) Wright, D. Oceanographic Data Collected from Station Scripps Pier in the Coastal Waters of California by Southern California Coastal Ocean Observing System (SCCOOS) at Scripps Institution of Oceanography (SIO) and Assembled by Southern California Coastal Ocean Obser. NOAA National Centers for Environmental Information 2016.

(58) Bariteau, L.; Helmig, D.; Fairall, C. W.; Hare, J. E.; Hueber, J.; Lang, E. K. Determination of Oceanic Ozone Deposition by Ship-Borne Eddy Covariance Flux Measurements. *Atmos. Meas. Tech.* **2010**, *3* (2), 441–455. https://doi.org/10.5194/amt-3-441-2010.

(59) Liss, P. S.; Slater, P. G. Flux of Gases across the Air-Sea Interface. *Nature* **1974**, *247* (5438), 181–184. https://doi.org/10.1038/247181a0.

(60) Johnson, M. T. A Numerical Scheme to Calculate Temperature and Salinity Dependent Air-Water Transfer Velocities for Any Gas. *Ocean Sci.* **2010**, *6* (4), 913–932. https://doi.org/10.5194/os-6-913-2010.

(61) Wilczak, J. M.; Oncley, S. P.; Stage, S. A. Sonic Anemometer Tilt Correction Algorithms. *Boundary-Layer Meteorol.* **2001**, *99* (1), 127–150. https://doi.org/10.1023/a:1018966204465.

(62) Mauder, M.; Cuntz, M.; Drüe, C.; Graf, A.; Rebmann, C.; Schmid, H. P.; Schmidt, M.; Steinbrecher, R. A Strategy for Quality and Uncertainty Assessment of Long-Term Eddy-Covariance Measurements. *Agric. For. Meteorol.* **2013**, *169*, 122–135.

https://doi.org/10.1016/j.agrformet.2012.09.006.

(63) Foken, T.; Wichura, B. Tools for Quality Assessment of Surface-Based Flux Measurements. *Agric. For. Meteorol.* **1996**, *78* (1–2), 83–105. https://doi.org/10.1016/0168-1923(95)02248-1.

(64) Langford, B.; Acton, W.; Ammann, C.; Valach, A.; Nemitz, E. Eddy-Covariance Data with Low Signal-to-Noise Ratio: Time-Lag Determination, Uncertainties and Limit of Detection. *Atmos. Meas. Tech.* **2015**, *8* (10), 4197–4213. https://doi.org/10.5194/amt-8-4197-2015.

(65) Spirig, C.; Neftel, A.; Ammann, C.; Dommen, J.; Grabmer, W.; Thielmann, A.; Schaub, A.; Beauchamp, J.; Wisthaler, A.; Hansel, A. Eddy Covariance Flux Measurements of Biogenic VOCs during ECHO 2003 Using Proton Transfer Reaction Mass Spectrometry. *Atmos. Chem. Phys.* **2005**, *5*, 465–481. https://doi.org/10.5194/acp-5-465-2005.

(66) Wienhold, F. G.; Welling, M.; Harris, G. W. Micrometeorological Measurement and Source Region Analysis of Nitrous Oxide Fluxes from an Agricultural Soil. *Atmos. Environ.* **1995**, *29* (17), 2219–2227. https://doi.org/10.1016/1352-2310(95)00165-U.

(67) Kaimal, J. C.; Wyngaard, J. C.; Izumi, Y.; Coté, O. R. Spectral Characteristics of Surface-layer Turbulence. *Q. J. R. Meteorol. Soc.* **1972**, *98* (417), 563–589. https://doi.org/10.1002/qj.49709841707.

(68) Massman, W. J. The Attenuation of Concentration Fluctuations in Turbulent Flow through a Tube. *J. Geophys. Res. Atmos.* **1991**, *96* (D8), 15269–15273. https://doi.org/10.1029/91JD01514.

(69) Horst, T. W. A Simple Formula for Attenuation of Eddy Fluxes Measured with First-Order-Response Scalar Sensors. *Boundary-Layer Meteorol.* **1997**, *82* (2), 219–233. https://doi.org/10.1023/A:1000229130034.

(70) Lawson, S.; Law, C.; Harvey, M.; Bell, T.; Walker, C.; Saltzman, E. Methanethiol, Dimethyl Sulfide and Acetone over Biologically Productive Waters in the SW Pacific Ocean. *Atmos. Chem. Phys. Discuss.* **2019**. https://doi.org/10.5194/acp-2019-856.

(71) Kameyama, S.; Tanimoto, H.; Inomata, S.; Suzuki, K.; Komatsu, D. D.; Hirota, A.; Konno, U.; Tsunogai, U. Application of PTR-MS to an Incubation Experiment of the Marine Diatom Thalassiosira Pseudonana. *Geochem. J.* **2011**, *45* (5), 355–363. https://doi.org/10.2343/geochemj.1.0127.

(72) Guo, J.; Zhou, Y.; Zhang, B.; Zhang, J. Distribution and Evaluation of the Fate of Cyclic Volatile Methyl Siloxanes in the Largest Lake of Southwest China. *Sci. Total Environ.* **2019**, *657*, 87–95. https://doi.org/10.1016/j.scitotenv.2018.11.454.

(73) Coggon, M. M.; McDonald, B. C.; Vlasenko, A.; Veres, P. R.; Bernard, F.; Koss, A. R.; Yuan, B.; Gilman, J. B.; Peischl, J.; Aikin, K. C.; et al. Diurnal Variability and Emission

Pattern of Decamethylcyclopentasiloxane (D5) from the Application of Personal Care Products in Two North American Cities. *Environ. Sci. Technol.* **2018**, *52* (10), 5610–5618. https://doi.org/10.1021/acs.est.8b00506.

(74) Atkinson, R. Kinetics of the Gas-Phase Reactions of a Series of Organosiiicon Compounds with OH and NO 3 Radicals and O 3 at 297 ± 2 K. *Environ. Sci. Technol.* **1991**, *25* (5), 863–866. https://doi.org/10.1021/es00017a005.

(75) Brüggemann, M.; Hayeck, N.; George, C. Interfacial Photochemistry at the Ocean Surface Is a Global Source of Organic Vapors and Aerosols. *Nat. Commun.* **2018**, *9* (1), 1–19. https://doi.org/10.1038/s41467-018-04528-7.

(76) Ciuraru, R.; Fine, L.; Pinxteren, M. Van; D'Anna, B.; Herrmann, H.; George, C. Unravelling New Processes at Interfaces: Photochemical Isoprene Production at the Sea Surface. *Environ. Sci. Technol.* **2015**, *49* (22), 13199–13205. https://doi.org/10.1021/acs.est.5b02388.

Figures

COMPOUND	MIXING RATIO (PPB)	STD ADD 1 MIXING RATIO (PPT)	STD ADD 2 MIXING RATIO (PPT)	CYLINDER #	CAS
Acetonitrile	1092± 5%	592	1184	1	70-05-8
Ethyl alcohol	1076 ± 5%	538	1076	1	64-17-5
acrylonitrile	1016± 5%	508	1016	1	107-13-1
Acetone	1042± 5%	521	1042	1	67-64-1
Isoprene	1035± 5%	518	1036	1	78-79-5
Methyl Vinyl Ketone (MVK)	1039± 5%	520	1040	1	78-94-4
Methyl Ethyl Ketone (MEK)	1013± 5%	507	1014	1	78-93-3
Benzene	1001± 5%	501	1002	1	71-43-2
Xylene	1015± 5%	510	1020	1	108-38-3
1,2,4-Trimethylbenzene	971± 5%	508	1016	1	95-63-6
α-pinene	973± 5%	487	974	1	80-56-8
B-Caryophyllene	941± 5%	471	942	1	87-44-5
Octamethylcyclotetrasiloxane (D4)	981± 5%	491	982	1	556-67-2
Decamethylcyclopentasiloxane (D5)	1001± 5%	500	1000	1	541-02-6
Dimethyl Sulfide (DMS)	5080± 100	1280	2560	2	75-18-3

Table 2.1. Components and concentrations of the NMVOC standard compressed gas cylinders used for in field calibrations. The DMS calibration standard was a second compressed gas cylinder. Both NMVOC cylinders were added simultaneously during standard addition calibration periods.

Molecular Composition	Exact mass	Ion Identification	Mean Flux (pptv m s^{-1})	k_{OH} (cm^3 $molecules^{-1}$ s^{-1})	Notes
CH4OH	33.03349	methanol	-0.34	9.28E-13	
C2H3NH	42.03383	acetonitrile	-0.045	2.30E-14	
C2H2OH	43.01784	acetate fragment	-0.78	8E-13	
C2H4OH	45.03349	acetaldehyde	-0.30	1.62E-11	
CH4SH	49.01065	methanethiol	0.064	1.82E-11	
C3H3NH	54.03383	acrylonitrile	0.013	8.50E-12	
C3H6OH	59.04914	acetone	-0.78	2.19E-13	
H2CO3H	63.00767		-0.06	1.82E-11	
C2H6SH	63.0263	DMS	0.98	4.80E-12	
C4HNH	64.01818		0.008	1.82E-11	
C5H3H	64.03075		0.0089	1.82E-11	
CH4O3H	65.02332		0.044	1.82E-11	
C5H8H	69.06988	isoprene	0.079	1.00E-10	
C3H8O2H	77.05971		-0.050	1.82E-11	
C2H8O3H	81.05462		0.0011	1.82E-11	
C6H8H	81.06988	MT fragment	0.035	5.3E-11	Used for all reported MT values
C4H4SH	85.01065	thiophene	-0.0018	1.82E-11	
C7H8H	93.06988	toluene	0.038	5.48E-11	
C7H10H	95.08553		0.019	1.82E-11	
C5H4SH	97.04065		-0.0046	1.82E-11	
C4H8NO2	102.055		0.0011	1.82E-11	
C8H10H	107.0855	C8 aromatics	0.019	1.30E-11	
C2H4O5H	109.0132		-0.14	1.82E-11	
C6H8N2H	109.076		0.082	1.82E-11	
C8H12H	109.1012		0.0027	1.82E-11	
C5H2O3H	111.0077		-4E-06	1.82E-11	
C7H10OH	111.0804		0.016	1.82E-11	
C8H14H	111.1168		0.0006	1.82E-11	
C3H2O5H	118.9975		-0.0006	1.82E-11	
C9H12H	121.1012	C9 aromatics	0.023	3.25E-11	
C5H15NO2H	122.1176		0.0012	3.25E-11	
C5H2O4H	127.0026		-0.0043	1.82E-11	
C7H10O2H	127.0754		0.013	1.82E-11	
C7H13NOH	128.107		2E-05	1.82E-11	
C10H16H	137.1325	MT parent	0.015	1.82E-11	Used MT fragment (C6H8H) for all calculations
C8H14O2H	143.1067		-0.0008	1.61E-10	

C10H16OH	153.1274	camphor	0.0045	1.82E-11	
C6H5O3ClH	161		-0.0037	1.82E-11	
C11H17O3Si3	281.048	Siloxane	0.0033	4.80E-12	
C11H11O7Si	283.0269	Siloxane	0.0039	4.80E-12	
C12H21O3Si3	297.0793	Siloxane	0.018	4.80E-12	
C12H15O7Si	299.0582	Siloxane	0.022	4.80E-12	
C9H27O5Si5	355.0699	Siloxane	0.012	4.80E-12	
C10H31O5Si5	371.1012	D-5 Siloxane	0.025	4.80E-12	
C10H25O9Si3	373.0801	Siloxane	0.01	4.80E-12	

Table 2.2. All detected ions with statistically significant air-sea flux. Molecular composition assignments were made determined as the most reasonable structure for the ions exact mass. Molecular compositions listed include the added proton from the proton-transfer reaction ionization mechanism. MT was detected at both the parent mass ($C_{10}H_{16}H$) and at a fragment mass (C_6H_8H). For the instrument configuration used in this work the fragment mass was detected at higher sensitivities and was used for all reported values in this work. We neglect the MT parent mass from all reported values to avoid double counting.

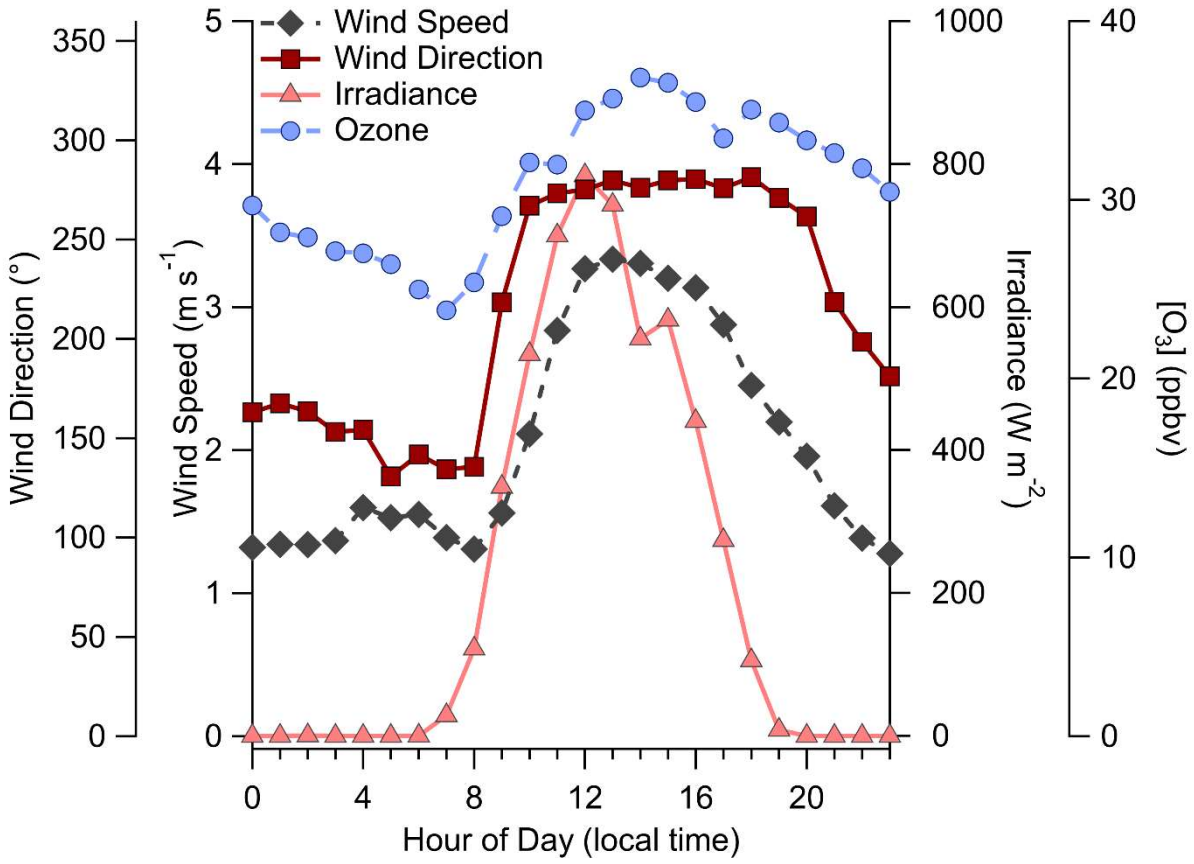

Figure 2.1. Campaign mean diel profiles of windspeed, wind direction, solar irradiance, and O_3 gas phase mixing ratios observed at Scripps Pier. Wind directions from 200 to 360° are from the ocean and otherwise are from the land.

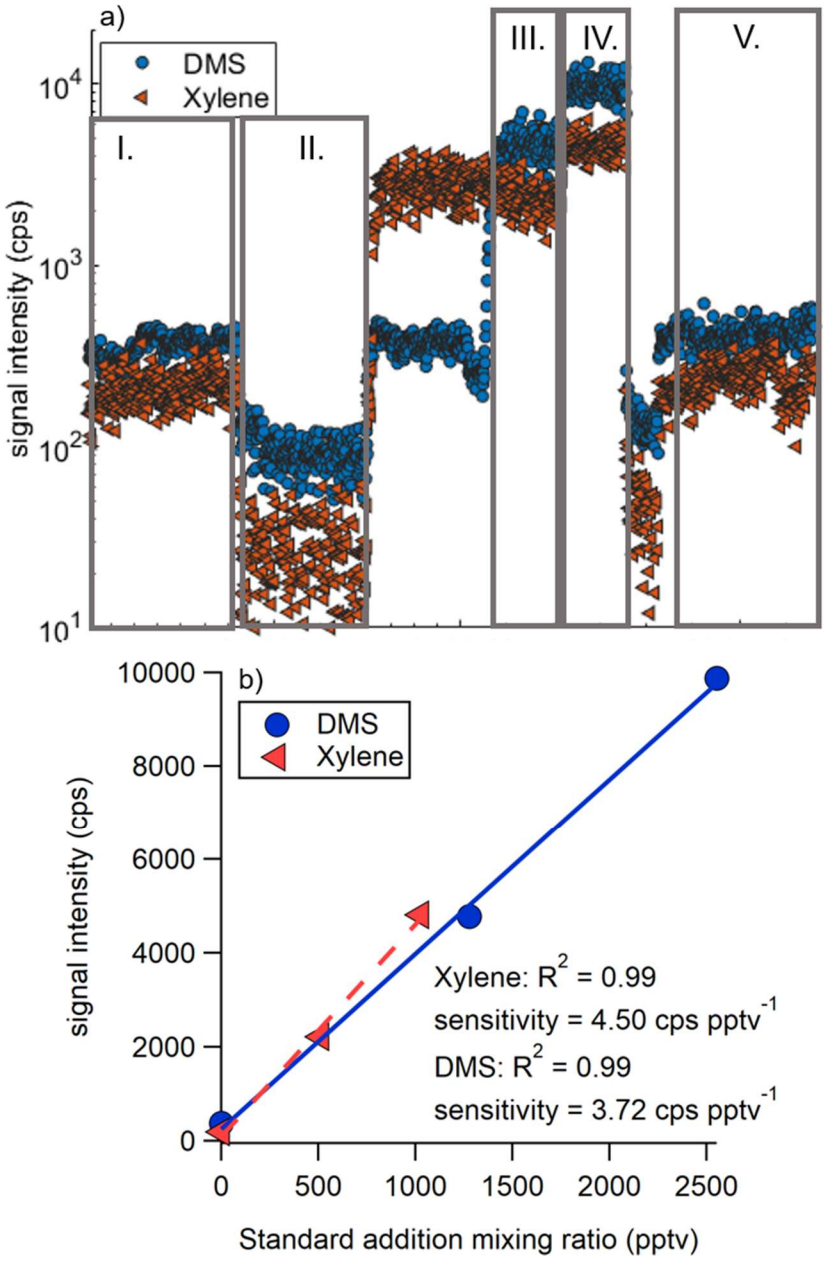

Figure 2.2. (a) timeseries of Vocus signal backgrounds and calibration factors determined during ambient sampling for DMS and xylene. Periods I. and V. are ambient sampling periods, period II. is a background determination by dry N_2 overflow, and periods III. and IV. are standard additions to ambient air at 510 and 1020 pptv for xylene and 1280 and 2560 pptv for DMS. (b). resulting calibration curve and instrument sensitivities for DMS and xylene from standard addition calibration in (a). Points at standard addition mixing ratio of 0 pptv are mean ambient count rates prior to the standard addition.

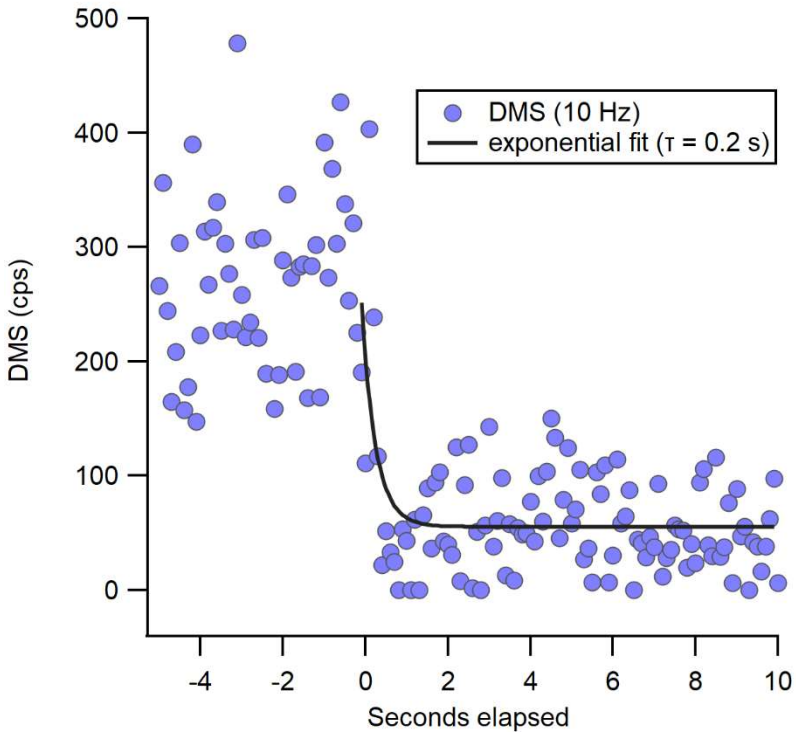

Figure 2.3. Instrument signal decay at 10 Hz during a dry UHP N_2 overflow background determination and exponential decay fit to data used to determine instrument response time (τ = 0.2 s).

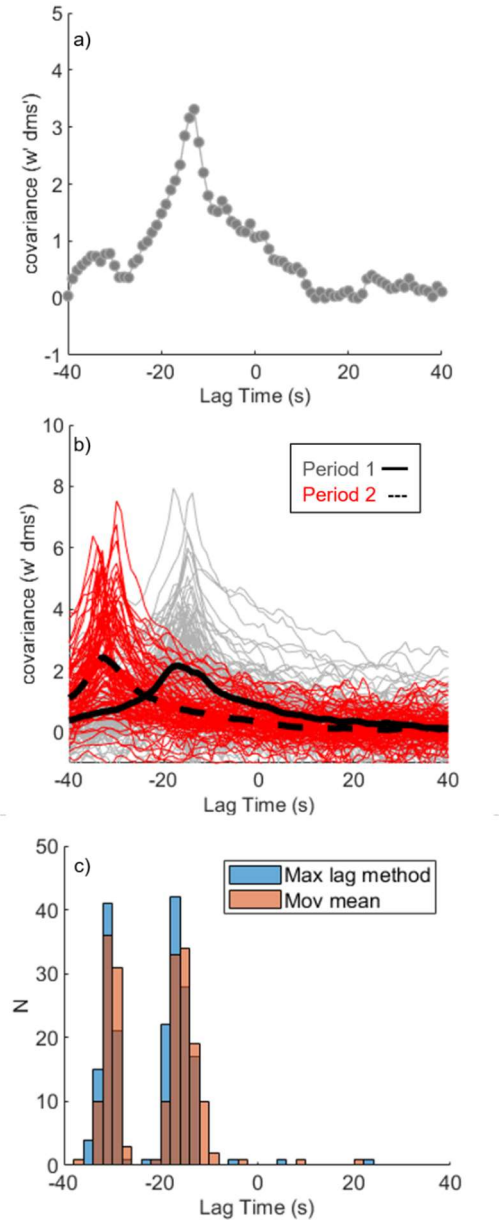

Figure 2.4. (a) EC flux lag time determination by cross covariance analysis of DMS flux during a single flux period. The maximum of the cross-covariance was found at -13 seconds. (b) Cross-covariance curves for all EC flux periods separated into Period 1 which was before an instrument shutdown and Period 2 which was after an instrument shutdown. Determined lag times showed a step change between the two periods due to data logging computers becoming further desynchronized following the power outage. Solid and dashed black lines are the mean cross-covariance from Periods 1 and 2 respectively. (c) optimum lag time taken as the absolute maximum (Max lag method), or the maximum of a 10-point moving median function (Mov mean) of the DMS cross-covariance function from each flux calculation period. The bimodal distribution corresponds to lag times determined for periods before and after the instrument shutdown period.

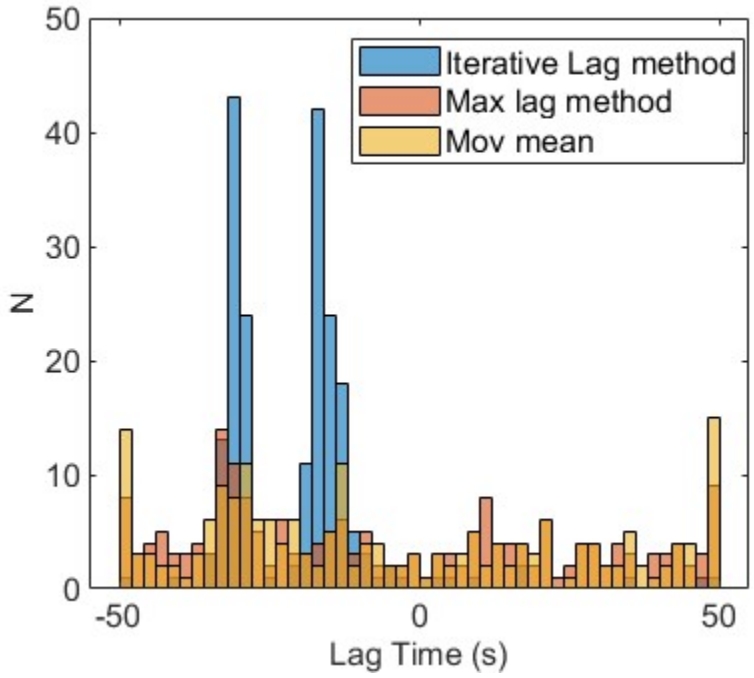

Figure 2.5. Optimum lag time determination for isoprene fluxes taken as the absolute maximum (Max lag method), or the maximum of a 10-point moving median function (Mov mean) of the DMS cross covariance function from each flux calculation period. The Iterative Lag method is the mean lag time determined by the Max Lag method for DMS, MeSH, and acetone for each flux averaging period. Isoprene EC flux has lower S/N resulting in higher variance in the determined optimum lag time by the Max or Mov mean lag methods compared to the Iterative method.

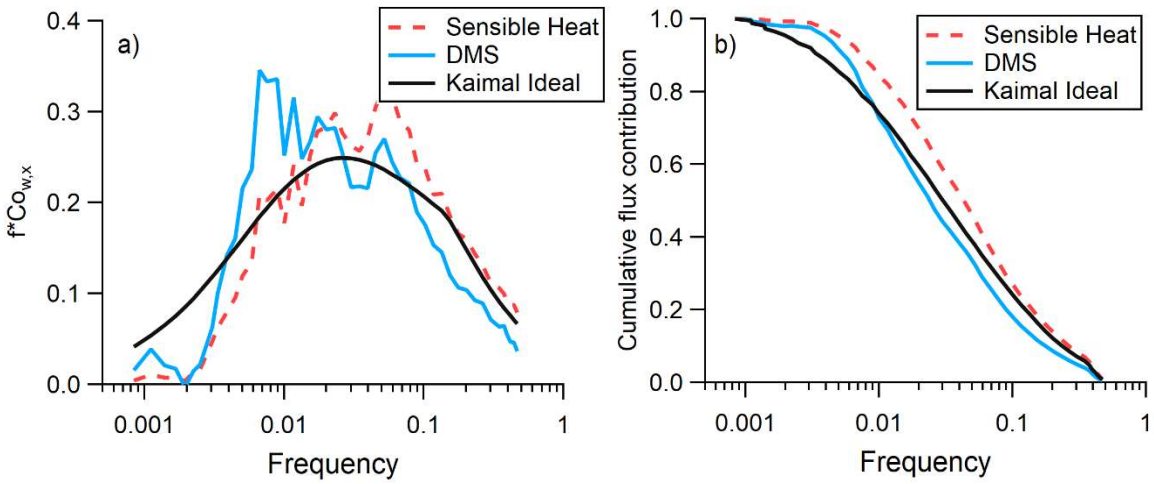

Figure 2.6. Representative (a) frequency weighted cospectra, and (b) cumulative flux contribution (ogives) for DMS, sensible heat, and the ideal cospectrum from Kaimal et al. (1972),[67] from a single 30-minute flux averaging period with wind speed of 4.3 m s^{-1}.

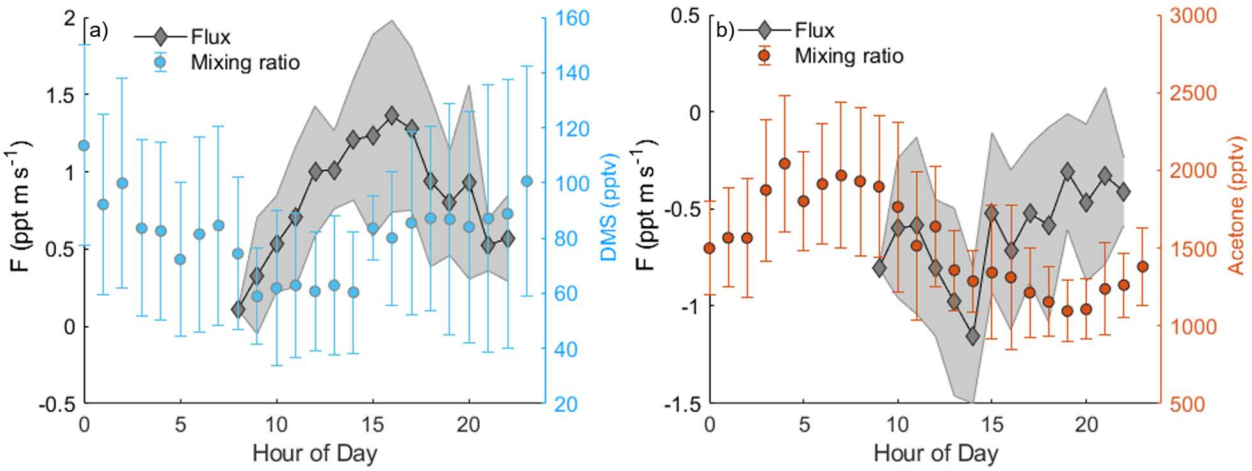

Figure 2.7. Campaign mean diel profiles of flux magnitude and gas phase mixing ratios for (a) DMS, and (b) acetone.

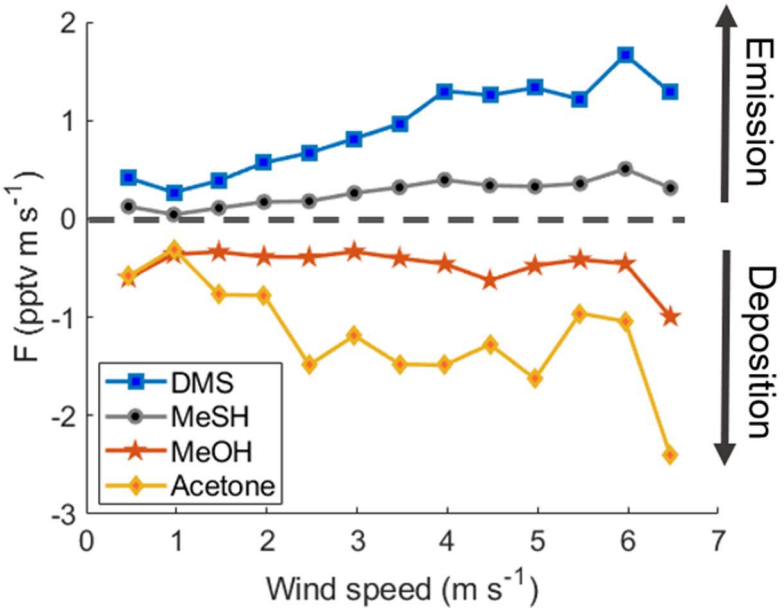

Figure 2.8. Campaign mean flux (*F*) wind-speed relationships for DMS, MeSH, MeOH, and acetone. *F* less than 0 represent deposition into the ocean and *F* greater than 0 are emissions into the atmosphere.

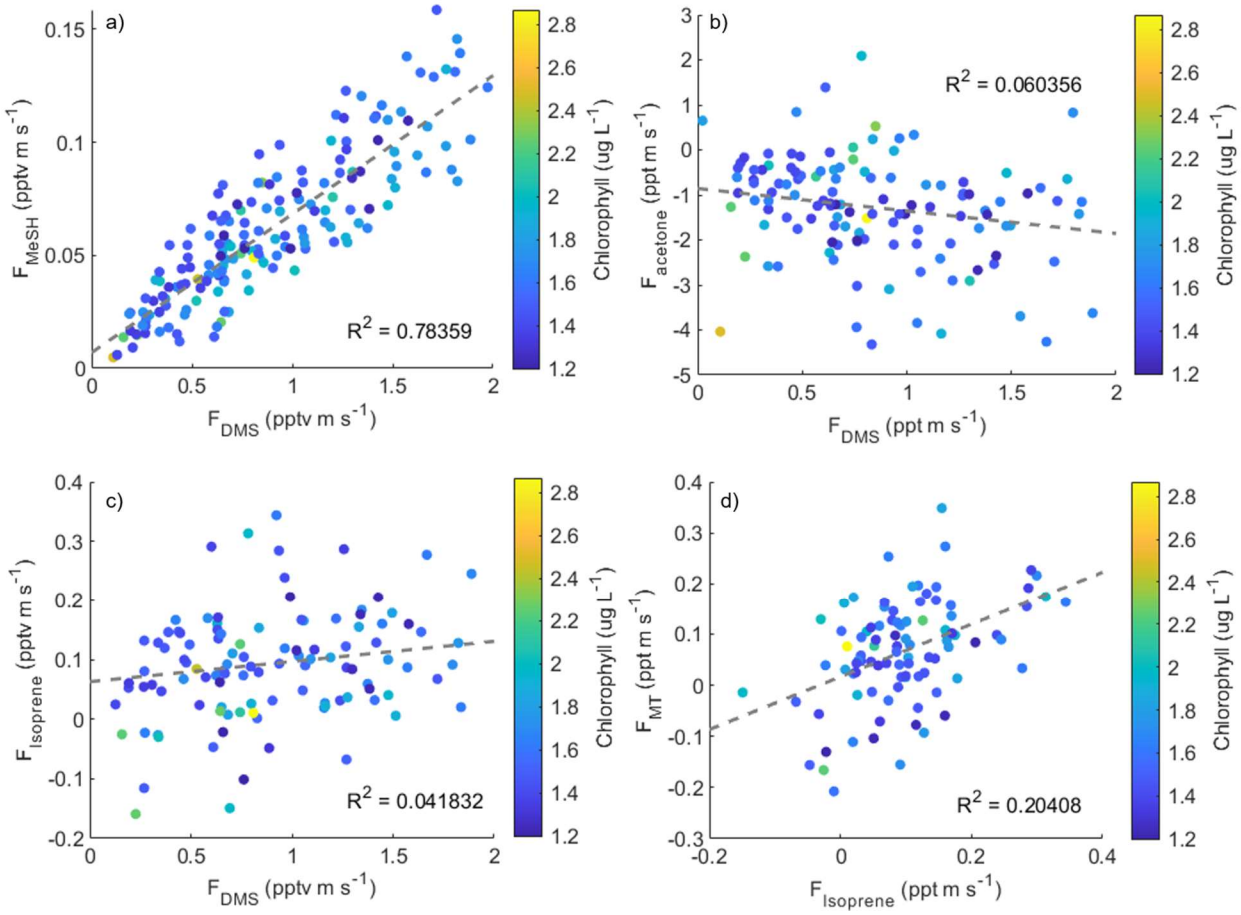

Figure 2.9. Flux regressions from individual 30-minute flux averaging periods of (a) MeSH vs DMS (R^2 = 0.78), (b) acetone vs DMS (R^2 = 0.06), (c) isoprene vs DMS (R^2 = 0.04), and (d) monoterpene (MT) vs isoprene (R^2 = 0.20), with points coloured by ocean chlorophyll concentration. Dashed grey lines are linear-least squares best fit lines.

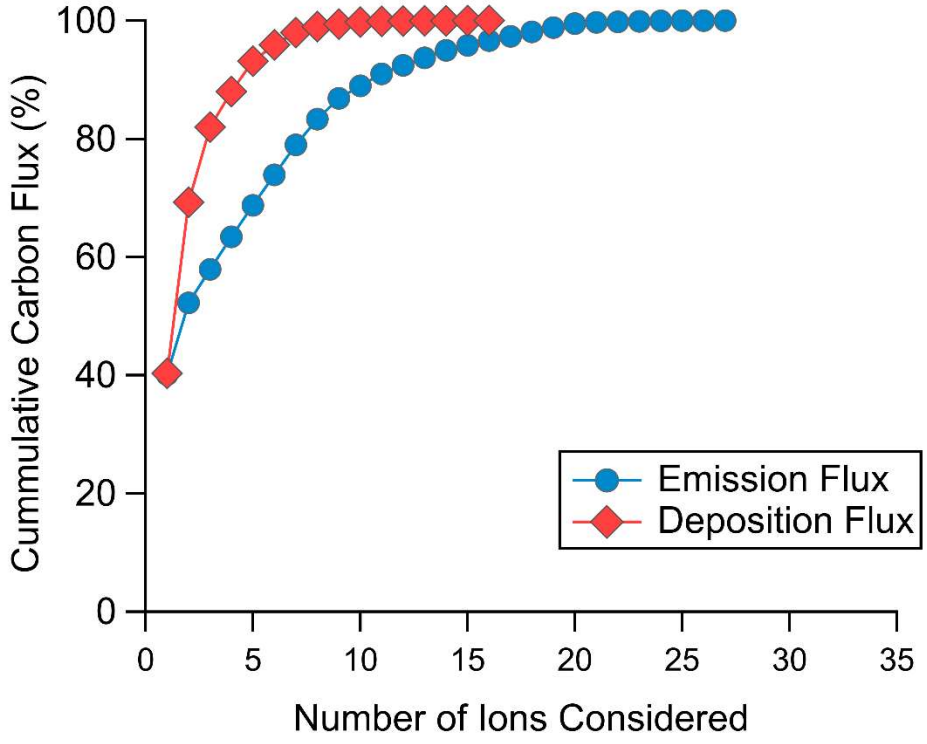

Figure 2.10. The fraction of the total gross emission and deposition NMVOC carbon mass flux that is accounted for as a function of the number of ions considered. DMS emission flux accounts for 40% of NMVOC carbon mass emission flux and acetone accounts for 40% of deposition flux.

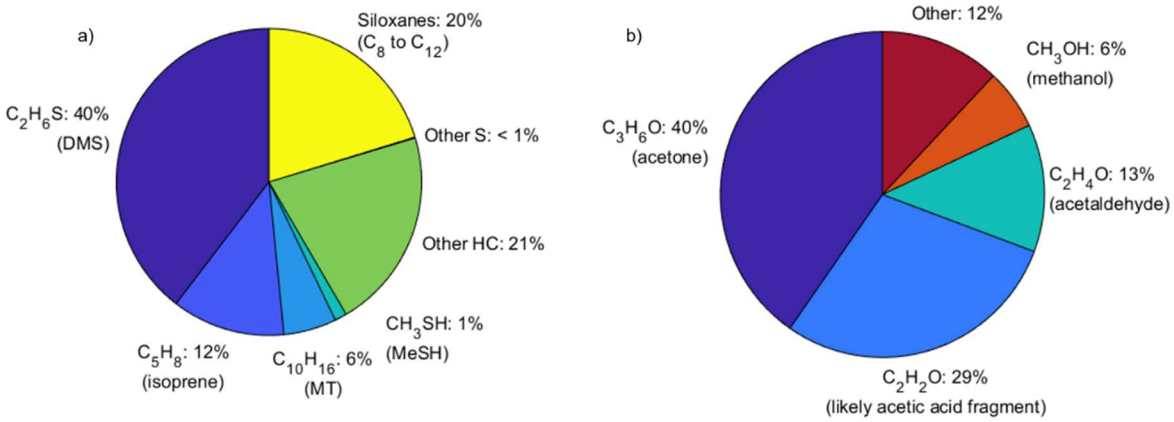

Figure 2.11. Pie chart of NMVOC carbon mass flux for (a) net emitting, and (b) net depositing species.

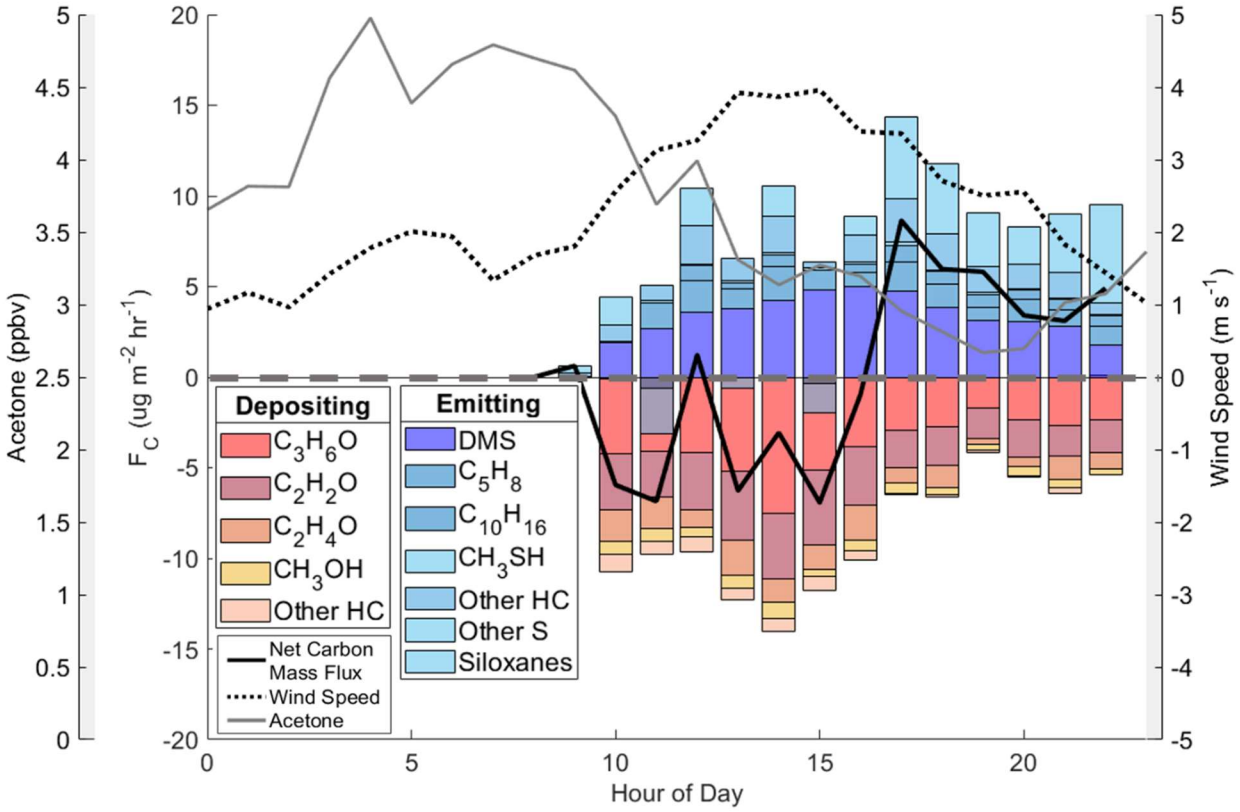

Figure 2.12. Campaign mean diel profile of speciated NMVOC carbon mass flux (F_C) with emissions being F_C greater than 0 μg m^{-2} hr^{-1}. Wind direction for hour of day 0 – 10 were consistently from land throughout the campaign and flux values are not reported. Mean diel profiles of horizontal wind-speed (dotted line), and acetone gas phase mixing ratios (light grey solid line) are also plotted.

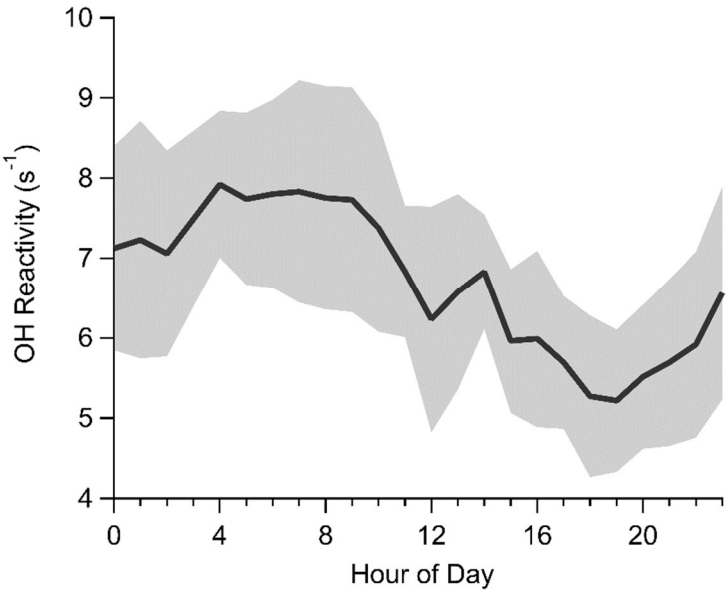

Figure 2.13. Campaign mean diel profile of OH reactivity from gas phase mixing ratios of all observed NMVOC with statistically significant EC flux. Shaded regions are the ±1σ variance.

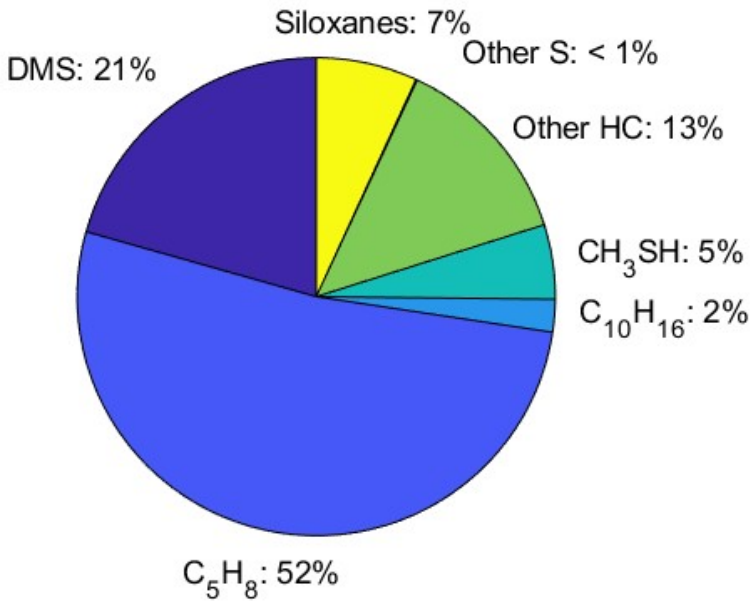

Figure 2.14. Pie chart of NMVOC emission fluxes weighted by NMVOC bimolecular rate constant with OH.

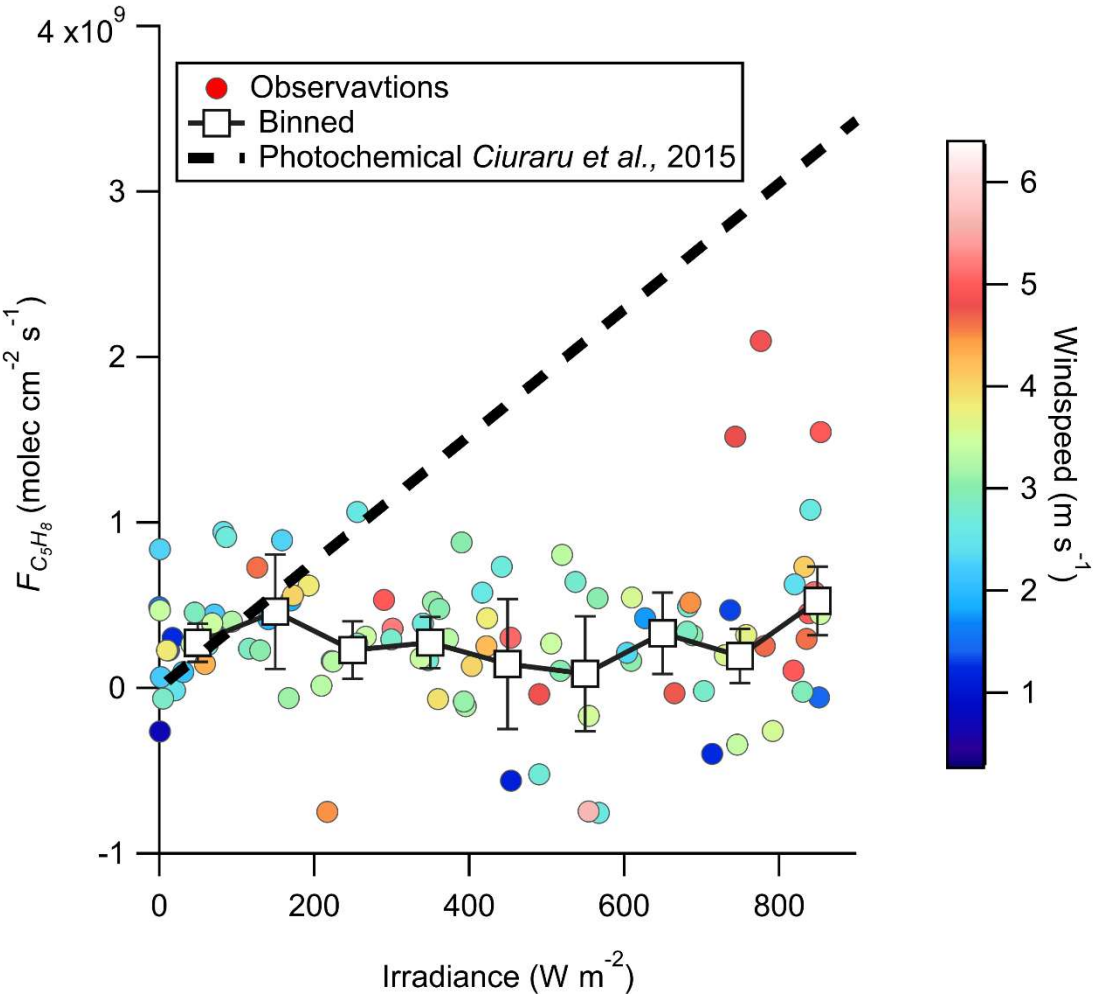

Figure 2.15. Eddy covariance flux measurements of isoprene sea-to-air exchange as a function of total solar irradiance (black squares, binned means with standard deviation). Individual flux measurements are shown colored by windspeed (m s^{-1}). Laboratory determination of photochemical isoprene production from sea surface microlayer samples, as determined by Ciuraru et al. (2015),[76] is also shown with the black dashed line (for ER = 1) linearly scaled to short wave radiation fluxes (e.g., F_{C5H8} = 8.0 × 108 molecules cm^{-2} s^{-1} at irradiance = 200 W m^{-2}).

Chapter 3. Assessing irreversible trace gas uptake to cloud droplets using airborne vertical flux measurements

Abstract

The uptake of reactive trace gases to cloud droplets is a significant loss process in the atmosphere for molecules that are both soluble and have fast aqueous phase reaction rates. Laboratory studies of trace gas uptake to water droplets have provided constraints on appropriate uptake rates for use in global chemistry models. To date, a method to directly measure reactive gas cloud uptake rates *in situ* in the atmosphere has been elusive. Here we present airborne vertical flux observations of hydroperoxy methylthioformate (HPMTF, $C_2H_4O_3S$) under cloudy and clear sky conditions as a method to directly assess cloud loss rates. For flights in a stratocumulus cloud-capped planetary boundary layer (PBL), we determine vertical exchange velocities (v_{ex}) of HPMTF of > 5 cm s^{-1} (measured at ½ the boundary layer depth) suggesting rapid HPMTF loss aloft. This vertical flux is much faster than what can be explained by the clear sky entrainment flux into the free troposphere (FT), as FT entrainment velocities (w_e) range from 0.12 to 0.72 cm s^{-1} for marine stratocumulus clouds. Measured v_{ex} of HPMTF under clear sky conditions were <1 cm s^{-1} which is generally consistent with entrainment driven flux. The observed v_{ex} of +5 cm s^{-1} under cloudy conditions implies an HPMTF lifetime to cloud uptake of approximately 2.1 hrs in the PBL. HPMTF cloud loss represents an important terminal sink for marine reactive sulfur which is not accounted for in current models. Up to 40% of emitted DMS goes on to form HPMTF, which if lost to clouds will make no contribution to aerosol production or growth. Interpolation of the observed flux divergence profile to the cloud base height allows for calculation of a cloud entrainment velocity from the cloud free fraction of the PBL into the cloud layer (v_c) at the cloud base to be 10.3 cm s^{-1}, which we take as the rate of turbulent mixing from the cloud free fraction of the PBL into the cloud layer. Vertical concentration profiles show that HPMTF is highly depleted (<2 pptv) in the

FT above the cloud capped PBL, supporting irreversible loss to cloud droplets. In clear sky cases, HPMTF concentrations were sustained into the FT. Vertical flux measurements of HPMTF from a ground site (measurement height 13 m) showed mean v_{ex} of -0.78 ± 37 cm s^{-1} to the coastal ocean surface at a mean windspeed of 3 m s^{-1}, supporting that HPMTF is a soluble molecule which deposits into the ocean at the air-side resistance limit. We propose that HPMTF is uniquely suited for assessing cloud loss in the PBL, as HPMTF shows irreversible uptake to cloud droplets and is continuously produced by dimethyl sulfide (DMS) oxidation during daytime within the PBL which sustains measurable HPMTF signal despite rapid consumption in clouds aloft. Work to incorporate these vertical flux observations and calculated cloud entrainment rates into large eddy simulation (LES) and global chemical transport models (CTM) for a comprehensive treatment of cloud uptake is ongoing.

3.1. Introduction

Cloud droplets in the atmosphere can act as a terminal sink or reaction site for trace gases affecting reactive trace gas budgets and contributing to acid rain. The total transfer rate of a gas into a droplet incorporates multiple processes including 1) diffusion in the gas phase to the liquid surface, 2) accommodation of the gas onto the liquid surface, 3) possible chemical conversion in the liquid phase, and 4) diffusion in the liquid away from the interface. For very high solubility gases like nitric acid (HNO_3, $K_H = 2.1 \times 10^5$ M atm^{-1}), reactive uptake coefficients (γ) to cloud droplets are large (>0.05), uptake is irreversible, and total gas transfer rates are limited by gas diffusion rather than mass accommodation rates.[1] For partially soluble gases that are not rapidly converted to soluble products in the liquid phase, such as hydrogen peroxide (H_2O_2), the liquid surface becomes saturated driving re-evaporation and an equilibrium between droplet and gas phase concentrations. Heterogeneous reactions can act to enhance droplet uptake by reacting with sparingly soluble

species. For example, sulfur dioxide (SO_2) which is sparingly soluble (K_H = 1.2 M atm^{-1}) can be oxidized by H_2O_2 and other species in droplets to form sulfate (SO_4^{2-}).[2] Laboratory studies of gas entrainment rates and mass accommodation factors onto droplets and of droplet heterogeneous reactivity have been performed for select species.

Ambient observations of depletion of N_2O_5 in clouds and fog has been noted several times in the literature, with an observed lifetime of NO_3 of less than 1 minute in fog.[3,4] Those observations are consistent with expectations of fast loss rates for species with irreversible uptake. A newly observed significant dimethyl sulfide (DMS) oxidation product hydroperoxymethyl thioformate (HPMTF, $HOOCH_2SCHO$), has been observed to be ubiquitous in the global marine atmosphere by airborne sampling.[5] HPMTF was observed to be rapidly depleted within clouds, which suggests cloud processing may be an important sink for marine sulfur with unclear overall impacts on aerosol formation and growth. However, to date no general method exists to directly measure the effective total loss rates to clouds and corresponding lifetimes in the ambient atmosphere, with prior ambient studies only noting depletion in concentration.

For a soluble species with irreversible uptake, uptake once within the cloud layer is expected to be fast, following diffusion limited uptake. For instance, Levine and Schwartz (1982)[6] calculated the lifetime of HNO_3 in a fair weather cumulus cloud layer to be 5 s, set by diffusion limited uptake. Residence times (τ_c) within stratocumulus clouds are significantly longer, on the order of 15 minutes to 2 hours.[7] This suggests that species with irreversible uptake will be completely depleted in the cloud layer, as the cloud residence time is much longer than the diffusion limited uptake lifetime. The lifetime of a molecule within the cloud layer is dependent on the droplet size distribution, gas phase diffusion constants (D), and uptake coefficients (γ), all of which are readily measurable products. Values for γ on liquid water droplets have been determined in laboratory

studies to be 0.07 to 0.193 for HNO_3 at 268 K and 293 K respectively, 0.064 to 0.177 for HCl at 294 K and 274 K respectively, 0.04 to 0.061 for N_2O_5 (282 and 271 K), 0.18 for H_2O_2 at 273 K with an observed decrease at higher temperatures, and 0.11 for SO_2 with no observed temperature dependence.[1,8] All of the listed γ are larger than the threshold for diffusion limited uptake which is typically taken as γ=0.03. Less clear are the appropriate rates for mixing of an airmass into the cloud layer and residence time within the cloud. A model evaluation of cloud uptake to marine stratocumulus clouds using LES coupled to a trajectory-ensemble model by Feingold et al. (1998)[9] calculated that individual turbulent air parcels spend *ca*. 25% of their time within cloud for a 750 m BLH height where the top 250 m contained cloud droplets. Results from this study were consistent with fast uptake within the cloud layer with diffusion limited lifetimes of <10 s for HPMTF, with total PBL integrated cloud loss rates controlled by the entrainment rate of parcels into the cloud. Holmes et al. (2019)[10] implemented a revised scheme for cloud uptake in a CTM which included cloud spatial information and explicitly treated the entrainment rate of parcels into clouds. Overall cloud loss rates of N_2O_5 in that study were limited by the entrainment rate of PBL air parcels into clouds, with the lifetime of N_2O_5 within the cloud layer found to be 10 s. A fixed cloud residence time of 1 hr was used in that study which was based on mean residence times for stratus and stratocumulus clouds. As noted in that work, total cloud loss rates are acutely sensitive to the cloud entrainment rate and the residence time within the cloud and that implementation of spatiotemporal variation in those parameters will be necessary. The net effect of cloud uptake of N_2O_5 in that study accounted for 5% of global NO_x loss and a reduction of OH and O_3 loadings by 2%, comparable to the effects of N_2O_5 uptake to aerosol. These model results are consistent in validating that uptake of highly soluble species once within clouds is fast but that constraints on

the entrainment rate into clouds are needed to more accurately treat the net effect of cloud processing on the lifetimes of soluble species.

Stratocumulus clouds within the turbulent PBL are a common feature over cooler regions of the subtropical and mid-latitude oceans, where mean annual coverage can exceed 50%.[11] Globally stratus and stratocumulus clouds are typically present over 10-70% of the PBL, suggesting loss to clouds within the PBL to be a potentially significant term in reactive trace gas budgets. Here we present airborne flux observation of HPMTF under cloudy and clear sky conditions which show divergent vertical flux profiles. Vertical flux of HPMTF in the cloud-capped PBL is fast and positive (v_{ex} 4-6 cm s^{-1}) indicative of rapid loss aloft in the cloud layer. We use these observations to directly assess cloud loss rates and lifetimes of HPMTF and to explore the impacts of HPMTF cloud loss on marine sulfur cycling.

3.2 Methods

3.2.1 Airborne Observations

Airborne observations of HPMTF and several additional chemical tracers were made from the NASA DC-8 platform as part of the NASA Atmospheric Tomography (ATom) the NASA Student Airborne Research Program (SARP) campaigns. The SARP flight was split into two legs, one over the coastal ocean (hereon termed SARP Marine) and one over the inland Salton Sea (SARP Salton). The SARP Marine leg was used for flux assessment in the cloud capped PBL. The SARP Salton leg was not suitable for flux analysis but allowed for comparison of DMS and HPMTF mixing ratios and vertical profiles in clear sky conditions. The ATom flight planning was not optimized for flux analysis and only one best case clear sky set of flights was used for HPMTF flux analysis. Further specific details of each flight campaign are presented in Sections 3.2.1.4 and 3.2.1.5. All measurements of HPMTF were made with the NOAA iodide chemical ionization mass

spectrometer described in detail in Veres et al. (2020).[5] Three-dimensional wind speeds on both campaigns were recorded with the Meteorological Measurement System (MMS).[12] Observations of HPMTF mixing ratio and vertical wind speed from the MMS system were used to calculate vertical flux by the eddy covariance method as described in Sections 3.2.1.1 to 3.2.1.3.

3.2.1.1. Eddy covariance and wavelet flux analysis

Eddy covariance is a well-established method for the determination of the vertical flux of trace gases and energy in a turbulently mixed environment. EC flux (F) is calculated as the time-averaged product of the deviations in vertical wind (w) and a scalar (c) over some characteristic averaging time shown in Equation 1., where overbars represent means, primes represent instantaneous deviations from the mean, and n is the total number of sample points in a given flux averaging period. Exchange velocity (v_{ex}) is calculated from F following Equation 2, where c_a is the mean gas phase mixing ratio during the flux averaging period.

$$F = \frac{1}{n}\sum_{i=1}^{n}(w_i - \bar{w})(c_i - \bar{c}) = \overline{w'c'} \quad \text{E1}$$

$$v_{ex} = \frac{F}{C_a} \quad \text{E2}$$

Airborne vertical flux measurements have long been used to assess budgets of trace gases in the atmosphere.[13–15] Recent advances in instrumentation for detection of trace gases has enhanced the number of atmospheric constituents which can be characterized simultaneously in airborne flux studies.[15,16] These studies have enabled determination of emission rates from heterogeneous across heterogeneous ecosystems,[15,17] vertical flux divergence driven by fast chemical reactions,[15] and direct determination of entrainment rates (w_e) of air from the free troposphere into the PBL.[18]

3.2.1.2 EC Data Treatment

All EC flux determinations were performed at 1 Hz time resolution. The following standard data processing procedures were applied prior to EC flux calculations: 1) despiking of scalar data following Mauder etl al. (2013).[19] 2.) detrending of scalar data by linear interpolation over the flux averaging period. 3.) At 1 Hz data resolution, all instruments had sufficiently fast response and clocks were sufficiently well synchronized that time that no time lag was observed between scalar and vertical wind velocity signal when flux signal was strong. Therefore, a fixed lag time of 0 s was applied for all calculations.

Flux averaging periods were manually selected via the following criteria: 1.) aircraft altitude was level to within 30 m over the full leg. 2.) aircraft pitch and roll did not exceed 5° during the leg. 3.) data periods were selected to avoid gaps in data for any of the scalars of interest driven by instrument calibration or zeroing periods or other outages.

Continuous wavelet transform (CWT) methods for computing EC flux have emerged as powerful technique in airborne flux studies as it does not require homogeneity or stationarity over the averaging period and because it preserves time information. This allows for the computed flux to resolve changes over heterogeneous surfaces. We present flux results using the continuous wavelet transfer using the Morlet mother wavelet. See Torrence and Campo (1998)[20] for further information on wavelet methodologies and Mistzal et al., (2014)[21] and Wolfe et al., (2015)[15] for details on application of wavelet methods for airborne EC flux applications. An example CWT EC flux determination is presented in **Figure 3. 1**, including the scalar and CWT flux timeseries and spectral analysis.

3.2.1.3 Flux error analysis

Uncertainties in EC measurements arise from sensor noise, biases in sampling, and fundamental uncertainties driven by the stochastic nature of turbulence.[16] Systematic error from the under sampling of turbulent eddies at high or low frequencies was assessed following. Lenschow et al. (1994)[22] derived a method for assessing the upper limit of this systematic error (SE_{turb}) as a function of sampling height (z), PBL height (z_i) and the flux leg length (L) as shown in Equation 3. This error ranged from 2-3 %, suggesting flux legs were sufficiently long to capture a representative distribution of eddies. Random error arising from the stochastic nature of turbulence (RE_{turb}) was calculated following Lenschow et al. (1994)[22] as shown in Equation 4, which was found to be from 11 to 16% for the SARP Marine flux observations. Total random flux error (RE_s) from uncorrelated sensor noise was assessed following the methodology of Finkelstein and Sims (2001), which treats random error as the variance of the covariance between x and w as shown in Equation 5.[16,23] Terms such as $\overline{x'w'_p}$ represent the cross-covariance or auto-covariance at a lag time p. RE_s was calculated using a lag time range of 0 to one-half the length of the flux timeseries.

$$SE_{turb} \leq 2.2 \left(\frac{z}{z_i}\right)^{0.5} \frac{z_i}{L} \quad \text{E3}$$

$$\frac{RE_{turb}}{F} \leq 1.75 \left(\frac{z}{z_i}\right)^{0.25} \left(\frac{z_i}{L}\right)^{0.5} \quad \text{E4}$$

$$RE_s = \sqrt{\frac{1}{N}\sum_{p=-m}^{m}\left(\overline{x'x'_p}\,\overline{w'w'_p} + \overline{x'w'_p}\,\overline{w'x'_p}\right)} \quad \text{E5}$$

For HPMTF RE_s was from 0.07 to 0.13 pptv m s^{-1} (or approximately 30%) for the SARP Marine legs and 0.32-0.46 pptv m s^{-1} (80-120%) for the ATom-4 flux legs.

3.2.1.4 NASA ATom mission

The NASA Atmospheric Tomography (ATom) study was a series of research campaigns from 2016-2018 on the instrumented NASA DC-8 aircraft which sampled the daytime remote marine atmosphere over the Pacific and Atlantic Oceans.[24] Typical flight patterns consisted of vertical profiles from 0.2 to 14 km above the ocean surface between latitudes 80°N and 85°N. Following each vertical profile, a stable flight leg of duration *ca. 5* minutes was flown within the boundary layer, typically at an altitude of 150 to 200 m above the ocean surface. The NOAA iodide chemical ionization time-of-flight mass spectrometer (iodide CIMS) sensor for HPMTF was included on aircraft payload for ATom-3 occurring in September to October 2017, and ATom-4 from April to May 2018. HPMTF is an oxidation product of DMS which was observed on ATom to be a ubiquitous sulfur reservoir species in the remote marine troposphere.[5] Observations from ATom-1 and ATom-2 are not included in this work. All data used in this work was taken from the publicly available 1 Hz data merge.[25] **Table 3.1** describes instruments details and uncertainties for all measured species used in this work.

3.2.1.5 NASA SARP flights

A targeted marine airborne flux flight was flown on the NASA DC-8 as part of the NASA Student Airborne Research Program (SARP) on August 17th 2019. The flight path included three targeted flux legs of greater than 5 minutes (>30 km) at altitudes of 170, 250, and 170 m sequentially, within the PBL offshore of Los Angeles, CA. The PBL during these flights was capped by marine stratocumulus clouds for the full flight path, verified by analysis of the archived front-facing camera on the DC-8. This flight will be referred to hereafter in the text as SARP Marine. The flight track of the SARP Marine flight is shown in **Figure 3.2**.

An additional flight under clear sky conditions was also performed with the same platform on the same day over the Salton Sea at an altitude of 350 m, which showed enhancements of both DMS and HPMTF immediately over the Salton Sea. This flight was not flown as a targeted airborne flux study, unlike the SARP marine, resulting in flight maneuvers not conducive to EC analysis and all calculated HPMTF flux values being below the limit of detection. This flight will be referred to hereafter in the text as SARP Salton. The Salton Sea is an inland saline lake with dimensions 24 by 56 km, located approximately 200 km south west of Los Angeles, CA. The flight track of the SARP Salton flight is shown in **Figure 3.3**. An overview of instrumentation on the DC-8 for both SARP flights is given in **Table 3.2**. Front-facing camera images showing cloud cover during the SARP Marine, SARP Salton, and ATom-4 May 1st PBL legs are shown in **Figure 3.4**.

3.2.2 Ground site coastal ocean HPMTF deposition study

The HPMTF exchange velocity (v_{ex}) was also measured from a ground site at the end of the 330 m Scripps Pier at the Scripps Institute of Oceanography, La Jolla CA in July and August 2018. HPMTF was detected with a compact time-of-flight mass spectrometer utilizing iodide reagent ion chemistry (cToF). The cToF was deployed to a climate-controlled trailer at the end of the pier and sampled through a 0.625 cm i.d. PFA Teflon inlet with a length of 20 m. The inlet was pumped at a rate of 20 slpm with the cToF subsampling at 1.5 slpm. Temperature and relative humidity were recorded inline downstream of the cToF subsampling point. The inlet sampling point was collocated with a sonic anemometer (Gil HS-50) located on a boom extending 7 m beyond the end of the pier at a measurement height 10 m above the mean lower low tide level. The cToF recorded the full mass spectrum at 10 Hz. Mass resolution of the cToF is *ca* 1000 $m/\Delta m$ and signals were integrated at unit mass resolution. HPMTF was detected as a stable adduct with iodide at -m/Q 235 which is isobaric with the detection product N_2O_5. NO_3 and N_2O_5 are rapidly photolyzed during

the day (τ<10 min) and N_2O_5 is therefore expected to have negligible contribution to the observed signal during daytime. The lifetime of N_2O_5 was calculated throughout the campaign and data periods were rejected if the N_2O_5 lifetime was greater than 2 minutes. For periods when the N_2O_5 lifetime was less than 2 minutes, all signal at -*m/Q* 235 was treated solely as HPMTF. Instrument sensitivity to HPMTF was determined by scaling normalized signal intensity to humidity dependent sensitivities determined in the laboratory following the campaign. Instrument backgrounds were determined by overflowing the full inlet with dry ultra-high purity N_2 approximately every 30 minutes. Further details of the instrument deployment and flux data processing from the same instrument and deployment but utilizing a different reagent ion chemistry are provided in Novak et al (2019).[31]

3.3 Results

3.3.1 DMS to HPMTF Ratios

The ratio of DMS to HPMTF mixing ratios ([DMS]/[HPMTF]) from the SARP Marine (cloudy) and SARP Salton (clear-sky) binned by altitude are shown in **Figure 3.5.** Observed [DMS]/[HPMTF] serves as a tracer of the relative loss rate of HPMTF in different sampling environments assuming that HPMTF production rates from DMS are constant. Mean [DMS]/[HPMTF] was 29.5 ± 22.5 for the SARP Marine flight, and 4.4 ± 2.1 for the SARP Salton Sea flight at altitudes 100-400 m. The larger ratio observed for the SARP Marine flight implies that either HPMTF production from DMS oxidation was slower or that HPMTF loss rates were higher compared to the SARP Salton flight. Rapid loss of HPMTF to cloud droplets during the SARP Marine flights would be one potential explanation for the large difference in observed [DMS]/[HPMTF]. The increase in observed [DMS]/[HPMTF] with altitude for the SARP Marine flight is a useful additional indicator for HPMTF cloud loss, as DMS concentration and HPMTF

production are constant with altitude in the PBL but HPMTF loss is enhanced in the cloud layer. [DMS]/[HPMTF] within the cloud layer was 940, driven by the near complete consumption of HPMTF in the cloud. [DMS]/[HPMTF] below cloud also increased with altitude and was measured to be 21 and 84 at bin mean altitudes of 215 and 315 m respectively. The observed [DMS]/[HPMTF] on the SARP Salton flight was below 6 for all altitudes within the PBL and into the FT. This much smaller ratio compared to the SARP Marine flight suggests HPMTF loss rates were significantly lower in the clear sky Salton Sea flight. Determination of [DMS]/[HPMTF] from individual boundary layer profiles during ATom was not possible due to the 2-minute time resolution of DMS measurements during that campaign. However, observed boundary layer [DMS]/[HPMTF] across the campaign was consistently less than 2, with a mean of 0.4 for altitudes of 200-400 m, consistent with the typical low to no cloud flight conditions during ATom. The SARP Marine and SARP Salton flights were flown on the same aircraft with the same instrument payload on the same day, allowing direct comparison of observations.

3.3.2 Vertical flux in stratocumulus capped MBL

Vertical fluxes of HPMTF were assessed in the stratocumulus capped MBL at altitudes of 170 and 250 m during the SARP Marine flights. A map of HPMTF across the flight track is shown in **Figure 3.1** with the altitude and spatial midpoint of each leg indicated on the map. HPMTF mixing ratios were roughly constant across the marine flux legs ranging from 3 to 10 pptv and were constant with altitude within the PBL. DMS, which is the precursor species of HPMTF ranged from 50 to 140 pptv as determined by proton transfer reaction mass spectrometer measurements (PTR-MS). A timeseries of HPMTF and DMS mixing ratios during the flux legs the is shown in **Figure 3.6**. HNO_3 within the stratocumulus capped MBL was below 15 pptv and showed high variance (σ = 12 pptv) precluding the possibility the use of HNO_3 in EC flux analysis as a tracer

of cloud processing. Ocean surface spatial heterogeneity is assumed to be negligible over the sampling region and we therefore report a single mean flux value for each calculated flux region and do not make use of the temporal flux data provided by the CWT analysis.

The SARP Marine flight was divided into three flux analysis legs (L1-L3) flown sequentially at altitudes of 180, 255, and 170 m. Observed mean HPMTF mixing ratios for legs 1-3 were 6.6, 4.9 and 5.8 pptv respectively. Observed HPMTF v_{ex} calculated by CWT EC analysis were 5.6, 6.0, and 5.2 cm s^{-1} respectively. The vertical flux divergence profile of HPMTF is shown in **Figure 3.7**. The increase in observed v_{ex} at 255 m of 6.0 cm s^{-1} compared to v_{ex} of 5.4 cm s^{-1} is qualitatively consistent with a flux divergence term driving enhanced positive flux aloft from cloud processing. Also plotted in **Figure 3.7** is the mean observed HPMTF v_{ex} of -0.78 cm s^{-1} observed from a coastal ground site at Scripps Pier, La Jolla CA discussed further in Section 3.3.3. The large positive v_{ex} observed aloft compared to the measured surface deposition flux of -0.78 cm s^{-1} implies a strong vertical flux divergence for HPMTF. Liner fitting of the observed flux vertical profile gives a best fit line with equation: v_{ex} = (*altitude* – 19.4)/33.15. Interpolation of the observed profile to the top of the PBL implies a w_e of 16.3 cm s^{-1} in order to drive the observed vertical flux profile. As noted previously, w_e rates of entrainment from the FT in stratocumulus clouds have been measured from 0.12 to 0.7 cm s^{-1}, which is 1-2 orders of magnitude lower than needed to explain our observations. The observed large positive v_{ex} aloft necessitates a rapid consumption of HPMTF aloft in the PB. Rapid consumption of HPMTF in the cloud layer is supported by analysis of the vertical mixing ratio profile of HPMTF, where HPMTF in cloud was <2 pptv and below cloud was >5 pptv, discussed further in Section 3.3.1. The use of a linear fit to the observed flux profile is a simplifying assumption and the profile within the cloud layer may have a more complex functional form that would change the calculated w_e at the top of the cloud layer. Determination of an

idealized HPMTF flux profile following a mass balance approach following Wolfe et al. (2015) is in progress.[32] Extrapolation of the vertical profile within the cloud free fraction of the PBL is expected to be less sensitive to shape of the fit, given the direct observational constraints, and so confidence in the determined cloud uptake lifetime discussed in Section 3.4.1 is higher.

3.3.3 Vertical flux in clear sky MBL

Vertical flux of HPMTF was also assessed under clear sky conditions using data from the ATom campaign. ATom was not designed for flux analysis and the number of stable level legs within the PBL were limited. Additionally, flight legs at multiple altitudes within the PBL were only performed twice each during ATom 3 and 4, limiting the opportunity for vertical flux divergence analysis. We therefore selected flight legs conducted on May 1st, 2018 during ATom 4 as a case study for HPMTF vertical flux under clear sky conditions. The May 1st flight legs were selected due to the very high observed HPMTF mixing ratios in the PBL (>70 pptv), which were among the highest observed values across ATom 3-4. A spatial map of the May 1st flight region and a timeseries of HPMTF, SO_2, and altitude are shown in **Figure 3.8**.

HPMTF EC flux was calculated for four sequential flux legs (L1-L4) at altitudes of 180, 390, 570, and 170 m respectively. Mean HPMTF mixing ratios for all legs were from 60 – 80 pptv. The observed vertical profile of HPMTF mixing ratio and v_{ex} is shown in **Figure 3.9**. Observed v_{ex} for all legs was from 0.44 to 0.84 cm s^{-1}, with an observed positive vertical flux divergence. For the sequential stacked flux legs (L1-L3), v_{ex} at altitudes 180, 390, and 570 m were 0.50, 0.67, and 0.84 cm s^{-1} respectively. Linear fitting of the observed vertical flux profile and interpolation to the top of the PBL allows for a calculation of w_e which was found to be 1.5 cm s^{-1}. While this is a factor of two higher than observations of w_e in stratocumulus clouds (0.12-0.7 cm s^{-1}) derived from DMS profiles, it still shows clear divergence from the derived w_e in the cloud capped MBL of 16.2 cm

s^{-1}. HPMTF is likely non well suited as a conserved tracer for determining w_e compared to DMS, as HPMTF is expected to have faster loss to oxidation by OH and potential experiences irreversible heterogenous uptake. The rate constants for HPMTF production from DMS oxidation also decrease with temperature, creating an additional term in the vertical profile that must be resolved.

3.3.4 Ground site deposition flux

HPMTF mixing ratios observed at the ground based Scripps pier coastal ocean site were found to be from 0 to 20 pptv, with a clear diel profile peaking in early afternoon and rapid falloff in the evening as shown in **Figure 3.10a**. HPTMF flux showed a consistent deposition flux to the ocean (negative v_{ex}). Mean HPMTF v_{ex} was -0.78 ± 0.37 cm s^{-1} with magnitude increasing with wind-speed as expected deposition of a species where deposition is controlled by air-side resistance (as shown in **Figure 3.10b**).[33,34] These observations of deposition to the surface ocean are consistent with expectations of a highly soluble molecule that has irreversible uptake to water surfaces. Preliminary box model studies of HPMTF production and loss rates suggest that the observed rapid fall off in HPMTF mixing ratios in the late afternoon is faster than can be explained by dry deposition and oxidation by OH using available literature determinations of the bimolecular rate constant.[35] This suggests the presence of additional fast loss processes for HPMTF including heterogeneous and cloud processing. Marine stratocumulus clouds from early evening through late morning were a persistent feature at this sampling site. The development of late afternoon stratocumulus clouds was observed for all days of this study as confirmed by MODIS remote sensing imagery. An assessment of the consistency of the observed diel profile of HPMTF with rapid cloud uptake is in progress.

3.3.5 Vertical concentration profiles as indicators of cloud processing

Analysis of vertical concentration profiles in cloudy and clear sky allows for qualitative assessment of cloud processing for species where the EC analysis was not inconclusive or not statistically significant. The vertical profiles of HPMTF and H_2O_2 mixing ratios from the SARP Marine observations show depletion starting at approximately 360 m through to the PBL height of 560 m as shown in **Figure 3.11**. These observations are indicative of rapid loss within the cloud layer for those molecules. Notably, HPMTF in the cloud layer is completely depleted (<2 pptv), while H_2O_2 in cloud is from 300 – 500 pptv. This indicates that HPMTF cloud uptake is irreversible, while H_2O_2 shows equilibration and re-evaporation from cloud droplets. O_3, CO, and DMS vertical concentration profiles are constant across the cloud free and cloudy fractions of the PBL, consistent with expectations for low solubility molecules. HNO_3, H_2O_2, and O_3 mixing ratios are enhanced in the FT immediately above the cloud layer. This enhancement may be driven by several factors including, increased photochemistry immediately above the cloud layer from reflection of solar radiation, presence of a stable stratified layer of urban influenced air above the cloud height, or evaporation of cloud droplets at the cloud top releasing photochemical precursors. It is not clear what mechanism is responsible for the observed enhancement in mixing ratios. This enhancement of HNO_3, H_2O_2, and O_3 mixing ratios in the FT troposphere relative to the PBL is expected to drive an entrainment flux of these molecules into the PBL which would complicate EC flux observations of those species within the PBL. Mixing ratios of both DMS and HPMTF are low above the cloud top in the FT, consistent with expectations for molecules controlled by a sea-surface emission source.

Observed vertical concentration profiles under clear sky conditions from the ATom-4 May 1st flight legs show distinct behavior from the cloudy PBL case as shown in **Figure 3.12**. Both

HPMTF and H_2O_2 mixing ratios follow a roughly linear profile across the boundary layer top at approximately 700 m. HPMTF mixing ratios decrease with altitude up to 2000 m, which is consistent with expectations for production in the PBL from ocean DMS emissions and loss aloft to reactions with OH and heterogeneous uptake.

3.4 Discussion

3.4.1 Assessing HPMTF lifetime to cloud processing

Linear interpolation of the observed flux divergence profile during the SARP Marine flight allows for assessment of the net effective PBL cloud entrainment velocity (v_c) and cloud uptake lifetimes of HPMTF. Taking the cloud base height of 360 m based on observed change points of HPMTF and H_2O_2 concentration profiles as shown in **Figure 3.9**. Extrapolating the observed flux profile to cloud base gives a calculated v_c of 10.3 cm s^{-1}. We take this determination of cloud base v_c to be the overall velocity of turbulent transfer into the cloud layer. It is this rate which fundamentally sets the total loss rate to cloud uptake in the PBL. It is not clear what functional shape the flux divergence profile should take within the cloud layer. Observations of w_e of entrainment from the FT into the PBL have been measured to be from 0.12 to 0.7 cm s^{-1} for marine stratocumulus clouds. For HPMTF, which is completely depleted in the FT, this entrainment would also contribute a positive flux term for HPMTF aloft. However, based on the magnitude of v_c vs w_e, we elect to treat the influence of w_e as negligible on the observed flux divergence profile for this analysis and use a linear interpolation.

Following the same linear interpolation approach, we calculate the effective cloud entrainment velocity ($v_{c,eff}$) at the mid height of the cloud-free PBL (180 m) to be 4.8 cm s^{-1}. This value is taken as the mean cloud entrainment flux experienced by the cloud free fraction of the PBL which is subject to cloud uptake and processing. Dividing the height of the cloud free fraction of the

boundary layer (360 m) by $v_{c,eff}$ then yields an estimate of the overall lifetime of HPMTF to cloud loss in the PBL (τ_{cloud}). τ_{cloud} was calculated to be 2.1 hrs by this approach. This approach assumes that loss inside the cloud is fast and so only the mixing time into the cloud base is significant. This also implies that v_{ex} measured in the middle of the cloud layer would be 0 as all HPMTF consumption has already occurred near the cloud base. The lifetime of HPMTF to dry deposition to the surface ocean is *ca*. 1.1 days based on observed deposition rates at Scripps Pier, and lifetime to oxidation by OH is *ca.* 9.3 hrs taking [OH] = 1×10^6 molecules cm^{-3} and the bimolecular rate constant $k_{OH} = 3 \times 10^{-11}$ cm^3 $molecule^{-1}$ s^{-1} recently determined in laboratory studies. Uptake of HPMTF to aerosols has not yet been quantified, but based on relative surface area we expect loss rates to clouds will be dominant.[7]

The observed lifetime of HPMTF to cloud uptake (2.1 hrs) is short compared to deposition and oxidation suggests that cloud loss is the dominant HPMTF loss process in the cloud capped PBL. HPMTF lost to clouds is a terminal sink of sulfur that will not contribute to aerosol formation or growth, which will act to dampen the link between DMS emissions and aerosol growth and CCN concentrations. Chemical box modelling constrained by the ATom observations suggested that up to 40% of emitted DMS goes on to form HPMTF.[5] Therefore, in the cloudy PBL, up to 40% of total emitted sulfur may be lost to cloud droplets before contributing to aerosol growth. This represents a major fraction of the marine sulfur budget which is not accounted for in any current GCM.

3.4.2 HPMTF as a unique tracer for determining cloud loss rates

These observations suggest that HPMTF is uniquely suited as an ambient tracer of cloud uptake given that: 1) it shows irreversible uptake to cloud droplets, simplifying treatment of the flux divergence profile. 2) It is continually produced in the marine PBL during daytime, sustaining

observable mixing ratios in the PBL despite rapid loss rates in clouds. NO_x is the remote MBL is low <50 ppt and cannot sustain HNO_3 production. HNO_3 once produced will be irreversibly lost to cloud droplets, resulting in HNO_3 being depleted in the cloudy PBL and not suitable as a EC tracer of cloud uptake. SO_2, H_2O_2 and other moderately soluble species do not have irreversible uptake to cloud droplets and will instead show equilibration between the liquid and gas phase. 3) HPMTF is ubiquitous in the marine PBL, which is where PBL cloud coverage is most often present globally.[5,11]

We propose that future airborne EC flux studies of cloud processing might incorporate the following experiment design and data products which will provide robust constraints for cloud processing rates in CTMs. 1.) Flight paths within the PBL at multiple altitudes including as near to the surface and cloud base as possible flown at long legs (>5 minute), level altitude, and stable aircraft pitch to enable high quality EC flux observations. 2.) Measurements of DMS and HPMTF vertical flux at multiple measurement altitudes in the turbulent marine PBL under both cloudy and clear sky conditions. DMS vertical flux divergence will be used to directly determine w_e following the approach of Faloona et al. (2005).[18] HPMTF vertical flux divergence under cloudy conditions will be used to directly assess cloud uptake flux, and to infer cloud residence times and HPMTF lifetime to cloud uptake as described in this work. HPTMF vertical flux divergence in clear sky conditions will be used to independently determine w_e. Consistency of w_e determined from the HPMTF and DMS under clear sky conditions will be used to validate that there are no other processes contributing to the observed vertical flux profile of HPMTF that would otherwise be assigned to cloud processing. 3.) Vertical flux divergence profiles of any other species of interest with reversible cloud uptake (*i.e.* H_2O_2 and SO_2) that will be compared to observed HPMTF cloud uptake rates and the observed w_e to determine speciated *effective* cloud uptake rates. We

hypothesize this method will allow determination of cloud uptake rates for any species provided it shows statistically significant EC flux and that the coincident HPMTF and DMS flux observations were successful. 4.) Observations of vertical concentration profiles within and above the PBL with spatiotemporal sampling point as close as possible to the EC flux flight legs. 5.) Inclusion of a zenith facing camera or preferably high spectral resolution lidar instruments on the aircraft payload to allow direct quantification of cloud cover, droplet vertical profiles, and cloud droplet size distributions in time when flying below cloud in the PBL.

3.5 Conclusions

We present airborne observations of HPMTF vertical flux profiles as a unique direct tracer of cloud entrainment velocity and the integrated boundary layer lifetime to cloud uptake. V_{ex} of HPMTF aloft in the cloudy PBL was measured to be *ca* 5 cm s^{-1} which is faster than can be explained by known entrainment rates of air from the FT into the PBL (w_e from 0.12 to 0.7 cm s^{-1}). HPMTF v_{ex} in the cloud free PBL were measured to be <1 cm s^{-1}, consistent with deposition of HPMTF at the ocean surface and entrainment flux from the FT aloft. Cloud entrainment velocity at the cloud base height was calculated to be 10.3 cm s^{-1} representing the rate of turbulent mixing from the cloud free fraction of the PBL into the cloud layer. Mean HPMTF lifetime to cloud loss was determined to be 2.1 hrs, representing the major loss process of HPMTF in the cloudy marine PBL. Up to 40% of emitted DMS goes on to form HPMTF, which is terminally lost to clouds and does not contribute to aerosol formation or growth. Due to the extensive global coverage of stratocumulus clouds in marine regions, this is likely a significant global sink for reactive sulfur which is not accounted for in any current CTM. We propose this method of assessing cloud loss rates to be widely applicable in airborne flux studies which will provide a necessary constraint on cloud loss rates for many other soluble species such as isoprene oxidation products in CTMs.

Acknowledgments

This work utilizes publicly available data collected during the NASA Atmospheric Tomography (ATom) and Student Airborne Research Project (SARP) projects. We thank all researchers involved in those projects for use of their data. Specifically, we thank Patrick Veres, and Andy Neuman for facilitating access to their observations of HPMTF which are the central component of this work. We thank Glenn Wolfe for providing guidance on airborne flux analysis and for making a Matlab based wavelet EC flux toolbox publicly available which was used for the airborne flux analysis in this work. We also thank Ian Faloona for valuable discussions on cloud processing and entrainment rates. Finally, we thank Chris Jernigan for discussion of HPMTF production and solubility.

References

(1) Van Doren, J. M.; Watson, L. R.; Davidovits, P.; Worsnop, D. R.; Zahniser, M. S.; Kolb, C. E. Temperature Dependence of the Uptake Coefficients of Nitric Acid, Hydrochloric Acid and Nitrogen Oxide (N2O5) by Water Droplets. *J. Phys. Chem.* **1990**, *94* (8), 3265–3269. https://doi.org/10.1021/j100371a009.

(2) Liu, T.; Clegg, S. L.; Abbatt, J. P. D. Fast Oxidation of Sulfur Dioxide by Hydrogen Peroxide in Deliquesced Aerosol Particles. *Proc. Natl. Acad. Sci.* **2020**, 201916401. https://doi.org/10.1073/pnas.1916401117.

(3) Platt, U.; Perner, D.; Schroder, J.; Kessler, C.; Toennissen, A. The Diurnal Variation of NO3. *J. Geophys. Res.* **1981**, *86* (C12), 11965–11970. https://doi.org/10.1029/JC086iC12p11965.

(4) Brown, S. S.; Dubé, W. P.; Tham, Y. J.; Zha, Q.; Xue, L.; Poon, S.; Wang, Z.; Blake, D. R.; Tsui, W.; Parrish, D. D.; et al. Nighttime Chemistry at a High Altitude Site above Hong Kong. *J. Geophys. Res.* **2016**, *121* (5), 2457–2475. https://doi.org/10.1002/2015JD024566.

(5) Veres, P. R.; Neuman, J. A.; Bertram, T. H.; Assaf, E.; Wolfe, G. M.; Williamson, C. J.; Weinzierl, B.; Tilmes, S.; Thompson, C. R.; Thames, A. B.; et al. Global Airborne Sampling Reveals a Previously Unobserved Dimethyl Sulfide Oxidation Mechanism in the Marine Atmosphere. *Proc. Natl. Acad. Sci.* **2020**, 201919344. https://doi.org/10.1073/pnas.1919344117.

(6) Levine, S. Z.; Schwartz, S. E. In-Cloud and below-Cloud Scavenging of Nitric Acid Vapor. *Atmos. Environ.* **1982**, *16* (7), 1725–1734. https://doi.org/10.1016/0004-6981(82)90266-9.

(7) Holmes, C. D.; Bertram, T. H.; Confer, K. L.; Graham, K. A.; Ronan, A. C.; Wirks, C. K.; Shah, V. The Role of Clouds in the Tropospheric NO x Cycle: A New Modeling Approach for Cloud Chemistry and Its Global Implications. *Geophys. Res. Lett.* **2019**, 4980–4990. https://doi.org/10.1029/2019GL081990.

(8) Worsnop, D. R.; Zahniser, M. S.; Kolb, C. E.; Gardner, J. A.; Watson, L. R.; Van Doren, J. M.; Jayne, J. T.; Davidovits, P. The Temperature Dependence of Mass Accommodation of Sulfur Dioxide and Hydrogen Peroxide on Aqueous Surfaces. *J. Phys. Chem.* **1989**, *93* (3), 1159–1172. https://doi.org/10.1021/j100340a027.

(9) Feingold, G.; Kreidenweis, S. M.; Zhang, Y. Stratocumulus Processing of Gases and Cloud. *J. Geophys. Res.* **1998**, *103* (D16), 19527–19542.

(10) Holmes, C. D.; Bertram, T. H.; Confer, K. L.; Graham, K. A.; Ronan, A. C.; Wirks, C. K.; Shah, V. The Role of Clouds in the Tropospheric NO x Cycle : A New Modeling Approach for Cloud Chemistry and Its Global Implications. **2019**, 1–11. https://doi.org/10.1029/2019GL081990.

(11) Wood, R. Stratocumulus Clouds. *Mon. Weather Rev.* **2012**, *140* (8), 2373–2423. https://doi.org/10.1175/MWR-D-11-00121.1.

(12) Scott, S. G.; Bui, T. P.; Chan, K. R.; Bowen, S. W. The Meteorological Measurement System on the NASA ER-2 Aircraft. *J. Atmos. Ocean. Technol.* **1990**, *7* (4), 525–540. https://doi.org/10.1175/1520-0426(1990)007<0525:tmmsot>2.0.co;2.

(13) Lenschow, D. H.; Pearson, R.; Stankov, B. B. Estimating the Ozone Budget in the Boundary Layer by Use of Aircraft Measurements of Ozone Eddy Flux and Mean Concentration. *J. Geophys. Res.* **1981**, *86* (C8), 7291. https://doi.org/10.1029/JC086iC08p07291.

(14) Faloona, I.; Conley, S. A.; Blomquist, B.; Clarke, A. D.; Kapustin, V.; Howell, S.; Lenschow, D. H.; Bandy, A. R. Sulfur Dioxide in the Tropical Marine Boundary Layer: Dry Deposition and Heterogeneous Oxidation Observed during the Pacific Atmospheric Sulfur Experiment. *J. Atmos. Chem.* **2009**, *63* (1), 13–32. https://doi.org/10.1007/s10874-010-9155-0.

(15) Wolfe, G. M.; Hanisco, T. F.; Arkinson, H. L.; Bui, T. P.; Crounse, J. D.; Dean-Day, J.; Goldstein, A.; Guenther, A.; Hall, S. R.; Huey, G.; et al. Quantifying Sources and Sinks of Reactive Gases in the Lower Atmosphere Using Airborne Flux Observations. *Geophys. Res. Lett.* **2015**. https://doi.org/10.1002/2015GL065839.

(16) Wolfe, G. M.; Kawa, S. R.; Hanisco, T. F.; Hannun, R. A.; Newman, P. A.; Swanson, A.; Bailey, S.; Barrick, J.; Thornhill, K. L.; Diskin, G.; et al. The NASA Carbon Airborne Flux Experiment (CARAFE): Instrumentation and Methodology. **2018**, 1757–1776.

(17) Karl, T.; Apell, E.; Hodzic, A.; Riemer, D. D.; Blake, D. R.; Wiedinmyer, C. Emissions of Volatile Organic Compounds Inferred from Airborne Flux Measurements over a Megacity. *Atmos. Chem. Phys.* **2009**, *9* (1), 271–285. https://doi.org/10.5194/acp-9-271-2009.

(18) Faloona, I.; Lenschow, D. H.; Campos, T.; Stevens, B.; van Zanten, M.; Blomquist, B.; Thornton, D.; Bandy, A.; Gerber, H. Observations of Entrainment in Eastern Pacific Marine

Stratocumulus Using Three Conserved Scalars. *J. Atmos. Sci.* **2005**, *62* (9), 3268–3285. https://doi.org/10.1175/JAS3541.1.

(19) Mauder, M.; Cuntz, M.; Drüe, C.; Graf, A.; Rebmann, C.; Schmid, H. P.; Schmidt, M.; Steinbrecher, R. A Strategy for Quality and Uncertainty Assessment of Long-Term Eddy-Covariance Measurements. *Agric. For. Meteorol.* **2013**, *169*, 122–135. https://doi.org/10.1016/j.agrformet.2012.09.006.

(20) Torrence, C.; Compo, G. P. A Practical Guide to Wavelet Analysis. *Bull. Am. Meteorol. Soc.* **1998**, *79* (1), 61–78. https://doi.org/10.1175/1520-0477(1998)079<0061:APGTWA>2.0.CO;2.

(21) MacKay, D. J. C. Bayesian Interpolation. *Neural Comput.* **1992**, *4* (3), 415–447. https://doi.org/10.1162/neco.1992.4.3.415.

(22) Lenschow, D. H.; Mann, J.; Kristensen, L. How Long Is Long Enough When Measuring Fluxes and Other Turbulence Statistics? *Journal of Atmospheric and Oceanic Technology*. 1994, pp 661–673. https://doi.org/10.1175/1520-0426(1994)011<0661:HLILEW>2.0.CO;2.

(23) Finkelstein, P. L.; Sims, P. F. Sampling Error in Eddy Correlation Flux Measurements. *J. Geophys. Res. Atmos.* **2001**. https://doi.org/10.1029/2000JD900731.

(24) Wofsy, S. C.; Afshar, S.; Allen, H. M.; Apel, E.; Asher, E. C.; Barletta, B.; Bent, J.; Bian, H.; Biggs, B. C.; Blake, D. R.; et al. Merged Data from the Atmospheric Tomography Mission. ORNL DAAC, Oak Ridge, Tennessee, USA 2018. https://doi.org/https://doi.org/10.3334/ORNLDAAC/1581.

(25) Wofsy, S. C.; Afshar, S.; Allen, H. M.; Apel, E. C.; Asher, E. C.; Barletta, B.; Bent, J.; Bian, H.; Biggs, B. C.; Blake, D. R.; et al. ATom: Merged Atmospheric Chemistry, Trace Gases, and Aerosols. ORNL DAAC, Oak Ridge, Tennessee, USA 2018. https://doi.org/https://doi.org/10.3334/ORNLDAAC/1581.

(26) Crounse, J. D.; McKinney, K. A.; Kwan, A. J.; Wennberg, P. O. Measurement of Gas-Phase Hydroperoxides by Chemical Ionization Mass Spectrometry. *Anal. Chem.* **2006**, *78* (19), 6726–6732. https://doi.org/10.1021/ac0604235.

(27) Apel, E. C.; Hills, A. J.; Lueb, R.; Zindel, S.; Eisele, S.; Riemer, D. D. A Fast-GC-MS System to Measure C2 to C4 Carbonyls and Methanol Aboard Aircraft. *J. Geophys. Res. D Atmos.* **2003**, *108* (20). https://doi.org/10.1029/2002jd003199.

(28) Rollins, A. W.; Thornberry, T. D.; Ciciora, S. J.; McLaughlin, R. J.; Watts, L. A.; Hanisco, T. F.; Baumann, E.; Giorgetta, F. R.; Bui, T. V.; Fahey, D. W. A Laser-Induced Fluorescence Instrument for Aircraft Measurements of Sulfur Dioxide in the Upper Troposphere and Lower Stratosphere. *Atmos. Meas. Tech.* **2016**, *9* (9), 4601–4613.

https://doi.org/10.5194/amt-9-4601-2016.

(29) Yuan, B.; Koss, A.; Warneke, C.; Gilman, J. B.; Lerner, B. M.; Stark, H.; De Gouw, J. A. A High-Resolution Time-of-Flight Chemical Ionization Mass Spectrometer Utilizing Hydronium Ions (H3O+ ToF-CIMS) for Measurements of Volatile Organic Compounds in the Atmosphere. *Atmos. Meas. Tech.* **2016**, *9* (6), 2735–2752. https://doi.org/10.5194/amt-9-2735-2016.

(30) Ryerson, T. B.; Williams, E. J.; Fehsenfeld, F. C. An Efficient Photolysis System for Fast-Response NO2 Measurements. *J. Geophys. Res. Atmos.* **2000**, *105* (D21), 26447–26461. https://doi.org/10.1029/2000JD900389.

(31) Novak, G.; Vermeuel, M.; Bertram, T. Simultaneous Detection of Ozone and Nitrogen Dioxide by Oxygen Anion Chemical Ionization Mass Spectrometry: A Fast Time Response Sensor Suitable for Eddy Covariance Measurements. *Atmos. Meas. Tech. Discuss.* **2019**. https://doi.org/10.5194/amt-2019-445.

(32) Wolfe, G. M.; Hanisco, T. F.; Arkinson, H. L.; Bui, T. P.; Crounse, J. D.; Dean-Day, J.; Goldstein, A.; Guenther, A.; Hall, S. R.; Huey, G.; et al. Quantifying Sources and Sinks of Reactive Gases in the Lower Atmosphere Using Airborne Flux Observations. *Geophys. Res. Lett.* **2015**, *42* (19), 8231–8240. https://doi.org/10.1002/2015gl065839.

(33) Johnson, M. T. A Numerical Scheme to Calculate Temperature and Salinity Dependent Air-Water Transfer Velocities for Any Gas. *Ocean Sci.* **2010**, *6* (4), 913–932. https://doi.org/10.5194/os-6-913-2010.

(34) Liss, P. S.; Slater, P. G. Flux of Gases across the Air-Sea Interface. *Nature* **1974**, *247* (5438), 181–184. https://doi.org/10.1038/247181a0.

(35) Wu, R.; Wang, S.; Wang, L. New Mechanism for the Atmospheric Oxidation of Dimethyl Sulfide. The Importance of Intramolecular Hydrogen Shift in a CH3SCH2OO Radical. *J. Phys. Chem. A* **2015**, *119* (1), 112–117. https://doi.org/10.1021/jp511616j.

Figures

Measurement	Method	Sensitivity/precision/LOD	Reference
HPMTF	Iodide CIMS	Precision: 0.1 ppt LOD: <1ppt Uncertainty: 55% + 0.06 ppt	Veres et al. (2020)[5]
HNO_3	CF_3O^- CIMS	Uncertainty (1σ): ± 30% + 50ppt	Crounse et al. (2006)[26]
DMS	GC-MS	Uncertainty (1σ): ± 30%	Apel et al. (2002)[27]
SO_2	Laser induced fluorescence (LIF)	Uncertainty (1σ): ± 9% + 2ppt	Rollins et al. (2016)[28]
3-D Winds	MMS	Uncertainty (1σ): ±1 m s^{-1}	Scott et al. (1990)[12]

Table 3.1. NASA ATom instrumentation

Measurement	Method	Sensitivity/precision/LOD	Reference
HPMTF	Iodide CIMS	Precision: 0.1 ppt LOD: <1ppt Uncertainty (1σ): 55% + 0.06 ppt	Veres et al. (2020)[5]
HNO_3, HNO_3	CF_3O^- CIMS	Uncertainty (1σ): ± 30% + 50ppt	Crounse et al. (2006)
DMS	Proton-transfer-reaction mass spectrometer	LOD: *ca* 50 ppt	Yuan et al. (2016)[29]
SO_2	Laser induced fluorescence (LIF)	Uncertainty (1σ): ± 9% + 2ppt	Rollins et al. (2016)[28]
O_3, NO, NO_2	Chemiluminescence	Uncertainty (2σ): 1 ppbv (O_3), 50 pptv (NO, NO_2)	Ryerson et al. (2000)[30]
H_2O	Digital Laser Hygrometer	Uncertainty (1σ): ± 5%	Diskin (2002)
3-D Winds	MMS	Uncertainty (1σ): ±1 m s^{-1}	Scott et al. (1990)

Table 3.2. NASA SARP instrumentation

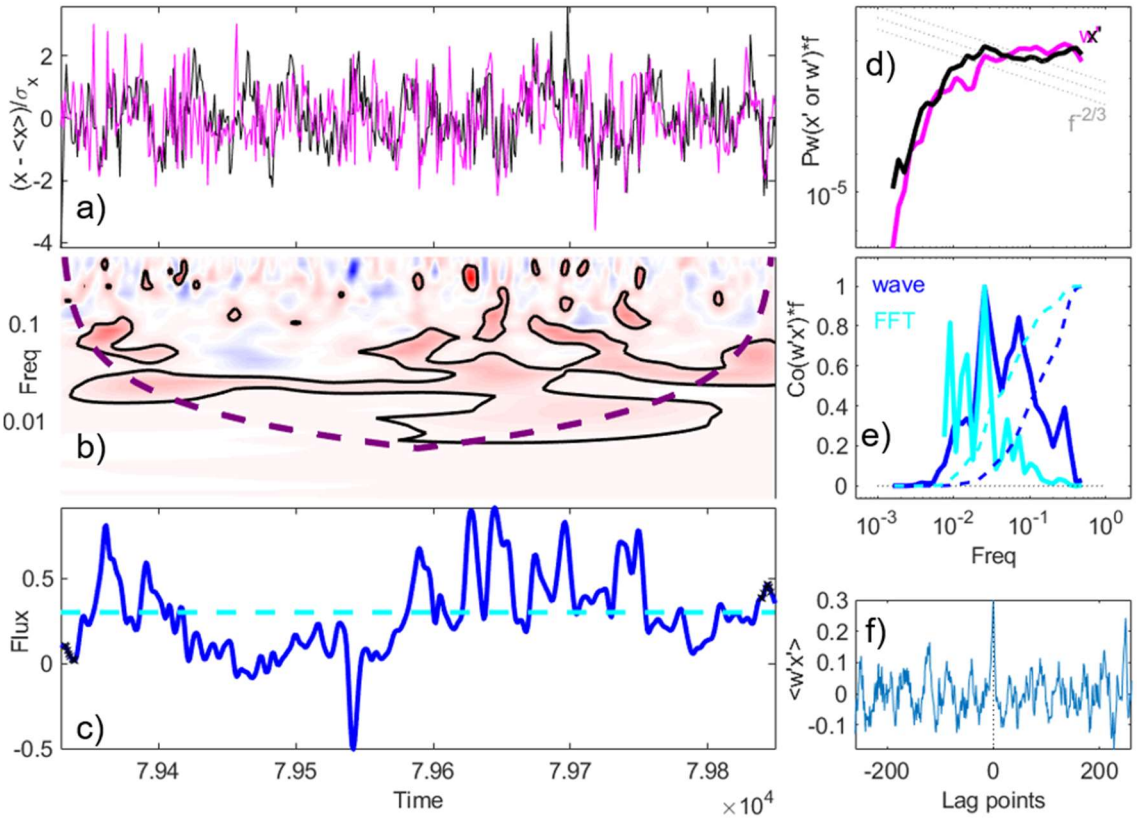

Figure 3.1. Wavelet flux calculation of HPMTF from a flight leg at 170 m altitude in a stratocumulus capped marine boundary layer on the SARP 2019 flight. (a) Normalized 10 Hz time series of vertical wind speed (w, magenta) and HPMTF (gray) fluctuations. (b) Local wavelet cospectrum. Red areas denote positive power, blue areas negative. Power is bias-corrected (multiplied by scale) as suggested by Liu et al. (2007). The dashed line indicates the cone of influence (COI). (c) Scale-integrated wavelet flux (blue solid line) and ensemble-average flux (cyan dashed line). (d) wavelet power spectra of vertical wind speed (w, magenta) and HPMTF (gray) fluctuations. (e) normalized frequency weighted cospectra (solid lines) and ogives (dashed lines) for HPMTF. Dark blue traces indicated wavelet calculations and cyan traces indicated fast-fourier transform (FFT) based flux calculations. (f) HPMTF flux cross-covariance showing flux noise at long lag times, and clear authentic flux peak at a lag time of 0 points.

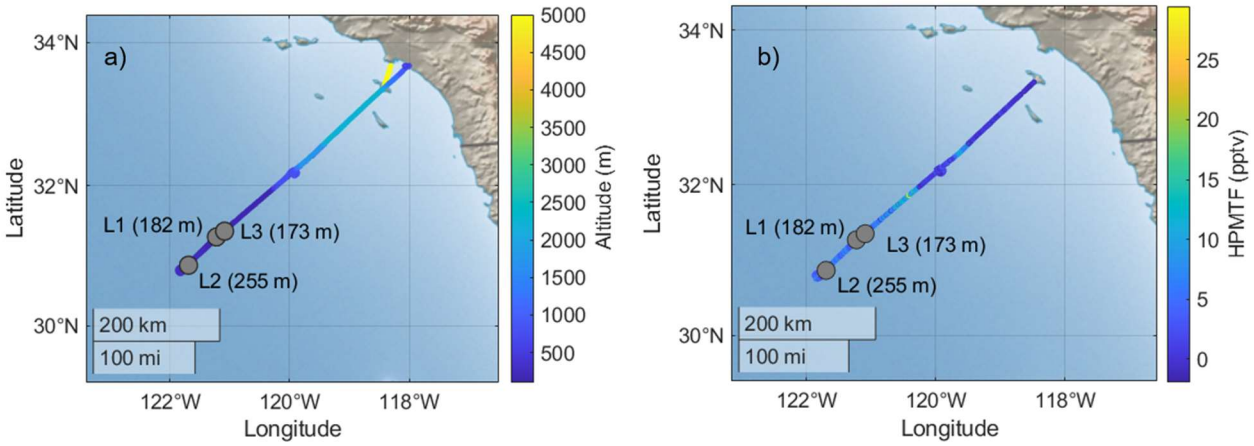

Figure 3.2. Flight path of SARP Marine legs showing profiles of (a) Altitude, and (b) HPMTF. Locations and altitudes of midpoints of EC flux legs are indicated by the labelled larger grey dots.

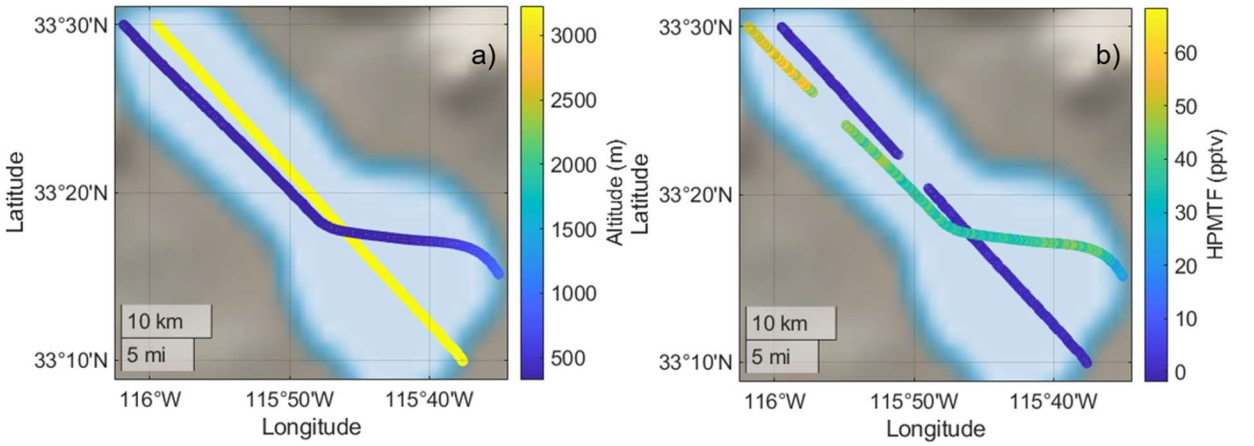

Figure 3.3. Flight path of SARP Salton Sea showing profiles of (a) Altitude, and (b) HPMTF mixing ratios.

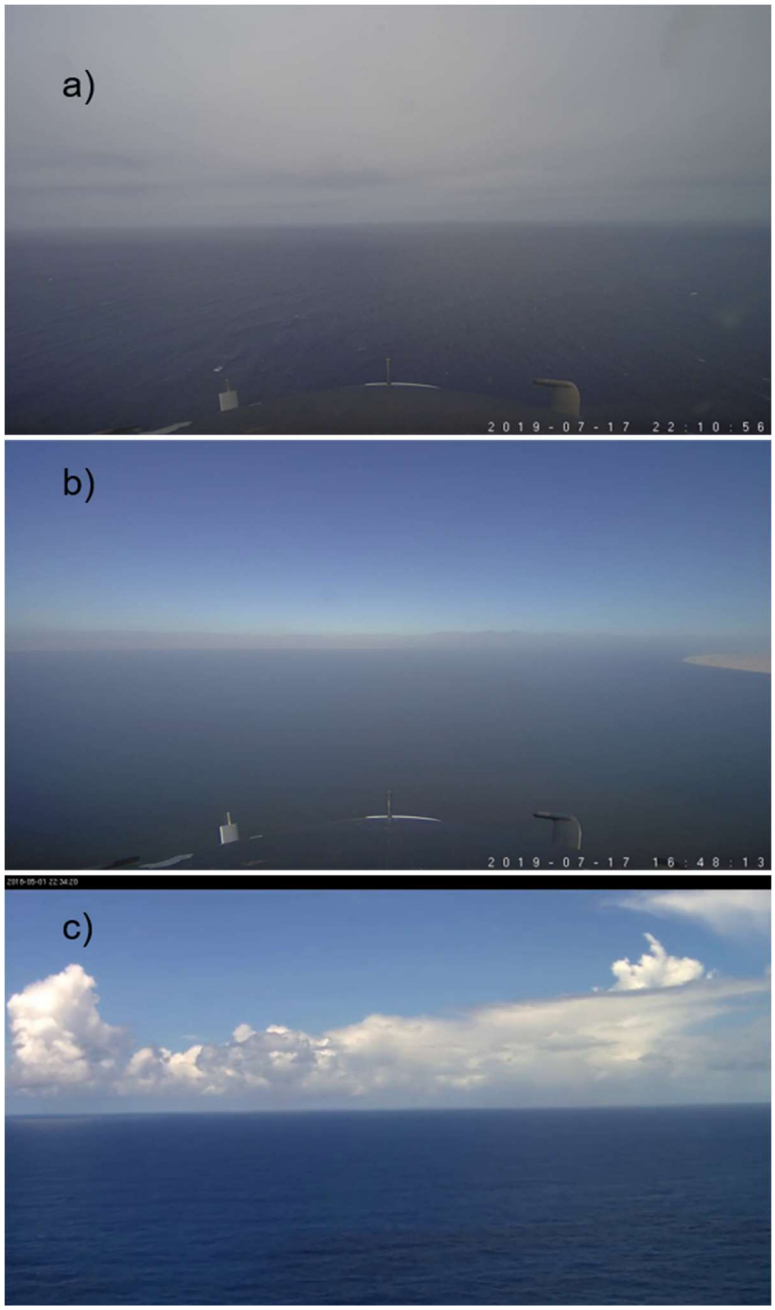

Figure 3.4. Front-facing camera images on the DC-8 showing cloud cover during (a) SARP Marine, (b) SARP Salton Sea, and (c) ATom 4 May 1st flight legs in the PBL.

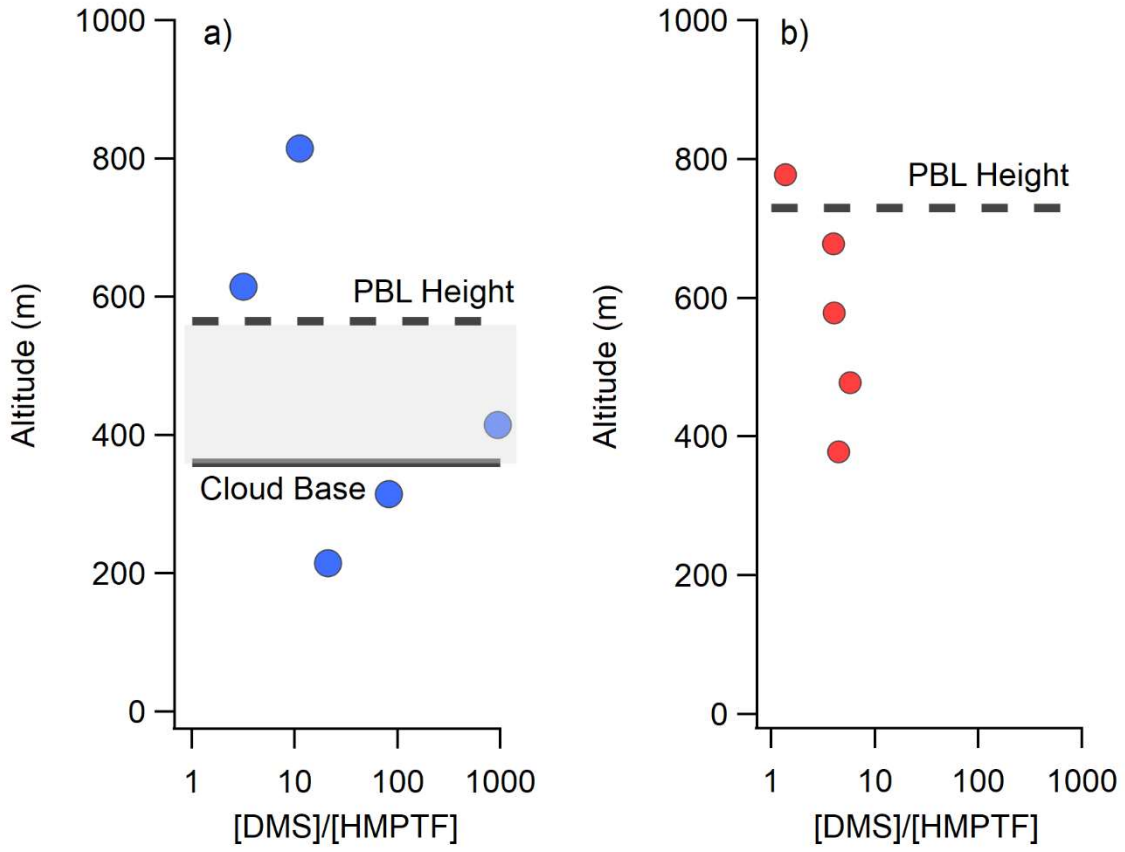

Figure 3.5. Observed [DMS]/[HPMTF] ratios as a function of altitude from (a) SARP Marine, (b) SARP Salton flights.

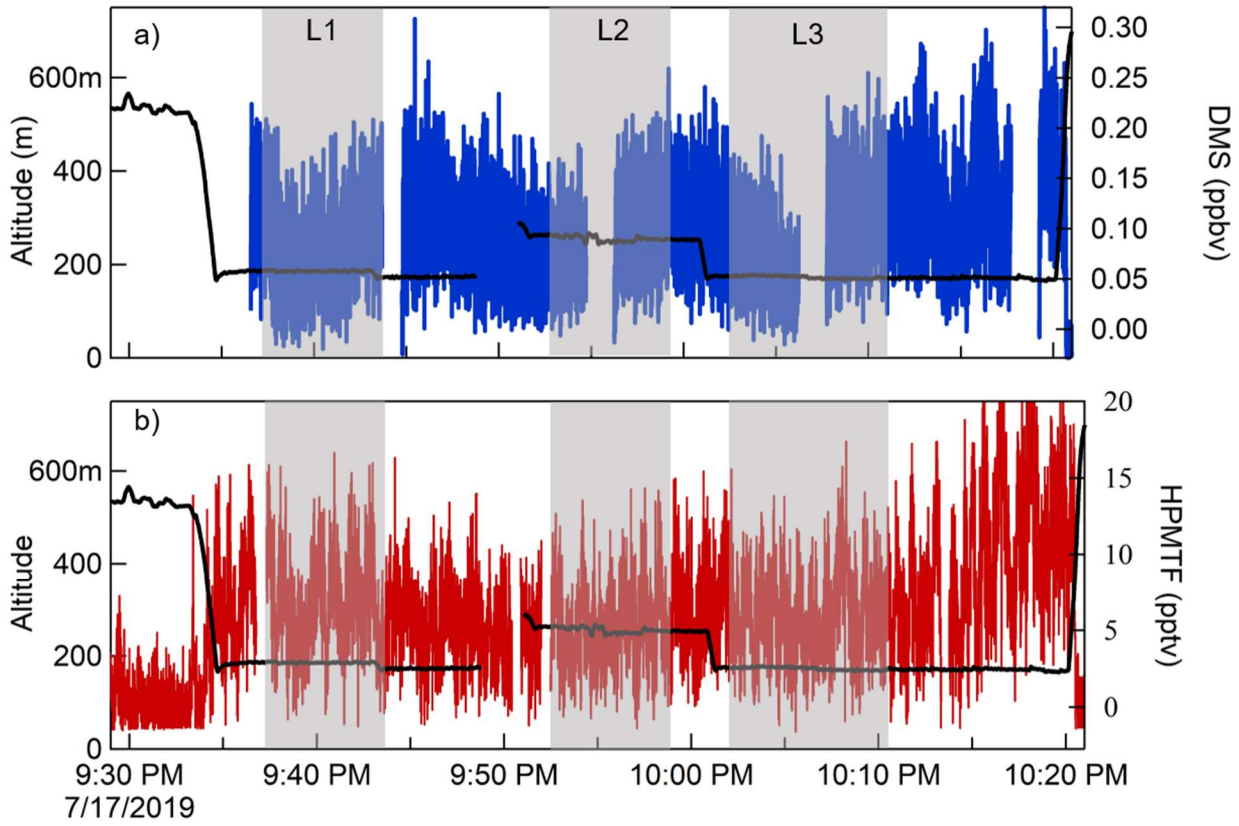

Figure 3.6. Timeseries of observed (a) DMS and (b) HPMTF at 1 Hz time resolution during the SARP Marine flights in a stratocumulus cloud capped marine PBL. Flight legs used in EC flux analysis are shown in grey shaded regions labelled L1, L2, and L3.

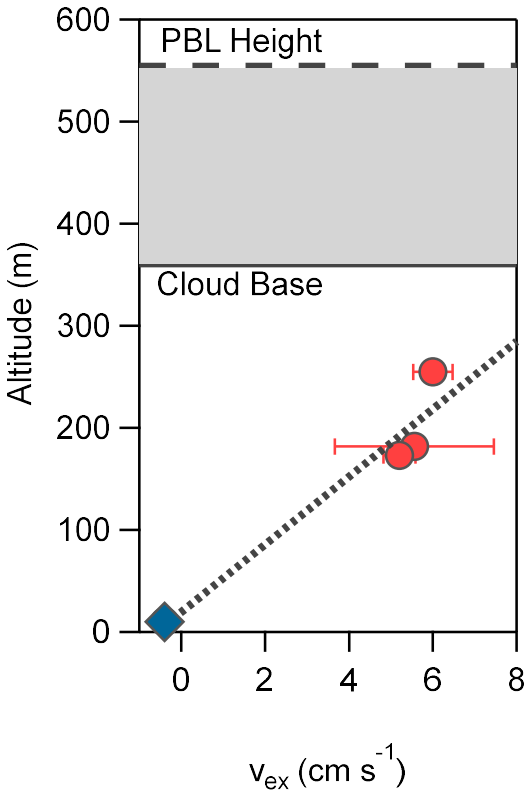

Figure 3.7. HPMTF flux divergence vertical profile observed during the SARP Marine flight. HPMTF deposition velocity measured from a coastal ocean site at height 10 m is also shown (blue diamond). The flux divergence profile from the airborne and ground-based measurements were fit to a linear-least squares regression plotted as the grey dotted line.

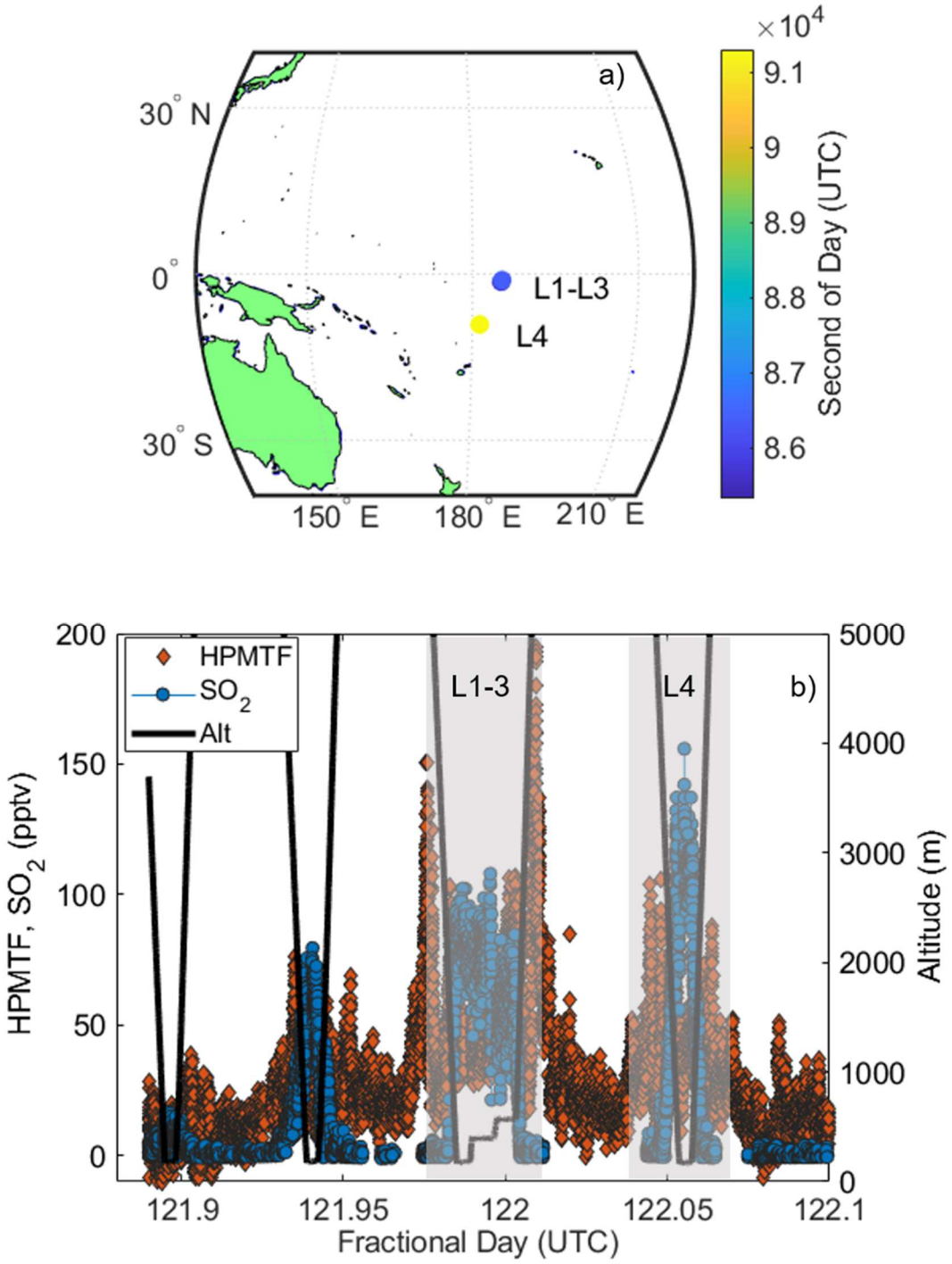

Figure 3.8. (a) Spatial map of selected EC flux legs from ATom 4 May 1st, 2018 observations. (b) Timeseries of altitude, HPMTF, and SO_2 over flight period. Flux legs are indicated by grey shaded regions and labelled L1-L4. Legs L1-L3 were a series of sequential stacked legs at altitudes 180, 390 and 570 m respectively.

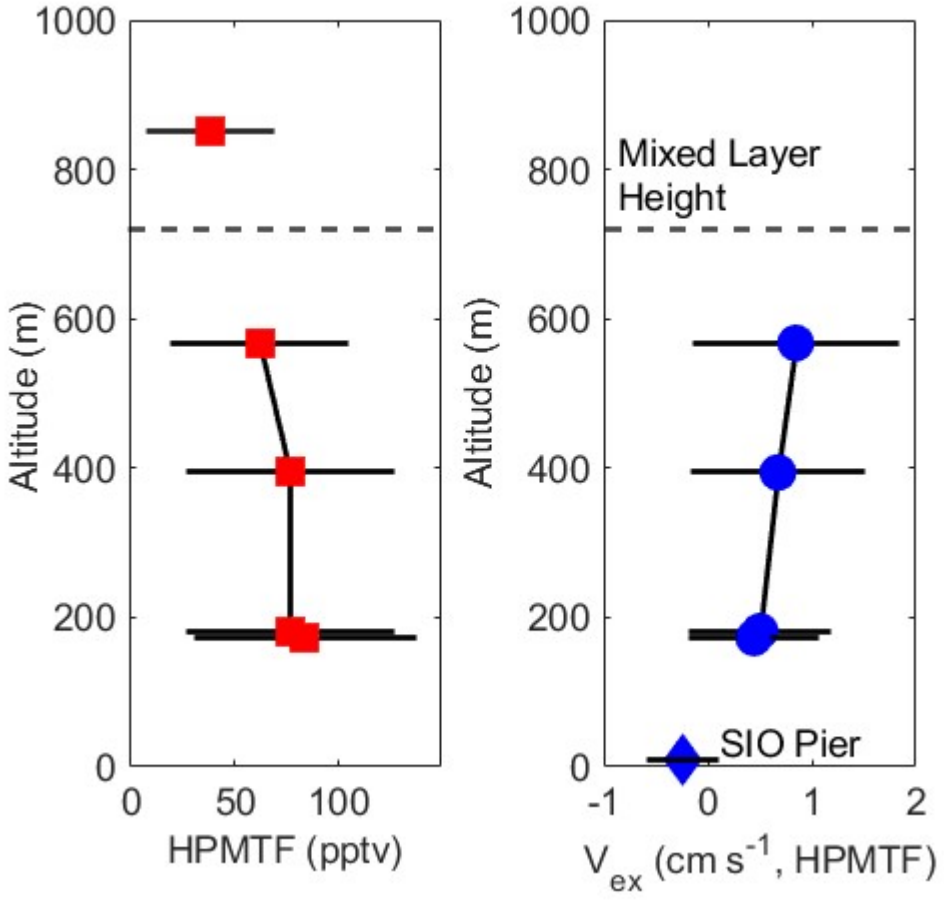

Figure 3.9. Vertical profiles of (a) HPMTF mixing ratio and (b) HPMTF exchange velocity (v_{ex}) measured on the ATom 4 May 1st, 2018 flux sampling legs. Also plotted on panel (b) is the observed mean v_{ex} of -0.4 cm s^{-1} from a coastal ocean site (SIO Pier).

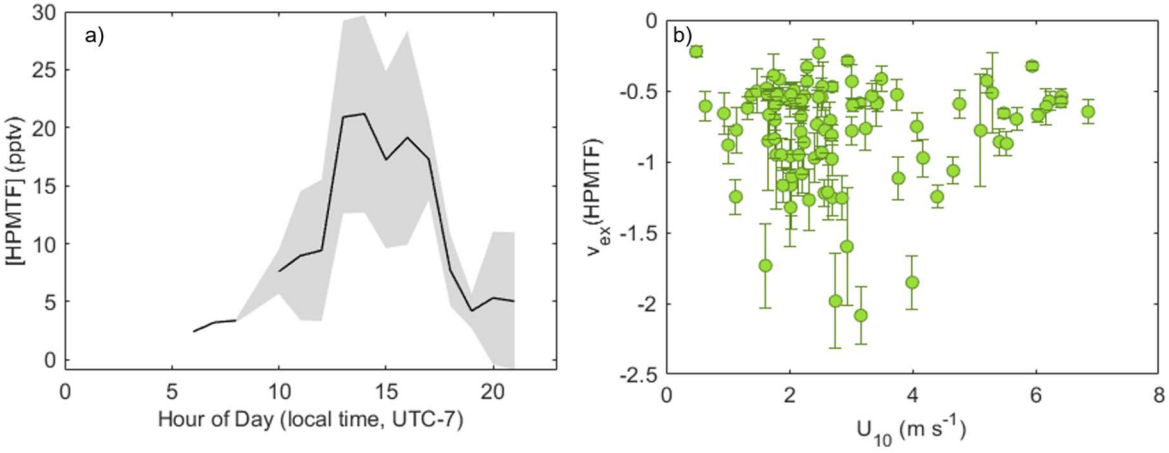

Figure 3.10. Observed HPMTF (a) mixing ratio diel profile and (b) v_{ex} wind speed dependence from Scripps Pier coastal ocean ground site observations. Mean HPMTF v_{ex} was -0.78 cm s^{-1}.

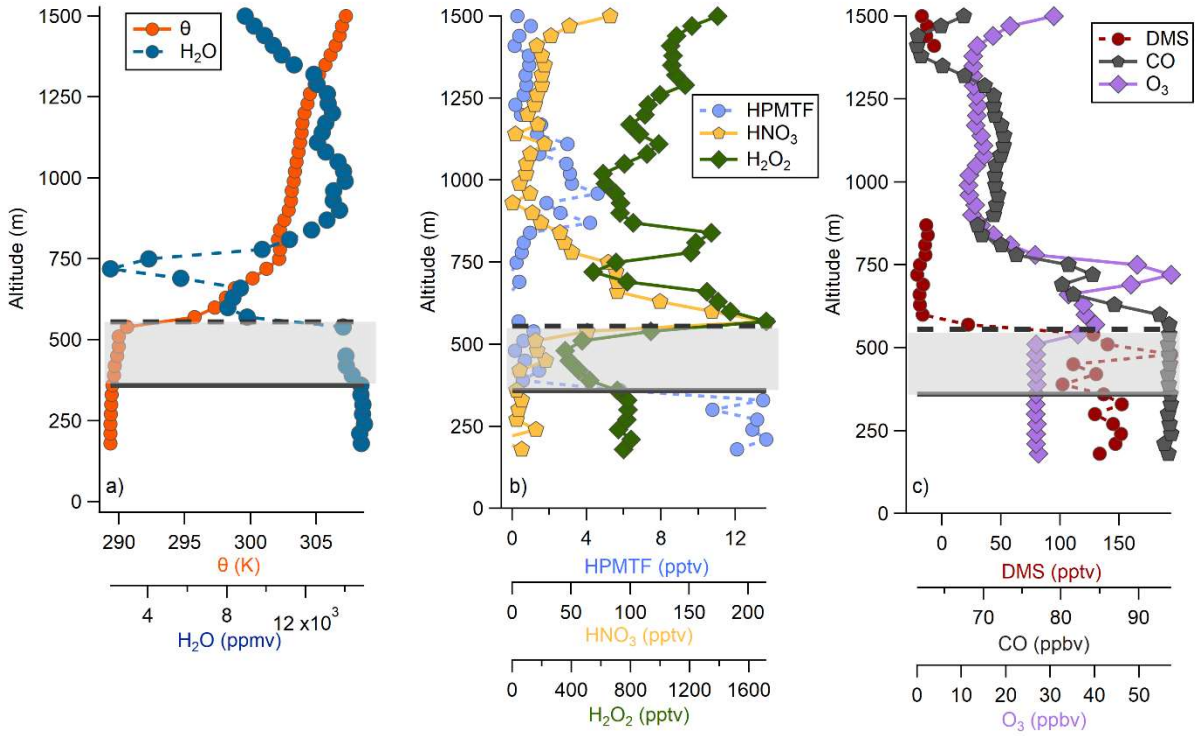

Figure 3.11. Vertical profiles from aircraft ascent during SARP Marine flight in the stratocumulus capped marine PBL. Cloud base height is indicated by the solid grey horizontal line and PBL height by the dashed grey horizontal line, with the shaded error representing the vertical extent of clouds. (a) Profiles of gas phase H_2O mixing ratio and potential temperature (θ). (b) Profiles of HPMTF, HNO_3 and H_2O_2 mixing ratios. (c) Profiles of DMS, carbon monoxide (CO), and O_3 mixing ratios.

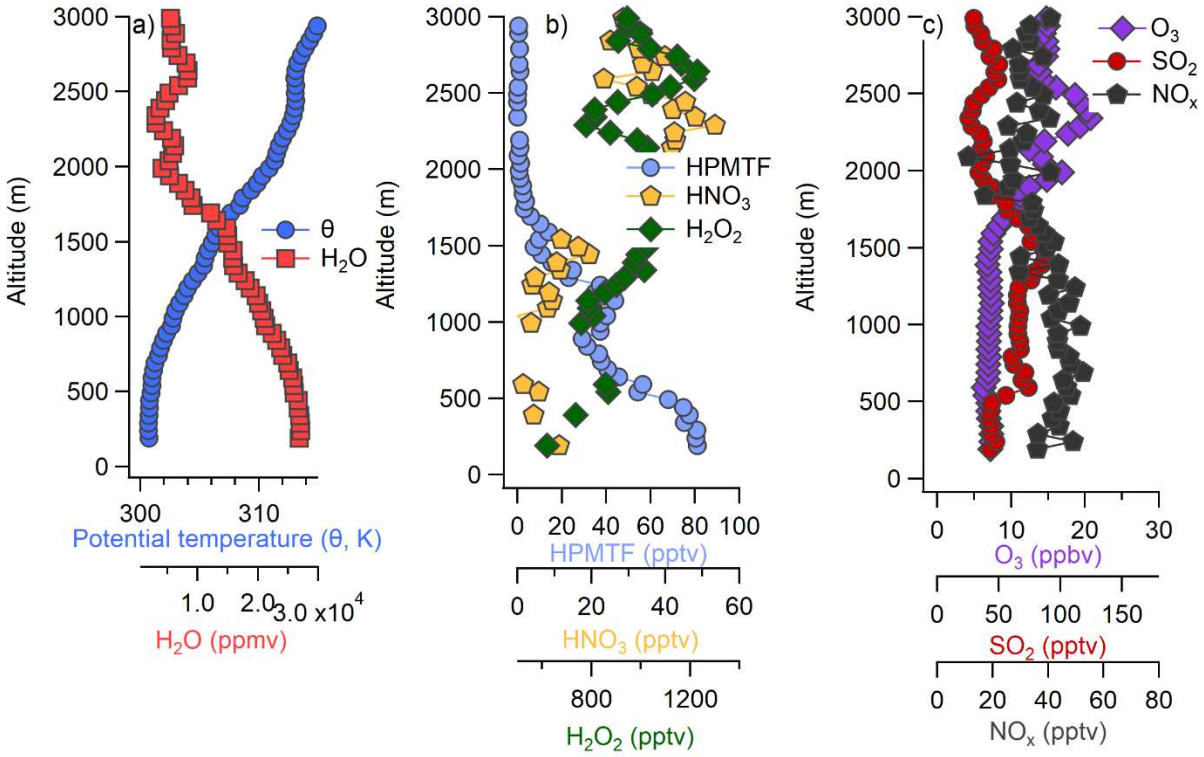

Figure 3.12. Vertical profiles from aircraft ascent during ATom 4 May 1st, 2018 flight in a clear sky PBL. Cloud base height is indicated by the solid grey horizontal line and PBL height by the dashed grey horizontal line, with the shaded error representing the vertical extent of clouds. (a) Vertical profiles of gas phase H_2O mixing ratio and potential temperature (θ). (b) Vertical profiles of HPMTF, HNO_3 and H_2O_2 mixing ratios. (c) Vertical profiles of O_3, NO_x, and SO_2 mixing ratios

Chapter 4. Simultaneous Detection of Ozone and Nitrogen Dioxide by Oxygen Anion Chemical Ionization Mass Spectrometry: A Fast Time Response Sensor Suitable for Eddy Covariance Measurements

Abstract.

We report on the development, characterization, and field deployment of a fast time response sensor for measuring ozone (O_3) and nitrogen dioxide (NO_2) concentrations utilizing chemical ionization time-of-flight mass spectrometry (CI-ToFMS) with oxygen anion (O_2^-) reagent ion chemistry. We demonstrate that the oxygen anion chemical ionization mass spectrometer (Ox-CIMS) is highly sensitive to both O_3 (180 counts s^{-1} $pptv^{-1}$) and NO_2 (97 counts s^{-1} $pptv^{-1}$), corresponding to detection limits (3σ, 1 s averages) of 13 and 9.9 pptv, respectively. In both cases, the detection threshold is limited by the magnitude and variability in the background determination. The short-term precision (1 s averages) is better than 0.3% at 10 ppbv O_3 and 4% at 10 pptv NO_2. We demonstrate that the sensitivity of the O_3 measurement to fluctuations in ambient water vapor and carbon dioxide is negligible for typical conditions encountered in the troposphere. The application of the Ox-CIMS to the measurement of O_3 vertical fluxes over the coastal ocean, via eddy covariance (EC), was tested during summer 2018 at Scripps Pier, La Jolla CA. The observed mean ozone deposition velocity ($v_d(O_3)$) was 0.013 cm s^{-1} with a campaign ensemble limit of detection (LOD) of 0.0027 cm s^{-1} at the 95% confidence level, from each 27-minute sampling period LOD. The campaign mean and one standard deviation range of O_3 mixing ratios were 41.2 ± 10.1 ppbv. Several fast ozone titration events from local NO emissions were sampled where unit conversion of O_3 to NO_2 was observed, highlighting instrument utility as a total odd oxygen (O_x = O_3 + NO_2) sensor. The demonstrated precision, sensitivity, and time resolution of this instrument highlight its potential for direct measurements of O_3 ocean–atmosphere and biosphere–atmosphere exchange from both stationary and mobile sampling platforms.

4.1 Introduction

The deposition of O_3 to the ocean surface is a significant component of the tropospheric ozone budget. Global chemical transport model studies that explicitly treat O_3 deposition, indicate that approximately one-third of total ozone dry deposition is to water surfaces.[1] However, the magnitude of total annual global ozone deposition to ocean surfaces is highly sensitive to the deposition velocity parameterization used, with model estimates ranging from 95 to 360 Tg yr^{-1}. [1,2] Several common global chemical transport models including GEOS-Chem,[3] MOZART-4,[4] and CAM-chem,[5] apply a globally uniform deposition velocity (v_d) that ranges between 0.01–0.05 cm s^{-1} depending on the model. In comparison to terrestrial measurements, where O_3 dry deposition velocities are relatively fast (>0.1 cm s^{-1},[6]), there is a paucity of direct observations of ozone deposition to the ocean surface necessary to constrain atmospheric models. Previous studies of O_3 deposition to water surfaces have been made from coastal towers, [7] aircraft, [8–10] underway research vessels,[11], and in the laboratory,[12] with observed $v_d(O_3)$ ranging between 0.01 and 0.15 cm s^{-1}There is only one reported study of O_3 deposition to freshwater, which showed $v_d(O_3)$ of 0.01 cm s^{-1}.[13]. Measured deposition rates to snow and ice vary widely, with most observations of $v_d(O_3)$ from 0 to 0.2 cm s^{-1}, while models suggest $v_d(O_3)$ from 0 to 0.01 cm s^{-1}. [14] Reactions of O_3 with iodide and dissolved organic compounds (DOC) in the ocean are known to play a controlling role in setting $v_d(O_3)$ and may explain some of the variability in observations. [1,15] However, these quantities have not typically been measured during field studies of $v_d(O_3)$. To date there is no consensus on whether measured ocean O_3 deposition velocities show a wind speed dependence. [16] The most comprehensive dataset is from Helmig et al.,(2012),Helmig et al., (2012), which reported a deposition velocity range of 0.009 – 0.034 cm s^{-1} from 1700 hours of observation over five research cruises. This dataset showed variability of $v_d(O_3)$ with wind speed (U_{10}) and sea–surface

temperature (SST), highlighting the need for further field observations as constraints for model parameterizations.

The small magnitude of O_3 ocean–atmosphere vertical fluxes presents a significant analytical challenge for existing ozone sensors used in eddy covariance (EC) analyses. Driven in part by stringent sensor requirements for EC techniques, significant uncertainties in the magnitude and variability of ozone deposition to water surfaces remain. In contrast, O_3 vertical fluxes to terrestrial surfaces are 10 to 100 times faster than to water surfaces, significantly loosening sensor precision requirements. Nonetheless, significant variability in $v_d(O_3)$ exists between surface types (e.g. soil *vs.* leaf).[17] Terrestrial deposition velocities also show strong diel and seasonal variability due to factors such as stomatal opening and within-canopy chemistry.[18–20] Highly accurate and precise measurements of O_3 are required to correctly model the response of $v_d(O_3)$ to each of these factors. While terrestrial and ocean exchange studies have substantial differences in experimental design, a sensor suitable for ocean–atmosphere ozone deposition measurements *via* EC is expected to be highly capable of biosphere–atmosphere measurements due to the significantly larger deposition rates and similar accuracy requirements.

Eddy covariance measurements typically require fast (1-10 Hz), high precision sensors in order to resolve covariance on the timescales of the fastest atmospheric turbulent eddies. Due to this constraint, standard O_3 monitoring instruments which utilize UV-absorption detection do not have suitable time response or precision for EC measurements and ozone flux measurements have primarily utilized fast response chemiluminescence sensors. Chemiluminescence detectors can use either gas-phase, dry, or wet reagents for detection with important differences between them.[21] Gas-phase chemiluminescence sensors are typically based on the reaction of O_3 with nitric oxide (NO) to form an excited state NO_2^* which then relaxes to the ground state, emitting a photon that

can be detected. This method has well understood reaction kinetics and allows for high sensitivity detection on the order of 2.8 counts s^{-1} $pptv^{-1}$.[22,23] A practical disadvantage to this technique is the necessity of a compressed cylinder of NO which is highly toxic. Wet chemiluminescence techniques are used less, as they exhibit generally lower sensitivity than dry chemiluminescence sensors and can be limited by issues in the liquid flow. [24]

Dry chemiluminescence sensors have the simplest operation and have seen the most regular use for EC studies. [25,26] However, dry chemiluminescence sensor discs require conditioning with high ozone (up to 400 ppbv for several hours) before operation, are known to degrade over time, and have high variability in sensitivity between sensor discs.[27] These factors have led to limitations in long term stability and to uncertainty in calibration factors for dry chemiluminescence sensors, resulting in uncertainty in the accuracy of the flux measurement.[21] Muller et al.(2010), also reported a comparison of two identical co-located dry chemiluminescence sensors with half-hourly flux values differing by up to a factor of two and a mean hourly flux difference ranging from 0 to 23% between sensors. Recently Zahn et al.,(2012)Zahn et al., (2012) reported the development of a commercial dry chemiluminescence ozone detector capable of fast (>10 Hz) measurements with high sensitivity (~9 counts s^{-1} $pptv^{-1}$) suitable for EC or mobile platform sampling. However, they also report issues of short- and long-term drift and variability between sensor discs. These accuracy and drift concerns have driven an interest in the development of a new, stable and fast ozone sensor suitable for EC measurements from both stationary and mobile sampling platforms.

In addition to the inherently small magnitude of $v_d(O_3)$, the fast chemical titration of O_3 by NO (R1) often complicates the interpretation of $v_d(O_3)$ measurements. Surface emissions of NO result in a high bias in the measured deposition velocity when the titration reaction (R1) is fast relative to the transport time to the height of the sensor.

$O_3 + NO \rightarrow NO_2 + O_2$ $k(O_3+NO) = 1.8 \times 10^{-14}$ cm^3 molecule^{-1} s^{-1} (R1)

Surface NO emissions from both biogenic and anthropogenic sources are widespread, with ocean emissions on the order of 1×10^8 molecules cm^{-2} s^{-1},[29] and soil emissions ranging from 5×10^9 to 2×10^{11} molecules cm^{-2} s^{-1}.[30] These emissions correspond to a positive bias in the observed $v_d(O_3)$ dry deposition rate on the order of 5% in the marine atmosphere (discussed in section 4.3.7.1) and up to 50% in a forested site.[31] Simultaneous flux detection of O_3 with one or both of NO or NO_2 is commonly used to address this flux divergence problem.[32,33] However, these studies typically require separate sensors for O_3 and NO_x which can introduce additional sources of uncertainty. Related challenges of fast O_3 titration exists for quantification of O_3 from mobile platforms where there is dynamic sampling of different airmasses with potentially differing O_3–NO–NO_2 steady-state conditions.

In what follows, we describe the characterization and first field observations of a novel oxygen anion chemical ionization time-of-flight mass spectrometer (Ox-CIMS) sensor for O_3 and NO_2. Over the past two decades, chemical ionization mass spectrometry (CIMS) techniques have emerged as sensitive, selective, and accurate detection methods for a diverse suite of reactive trace gases (Huey, 2007). Successful application of CIMS for EC flux measurements have been demonstrated from many sampling platforms including ground sites,[34,35] aircraft,[36] and underway research vessels[37–39] employing a variety of reagent ion chemistry systems. Here we demonstrate the suitability of the Ox-CIMS for EC flux measurements and provide detailed laboratory characterization of the instrument.

4.2 Laboratory Characterization

4.2.1 Chemical-ionization time-of-flight mass spectrometer

A complete description of the CI-ToFMS instrument (Aerodyne Research Inc., TOFWERK AG) can be found in Bertram et al. (2011).[40] In what follows we highlight significant differences in the operation of the instrument from what is discussed in Bertram et al., (2011). Oxygen anions are generated by passing an 11:1 volumetric blend of Ultrahigh Purity (UHP) N_2 and O_2 gas (both Airgas 5.0 grade) through a polonium-210 α-particle source (NRD, P-2021 Ionizer). This N_2:O_2 volume ratio was found empirically to maximize total reagent ion signal in our instrument while minimizing background signal at the O_3 detection product (CO_3^-,– 60 m/Q). Further discussion of the reagent ion chemistry and precursor concentration can be found in sections 4.2.2 and 4.2.8. The reagent ion stream then mixes with ambient air in an ion-molecule reaction (IMR) chamber held at 95 mbar where product ions were generated. Further discussion of the dependence of instrument sensitivity on IMR pressure can be found in section 4.2.6. At this pressure, the residence time in the IMR is estimated to be on the order of 100 ms. Product ions then pass into three differentially pumped chambers before reaching the ToF mass analyzer. Ions first move from the IMR to a collisional dissociation chamber (CDC) held at 2 mbar which houses a short-segmented RF-only quadrupole ion guide. Field strengths in the IMR and CDC were tuned to be as soft as possible to preserve the transmission of weakly bound clusters while still maintaining acceptable total ion signals (ion optic potentials are listed in **Table 4.S1**). Ions then sequentially pass into a second RF-only quadrupole chamber held at 1.4×10^{-2} mbar and a final chamber containing focusing optics which prepare the ion beam for entry into the compact ToF mass analyzer (CToF, TOFWERK AG and Aerodyne Research Inc.). The mass resolving power ($M/\Delta M$) of the instrument as configured for these experiments was greater than 900 at –60 m/Q. All ion count

rates reported here are for unit mass resolution integrated peak areas. In this work extraction frequencies of 75 kHz were used, resulting in mass spectra from 27-327 –m/Q. All mass spectra were saved at 10 Hz for analysis.

4.2.2 Oxygen Anion Chemistry

Oxygen anion (O_2^-) reagent ion chemistry has been investigated previously for its use in the detection of nitric acid and more recently hydrogen peroxide.[42–44] Oxygen anion chemistry has also been used for chemical analysis of aerosol particles in a thermal desorption instrument, primarily for detection of particle sulfate and nitrate [45]. Oxygen anion chemistry has also been used for the detection of SO_2 *via* a multi-step ionization process where CO_3^- reagent ions are first generated by the reaction of O_2^- with added excess O_3 in the presence of CO_2. The CO_3^- reagent ion then ligand switches with SO_2 to form SO_3^- which then quickly reacts with ambient O_2 to form the primary detected SO_5^- product.[46,47] Ionization of analytes by oxygen anion reagent ion chemistry proceeds through both charge transfer (R2) and adduct formation (R3).

$$O_2(H_2O)_n^- + A \rightarrow O_2(H_2O)_n + A^- \quad \text{(R2)}$$

$$O_2(H_2O)_n^- + B \rightarrow B \cdot O_2(H_2O)_n^- \quad \text{(R3)}$$

It is expected that charge transfer from oxygen will occur to any analyte with an electron affinity (E.A.) greater than O_2 (0.45 eV, [48]) resulting in a relatively non-specific reagent ion chemistry (see Rienstra-Kiracofe et al., (2002)[49] for a compilation of molecular E.A. values).. Adduct formation is observed when the binding enthalpy of the adduct is larger than that of the oxygen-water adduct and the adduct is stable enough to be preserved through the ion optics. This adduct formation framework is analogous to what has been shown for iodide reagent ion chemistry.[50]

The O_2^- reagent ions present in the IMR are expected to have a series of attached water molecules at ambient humidity and the IMR pressure (95 mbar) and electric field strengths used in this study.[51] The reagent ion is therefore reported as $O_2(H_2O)_n^-$ for the remainder of this work. In the recorded mass spectra from our instrument, all reagent ion signal is observed as n = 0–1 (i.e., O_2^- and $O_2(H_2O)^-$) as seen in **Fig. 4.1**. Oxygen anion-water clusters larger than n = 1 are likely present in the IMR but H_2O evaporates off of the cluster in the CDC before detection due to the lower binding enthalpy of each additional water in $O_2(H_2O)_n^-$ and the high filed strength at the exit of the CDC.[51,52] Variability in the number of attached water molecules (n) as a function of humidity introduces the possibility of a water dependence on the ion chemistry, which is discussed further in Section 4.2.5.

The detection of ozone (O_3) by oxygen anion reagent ion chemistry proceeds *via* a two-step reaction leading to the formation of a carbonate anion (CO_3^-), which is the final detected product. First, the oxygen anion ($O_2(H_2O)_n^-$) either transfers an electron to ozone forming O_3^- (R4a) or forms a stable cluster with ozone (R4b). The ozone anion (either bare or as a cluster with $O_2(H_2O)_n$) then reacts with a neutral CO_2 molecule to form CO_3^- (R5a–5b) which is the primary, detected product in the mass spectrometer. The electron affinity of O_3 is 2.1 eV.[53]

$$O_3 + O_2(H_2O)_n^- \rightarrow O_3^- + O_2 + nH_2O \quad \text{(R4a)}$$

$$O_3 + O_2(H_2O)_n^- \rightarrow O_2(O_3)(H_2O)_n^- \quad \text{(R4b)}$$

$$O_3^- + CO_2 \rightarrow CO_3^- + O_2 \quad \text{(R5a)}$$

$$O_2(O_3)(H_2O)_n^- + CO_2 \rightarrow CO_3^- + 2O_2 + nH_2O \quad \text{(R5b)}$$

It is not clear whether it is the bare ozone anion (R4a & R5a) or the cluster (R4b & R5b) that goes on to react with CO_2 to form the carbonate anion. The $O_2(O_3)(H_2O)_n^-$ product has not been observed in the mass spectrometer, but it may exist in the IMR and dissociate as it transfers into the CDC prior to detection. A small amount of ozone is detected directly as O_3^- but the magnitude of this signal is less than 1% of the signal of CO_3^- during ambient sampling. The proposed mechanism of CO_3^- formation is supported by a study using isotopically labelled oxygen to form labelled ozone anions ($^{18}O_3^-$) in a corona discharge source which then reacted with CO_2 to form the detected product $C^{18}OO_2^-$.[54] This product supports that a single oxygen is transferred from the ozone anion to carbon dioxide (as in R5a).

The detection of NO_2 proceeds directly through a charge transfer reaction with $O_2(H_2O)_n^-$ to form the detected NO_2^- product (R6). This is expected based upon the high E.A. of NO_2 (2.27 eV)[55] compared to O_2 (E.A 0.45 eV).

$$NO_2 + O_2(H_2O)_n^- \rightarrow NO_2^- + O_2 + nH_2O \quad \text{(R6)}$$

Oxygen anions are expected to be a highly general reagent ion chemistry, showing sensitivity to an array of analytes. While the focus of this work is on detection of O_3 and NO_2, detection of hydrogen peroxide, nitric acid, formic acid, sulfur dioxide and other species with the Ox-CIMS has demonstrated good performance.[44] An example ambient mass spectrum recorded at 1 Hz sampling is shown in **Fig. 4.1**, with several major peaks highlighted. Also apparent are an abundance of peaks throughout the spectra with high signal intensity. During ambient observations, over one third of masses from –m/Q 27-327 showed signal intensity greater than 1 x 10^4 counts per second (cps). A larger survey and classification of oxygen anion reagent ion chemistry to utilize this versatility is underway.

4.2.3 Laboratory calibration

Laboratory calibrations of the Ox-CIMS were performed to determine instrument sensitivity to O_3 and NO_2. Ozone was generated by passing UHP Zero Air (ZA, Airgas 5.0 grade) through a mercury lamp UV source (Jelight Co, Irvine CA). Outflow from the lamp source was diluted in UHP ZA and split between the Ox-CIMS and a factory calibrated 2B POM ozone monitor (2B Technologies) with an accuracy of ± 1.5 ppbv, which served as our reference standard. Ozone concentrations were varied over the range 0–80 ppbv and instrument response was determined to generate a calibration curve. NO_2 was delivered from a certified standard cylinder (Scott-Marrin 4.84 ± 0.1 ppmv). The primary NO_2 standard was diluted in UHP ZA to span the range of 0–10 ppbv. Dilutions of calibration standards were made in UHP ZA which was humidified to the desired amount by splitting a portion of the flow through a bubbler containing 18 MΩ water. CO_2 (Airgas Bone Dry grade) was added to the dilution flow to maintain mixing ratios of 380 ppmv for all calibrations (See Section 4.2.6). A Vaisala HMP 110 sensor continuously measured relative humidity and temperature inline downstream of the Ox-CIMS and POM inlets. All flows were controlled by mass flow controllers (MKS instruments, 1179C series) with an estimated total uncertainty of 10%. Example calibration curves for O_3 and NO_2 are shown in **Fig. 4.2**. An overview of instrument sensitivity, limits of detection (LOD), and precision to O_3 and NO_2 is given in **Table 4.1**.

4.2.4 Absolute sensitivity

The absolute sensitivity of the Ox-CIMS for detection of analytes is controlled by the kinetics and thermodynamics of the reagent ion chemistry and the total ion generation and transmission efficiency of the instrument. Under the operational configuration described in Section 4.2.1, typical reagent ion signal ($O_2^- + O_2(H_2O)_n^-$) ranged from 0.8 to 2.2 × 10^7 counts s^{-1} (**Fig. 4.S1**).

The mean total reagent ion signal over 6 weeks of ambient sampling (Section 4.3.1) was 1.45 × 10^7 cps. The absolute instrument sensitivity at this reagent ion signal to O_3 and NO_2 is 180 and 97 cps $pptv^{-1}$ respectively (at 8 g kg^{-1} SH). Total instrument count rate is a complex function of instrument design, instrument ion optics tuning, Po-210 source decay, micro channel plate (MCP) detector decay, and ToF extraction frequency; all of which are either tunable parameters or vary in time. Conversely, the reagent ion charge transfer or adduct formation chemistry for a given analyte sets a fundamental limit on sensitivity for a given instrument configuration. Sensitivity values can be normalized by scaling all signals to a fixed total reagent ion signal of 1 × 10^6 cps to isolate the sensitivity component controlled by reagent ion chemistry, separate from changes in instrument performance due to decay in the ion source or other factors. The total reagent ion signal is taken as the sum of the O_2^- and $O_2(H_2O)^-$ signals. Sensitivity values through the remainder of the text are reported as either absolute sensitivities in counts per second (cps $pptv^{-1}$) or normalized sensitivities in normalized counts per second (ncps $pptv^{-1}$). Absolute sensitivity values control instrument limits of detection (LOD) and precision, while normalized sensitivities are used for comparison of calibration factors.

4.2.5 Dependence of instrument sensitivity on specific humidity

The dependence of instrument sensitivity on ambient water content was assessed for specific humidity (SH) ranging between 0–16 g kg^{-1} (approximately 0-80% RH at 25 °C) by triplicate calibrations as shown in **Fig. 4.3**. Sensitivity to O_3 had no significant dependence on specific humidity over the range 4-16 g kg^{-}. Sensitivity to NO_2 has a specific humidity dependence over the range 4–16 g kg^{-1}, decreasing from 7.9 to 4.6 ncps $pptv^{-1}$. A 30% and 45% decline in sensitivity was observed from 0 to 4 g kg^{-1} for O_3 and NO_2 respectively. This low humidity range is rarely sampled in the boundary layer over water surfaces but may be significant in some terrestrial or

airborne deployments and would require careful calibration. The SH range from 8 to 16 g kg^{-1} corresponds to approximately 40 to 80% RH at 25 °C which is typical of the humidity range over mid-latitude oceans.[56] *Ab initio* calculations of $O_2^-(H_2O)_n$and $O_3^-(H_2O)_n$ clusters performed by Bork et al. (2011)[51] showed that charge transfer from the bare (n=0) O_2^- to O_3 was exothermic at ca. -160 kJ/mol. At larger cluster sizes of n = 4–12, charge transfer becomes less favorable and converges to ca. -110 kJ/mol. An increase in n from 0 to 4 over the SH range 0–4 g kg^{-1} is a potential explanation for the initial decline in sensitivity observed with SH before levelling off from 4–16 g kg^{-1}. It is not known if the enthalpy of charge transfer from $O_2^-(H_2O)_n$ to NO_2 follows a similar trend with n. Ion mobility studies to determine the $O_2^-(H_2O)_n$ cluster size with SH and IMR pressure would provide valuable insight on the observed dependence of sensitivity on water content.

4.2.6 Dependence on CO_2

The ionization pathway for detection of O_3 with $O_2^-(H_2O)_n$ reagent ion chemistry differs from typical chemical ionization schemes, in that it involves a two-step reaction of charge transfer to ozone forming O_3^-, which then reacts with CO_2 to form the detected CO_3^- product (R4-R5). Therefore, we assessed the impact of CO_2 mixing ratio in the sample flow on O_3 sensitivity as shown in **Fig. 4.4**. Calibration curves were generated by diluting ozone in dry UHP N_2 and mixing in a flow of variable CO_2 (Airgas, Bone Dry Grade) mixing ratios before sampling. At nominally 0 ppmv CO_2, the O_3^- ionization product (–48 m/Q) was detected with sensitivity of 14 ± 2 ncps $pptv^{-1}$ and the CO_3^- product (–60 m/Q) at 5 ± 1 ncps $pptv^{-1}$. For CO_2 mixing ratios from 60 to 500 ppmv, the O_3^- signal is less than 1% of the CO_3^- product and the sensitivity at the CO_3^- product is independent of CO_2 within the uncertainty. The presence of a significant fraction (36%) of the CO_3^- product with nominally 0 ppmv CO_2 suggests the presence of a slight leak rate of CO_2 *via*

diffusion through the perfluoroalkoxy alkane (PFA) tubing, or CO_2 contamination in the UHP N_2 supply. The manufacturer stated upper limit of CO_2 in the UHP N_2 is 1 ppmv which we take to be the lower limit achievable in our system. A CO_2 mixing ratio of only 1 ppmv is still an order of magnitude excess relative to a high end ambient O_3 mixing ratio of 100 ppbv. An exponential fit of the O_3^- product *vs* CO_2 indicates that O_3^- makes up less than 1% of the detected ozone at CO_2 mixing ratios greater than 10 ppmv. This suggests ambient samples will always have a substantial excess of CO_2 necessary to drive the reaction completely to the CO_3^- product. The measured flat response from 60–500 ppmv CO_2 indicates that natural variability in ambient CO_2 will have negligible impact on ambient measurements of ozone. No other analytes that we have calibrated for with the Ox-CIMS (HCOOH, HNO_3, H_2O_2) have shown a CO_2 mixing ratio dependence, suggesting that CO_2 may be uniquely involved in the detection of O_3 and is not a general feature of the oxygen-anion chemistry. All other reported laboratory calibrations reported here were performed at CO_2 mixing ratios of 380 ppmv and all reported sensitivities are for the CO_3^- product. This CO_2 dependence also requires careful consideration during instrument background determinations by UHP N_2 overflow which is discussed in Section 4.2.8.

4.2.7 Dependence on IMR pressure

Instrument sensitivity to O_3 increases with increasing IMR pressure as shown in **Fig. 4.5**. The normalized signal of O_3 increases by 60% at an IMR pressure of 95 mbar compared to 70 mbar when sampling a constant O_3 source of 35 ppbv. IMR pressure was increased in approximately 5 mbar steps, with CDC pressure held constant at 2 mbar, and a three-minute dwell time at each step to ensure signal and pressure were stabilized. Total reagent ion signal did not change significantly over this pressure range. Pressures above 95 mbar were not investigated due to concerns over corresponding increases in CDC pressure with the pinhole and pumping configuration used in this

work. There is no evident plateauing in the signal increase over the IMR pressure range investigated here, indicating that further optimization is likely possible by operating at higher IMR pressures. The increase in sensitivity with IMR pressure could be fit well with an exponential least squares fit, which is plotted in **Fig. 4.5**. The physical meaning of the exponential relationship is not clear. The source of the response of sensitivity to pressure is not definitive but can possibly be attributed to the increase in the total number of collisions during the 100 ms residence time in the IMR and the corresponding weakening of those collisions. Higher collisional frequencies also lead to proportionally weaker collisions which could better preserve a weakly bound $O_2(O_3)(H_2O)_n^-$ cluster and allow a longer lifetime to react with CO_2 before dissociation. The operational IMR pressure of 95 mbar used here was empirically selected to maximize sensitivity to O_3 without increasing CDC pressure beyond the desired range. Investigation of higher IMR pressures, up to the operation of an atmospheric pressure interface, has the potential to further increase the instrument sensitivity to O_3.

4.2.8 Instrument background and limits of detection

Instrument backgrounds were assessed by periodically overflowing the inlet with UHP N_2 during field sampling. Details of the inlet and zeroing conditions used are discussed further in Section 4.3.1. During N_2 overflow, O_3 displayed a consistently elevated background on the order of 3.1 x 10^5 cps corresponding to 2.1 x 10^4 ncps, or approximately 1.3 ppbv O_3, at a typical total reagent ion signal of 1.45 x 10^7 cps. A representative background determination is shown in **Fig. 4.6**. The magnitude of the O_3 background was observed to vary with the O_2:N_2 ratio in the reagent ion precursor flow when sampling a UHP ZA overflow with 380ppm CO_2 as shown in **Fig. 4.S2**. The background O_3 count rate was observed to increase from 3.0 x 10^4 to 6.3 x 10^4 ncps as the O_2 volume fraction in the reagent ion delivery gas flow (f_{O2}) was increased from 0.05 to 0.4. The

dependence of the background O_3 signal on f_{O_2} suggests that the observed background O_3 is formed directly in the alpha ion source and is not from off-gassing of inlet and instrument surfaces. The magnitude of this background O_3 does not vary when sampling UHP zero air or N_2, further confirming that the background O_3 is formed directly in the ion source from the O_2 used to generate the reagent ion. An operational f_{O_2} of 0.08 (actual volumetric flow ratio O_2:N_2 of 200:2200 sccm) was selected to balance maximizing the total reagent ion signal while minimizing the O_3 ion-source background (3.1 x 10^5 cps). The magnitude of this O_3 background was observed to be highly consistent during field sampling at a constant f_{O_2} of 0.08 and well resolved from all ambient observations (**Fig. 4.S3**). The 1σ deviation of the distribution of normalized adjacent differences of O_3 signal during background periods gives an upper limit of variability of 9% between adjacent background periods. A variability of 9% corresponds to a difference of 70 pptv between subsequent O_3 background determinations. The magnitude of this O_3 background is a fundamental limit on the achievable limit of detection.

Because CO_2 was not added to the UHP N_2 overflow during field sampling, the reaction was not driven fully to the CO_3^- product and some O_3^- signal at –m/Q 48 was observed during UHP N_2 overflow periods as shown in **Fig. 4.S4**. The magnitude of the O_3 signal observed as O_3^- was approximately 55% of the CO_3^- product (mean 1.2 x 10^4 and 9.6 x 10^3 ncps respectively) during overflow periods. The total sensitivity to O_3 as the sum of the O_3^- and CO_3^- was observed to be constant as a function of CO_2 as shown in **Fig. 4.4**. We therefore assign equal sensitivity to each O_3 detection product and took the sum of signal at O_3^- and CO_3^- in order to determine the total background O_3 concentration. This issue will be corrected in future deployments by the addition of CO_2 to the N_2 overflow used for backgrounds which will drive the product fully to CO_3^-. The mean background of O_3 for the full field sampling period was 1.3 ± 0.3 ppbv. The 10 Hz precision

of O_3 during an individual N_2 overflow period was found to be 0.75%, corresponding to 7.5 pptv as shown in **Fig. 4.S5**. This suggests that variability in the O_3 signal from this background source is constant over short timescales and has a negligible impact on instrument precision during ambient sampling.

The 10 Hz limit of detection for O_3 is 42 pptv for a S/N of 3, and a mean background O_3 signal of 2.1 x 10^4 ncps as calculated using Eq. 1, below from Bertram et al., 2011, where C_f is the calibration factor, *[x]* is the analyte mixing ratio, t is averaging time in seconds, and B is the background count rate. The optimum LOD from the minimum of the Allan variance at an 11 second averaging time is 4.0 pptv (**Fig. 4.S6a**).

$$\frac{S}{N} = \frac{C_f[X]t}{\sqrt{C_f[X]t - 2Bt}} \qquad \text{E1}$$

The mean background signal during field sampling for NO_2 was 3.5 x 10^3 ncps which corresponds to 0.28 ppbv. At this background level, the 10 Hz LOD for NO_2 is 26 pptv for a S/N of 3. The optimum LOD for NO_2 is 2.3 pptv at an averaging time of 19 seconds, determined from the minimum of the Allan variance (**Fig. 4.S6b**). The background signal of NO_2 is notably above zero indicating either off gassing from inlet walls or a secondary production of NO_2 in the instrument. A possible source of this background is from degradation of other species such as nitric acid or alkyl nitrates on the inlet walls. Additional calibration will be necessary to ensure that observed NO_2 signal is not a secondary product of other species and we can currently quantify their potential interference on measured NO_2.

4.2.9 Reagent ion saturation and secondary ion chemistry

During ambient sampling the ozone signal (as CO_3^- detected at –60 m/Q) is of comparable magnitude to the O_2^- reagent ion signal as shown in **Fig. 4.1**. High analyte concentrations (> 5

ppbv) have been shown previously to result in non-linear calibration curves for unnormalized signals.[41,57] In our system we do not observe non-linearity in the normalized O_3 calibration for our highest concentration calibration point of 80 ppbv despite the CO_3^- signal being larger than the O_2^- reagent ion (9 x 10^6 cps and 6 x 10^6 cps respectively). The electron affinity (E.A.) of carbonate is from 3.26[58] to >3.34 eV[59] and is significantly higher than that of oxygen (E.A. 0.45 eV), making it unlikely that carbonate is involved in charge transfer reactions when excess O_2^- is present. . At high O_3 concentrations, the reagent ion signal magnitude is reduced, which necessitates normalizing sensitivities to the 1 x 10^6 cps of reagent ion signal before quantification. For NO_2 (E.A. 2.27 eV), the normalized sensitivity showed no dependence on O_3 concentrations from 0 to 80 ppbv. Carbonate reagent ion chemistry has been utilized for detection of HNO_3 and H_2O_2 *via* adduct formation raising additional concern about potential secondary ion chemistry.[60] In laboratory calibrations, shown in **Fig. 4.S7**, introduction of 0 to 40 ppb H_2O_2 resulted in the titration of the O_3 signal of 0.06 ppbv per ppbv H_2O_2. H_2O_2 was detected as an adduct with O_2^- and not CO_3^- , indicating that O_2^- reagent ion chemistry is more favorable despite high CO_3^- signal intensity. The Ox-CIMS O_3 measurement also compared well (R^2 =0.99) against an EPA AQS O_3 monitor over 1 month of ambient sampling where H_2O_2 and HNO_3 concentrations both exceeded 5 ppbv at times (see Section 4.3.1 for further discussion of field intercomparison), further supporting the CO_3^- detection product as a robust indicator of O_3 in complex sampling environments.

Ab initio calculations of the binding enthalpies of O_2^- and CO_3^- reagent ions with H_2O, HNO_3, H_2O_2, and CH_3OOH were performed with the MP2/aug-cc-pvdz-PP theory and basis set in order to assess the relative favorability of adduct formation between O_2^- and CO_3^- Adduct formation

with O_2^- was favorable relative to CO_3^- by 2.5 to 17 kcal mol^{-1} for all analytes that were calculated. All calculated binding enthalpy values are listed in **Table 4.S2**.

4.2.10 Short- and long- term precision

Short term precision of the instrument was assessed by calculating the normalized difference between adjacent 10 Hz data points over a 27-minute sampling period of a constant ambient analyte concentration *via* Eq. 2.

$$\mathrm{NAD} = \frac{[\mathrm{X}]_n - [\mathrm{X}]_{n-1}}{\sqrt{[\mathrm{X}]_n [\mathrm{X}]_{n-1}}} \qquad \text{E2}$$

The standard deviation of the Gaussian fit of the distribution of normalized adjacent differences (NAD) is a direct measure of the short-term instrument precision [41]. The 1σ precision from the NAD distribution for 10 Hz sampling of 38 ppbv ozone is 0.74% (**Fig. 4.7**). The 10 Hz precision for sampling of 2.3 ppbv NO_2 is 1.1% The short-term precision for both analytes was larger than expected if the noise was driven by counting noise alone (10 Hz counting noise limit for O_3 and NO_2 at the concentrations used above are 0.12% and 0.63% respectively), indicating that other potential points of optimization in the instrument configuration are required to further improve short-term precision. Notably, the observed noise source appears to be white noise given the Gaussian distribution of the NAD.[61]

Short term precision was assessed as a function of count rate by calculating the NAD for all masses in the spectrum over a stable 27-minute sampling period for both 1 Hz and 10 Hz data averaging. From this assessment, precision was observed to improve approximately linearly in a log-log scaling for count rates between 1 x 10^3 and 1 x 10^6 cps (**Fig. 4.S8**) as expected in the case where counting noise drives instrument precision. Above 1 x 10^6 cps there is an apparent asymptote where precision no longer improves with count rate. The counting noise limited 10 Hz precision

for 10^6 and 10^7 cps are 0.32% and 0.1% respectively, while the measured values were 0.75 and 2%. The counting noise limited precision is calculated as $\sqrt{N}/N$ where N is the number of counts during the integration time. This precision limit could be driven by an uncharacterized source of white noise in the instrument, including MFC drift, IMR turbulence, ion optic voltage drift, and pump drift. Measurement precision of O_3 and NO_2 could be improved by a factor of 5 and 2 respectively if this non-counting noise source of white noise was eliminated.

In theory, detection limits can be improved by signal averaging to a lower time resolution than the 10 Hz save rate. Signal–to–noise ratios are expected to improve with the square root of the integration time. At longer timescales, factors including instrument drift become significant, creating a limit on the upper end of averaging time which optimizes signal–to–noise. This was assessed quantitatively by calculation of the Allan variance as shown in **Fig. 4.S6**.[62]

4.3 Field results and discussion

4.3.1 Ozone field calibration and intercomparison

Performance of the Ox-CIMS was compared against a co-located EPA Air Quality System (AQS) O_3 monitor (Thermo-Fisher 49i, AQS ID 17-097-1007) over one month of ambient sampling during the Lake Michigan Ozone Study 2017 (LMOS 2017) in Zion, IL.[44] A regression analysis between the two instruments at one-minute averaging showed strong agreement (R^2 = 0.99) as shown in **Fig. 4.8**. Ox-CIMS concentrations were averaged to 1 ppbv bins which was the output data resolution of the EPA data logger system for the (Thermo-Fisher 49i). Error bars are the 1σ standard deviation of each Ox-CIMS bin average. Near one–to–one agreement (slope of 0.99) between instruments lends confidence to the calibration, baselining, and long-term stability of the Ox-CIMS. The Ox-CIMS was located on the roof of a trailer (approx. 5 m above ground) and sampled through a 0.7 m long, 0.925 cm i.d., PFA inlet. The inlet was pumped at flow rate of 18-

20 slpm from which the Ox-CIMS subsampled at 1.5 slpm. Temperature and RH were recorded inline downstream of the subsampling point. The Ox-CIMS sampling point was approximately 10 m horizontally from the Thermo-Fisher 49i and both instruments sampled at approximately equal heights. Instrument backgrounds of the Ox-CIMS were determined every 70 minutes by overflowing the inlet with dry UHP N_2. Calibration factors were determined by the in-field continuous addition of a C-13 isotopically labelled formic acid standard to the tip of the inlet. Laboratory calibrations of the Ox-CIMS to formic acid and O_3 as a function of specific humidity were determined immediately pre- and post-campaign and were used to calculate a humidity dependent sensitivity of O_3 relative to formic acid. That relative sensitivity was then used to determine the in-field sensitivity to O_3 by scaling field sensitivities of formic acid from the continuous additions. Full details of this deployment and calibration methods are described in Vermeuel et al., (2019). The EPA O_3 monitor shows a persistent high bias at low O_3 concentrations (<10 ppbv) relative to the Ox-CIMS. This discrepancy could arise from known interferences from water, mercury, and other species in 254 nm UV absorbance detection of ozone.[63]

4.3.2 Eddy covariance experiment overview

The Ox-CIMS was deployed to the 330 m long Ellen Browning Scripps Memorial Pier (hereon referred to as Scripps Pier) at the Scripps Institute of Oceanography (32° 52.0’ N, 117° 15.4’ W) during July and August 2018 for EC measurements of O_3 vertical fluxes. This site has been used regularly for EC flux observations from our group and others.[34,46,64] The Ox-CIMS was housed in a temperature-controlled trailer at the end of the pier. The Ox-CIMS sampled from a 20 m long PFA inlet manifold with the intake point co-located with a Gil-Sonic HS-50 sonic anemometer which recorded 3-dimensional winds sampling at 10 Hz. The Ox-CIMS inlet and sonic anemometer were mounted on a 6.1 m long boom that extended beyond the end of the pier to

minimize flow distortions. The inlet height was 13 m above the mean lower low tide level. The Ox-CIMS inlet was located 8 cm below the sonic anemometer with a 0 cm horizontal displacement. The inlet manifold consisted of a 0.64 cm i.d. sampling line, a 0.64 cm i.d. overflow line, and a 0.47 cm i.d. calibration line all made of PFA. The inlet sample line was pumped at 18-23 slpm (Reynolds number 3860-4940) by a dry scroll pump (SH-110, Agilent) to ensure a fast time response and maintain turbulent flow. Flow rates in the inlet sample line were recorded by a mass flow meter but were not actively controlled. The inlet manifold, including calibration and overflow lines, was held at 40 °C *via* a single resistively coupled circuit along the length of the manifold and controlled by a PID controller (Omega, model CNi 16). The Ox-CIMS front block and IMR were held at 35 °C. The Ox-CIMS subsampled 1.5 slpm from this inlet manifold through a critical orifice into the IMR. Ambient humidity and temperature were also recorded in-line downstream of the subsampling point.

4.3.2.1 Calibration

Instrument sensitivity was assessed by the standard addition of a C–13 isotopically labelled formic acid standard for 3 minutes every 35 minutes at the ambient end of the inlet manifold. Ozone mixing ratios were determined by scaling the humidity dependent sensitivity of O_3 from pre- and post-campaign calibrations to the field calibrations of C–13 formic acid. Ambient O_3 was also measured at 10 s time-resolution with a 2B technologies Personal Ozone Monitor (POM). The POM had a separate 10 m long, 0.47 cm i.d. PFA sampling line located 12 m from the Ox-CIMS inlet manifold and sonic anemometer. The POM was used as an independent verification of the Ox-CIMS measurement and was not used for calibration.

4.3.2.2 Backgrounds and inlet residence time

Instrument backgrounds were determined every 35 minutes by overflowing the entire inlet manifold with dry UHP N_2. Background and ambient count rates were first converted to concentrations using the laboratory determined humidity dependent sensitivities for O_3 and NO_2 scaled to the C-13 formic acid standard addition sensitivity. Background concentrations of O_3 and NO_2 from before and after each 30-minute ambient sampling period were interpolated over the ambient sampling period which was then subtracted from each 10 Hz concentration data point to obtain a background corrected time-series. Background concentrations of O_3 had a mean 1.5 ppbv and a drift of 1% between adjacent background periods, determined by the distribution of the NAD of the mean background concentrations.

The signal response of O_3 during dry N_2 overflows were fit to an exponential decay function to characterize inlet gas response times.[65] Best fit estimates for decay time constants for O_3 across overflow periods were from 0.2 to 0.44 seconds. NO_2 decay responses were fit to a bi-exponential decay to characterize inlet evacuation time (τ_1) and wall interaction times (τ_2).[65] τ_2 for NO_2 was determined to be approximately 3.2 s. This suggests a potential interference at the NO_2 peak, as NO_2 is expected to have minimal wall equilibration, similar to O_3. NO_2 also shows a continually elevated signal during overflow periods suggesting off gassing from inlet or instrument surfaces. The cause of this slow NO_2 decay and elevated background is not clear but could be from degradation of nitric acid or nitrate containing aerosol on the instrument surfaces.

The instrument response time (τ_r) for O_3 can be calculated during zeroing periods as the time required for the signal to fall to 1/e of its initial value. The response time of the instrument was calculated for each overflow period during field sampling, with a mean value of 0.28 s. The

cutoff frequency (f_{cut}) of the instrument is defined as the frequency where the signal is attenuated by a factor of $1/\sqrt{2}$ [22]. The cutoff frequency can also be calculated from τ_r according to Eq. 3.

$$f_{cut} = \frac{1}{2\pi\tau_r} \quad \text{E3}$$

The calculated f_{cut} from the measured mean response time was 0.57 Hz. This value suggests that minimal attenuation in the flux signal (cospectra) should be apparent at frequencies less than 0.57 Hz. The instrument response time and thus cutoff frequency are function of the flow rate and sampling line volume. The flow rate of 18-23 slpm was the maximum achievable with the tubing and pumping configuration used here but could be improved in future to minimize tubing interactions and shift f_{cut} towards higher frequencies.

4.3.2.3 Eddy covariance flux method

The transfer of trace gases across the air−sea interface is a complex function of both atmospheric and oceanic processes, where gas exchange is controlled by turbulence in the atmospheric and water boundary layers, molecular diffusion in the interfacial regions surrounding the air−water interface, and the solubility and chemical reactivity of the gas in the molecular sublayer. The flux (F) of trace gas across the interface is described by Eq. 4, as a function of both the gas-phase (C_g) and liquid phase (C_l) concentrations and the dimensionless gas over liquid Henry's law constant (H), where K_t, the total transfer velocity for the gas (with units cm s^{-1}), encompasses all of the chemical and physical processes that govern air−sea gas exchange. Surface chemical reactivity terms to the gas exchange rate are incorporated into the K_t term.

$$F = -K_t\left(C_g - HC_l\right) \quad \text{E4}$$

Trace gas flux (F) can be measured with the well-established eddy covariance (EC) technique where flux is defined as the time average of the instantaneous covariances from the

mean of vertical wind (w) and the scalar magnitude (here O_3) shown in Eq. 5. Overbars are means and primes are the instantaneous variance from the mean. Here N is the total number of 10 Hz data points during the 27-minute flux averaging period.

$$F = \frac{1}{N}\sum_{i=1}^{N}(w_i - \overline{w})\left(O_{3,i} - \overline{O_3}\right) = \langle w' O_3' \rangle \quad \text{E5}$$

$$v_d = \frac{F}{\overline{C_g}} \quad \text{E6}$$

For purely depositing species where the water side concentration is negligible, C_l and H can be neglected in Eq. 4 and K_t can be reformulated into a deposition velocity (v_d) calculated according to Eq. 6, where $\overline{C_g}$ is the mean gas phase mixing ratio during the flux averaging period. A summary of concentration and flux results for the full deployment period are given in **Table 4.2**.

4.3.3 General Data Corrections

Several standard eddy covariance data filters and quality control checks were applied before analysis. General filters included:

1.) Wind sector: Only periods of mean onshore flow (true wind direction 200-360°) were used.
2.) Friction velocity: A friction velocity (U_*) threshold was applied to reject periods of low shear driven turbulence described further below. [66]
3.) Stationarity: Each 27-minute flux period was divided into five even non-overlapping subperiods. Flux periods were rejected if any of the subperiods differed by more than 40%.[67]

The applied U_* filter was determined by comparing the observed $U*$ values to $U*$ calculated with the NOAA COARE bulk flux v 3.6 algorithm.[68] COARE $U*$ were calculated using measured meteorology including wind speed, sea-surface temperature, air temperature, and relative humidity. Flux periods were rejected if the observed $U*$ differed from the calculated $U*$ by more than 50%. The stress relationship of wind-speed to $U*$ is well understood over the ocean. Fixed $U*$

filters of *ca.* 0.2 m s^{-1} are used frequently as a default in terrestrial flux studies but would reject nearly all observation periods in this study. The observed friction velocities are consistent with other marine flux studies where surface roughness lengths are significantly smaller than over terrestrial surfaces.[46] Methods of determining site specific U_* thresholds typically require long-term data series which were not available here.[69] Papale et al., (2006)[69], applied a minimum U∗ threshold of 0.1 m s^{-1} for forest sites and 0.01 m s^{-1} for short vegetation sites where typical U∗ values are lower. The selected U_* filter rejects an additional 44% of the flux periods remaining after the wind direction filter. The stationarity criteria rejected a further 100 flux periods, potentially driven by periods of activity on the pier driving changes in the sampled O_3. Outliers in $v_d(O_3)$ and the flux limit of detection were determined and removed for points three scaled median absolute deviations from the median. This outlier filter removed an additional 16 data points. After the wind direction filter and all quality control filters were applied, 73% of flux periods were rejected leaving 246 quality-controlled flux periods. Eddy covariance flux values were calculated using 27-minute time windows. The O_3 timeseries was detrended with a linear function prior to the flux calculation. The O_3 and vertical wind data were despiked using a mean absolute deviation filter before the eddy covariance flux calculation following Mauder et al., (2013).[70]

4.3.3.1 Planar Fit Wind Coordinate Rotation

Coordinate rotation of the *u*, *v*, and *w* wind components was performed by the planar fit method to remove unintentional tilts in the sonic mounting and account for local flow distortions.[71] Briefly, the mean *u*, *v*, and *w* wind components and the stress tensor were determined for each 15-minute onshore flow period during the full campaign. A linear regression was used to find the best fit of a plane with a coordinate system where the z-axis is perpendicular to the mean streamline. Individual 27-minute flux periods are then rotated such that the x-axis is along the mean wind and

$\bar{v} = 0$. Vertical wind velocity ($\bar{w}$) in any individual rotation period may be non-zero due to mesoscale motions but $\bar{w}$ for the full campaign is zero. The residual mean vertical velocity in any individual rotation period is subtracted out, so it does not impact the Reynolds averaging.

4.3.3.2 Lag time shift

The Ox-CIMS signal is delayed relative to the sonic anemometer due to transit time in the inlet line which must be accounted for before calculating the covariance between the vertical wind and analyte concentration. The cross-covariance of the two timeseries were first calculated within a ± 5 s window to determine the lag time of the Ox-CIMS and synchronize with the anemometer. The volumetric evacuation time of the inlet is 1.65 to 2.1 s for the inlet volume and flow rates of 18 to 23 slpm used in this study. Following the method and terminology outlined in Langford et al., (2015), the position of the maximum (MAX) of the cross-covariance is taken as the lag time needed to align the vertical wind and analyte concentration for that flux period. A representative lag time determination with a larger lag window (± 10 s) using the MAX method is shown in **Fig. 4.10**. In low signal-to-noise (SNR) data, the use of the MAX leads to high variability in the determined lag time caused by uncertainty in the position of the peak in the cross-covariance. This results in a systematic high bias on the absolute magnitude of the resulting flux. The position of the maximum of a centered running median (AVG) function of the cross-covariance is an alternative method to determine lag time with less expected bias for low SNR data.[72,73] Lag times for each O_3 flux period determined by the MAX and a 10 point AVG method showed reasonable agreement, with a campaign average lag time from the MAX with a mean of 1.0 seconds and the AVG at 0.7 seconds (**Fig. 4.S9**). This agreement suggests that a clear peak in the cross-covariance was present for most flux periods leading to a convergence of the two methods. This lag time also shows agreement with the inlet response time of 0.9 s determined during dry N_2 overflows. Due to the convergence

of the determined lag times around a central value, a prescribed lag time of 0.9 s was used for all reported $v_d(O_3)$ values. A prescribed lag time has the least bias to extreme values caused by noise, provided that the true lag time is known well.[72] Deposition velocities were then recalculated with the prescribed lag time of 0.9 s and with the MAX and AVG method over a narrower lag window of ± 3 which is expected to be physically reasonable range for the flow rate and inlet line volume. The mean $v_d(O_3)$ using the prescribed, MAX, and AVG lag times were 0.013, 0.012, and 0.012 cm s^{-1} respectively, suggesting the campaign mean value was relatively insensitive to the lag time method.

4.3.4 Cospectra and Ogives

The frequency weighted cospectrum of O_3' with w' has a well characterized form with exhibited dependence on wind-speed and measuring height.[74] Comparison of observed cospectra shape against the idealized Kaimal cospectra is useful to validate that the observed signal was not significantly attenuated at low or high frequencies. Cospectral averaging is performed by binning frequency into 50 evenly log spaced bins and normalizing the integrated cospectra to 1. The integral of the unnormalized cospectra is the flux for that observation period. The mean wind-speed binned cospectra of sensible heat and O_3 appear to match well with the idealized Kaimal cospectra for an unstable boundary layer at sampling height z = 13m (**Fig. 4.11**).

The ogive is the normalized cumulative distribution of the cospectra, which is used to validate both that no high-frequency attenuation is present and that the flux averaging time is sufficiently long that all frequencies contributing for the flux is captured. **Figure 4.11** shows the averaged cospectra and ogives for O_3 and sensible heat flux from the average of two flux averaging periods 14:10 – 15:20 on July 20th. The asymptote to 1 at low frequencies validates that the 27-minute flux averaging time was sufficiently long for this site to capture the largest flux carrying eddies. High

pumping rates in sampling line ensured that turbulent flow was always maintained in the line (Reynolds number 3860-4940). Higher Reynolds numbers in the turbulent regime lead to smaller high frequency attenuation.[75] The overlap of the idealized Kaimal curve and the observed sensible heat and O_3 ogives suggest that high frequency attenuation in the sampling line is minimal above approximately 0.4 Hz, consistent with our calculated f_{cut} of 0.57 Hz. We calculate the high frequency correction transfer function for turbulent attenuation in a tube from Massman, (1991)[75] as a constraint, which is shown in **Fig. 4.11b**. This transfer function shows attenuation primarily above 1 Hz and is not sufficient to describe the observed attenuation above 0.4 Hz. This implies that the attenuation observed cannot be explained only as turbulent smearing in the inlet and that other wall interactions are likely present.

Due to the small magnitude of the O_3 EC flux there is low signal to noise in the cospectra at high frequency for many of the flux averaging periods. This makes application of cospectra based correction factors challenging and likely to introduce added variance on the signal. We therefore apply an attenuation correction factor following Bariteau et al., (2010). First we calculate the idealized unattenuated Kaimal cospectra (C_{wx_k}) (Eq. 7) for each flux period, and then apply frequency attenuation to that cospectra by applying a low-pass filter function ($H(f)$) characterized by τ_c (Eq. 8). The ratio of the flux of the unattenuated (F_{raw}) and attenuated (F_{att}) cospectra is then taken as the correction factor (A_f, Eq.9) to apply to the observed O_3 flux (Eq. 10). Where n is the surface layer normalized frequency defined as $n = f z/U$, where z is the measurement height and U is the horizontal wind speed. $F_{O_3,corr}$ is the attenuation corrected O_3 flux and $F_{O_3,obs}$ is the original measured flux. This approach has the benefit of applying a single correction factor to the total flux, rather than frequency dependent corrections which might serve to amplify noise at high

frequencies. The net impact of this correction factor was an increase of campaign mean $v_d(O_3)$ of 4%.

$$C_{wx\_k} = \frac{11n}{(1+11.3n)^{7/4}} \quad \text{E7.}$$

$$H(f) = [1 + (2\pi f \tau_c)^2]^{-1} \quad \text{E8.}$$

$$A_f = \frac{F_{raw}}{F_{att}} \frac{\int_0^{fn} C_{wx_k}(f)df}{\int_0^{fn} C_{wx_k}(f)\,[H(f)]^{1/2}\,df} \quad \text{E9.}$$

$$F_{O_3,corr} = A_f F_{O_3,obs} \quad \text{E10.}$$

We also calculate the attenuated flux from the model of Horst, (1997)[76] shown in Eq. 11, for a response time (τ_c) of 0.0.28 s, and a wind speed of 3 m s^{-1} to be 6%. The general agreement of the Horst and Bariteau attenuation correction factors indicate that the applied correction is reasonable.

$$\frac{F_m}{F_x} = \frac{1}{1+(2\pi n_m \tau_c U/z)^{\alpha}} \quad \text{E11}$$

Where F_m/F_x is the ratio of the measured flux to the unattenuated flux, U is wind speed, z is measurement height, and n_m and α are scaling factors for an unstable boundary layer taken as 0.085 and 7/8 respectively.

4.3.5 Uncertainty and flux limit of detection

Variance in the atmospheric O_3 signal was estimated by calculating the autocovariance of the signal during a 27-minute flux averaging period (**Fig. 4.S11**). Uncorrelated white noise only contributes to the first point in the autocovariance spectrum, while autocovariance at longer time shifts represents real atmospheric variance or correlated instrument drift [37,72]. For the analysed period, white noise is typically 45 to 65% of the total variance and atmospheric variance is 35 to 55%. This corresponds to a standard deviation from white noise $\sigma_{O_3,\,\text{noise}}$ of 0.4 ppbv.

The error in each flux averaging period (LOD_{σ}) can be determined by taking the standard deviation of the cross-covariance between vertical wind speed and mass spectrometer signal at lag times significantly longer than the calculated true lag time.[77,78] The random flux error is determined using lag windows of -150 to -180 and 150 to 180 s, which are significantly larger than the true lag time from sensor separation of 0.9 s as shown in **Figure 4.S12**. The selection of the -150 to -180 and 150 to 180 s lag windows is somewhat arbitrary and may still capture organized atmospheric structure that persists over long time periods. We also calculate the root mean squared deviation (LOD_{RMSE}) of the cross-covariance over the same lag windows as proposed by Langford et al., (2015), which captures the variance in the cross-covariance in those regions but also accounts for long term offsets from zero in the cross-covariance. The resulting error from the LOD_{σ} and LOD_{RMSE} methods showed good correlation (**Fig 4.S13**), with periods where the LOD_{RMSE} error is larger. We apply the RMSE method for our reported flux error determination. The final deposition velocity limit of detection was determined for each 27-minute flux averaging period by multiplying the LOD_{RMSE} error by 1.96 to give the flux limit-of-detection at the 95% confidence level. The flux error was then divided by the mean O_3 concentration for that averaging period to convert from flux to deposition velocity units. The campaign ensemble flux LOD_{RMSE} was 0.0027 cm s^{-1}, calculated using Eq. 12 following Langford et al.,(2015). A total of 59 out of 246 (24%) flux periods had deposition velocities below the campaign ensemble LOD. These values are still included in the reported mean $v_d(O_3)$.

$$\overline{\mathrm{LOD}} = \frac{1}{N}\sum_{i=1}^{N} \mathrm{LOD}^2 \qquad \text{E12}$$

4.3.6 Density fluctuation corrections

The Ox-CIMS measures O_3 as the apparent mixing ratio relative to moist air, as is true of all CIMS based measurements, which means fluctuations in the density of air due to changes in temperature,

pressure, and humidity could introduce a bias in the EC flux measurement.[79] The temperature and pressure in the Ox-CIMS and sampling lines were both actively controlled during sampling, making density fluctuations from those sources negligible. The long (20 m) inlet sampling line used likely also dampened a substantial portion of the water vapor flux. This has been demonstrated in an EC study utilizing a closed path H_2O sensor for EC flux measurements (through an 18 m long, 0.635 cm i.d. inlet, pumped at 18 slpm, comparable to the inlet used in this study) which showed complete attenuation above 0.1 Hz and overall attenuation of ~80% of the H_2O (latent heat) flux. [80] However, without a direct measure of water vapor fluctuations collocated with the Ox-CIMS this is difficult to definitively rule out in our measurement. We therefore calculate a conservative estimate of this correction factor from Eq 45b. in Webb et al., (1980)[79], assuming a latent heat flux of 50 W m^{-2} and neglecting the sensible heat term which is removed by active heating of the inlet. For a specific humidity of 12 g kg^{-1}, a temperature of 293 K, a pressure of 1 atm, and an O_3 mixing ratio of 40 ppbv, we calculate a flux correction term of 2.6 x 10^9 molecules cm^{-2} s^{-1}, which is 20% of our mean measured flux of -1.3 x 10^{10} molecules cm^{-2} s^{-1}. We expect that the actual density correction for our instrument much smaller given that water vapor fluctuations were likely dampened in the inlet line, and the high latent heat flux used in the calculation (50 W m^{-2}). Due to the uncertainty in this correction term for our instrument, we do not add it to our measured flux values and instead use the calculated value above as a conservative constraint on the magnitude. The addition of a Nafion drier on the inlet has been successfully implemented in other O_3 flux instruments to fully remove water fluctuations and will be used in future deployments of the Ox-CIMS [22].

4.3.7 Flux divergence

4.3.7.1 Surface NO emissions

The observed dry deposition velocity of ozone is potentially biased by simultaneous air-sea exchange of nitric oxide (NO). NO is expected to be emitted from the ocean on the order of 1 x 10^8 molecules cm^{-2} s^{-1} with dependence on dissolved surface nitrate and solar irradiance [29]. This NO source near the surface will cause titration of O_3 to NO_2 resulting in a positive bias for the observed $v_d(O_3)$. Assuming a maximum NO emission flux of 5 x 10^8 molecules cm^{-2} s^{-1} and that all NO reacts with O_3 before being advected to the sensor height, the resulting O_3 flux bias would be -5 x 10^8 molecules cm^{-2} s^{-1}. Our mean case of 40 ppbv O_3 and v_d (O_3) of 0.013 cm s^{-1} corresponds to a flux of -1.3 x 10^{10} molecules cm^{-2} s^{-1}. Therefore, the resulting bias in observed $v_d(O_3)$ from NO emissions is 3.8% or 4.9 x 10^{-4} cm s^{-1}. This value is an upper limit for expected ocean NO emissions and is well within the uncertainty of the observed $v_d(O_3)$. There is also potential for short term anthropogenic emissions of NO (such as from a boat engine passing by the sensor) to create a flux divergence term. We expect that the combination of signal despiking and the flux stationarity criteria described in Section 4.3.3 will minimize the impact of this potential divergence term. Despiking will remove most short term (<1 s) emission events and the stationarity criteria will filter out any period where longer term titration events cause large changes in the observed flux within a flux measurement period.

4.3.7.2 Free troposphere entrainment

The entrainment of O_3 enhanced or depleted air in the free troposphere to the marine boundary layer (MBL) creates a potential flux gradient that will contribute to the measured flux values at the near surface measurement height (z_o) of 13 m. Lenschow et al., (1982)[81] presented aircraft observations of O_3 deposition over the Gulf of Mexico at heights of 15, 60, and 325 m which

showed a strong flux gradient term driven by entrainment from the free troposphere. The boundary layer height (z_i) during those flights was approximately 1.2 km, suggests a strong flux gradient was present even within the surface layer (approximated as the lowest 10% of the boundary layer). The magnitude of this flux gradient depends on the magnitude of the O_3 concentration gradient (ΔC) and the entrainment velocity (w_e) of air from free troposphere into the MBL. Faloona et al., (2005)[8], reported entrainment velocities from 0.12 to 0.72 cm s^{-1} and an enhancement in O_3 (ΔC) of 20 ppbv in the free troposphere relative to the boundary layer in the summertime eastern subtropical pacific. Using those values and Equations 13and 14 below we calculate the percent fractional error from entrainment on the observed flux for a range of reasonable ΔC and w_e as shown in **Fig. 4.12** [37].

$$\frac{\Delta F_{0,est}}{F_0} = \frac{z}{z_i}\left(\frac{F_i}{F_0} - 1\right) \quad \text{E13}$$

$$F_i = w_e \Delta C \quad \text{E14}$$

Where z_i is the boundary layer height, z is the measurement height, and F_i and F_0 are the entrainment flux and surface flux respectively. We use the SIO measurement height (z) = 13 m and mean surface flux (F_o) = -5.2 x 10^{-3} ppbv m s^{-1} (from v_d = 0.013 cm s^{-1} and [O_3] = 40 ppbv), and an O_3 mixing ratio gradient (ΔC) from -20 to +20 ppbv in the free troposphere relative to the boundary layer. The resulting fractional error in our observed mean surface flux from Scripps Pier using the values from Faloona et al, 2005 (ΔC of +20 ppbv, MBL height of 800m) is 4.4% for w_e of 0.12 and 33% for 0.72 cm s^{-1}. This entrainment flux error is clearly significant for marine O_3 flux measurements assuming there is a gradient of O_3 in the free troposphere relative to boundary layer. This entrainment flux error is independent of the surface flux instrument measurement error and adds a systematic bias on the surface flux measurement. This calculation also makes clear that

marine O_3 measurements should be made as close to the surface as possible, and that the O_3 concentration gradient and entrainment rate should be explicitly measured if possible. We do not have an explicit measure of ΔC, w_e, or the MBL height so we tentatively assign entrainment error of up to 33% from the maximum values of those parameters reported in Faloona et al. (2005). We emphasize this source of uncertainty is independent of the O_3 sensor and is a systematic bias that should be considered in all O_3 air-sea exchange determinations.

4.4 Fast NO_2 measurements, eddy covariance and O_3 titration

Discussion of EC flux results have been limited to O_3 because ocean—atmosphere exchange of NO_2 is expected to be small and below the limit of detection of our instrument. The potential flux divergence from the reaction of O_3 with NO is also below the instrument flux limit of detection as discussed in section 4.3.6. However, over terrestrial surfaces where NO_2 emissions can be large, we expect this instrument would be well suited for measuring NO_2 flux. From Equations 15 and 16, following Bariteau et al., (2010)[22] and Lenschow and Kristensen, (1985)[82], we calculate the we calculate an expected flux LOD for the case where counting noise is the controlling term in the flux error. The calculated flux LOD is 4.3 x 10^9 molecules cm s^{-2} s^{-1} (1.6 pptv m s^{-1}) for an NO_2 mixing ratio of 1 ppbv and a friction velocity of 0.2 m s^{-1}.

$$F = C_a\sqrt{\frac{0.06u_*^2}{C_a\xi\Gamma}} \qquad \text{E15.}$$

$$\Gamma = \frac{a\,z}{U} \qquad \text{E16}$$

Where u_* is the friction velocity (m s^{-1}), C_a is the gas phase concentration (ppbv), ξ is the instrument sensitivity (cps $ppbv^{-1}$), and Γ is the integral time scale (s). Γ can be further expressed following Eq. 12 where a is constant taken as 0.3 for neutral conditions [82], z is the measurement

height (here 10 m), and *U* is the horizontal wind speed at that measurement height (taken as 5 m s^{-1}).

Observations of a short duration NO plume from a boat motor starting near our inlet at Scripps Pier highlights the utility of the simultaneous O_3 and NO_2 detection from this instrument (**Fig. 4.13**). Highly localized NO emissions were observed as the titration of O_3 and prompt production of NO_2. Observed total odd oxygen ($O_x = O_3 + NO_2$) was conserved during this titration event, where NO_2 and O_3 concentrations were determined from independent calibration factors and backgrounds. The 1:1 conversion of O_x from O_3 to NO_2 shown in **Fig. 4.13b**, validates the laboratory generated instrument calibration factors for O_3 and NO_2. The temporal agreement of the O_3 and NO_2 signals also demonstrates that both O_3 and NO_2 are transmitted through the inlet and detected with nearly identical instrument response times. This analysis assumes that there were no direct NO_2 emissions during the titration event. A NO_2 to NO_x emission ratio of 0.08 was observed for ship emissions from diesel motors on inland shipping vessels.[83] Without additional knowledge amount the NO_x emission source during this event, the observed conservation of total O_x could be partially driven by compensating errors within 10%. This simultaneous detection of both O_x species is likely also well suited for mobile sampling in the presence of dynamic NO emission sources, which challenge other fast ozone measurements. This method would also be well suited for direct measurement of flux divergence in the presence of strong surface NO emission sources.

4.5 Conclusions and Outlook

This study demonstrated the utility of oxygen anion chemical ionization mass spectrometry for the fast and sensitive detection of O_3 and NO_2. Field measurements of O_3 dry deposition to the ocean

surface from Scripps Pier, La Jolla CA demonstrate that this method has suitable time response, precision, and stability for successful EC measurements. The mean measured $v_d(O_3)$ with the Ox-CIMS is in within range of prior studies of O_3 ocean-atmosphere exchange. Further optimization and characterization of the Ox-CIMS is ongoing, including efforts to validate the specificity of the NO_2 detection, addition of a Nafion drier system, and better background determination methods. While this work has focused primarily on the deposition of O_3 to the ocean surface, the demonstrated instrument performance suggests the Ox-CIMS to be highly capable of O_3 and NO_2 flux measurements in the terrestrial biosphere and urban environments and from mobile platforms.

Acknowledgments

This work was supported by National Science Foundation (NSF) Grant GEO AGS 1829667.

The authors thank the staff at Scripps Pier, Scripps Institute of Oceanography and at the UW—Madison Department of Limnology for support in instrument deployments.

Glenn M. Wolfe is gratefully acknowledged for publicly providing a Matlab based “FluxToolbox” of analysis scripts, portions of which were altered for use in this analysis. Code is archived at https://github.com/AirChem

This research was performed using the computing resources and assistance of the UW-Madison Center for High Throughput Computing (CHTC) in the Department of Computer Sciences. The CHTC is supported by UW-Madison, the Advanced Computing Initiative, the Wisconsin Alumni Research Foundation, the Wisconsin Institutes for Discovery, and the National Science Foundation, and is an active member of the Open Science Grid, which is supported by the National Science Foundation and the U.S. Department of Energy's Office of Science.

References

(1) Ganzeveld, L.; Helmig, D.; Fairall, C. W.; Hare, J.; Pozzer, A. Atmosphere-Ocean Ozone Exchange: A Global Modeling Study of Biogeochemical, Atmospheric, and Waterside Turbulence Dependencies. *Global Biogeochem. Cycles* **2009**, *23* (4), 1–16. https://doi.org/10.1029/2008GB003301.

(2) Luhar, A. K.; Galbally, I. E.; Woodhouse, M. T.; Thatcher, M. An Improved Parameterisation of Ozone Dry Deposition to the Ocean and Its Impact in a Global Climate-Chemistry Model. *Atmos. Chem. Phys.* **2017**, *17* (5), 3749–3767. https://doi.org/10.5194/acp-17-3749-2017.

(3) Bey, I.; Jacob, D. J.; Yantosca, R. M.; Logan, J. A.; Field, B. D.; Fiore, A. M.; Li, Q.; Liu, H. Y.; Mickley, L. J.; Schultz, M. G. Global Modeling of Tropospheric Chemistry with Assimilated Meteorology: Model Description and Evaluation. *J. Geophys. Res. Atmos.* **2001**. https://doi.org/10.1029/2001JD000807.

(4) Emmons, L.; Lamarque, J.; Hess, P. G.; Pfister, G. Impact of Mexico City on Regional Air Quality from MOZART-4 Simulations and MILAGRO Observations. *Atmos. Chem. Phys. Discuss.* **2010**, *10*, 3457–3498.

(5) Lamarque, J. F.; Emmons, L. K.; Hess, P. G.; Kinnison, D. E.; Tilmes, S.; Vitt, F.; Heald, C. L.; Holland, E. A.; Lauritzen, P. H.; Neu, J.; et al. CAM-Chem: Description and Evaluation of Interactive Atmospheric Chemistry in the Community Earth System Model. *Geosci. Model Dev.* **2012**, *5* (2), 369–411. https://doi.org/10.5194/gmd-5-369-2012.

(6) Zhang, L.; Brook, J. R.; Vet, R. A Revised Parameterization for Gaseous Dry Deposition in Air-Quality Models. *Atmos. Chem. Phys.* **2003**. https://doi.org/10.5194/acp-3-2067-2003.

(7) Gallagher, M. W.; Beswick, K. M.; Coe, H. Ozone Deposition to Coastal Waters. *Q. J. R. Meteorol. Soc.* **2001**, *127* (572), 539–558. https://doi.org/10.1256/smsqj.57214.

(8) Faloona, I.; Lenschow, D. H.; Campos, T.; Stevens, B.; van Zanten, M.; Blomquist, B.; Thornton, D.; Bandy, A.; Gerber, H. Observations of Entrainment in Eastern Pacific Marine Stratocumulus Using Three Conserved Scalars. *J. Atmos. Sci.* **2005**, *62* (9), 3268–3285. https://doi.org/10.1175/JAS3541.1.

(9) Kawa, S. R.; Pearson, R. Ozone Budgets from the Dynamics and Chemistry of Marine Stratocumulus Experiment. *J. Geophys. Res.* **1989**, *94* (D7), 9809–9817. https://doi.org/10.1029/JD094iD07p09809.

(10) Lenschow, D. H.; Pearson, R.; Stankov, B. B. Estimating the Ozone Budget in the Boundary Layer by Use of Aircraft Measurements of Ozone Eddy Flux and Mean Concentration. *J. Geophys. Res.* **1981**, *86* (C8), 7291. https://doi.org/10.1029/JC086iC08p07291.

(11) Helmig, D.; Lang, E. K.; Bariteau, L.; Boylan, P.; Fairall, C. W.; Ganzeveld, L.; Hare, J.; Huebert, B. J.; Pallandt, M. Atmosphere-Ocean Ozone Fluxes during the TexAQS 2006, STRATUS 2006, GOMECC 2007, GasEx 2008, and AMMA 2008 Cruises. *J. Geophys. Res. Atmos.* **2012**, *117* (D4). https://doi.org/10.1029/2011JD015955.

(12) McKay, W. A.; Stephens, B. A.; Dollard, G. J. Laboratory Measurements of Ozone Deposition to Sea Water and Other Saline Solutions. *Atmos. Environ. Part A, Gen. Top.*

1992. https://doi.org/10.1016/0960-1686(92)90467-Y.

(13) Wesely, M. L.; Cook, D. R.; Williams, R. M. Field Measurement of Small Ozone Fluxes to Snow, Wet Bare Soil, and Lake Water. *Boundary-Layer Meteorol.* **1981**, *20* (4), 459–471. https://doi.org/10.1007/BF00122295.

(14) Helmig, D.; Ganzeveld, L.; Butler, T.; Oltmans, S. J. The Role of Ozone Atmosphere-Snow Gas Exchange on Polar, Boundary-Layer Tropospheric Ozone - A Review and Sensitivity Analysis. *Atmos. Chem. Phys.* **2007**, *7* (1), 15–30. https://doi.org/10.5194/acp-7-15-2007.

(15) Chang, W.; Heikes, B. G.; Lee, M. Ozone Deposition to the Sea Surface: Chemical Enhancement and Wind Speed Dependence. *Atmos. Environ.* **2004**, *38* (7), 1053–1059. https://doi.org/10.1016/j.atmosenv.2003.10.050.

(16) Fairall, C. W.; Helmig, D.; Ganzeveld, L.; Hare, J. Water-Side Turbulence Enhancement of Ozone Deposition to the Ocean. *Atmos. Chem. Phys.* **2007**, *7* (2), 443–451. https://doi.org/10.5194/acp-7-443-2007.

(17) Wesely, M. L.; Hicks, B. B. A Review of the Current Status of Knowledge on Dry Deposition. *Atmospheric Environment*. 2000. https://doi.org/10.1016/S1352-2310(99)00467-7.

(18) Fares, S.; McKay, M.; Holzinger, R.; Goldstein, A. H. Ozone Fluxes in a Pinus Ponderosa Ecosystem Are Dominated by Non-Stomatal Processes: Evidence from Long-Term Continuous Measurements. *Agric. For. Meteorol.* **2010**, *150* (3), 420–431. https://doi.org/10.1016/j.agrformet.2010.01.007.

(19) Fowler, D.; Flechard, C.; Cape, J. N.; Storeton-West, R. L.; Coyle, M. Measurements of Ozone Deposition to Vegetation Quantifying the Flux, the Stomatal and Non-Stomatal Components. *Water. Air. Soil Pollut.* **2001**. https://doi.org/10.1023/A:1012243317471.

(20) Kurpius, M. R.; Goldstein, A. H. Gas-Phase Chemistry Dominates O3 Loss to a Forest, Implying a Source of Aerosols and Hydroxyl Radicals to the Atmosphere. *Geophys. Res. Lett.* **2003**. https://doi.org/10.1029/2002GL016785.

(21) Muller, J. B. A.; Percival, C. J.; Gallagher, M. W.; Fowler, D.; Coyle, M.; Nemitz, E. Sources of Uncertainty in Eddy Covariance Ozone Flux Measurements Made by Dry Chemiluminescence Fast Response Analysers. *Atmos. Meas. Tech.* **2010**, *3* (1), 163–176. https://doi.org/10.5194/amt-3-163-2010.

(22) Bariteau, L.; Helmig, D.; Fairall, C. W.; Hare, J. E.; Hueber, J.; Lang, E. K. Determination of Oceanic Ozone Deposition by Ship-Borne Eddy Covariance Flux Measurements. *Atmos. Meas. Tech.* **2010**, *3* (2), 441–455. https://doi.org/10.5194/amt-3-441-2010.

(23) Pearson, R. Measuring Ambient Ozone with High Sensitivity and Bandwidth. *Rev. Sci. Instrum.* **1990**, *61* (2), 907–916. https://doi.org/10.1063/1.1141462.

(24) Keronen, P.; Reissell, A.; Rannik, Ü.¨; Pohja, T.; Siivola, E.; Hiltunen, V.; Hari, P.; Kulmala, M.; Vesala, T. Ozone Flux Measurements over a Scots Pine Forest Using Eddy Covariance Method: Performance Evaluation and Comparison with Flux-Profile Method. *Boreal Environ. Res.* **2003**, *8* (4), 425–443.

(25) Güsten, H.; Heinrich, G.; Schmidt, R. W. H.; Schurath, U. A Novel Ozone Sensor for Direct

Eddy Flux Measurements. *J. Atmos. Chem.* **1992**, *14* (1–4), 73–84. https://doi.org/10.1007/BF00115224.

(26) Tuovinen, J. P.; Ashmore, M. R.; Emberson, L. D.; Simpson, D. Testing and Improving the EMEP Ozone Deposition Module. In *Atmospheric Environment*; 2004. https://doi.org/10.1016/j.atmosenv.2004.01.026.

(27) Weinheimer, A. J. Chemical Methods: Chemiluminscence, Chemical Amplification, Electrochemistry, and Derivation. In *Analytical Techniques for Atmospheric Measurement*; 2007. https://doi.org/10.1002/9780470988510.ch7.

(28) Zahn, A.; Weppner, J.; Widmann, H.; Schlote-Holubek, K.; Burger, B.; Kühner, T.; Franke, H. A Fast and Precise Chemiluminescence Ozone Detector for Eddy Flux and Airborne Application. *Atmos. Meas. Tech.* **2012**, *5* (2), 363–375. https://doi.org/10.5194/amt-5-363-2012.

(29) Zafiriou, O. C.; McFarland, M. Nitric Oxide from Nitrite Photolysis in the Central Equatorial Pacific. *J. Geophys. Res.* **1981**, *86* (C4), 3173–3182. https://doi.org/10.1029/JC086iC04p03173.

(30) Yienger, J. J.; Levy, H. Empirical Model of Global Soil-Biogenic NO χ Emissions . *J. Geophys. Res.* **2004**. https://doi.org/10.1029/95jd00370.

(31) Dorsey, J. R.; Duyzer, J. H.; Gallagher, M. W.; Coe, H.; Pilegaard, K.; Weststrate, J. H.; Jensen, N. O.; Walton, S. Oxidized Nitrogen and Ozone Interaction with Forests. I : Experimental Observations and Analysis of Exchange with Douglas Fir. *Q. J. R. Meteorol. Soc.* **2004**. https://doi.org/10.1256/qj.03.124.

(32) Finco, A.; Coyle, M.; Nemitz, E.; Marzuoli, R.; Chiesa, M.; Loubet, B.; Fares, S.; Diaz-Pines, E.; Gasche, R.; Gerosa, G. Characterization of Ozone Deposition to a Mixed Oak-Hornbeam Forest - Flux Measurements at Five Levels above and inside the Canopy and Their Interactions with Nitric Oxide. *Atmos. Chem. Phys.* **2018**, *18* (24), 17945–17961. https://doi.org/10.5194/acp-18-17945-2018.

(33) Stella, P.; Kortner, M.; Ammann, C.; Foken, T.; Meixner, F. X.; Trebs, I. Measurements of Nitrogen Oxides and Ozone Fluxes by Eddy Covariance at a Meadow: Evidence for an Internal Leaf Resistance to NO2. *Biogeosciences* **2013**. https://doi.org/10.5194/bg-10-5997-2013.

(34) Kim, M. J.; Farmer, D. K.; Bertram, T. H. A Controlling Role for the Air-Sea Interface in the Chemical Processing of Reactive Nitrogen in the Coastal Marine Boundary Layer. *Proc Natl Acad Sci U S A* **2014**, *111* (11), 3943–3948. https://doi.org/10.1073/pnas.1318694111.

(35) Nguyen, T. B.; Crounse, J. D.; Teng, A. P.; St. Clair, J. M.; Paulot, F.; Wolfe, G. M.; Wennberg, P. O. Rapid Deposition of Oxidized Biogenic Compounds to a Temperate Forest. *Proc. Natl. Acad. Sci.* **2015**, *112* (5), E392–E401. https://doi.org/10.1073/pnas.1418702112.

(36) Wolfe, G. M.; Hanisco, T. F.; Arkinson, H. L.; Bui, T. P.; Crounse, J. D.; Dean-Day, J.; Goldstein, A.; Guenther, A.; Hall, S. R.; Huey, G.; et al. Quantifying Sources and Sinks of Reactive Gases in the Lower Atmosphere Using Airborne Flux Observations. *Geophys. Res.*

Lett. **2015**, *42* (19), 8231–8240. https://doi.org/10.1002/2015gl065839.

(37) Blomquist, B. W.; Huebert, B. J.; Fairall, C. W.; Faloona, I. C. Determining the Sea-Air Flux of Dimethylsulfide by Eddy Correlation Using Mass Spectrometry. *Atmos. Meas. Tech.* **2010**, *3* (1), 1–20. https://doi.org/10.5194/amt-3-1-2010.

(38) Kim, M. J.; Novak, G. A.; Zoerb, M. C.; Yang, M.; Blomquist, B. W.; Huebert, B. J.; Cappa, C. D.; Bertram, T. H. Air-Sea Exchange of Biogenic Volatile Organic Compounds and the Impact on Aerosol Particle Size Distributions. *Geophys. Res. Lett.* **2017**, *44* (8), 3887–3896. https://doi.org/10.1002/2017GL072975.

(39) Yang, M.; Beale, R.; Smyth, T.; Blomquist, B. Measurements of OVOC Fluxes by Eddy Covariance Using a Proton-Transfer- Reaction Mass Spectrometer-Method Development at a Coastal Site. *Atmos. Chem. Phys.* **2013**, *13* (13), 6165–6184. https://doi.org/10.5194/acp-13-6165-2013.

(40) Bertram, T. H.; Kimmel, J. R.; Crisp, T. A.; Ryder, O. S.; Yatavelli, R. L. N.; Thornton, J. A.; Cubison, M. J.; Gonin, M.; Worsnop, D. R. A Field-Deployable, Chemical Ionization Time-of-Flight Mass Spectrometer. *Atmos. Meas. Tech.* **2011**, *4* (7), 1471–1479. https://doi.org/10.5194/amt-4-1471-2011.

(41) Bertram, T. H.; Kimmel, J. R.; Crisp, T. A.; Ryder, O. S.; Yatavelli, R. L. N.; Thornton, J. A.; Cubison, M. J.; Gonin, M.; Worsnop, D. R. A Field-Deployable, Chemical Ionization Time-of-Flight Mass Spectrometer. *Atmos. Meas. Tech.* **2011**, *4* (7), 1471–1479. https://doi.org/10.5194/amt-4-1471-2011.

(42) Huey, L. G. The Kinetics of the Reaction of Cl-, O-, and O2- with HNO3: Implications for Measurements of HNO3 in the Atmosphere. *Int. J. Mass Spectrom.* **1996**, *153*, 145–150.

(43) O'Sullivan, D. W.; Silwal, I. K. C.; McNeill, A. S.; Treadaway, V.; Heikes, B. G. Quantification of Gas Phase Hydrogen Peroxide and Methyl Peroxide in Ambient Air: Using Atmospheric Pressure Chemical Ionization Mass Spectrometry with O2−, and O2−(CO2) Reagent Ions. *Int. J. Mass Spectrom.* **2018**. https://doi.org/10.1016/j.ijms.2017.11.015.

(44) Vermeuel, M. P.; Novak, G. A.; Alwe, H. D.; Hughes, D. D.; Kaleel, R.; Dickens, A. F.; Kenski, D.; Czarnetzki, A. C.; Stone, E. A.; Stanier, C. O.; et al. Sensitivity of Ozone Production to NOx and VOC Along the Lake Michigan Coastline. *J. Geophys. Res. Atmos.* **2019**, *124* (20), 10989–11006. https://doi.org/10.1029/2019JD030842.

(45) Voisin, D.; Smith, J. N.; Sakurai, H.; McMurry, P. H.; Eisele, F. L. Thermal Desorption Chemical Ionization Mass Spectrometer for Ultrafine Particle Chemical Composition. *Aerosol Sci. Technol.* **2003**, *37* (6), 471–475. https://doi.org/10.1080/02786820300959.

(46) Porter, J. G.; De Bruyn, W.; Saltzman, E. S. Eddy Flux Measurements of Sulfur Dioxide Deposition to the Sea Surface. *Atmos. Chem. Phys.* **2018**, *18* (20), 15291–15305. https://doi.org/10.5194/acp-18-15291-2018.

(47) Thornton, D. C.; Bandy, A. R.; Tu, F. H.; Blomquist, B. W.; Mitchell, G. M.; Nadler, W.; Lenschow, D. H. Fast Airborne Sulfur Dioxide Measurements by Atmospheric Pressure Ionization Mass Spectrometry (APIMS). *J. Geophys. Res. Atmos.* **2002**.

https://doi.org/10.1029/2002JD002289.

(48) Ervin, K. M.; Anusiewicz, I.; Skurski, P.; Simons, J.; Lineberger, W. C. The Only Stable State of O2- Is the X 2∏g Ground State and It (Still!) Has an Adiabatic Electron Detachment Energy of 0.45 EV. *J. Phys. Chem. A* **2003**, *107* (41), 8521–8529. https://doi.org/10.1021/jp0357323.

(49) Rienstra-Kiracofe, J. C.; Tschumper, G. S.; Schaefer, H. F.; Nandi, S.; Ellison, G. B. Atomic and Molecular Electron Affinities: Photoelectron Experiments and Theoretical Computations. *Chem. Rev.* **2002**, *102* (1), 231–282. https://doi.org/10.1021/cr990044u.

(50) Lee, B. H.; Lopez-Hilfiker, F. D.; Mohr, C.; Kurtén, T.; Worsnop, D. R.; Thornton, J. A. An Iodide-Adduct High-Resolution Time-of-Flight Chemical-Ionization Mass Spectrometer: Application to Atmospheric Inorganic and Organic Compounds. *Environ. Sci. Technol.* **2014**, *48* (11), 6309–6317. https://doi.org/10.1021/es500362a.

(51) Bork, N.; Kurtén, T.; Enghoff, M. B.; Pedersen, J. O. P.; Mikkelsen, K. V.; Svensmark, H. Ab Initio Studies of O - 2 (H 2O) n and O - 3 (H 2O) n Anionic Molecular Clusters, ≤12. *Atmos. Chem. Phys.* **2011**, *11* (14), 7133–7142. https://doi.org/10.5194/acp-11-7133-2011.

(52) Brophy, P.; Farmer, D. K. Clustering, Methodology, and Mechanistic Insights into Acetate Chemical Ionization Using High-Resolution Time-of-Flight Mass Spectrometry. *Atmos. Meas. Tech.* **2016**, *9* (8), 3969–3986. https://doi.org/10.5194/amt-9-3969-2016.

(53) Arnold, D. W.; Xu, C.; Kim, E. H.; Neumark, D. M. Study of Low-Lying Electronic States of Ozone by Anion Photoelectron Spectroscopy of O 3-. *J. Chem. Phys.* **1994**, *101* (2), 912–922. https://doi.org/10.1063/1.467745.

(54) Ewing, R. G.; Waltman, M. J. Production and Utilization of CO3 - Produced by a Corona Discharge in Air for Atmospheric Pressure Chemical Ionization. *Int. J. Mass Spectrom.* **2010**, *296* (1–3), 53–58. https://doi.org/10.1016/j.ijms.2010.08.024.

(55) Ervin, K. M.; Ho, J.; Lineberger, W. C. Ultraviolet Photoelectron Spectrum of Nitrite Anion. *J. Phys. Chem.* **1988**, *92* (19), 5405–5412. https://doi.org/10.1021/j100330a017.

(56) Liu, W. T.; Tang, W.; Niler, P. P. Humidity Profiles over the Ocean. *J. Clim.* **1991**, *4* (10), 1023–1034.

(57) Veres, P.; Roberts, J. M.; Warneke, C.; Welsh-Bon, D.; Zahniser, M.; Herndon, S.; Fall, R.; de Gouw, J. Development of Negative-Ion Proton-Transfer Chemical-Ionization Mass Spectrometry (NI-PT-CIMS) for the Measurement of Gas-Phase Organic Acids in the Atmosphere. *Int. J. Mass Spectrom.* **2008**, *274* (1–3), 48–55. https://doi.org/10.1016/j.ijms.2008.04.032.

(58) Hunton, D. E.; Hofmann, M.; Lindeman, T. G.; Castleman, A. W. Photodissociation Dynamics of CO3-. **1985**, *82* (1), 134–150.

(59) Snodgrass, J. T.; Roehl, C. M.; Van Koppen, P. A. M.; Palke, W. E.; Bowers, M. T. Photodissociation of CO3-: Product Kinetic Energy Measurements as a Probe of Excited State Potential Surfaces and Dissociation Dynamics. *J. Chem. Phys.* **1990**, *92* (10), 5935–5943. https://doi.org/10.1063/1.458363.

(60) Reiner, T.; Möhler, O.; Arnold, F. Improved Atmospheric Trace Gas Measurements with

an Aircraft-Based Tandem Mass Spectrometer: Ion Identification by Mass-Selected Fragmentation Studies. *J. Geophys. Res. Atmos.* **1998**, *103* (D23), 31309–31320. https://doi.org/10.1029/1998JD100003.

(61) Thornton, J. A.; Wooldridge, P. J.; Cohen, R. C. Atmospheric NO 2 : In Situ Laser-Induced Fluorescence Detection at Parts per Trillion Mixing Ratios . *Anal. Chem.* **2002**, *72* (3), 528–539. https://doi.org/10.1021/ac9908905.

(62) Werle, P.; Miicke, R.; Slemr, F. The Limits of Signal Averaging in Atmospheric Trace-Gas Monitoring by Tunable Diode-Laser Absorption Spectroscopy (TDLAS). **1993**, *139*, 131–139.

(63) Kleindienst, T. E.; Hudgens, E. E.; Smith, D. F.; McElroy, F. F.; Bufalini, J. J. Comparison of Chemiluminescence and Ultraviolet Ozone Monitor Responses in the Presence of Humidity and Photochemical Pollutants. *Air Waste* **1993**, *43* (2), 213–222. https://doi.org/10.1080/1073161X.1993.10467128.

(64) Ikawa, H.; Oechel, W. C. Temporal Variations in Air-Sea CO2 Exchange near Large Kelp Beds near San Diego, California. *J. Geophys. Res. Ocean.* **2015**, *120* (1), 50–63. https://doi.org/10.1002/2014JC010229.

(65) Ellis, R. a; Murphy, J. G.; Pattey, E.; Haarlem, R. Van; Brien, J. M. O. Characterizing a Quantum Cascade Tunable Infrared Laser Di Ff Erential Absorption Spectrometer (QC-TILDAS) for Measurements of Atmospheric Ammonia. *Atmos. Meas. Tech.* **2010**, No. x, 3309–3338.

(66) Barr, A. G.; Richardson, A. D.; Hollinger, D. Y.; Papale, D.; Arain, M. A.; Black, T. A.; Bohrer, G.; Dragoni, D.; Fischer, M. L.; Gu, L.; et al. Use of Change-Point Detection for Friction-Velocity Threshold Evaluation in Eddy-Covariance Studies. *Agric. For. Meteorol.* **2013**, *171–172*, 31–45. https://doi.org/10.1016/j.agrformet.2012.11.023.

(67) Foken, T.; Wichura, B. Tools for Quality Assessment of Surface-Based Flux Measurements. *Agric. For. Meteorol.* **1996**, *78* (1–2), 83–105. https://doi.org/10.1016/0168-1923(95)02248-1.

(68) Fairall, C. W.; Yang, M.; Bariteau, L.; Edson, J. B.; Helmig, D.; McGillis, W.; Pezoa, S.; Hare, J. E.; Huebert, B.; Blomquist, B. Implementation of the Coupled Ocean-Atmosphere Response Experiment Flux Algorithm with CO2, Dimethyl Sulfide, and O3. *J. Geophys. Res. Ocean.* **2011**, *116* (10). https://doi.org/10.1029/2010JC006884.

(69) Papale, D.; Reichstein, M.; Aubinet, M.; Canfora, E.; Bernhofer, C.; Kutsch, W.; Longdoz, B.; Rambal, S.; Valentini, R.; Vesala, T.; et al. Towards a Standardized Processing of Net Ecosystem Exchange Measured with Eddy Covariance Technique: Algorithms and Uncertainty Estimation. *Biogeosciences* **2006**, *3* (4), 571–583. https://doi.org/10.5194/bg-3-571-2006.

(70) Mauder, M.; Cuntz, M.; Drüe, C.; Graf, A.; Rebmann, C.; Schmid, H. P.; Schmidt, M.; Steinbrecher, R. A Strategy for Quality and Uncertainty Assessment of Long-Term Eddy-Covariance Measurements. *Agric. For. Meteorol.* **2013**, *169*, 122–135. https://doi.org/10.1016/j.agrformet.2012.09.006.

(71) Wilczak, J. M.; Oncley, S. P.; Stage, S. A. Sonic Anemometer Tilt Correction Algorithms. *Boundary-Layer Meteorol.* **2001**, *99* (1), 127–150. https://doi.org/10.1023/a:1018966204465.

(72) Langford, B.; Acton, W.; Ammann, C.; Valach, A.; Nemitz, E. Eddy-Covariance Data with Low Signal-to-Noise Ratio: Time-Lag Determination, Uncertainties and Limit of Detection. *Atmos. Meas. Tech.* **2015**, *8* (10), 4197–4213. https://doi.org/10.5194/amt-8-4197-2015.

(73) Taipale, R.; Ruuskanen, T. M.; Rinne, J. Lag Time Determination in DEC Measurements with PTR-MS. *Atmos. Meas. Tech.* **2010**. https://doi.org/10.5194/amt-3-853-2010.

(74) Kaimal, J. C.; Wyngaard, J. C.; Izumi, Y.; Coté, O. R. Spectral Characteristics of Surface-layer Turbulence. *Q. J. R. Meteorol. Soc.* **1972**, *98* (417), 563–589. https://doi.org/10.1002/qj.49709841707.

(75) Massman, W. J. The Attenuation of Concentration Fluctuations in Turbulent Flow through a Tube. *J. Geophys. Res. Atmos.* **1991**, *96* (D8), 15269–15273. https://doi.org/10.1029/91JD01514.

(76) Horst, T. W. A Simple Formula for Attenuation of Eddy Fluxes Measured with First-Order-Response Scalar Sensors. *Boundary-Layer Meteorol.* **1997**, *82* (2), 219–233. https://doi.org/10.1023/A:1000229130034.

(77) Spirig, C.; Neftel, A.; Ammann, C.; Dommen, J.; Grabmer, W.; Thielmann, A.; Schaub, A.; Beauchamp, J.; Wisthaler, A.; Hansel, A. Eddy Covariance Flux Measurements of Biogenic VOCs during ECHO 2003 Using Proton Transfer Reaction Mass Spectrometry. *Atmos. Chem. Phys.* **2005**, *5*, 465–481. https://doi.org/10.5194/acp-5-465-2005.

(78) Wienhold, F. G.; Welling, M.; Harris, G. W. Micrometeorological Measurement and Source Region Analysis of Nitrous Oxide Fluxes from an Agricultural Soil. *Atmos. Environ.* **1995**, *29* (17), 2219–2227. https://doi.org/10.1016/1352-2310(95)00165-U.

(79) Webb, E. K.; Pearman, G. I.; Leuning, R. Correction of Flux Measurements for Density Effects Due to Heat and Water Vapour Transfer. *Q. J. Roy. Meteorol. Soc.* **1980**, *106* (447), 85–100. https://doi.org/http://dx.doi.org/10.1002/qj.49710644707.

(80) Yang, M.; Prytherch, J.; Kozlova, E.; Yelland, M. J.; Parenkat Mony, D.; Bell, T. G. Comparison of Two Closed-Path Cavity-Based Spectrometers for Measuring Air-Water CO2 and CH4 Fluxes by Eddy Covariance. *Atmos. Meas. Tech.* **2016**, *9* (11), 5509–5522. https://doi.org/10.5194/amt-9-5509-2016.

(81) Lenschow, D. H.; Pearson, R. J.; Stankov, B. B. Measurements of Ozone Vertical Flux to Ocean and Forest. *J. Geophys. Res.* **1982**, *87* (C11), 8833–8837. https://doi.org/10.1029/JC087iC11p08833.

(82) Lenschow, D. H.; Kristensen, L. Uncorrelated Noise in Turbulence Measurements. *J. Atmos. Ocean. Technol.* **1985**, *2*, 68–81. https://doi.org/https://doi.org/10.1175/1520-0426(1985)002<0068:UNITM>2.0.CO;2.

(83) Kurtenbach, R.; Vaupel, K.; Kleffmann, J.; Klenk, U.; Schmidt, E.; Wiesen, P. Emissions of NO, NO2 and PM from Inland Shipping. *Atmos. Chem. Phys.* **2016**, *16* (22), 14285–14295. https://doi.org/10.5194/acp-16-14285-2016.

Figures

Species	Normalized Sensitivity (8 g kg^{-1} SH, 1σ)	Absolute Sensitivity (8 g kg^{-1} SH)	LOD optimum	LOD (1 Hz)	LOD (10 Hz)	Background (cps, 1σ)	Precision (10 Hz)	Field Calibration R^2
O_3	12.4 ± 1.2 ncps $pptv^{-1}$	180 cps $pptv^{-1}$	4.0 pptv (11s)	13 pptv	42 pptv	3.1×10^5 ± 5.0×10^4	0.74%	0.99
NO_2	6.7 ± 1.0 ncps $pptv^{-1}$	97 cps $pptv^{-1}$	2.3 pptv (19s)	9.9 pptv	32 pptv	5.1×10^4 ± 1×10^4	1.1%	— — —

Table 4.1. Summary of instrument sensitivity, precision, and accuracy for detection of O_3 and NO_2 from laboratory calibrations. Sensitivity is reported at a specific humidity (SH) of 8 g kg^{-1} which corresponds to 40% RH at 25 °C. All limits of detection (LOD) are for a S/N = 3. The optimum LOD is reported as the LOD at the optimum averaging time determined by the minimum of the Allan variance spectrum. Optimum averaging times were determined to be 11 s for O_3 and 19 s for NO_2. The reported field comparison (R^2) is from a regression of 1-minute bin averaged ozone concentration from the Ox-CIMS with an EPA (Thermo-Fisher 49i) monitor in Zion, Il during four weeks of ambient observation shown in **Fig. 4.7**.

Species	Concentration Mean (ppb) & 1σ range	5^{th} to 95^{th} percentile Concentration Range (ppbv)	v_d mean (cm s^{-1})	v_d 20-80% range (cm s^{-1})	v_d LOD 1.96σ (cm s^{-1})
O_3	41.2± 10.1	28.9 – 67.1	0.013	-0.0011 – 0.027	0.0027
NO_2	4.7 ± 5.5	0.45-16.9	----------	----------	----------

Table 4.2. Overview of flux and concentration measurements of O_3 and NO_2 from Scripps Pier. Concentration ranges are reported for all periods of onshore winds. Flux results are reported only for final quality-controlled flux periods Ozone mean deposition velocity (v_d) was well resolved from the campaign ensemble average LOD of 0.0027 cm s^{-1}. Reported v_d LOD is the ensemble mean of the LOD determined by the RMSE method at long lag times for each 27-minute flux period. 24% of quality-controlled flux periods fell below the campaign ensemble LOD. Deposition velocity of NO_2 across the air-sea interface is expected to be small (<0.002 cm s^{-1}) and was consistently below the LOD of our instrument so no values are reported here.

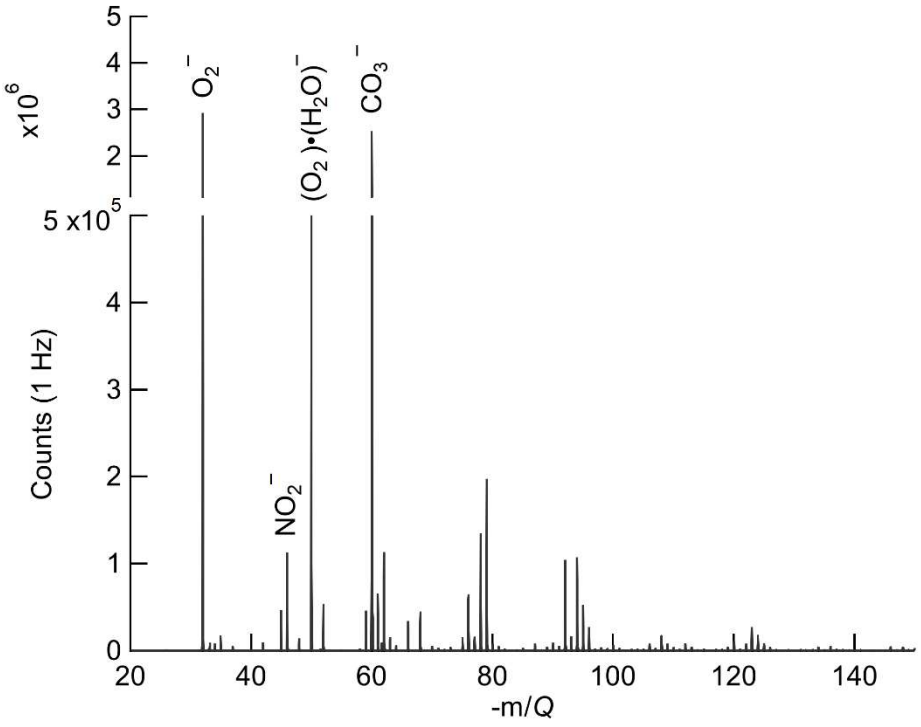

Figure 4.1. Ox-CIMS mass spectra collected at 1 Hz and mass resolution of 950 *M/ΔM* (at –60 m/*Q*), with major peaks highlighted. $\mathbf{O_2^-}$ **and** $\mathbf{O_2(H_2O)^-}$ at –32 m/*Q* and –50 m/*Q* respectively are the two observed forms of the reagent ion. The detected ozone product ($\mathbf{CO_3^-}$, –60 m/Q) is of comparable magnitude to the $\mathbf{O_2^-}$ reagent ion during ambient sampling. NO_2 is detected as the charge transfer product $\mathbf{NO_2^-}$ at –46 m/*Q*. Masses greater than –150 m/*Q* contribute less than 2% to the total signal and are not plotted.

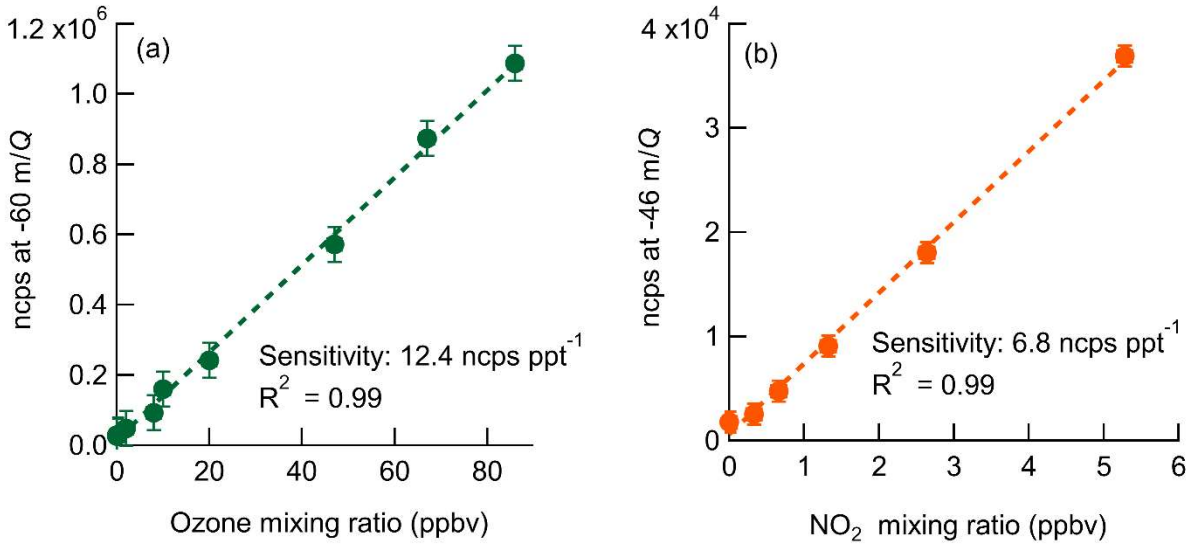

Figure 4.2. Normalized calibration curves of O_3 (**a**) and NO_2 (**b**) at 8 g kg^{-1} specific humidity (approximately 40% RH at 25 °C). Ozone is detected as $\mathbf{CO_3^-}$ at –60 m/Q. NO_2 is detected as the charge transfer product ($\mathbf{NO_2^-}$) at –46 m/Q. Error bars are the standard deviation in normalized count rate for each measurement point.

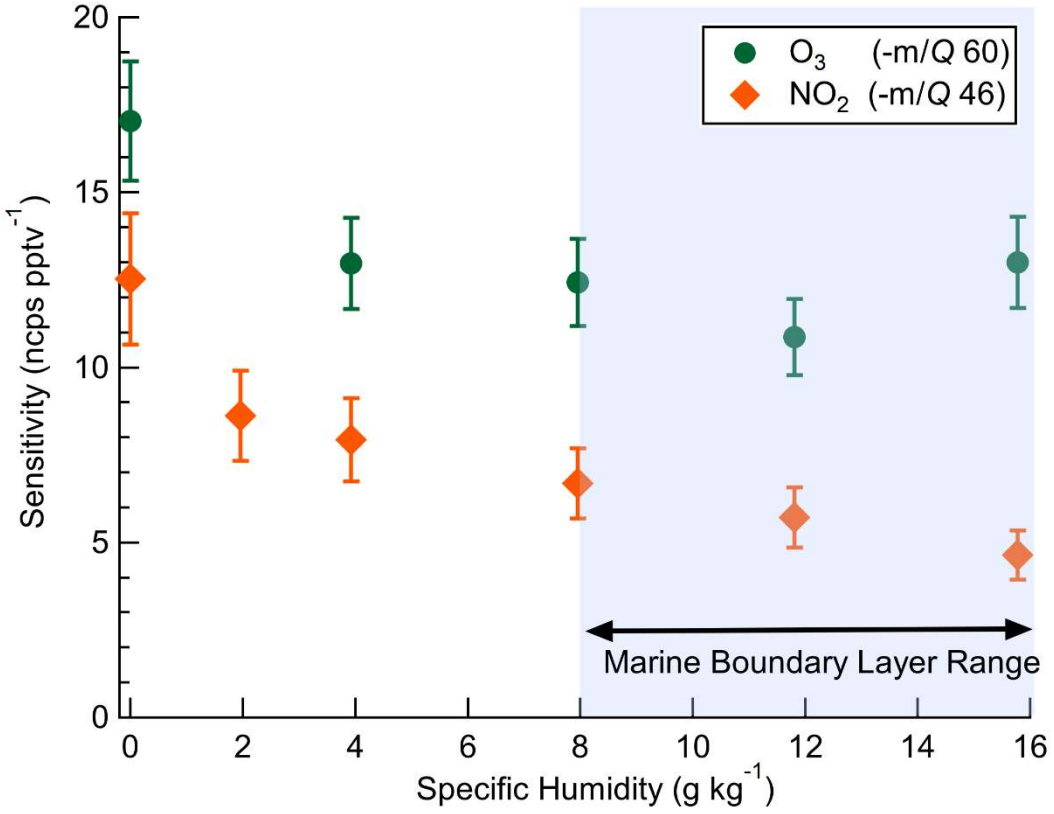

Figure 4.3. Dependence of O_3 and NO_2 sensitivities on specific humidity. Error bars indicate standard deviation of triplicate calibration curves. The blue shaded region from SH 8–16 g kg^{-1} is the approximate typical range of specific humidity in the mid-latitude marine boundary layer.

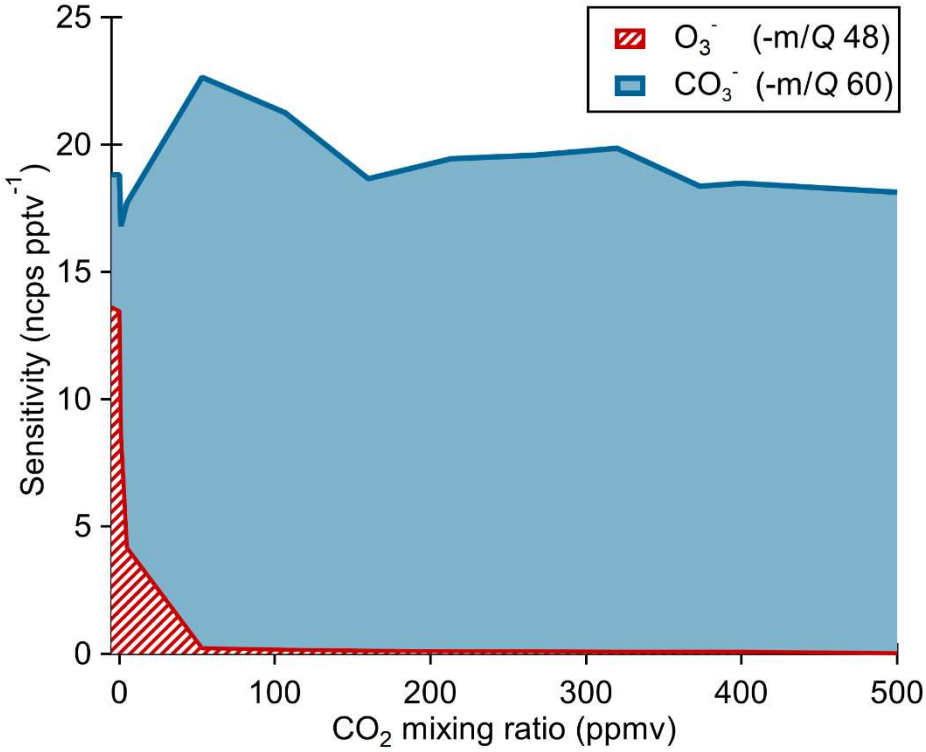

Figure 4.4. Ox-CIMS cumulative sensitivity to O_3 detected either directly as $\mathbf{O_3^-}$ or as $\mathbf{CO_3^-}$ as a function of CO_2 mixing ratio. The sum of sensitivity as $\mathbf{O_3^-}$ and $\mathbf{CO_3^-}$ shows that total sensitivity to O_3 is conserved as the product distribution shifts with CO_2 mixing ratio. Greater than 99% of O3 is observed as $\mathbf{CO_3^-}$ at CO_2 mixing ratios greater than 60 ppmv.

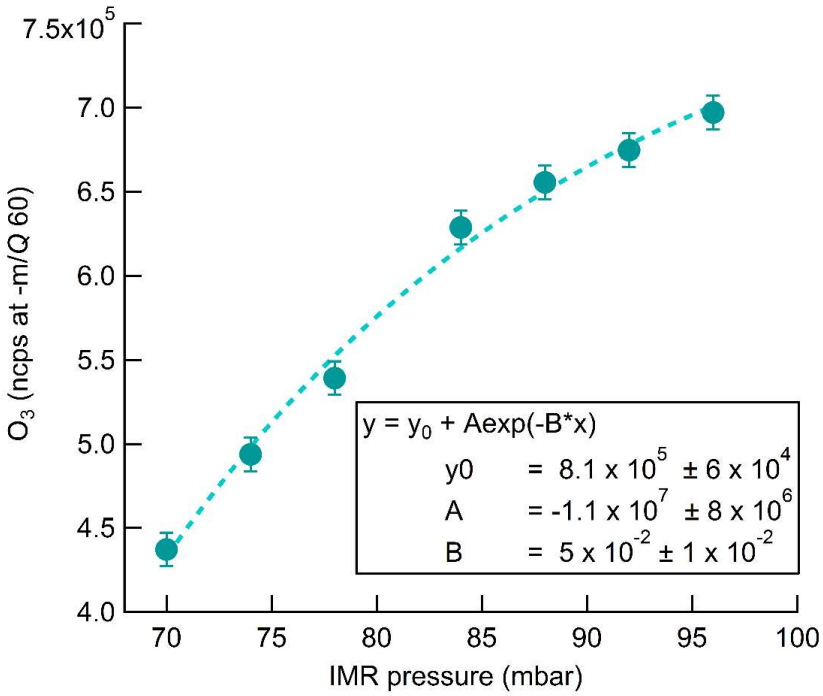

Figure 4.5. Normalized count rate of $\mathbf{CO_3^-}$ (–60 m/Q) ozone detection product as a function of pressure in the IMR during sampling of a constant 35 ppbv O_3 source. The exponential fit of the data is shown by the dashed line. Fit parameters are included to allow for calculation of potential sensitivity improvements with further increase in IMR pressure.

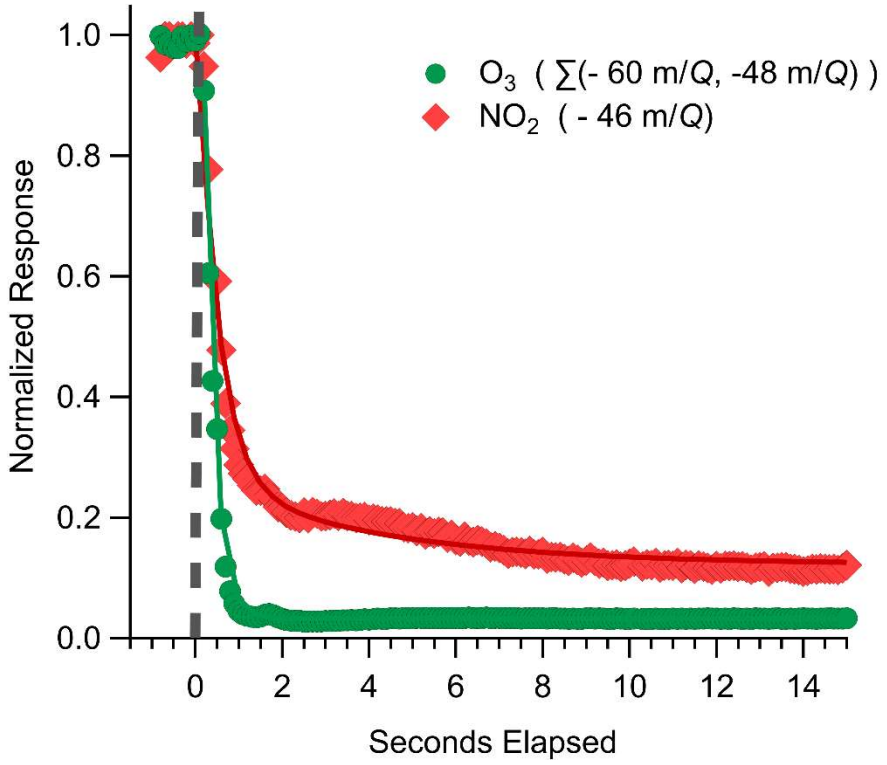

Figure 4.6. Representative instrument backgrounding determination for O_3 and NO_2 where the inlet was rapidly switched from ambient sampling to an overflow with dry UHP N_2 indicated by the grey dashed line. O_3 response is fit to an exponential decay, plotted as solid lines with a mean response time of 0.28 s.,NO_2 is fit to a bi-exponential decay where the initial rapid decay ($\boldsymbol{\tau_1}$) in attributed to gas evacuation of the inlet line and the second slower decay ($\boldsymbol{\tau_2}$) is attributed to equilibration with the inlet walls. Best fit estimates for $\boldsymbol{\tau_1}$ of NO_2 from 0.7 to 1.2 seconds. $\boldsymbol{\tau_2}$ for NO_2 was determined to be 3.2 s for this decay period.

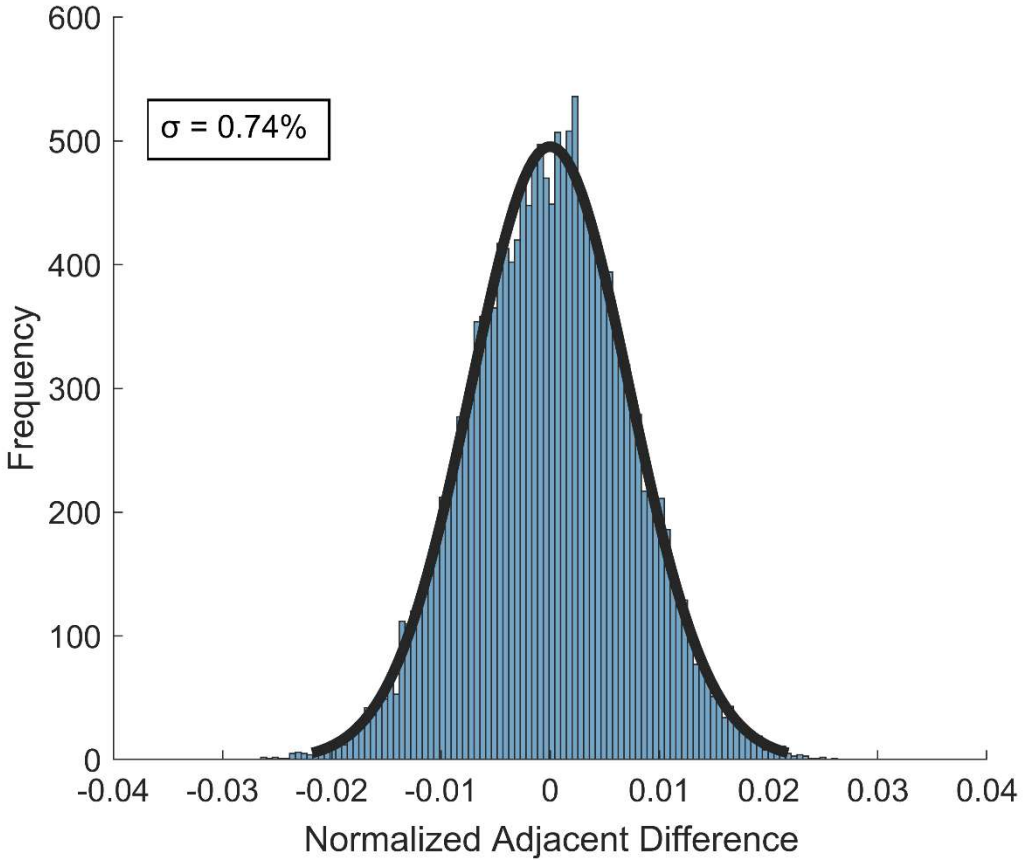

Figure 4.7. Distribution of normalized adjacent differences measured at 10 Hz during a stable 27-minute ambient sampling period of 38 ppbv O_3 from Scripps Pier. The 1σ value of the distribution gives an upper limit of instrument precision of 0.74%.

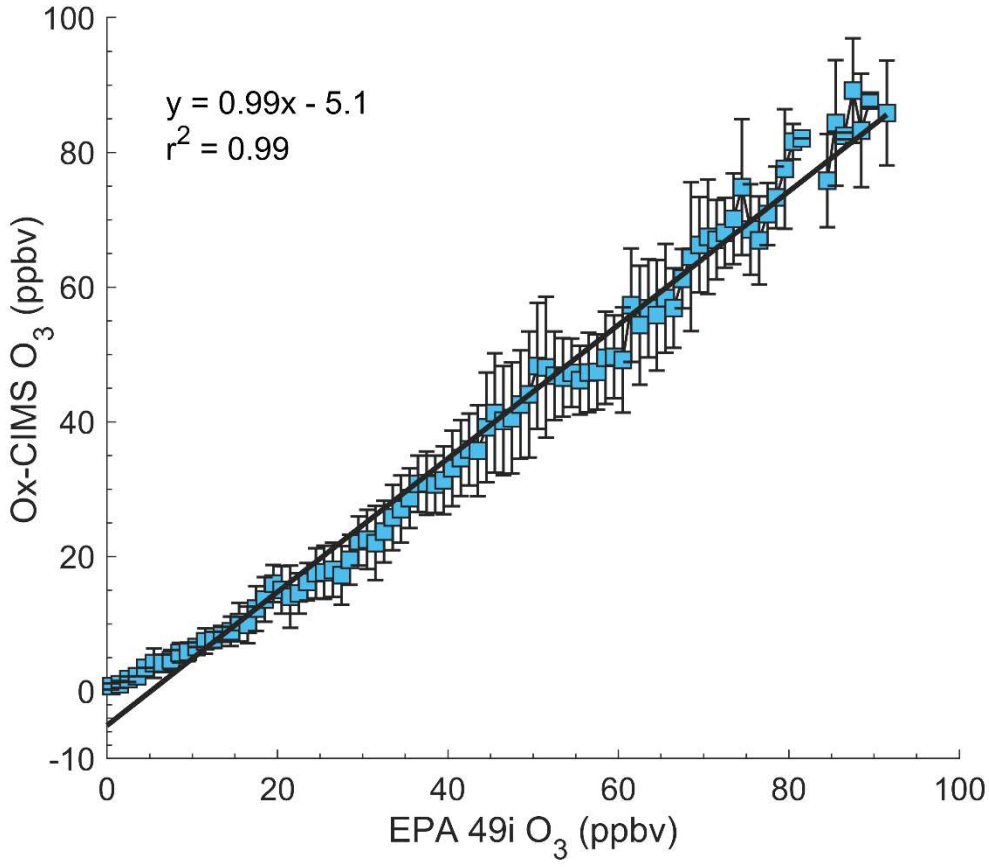

Figure 4.8. Regression of 1-minute average O_3 mixing ratios from the Ox-CIMS against an EPA O_3 monitor (Thermo-Fisher 49i) binned to 1 ppbv over four weeks of ambient sampling in Zion, Illinois in May- June 2017. The solid black line is the linear least-squares regression. Error bars represent the standard deviation of each bin. Instrument agreement is strong for O_3 greater than 10 ppbv, with an apparent bias in one or both instruments below 10 ppbv.

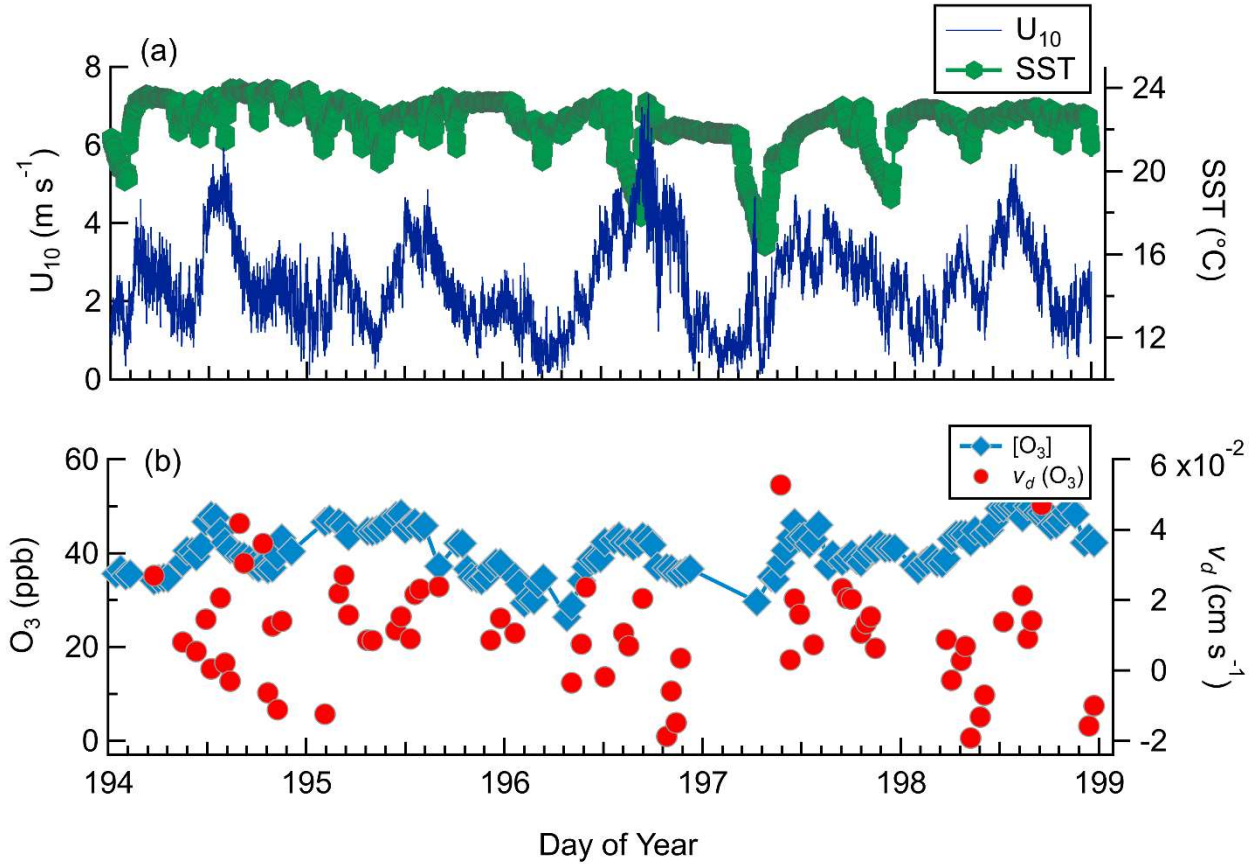

Figure 4.9. Observed meteorology and O_3 mixing ratio and deposition velocities for DOY 194-199 from Scripps Pier (**a**) Horizontal wind speed (U_{10}) and sea-surface temperature (SST). (**b**) O_3 mixing ratios and $v_d(O_3)$.

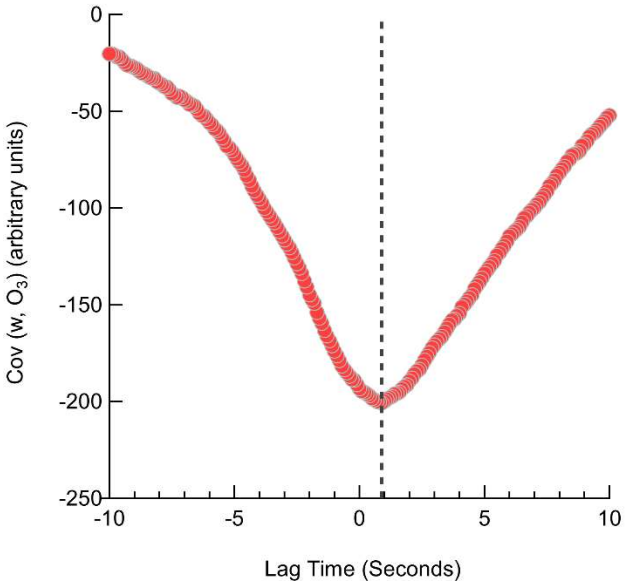

Figure 4.10. Lag time determination for an individual 27-minute O_3 flux averaging period. The lag time for this flux period determined from the maximum of the covariance to be 0.9 seconds which compares reasonably with the volumetric evacuation time of the inlet of 1.7 to 2.1 seconds.

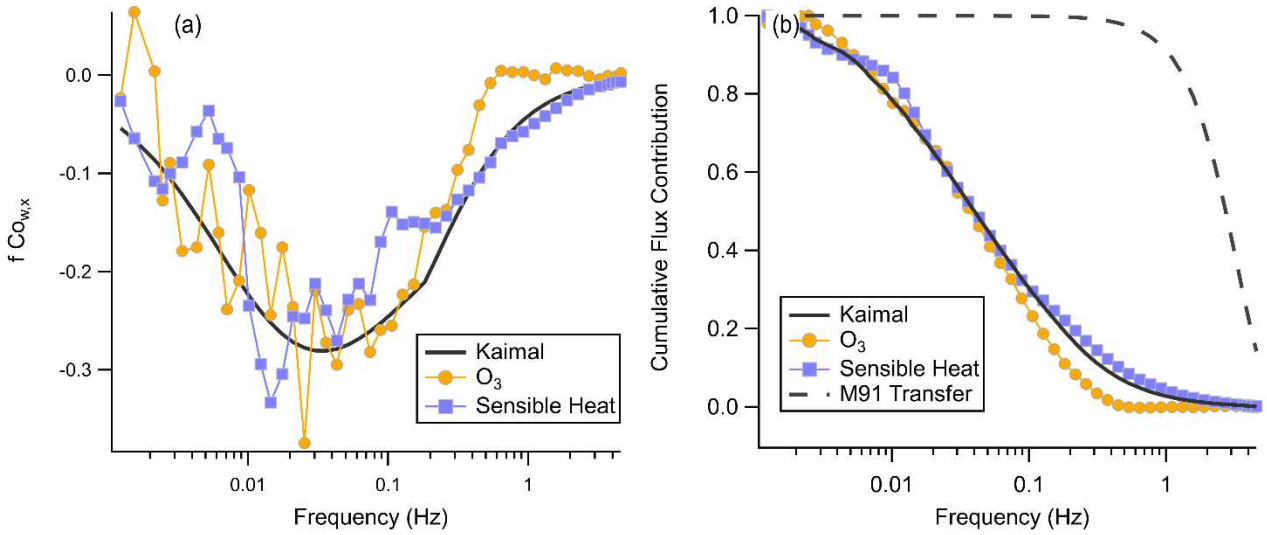

Figure 4.11. (**a**) Mean binned frequency weighted cospectra O_3 and sensible heat flux with vertical wind from the average of two consecutive flux periods from 14:10 – 15:20 local time on July 20th. The Kaimal trace is the idealized cospectra Kaimal et al. (1972) for mean windspeed of 4.4 m s^{-1} and an unstable atmosphere. The sensible heat trace is inverted, and the observed net sensible heat flux was positive for this period (**b**) Corresponding ogives for cospectra shown in (a). The M91 Transfer trace is the calculated transfer function for turbulent attenuation in a tube from (Massman, 1991).

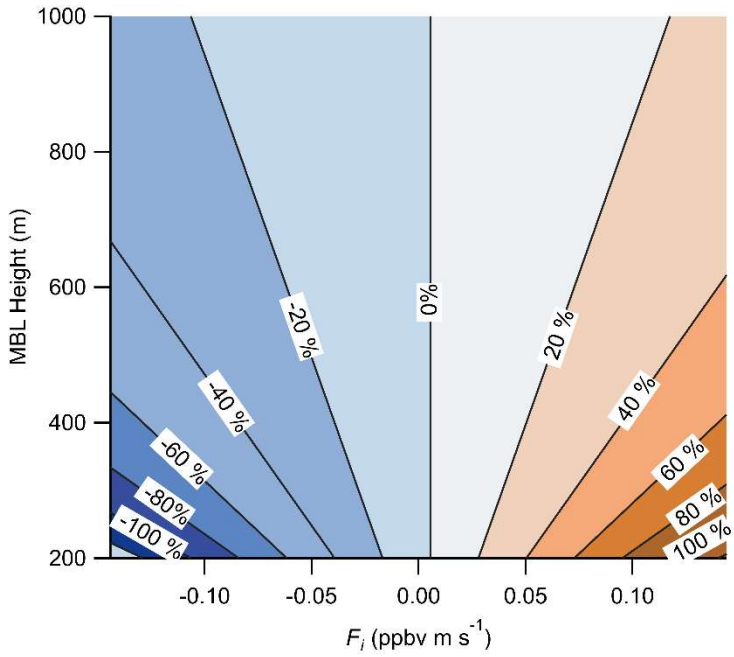

Figure 4.12. Calculated percent error in the measured O_3 surface flux due to entrainment from the free troposphere as a function of the MBL height and the entrainment flux (F_i). Entrainment flux is the product of the free troposphere to boundary layer concentration gradient (ΔC), and the entrainment velocity (w_e). Calculation of percent error used the Scripps Pier measuring height of 13 m, and mean surface flux of -5.6 x 10^{-3} ppbv m s^{-1}.

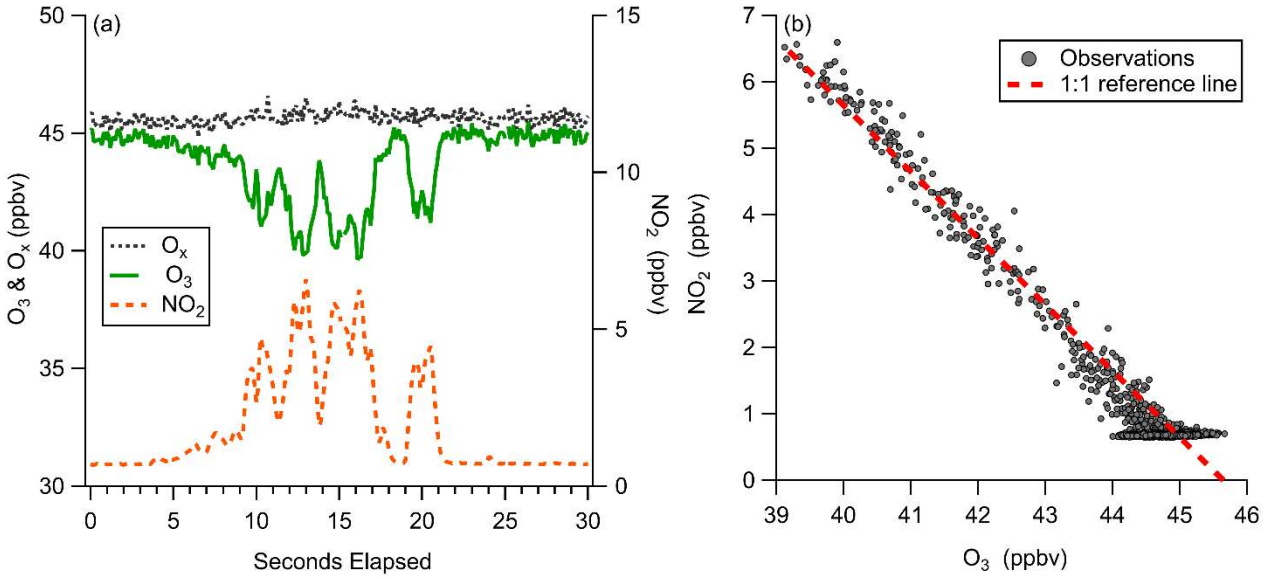

Figure 4.13. Observations of ozone titration by NO emissions from a boat engine near the SIO pier. (a) 10 Hz timeseries of O_3, NO_2, and O_x (O_3 + NO_2) demonstrating ability to capture transient titration events. (b) Regression of O_3 and NO_2 plotted with a reference line of slope -1, showing conservation of total O_x at 10 Hz during a NO titration event.

Supplemental Figures

Component	Voltage (V)
IMR Region (95 mbar)	
IMR	1.5
CDC/ Short Segmented Quadrupole Region (2mbar)	
Lens Nozzle	-1.1
SSQ Entrance Plate	-3.5
SSQ Front	-4.2
SSQ Back	-5.8
Lens Skimmer	-5.7
Skimmer	-3.9
Big Segmented Quadrupole Region (1.2 x 10^{-3} mbar)	
BSQ Front	-1.0
BSQ Back	-1.0
Skimmer 2	5.0

Table 4.S1. Operational ion optic voltages and chamber pressures for the three front end chambers of the Ox-CIMS. Ion declustering strength is primarily determined by the voltage difference between the Skimmer and BSQ Front. The nomenclature of Brophy and Farmer. (2016) is used for ion optic component labelling.

Reagent Ion	O_2^- (kcal mol^{-1})	CO_3^- (kcal mol^{-1})
H_2O	-18.97	-13.18
H_2O_2	-29.42	-21.15
CH_3OOH	-25.00	-7.92
HNO_3	-26.76	-24.10

Table 4.S2. Calculated binding enthalpies in kcal mol^{-1} for $\boldsymbol{O_2^-}$ and $\boldsymbol{CO_3^-}$ reagent ions to water (H_2O), hydrogen peroxide ($\boldsymbol{H_2O_2}$), methyl hydrogen peroxide ($\boldsymbol{CH_3OOH}$), and nitric acid ($\boldsymbol{HNO_3}$) in kcal mol^{-1}. Calculations were performed with the MP2/aug-cc-pvdz-PP theory and basis set.

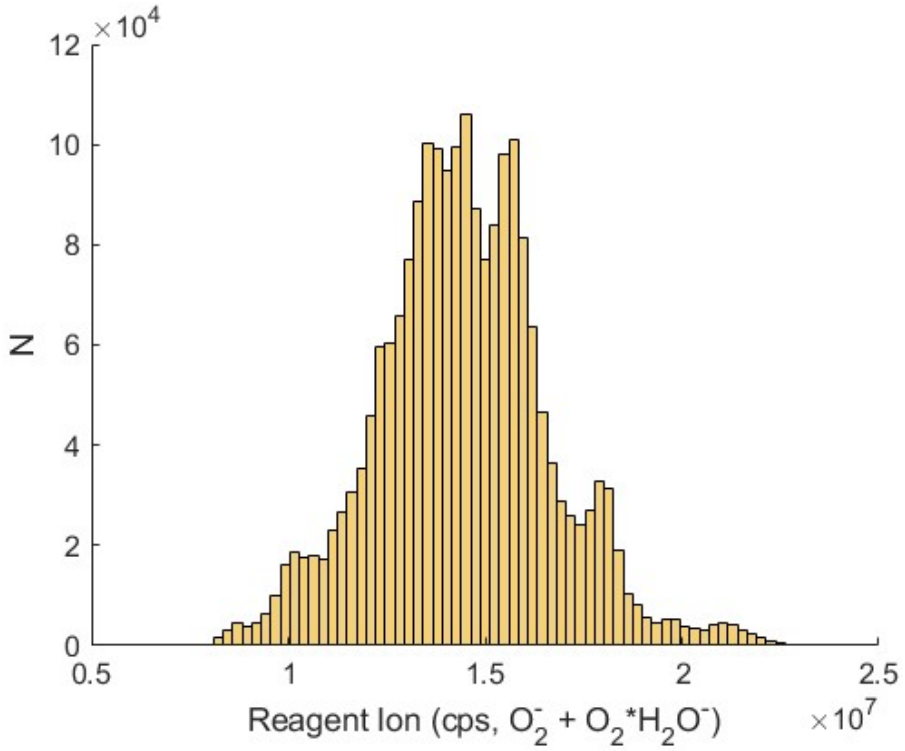

Figure 4.S1. Distribution of 1 Hz reagent ion signal as the sum of $\mathbf{O_2^-}$ **and** $(\mathbf{O_2 \cdot H_2O})^-$ during the full ambient sampling period from Scripps Pier. Absolute sensitivity to O3 and NO2 scales directly with the magnitude of reagent ion signal. Mean reagent ion signal during the campaign was 1.45 x 107 cps corresponding to an absolute sensitivity to O3 and NO2 of 1.8 x 105 and 1.05 x 105 cps ppbv-1 respectively at a specific humidity of 8 g kg-1.

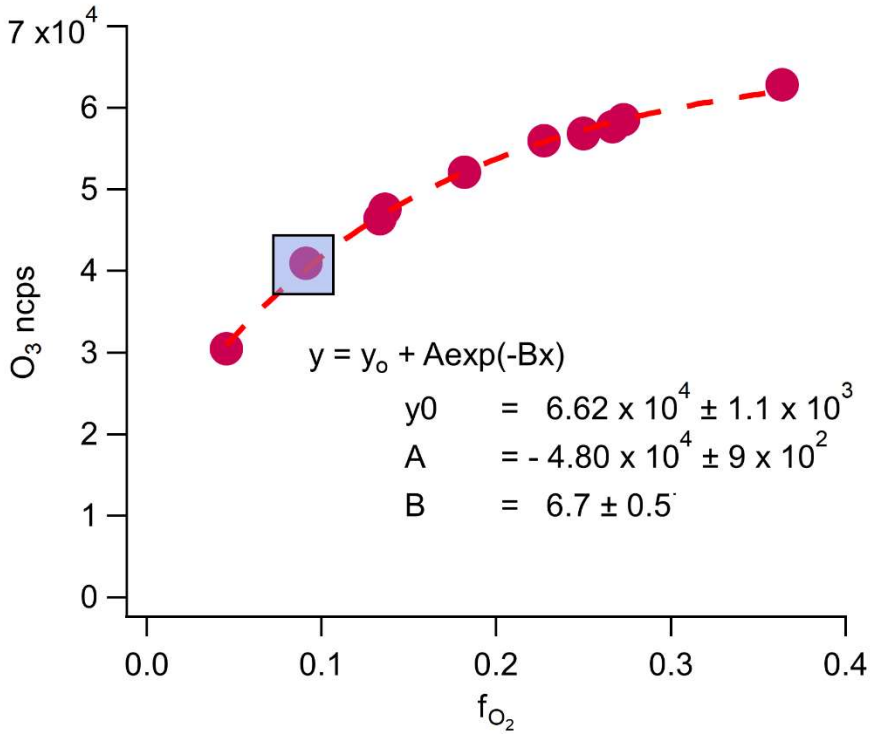

Figure 4.S2. Normalized count rate of background $\mathbf{CO_3^-}$ signal at the sum of —m/Q 60 and —m/Q 48 as a function of oxygen fraction in the reagent ion precursor flow ($\boldsymbol{f_{O_2}}$), with least squares exponential fit line. Reagent ion flow $\boldsymbol{f_{O_2}}$ was varied while the inlet was overflowed with zero air containing 380 ppmv CO2, to isolate the background production of $\mathbf{CO_3^-}$ in the reagent ion generation source. The background O3 production was 1.5 ppbv at $\boldsymbol{f_{O_2}}$ of 0.08 (blue square overlay) used during ambient sampling.

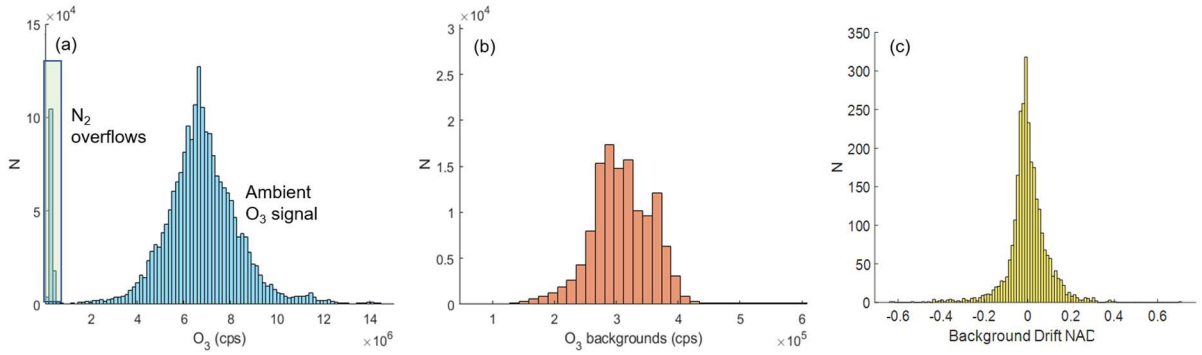

Figure 4.S3. (a) Distribution of observed count rates of the sum of $\mathbf{CO_3^-}$ - (-60 m/Q) and $\mathbf{O_3^-}$ (-48 m/Q) during the full sampling period from Scripps Pier. The green shaded region shows periods of dry UHP N2 overflow of the sampling line. (b) Distribution of observed count rates during dry N2 overflow periods overflow only. Count rates during overflow periods show high consistency between overflow periods with a mean of 3.1 x 105 and standard deviation of 5.0 x 104 counts per second. Residual $\mathbf{CO_3^-}$ during overflow periods is from generation in the reagent ion source rather than off gassing from instrument surfaces. (c) Distribution of normalized adjacent differences of the mean summed $\mathbf{CO_3^-}$ and $\mathbf{O_3^-}$ signal during each three-minute overflow period. The NAD of overflow periods is a measure of point to point stability of the background over the full campaign. The 1 σ deviation of the NAD distribution is 9% which gives an upper limit of the variability between subsequent O3 backgrounds. A 9% variability in the background corresponds to 110 pptv O3 at mean overflow signal of 3.1 x 105 cps.

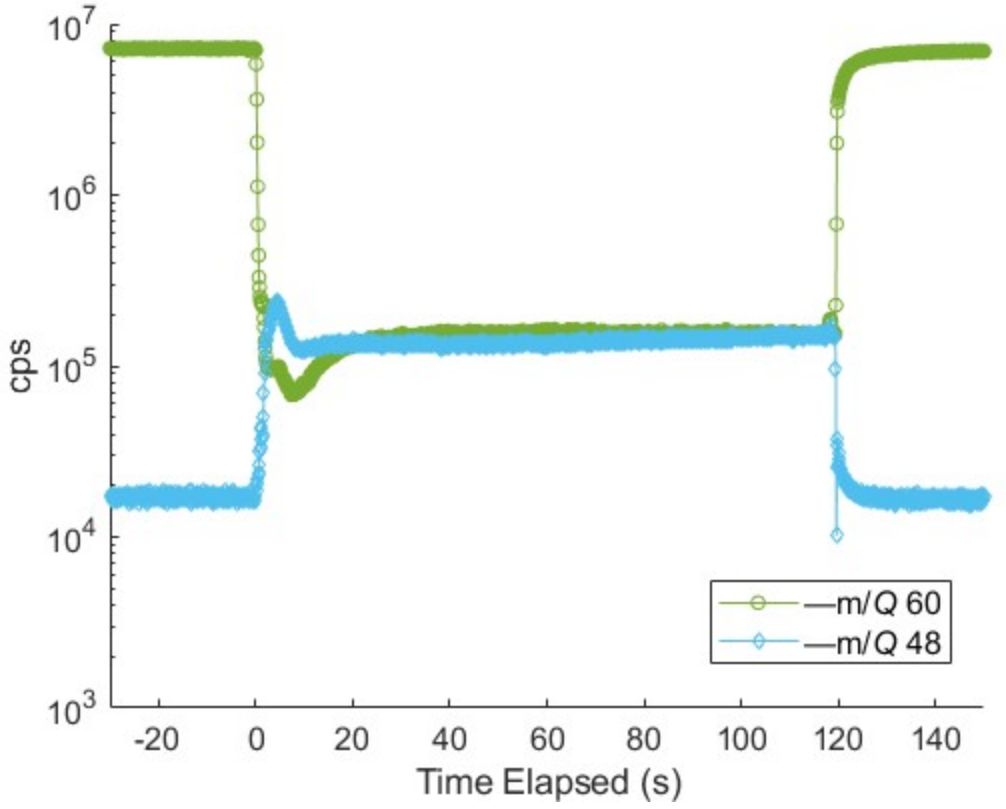

Figure 4.S4. Background count rate of ozone detected as $\mathbf{CO_3^-}$ at —60 m/Q and as $\mathbf{O_3^-}$ at —48 m/Q during an N2 overflow background determination period during ambient sampling at Scripps Pier. Overflow of dry N2 was started at 0 s and stopped at 120 s. During N2 overflow periods during field sampling, no CO2 was added to drive the reaction product to $\mathbf{CO_3^-}$. This leads to the detection of a portion of the O3 background signal as $\mathbf{O_3^-}$during N2 overflow which must be accounted for. Count rates of $\mathbf{O_3^-}$ were of similar magnitude to the $\mathbf{CO_3^-}$ signal during N2 overflow periods during field sampling. From lab calibrations the sensitivity to $\mathbf{O_3^-}$ at 0 ppmv CO2 and 0 g kg-1 SH is approximately a factor of three higher than $\mathbf{CO_3^-}$. Accounting for the background signal at $\mathbf{O_3^-}$ increases the mean O3 background during field sampling by 0.6 ppbv (from approximately 0.7 to a 1.3 ppbv total O3 background).

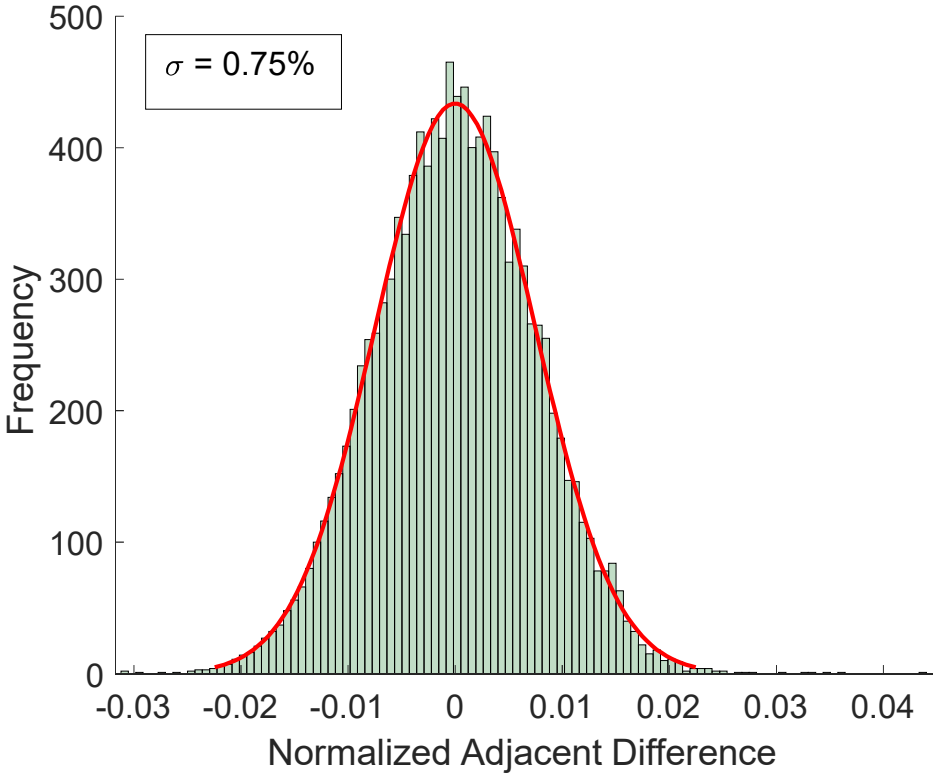

Figure 4.S5. Distribution of normalized adjacent differences of 10 Hz O3 signal during a 2-minute dry N2 overflow period during ambient sampling at Scripps Pier. The 1σ upper limit of precision is 0.75% corresponding to 7.5 pptv precision in the 1.3 ppbv background O3 signal. Precision limitations from background O3 generation in the ion source are unlikely to be significant in the overall precision of the instrument during ambient sampling where precision is 300 pptv at 40 ppbv ambient O3 concentrations.

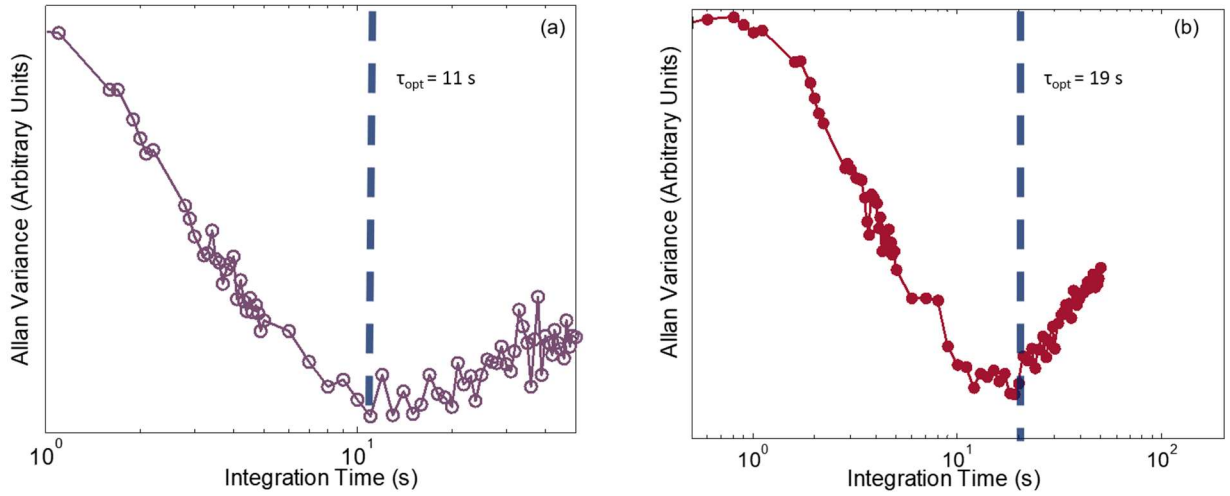

Figure 4.S6. Allan variance determination of optimal averaging time for (a) O3 and (b) NO2 for sampling of a constant calibration source in lab for approximately 10 minutes with 10 Hz data collection. The minimum of the Allan variance curve is the optimum averaging time ($\boldsymbol{\tau_{opt}}$) that results in the lowest achievable LOD. For O3 $\boldsymbol{\tau_{opt}}$ was 11 s, and for NO2 $\boldsymbol{\tau_{opt}}$ was 19 s.

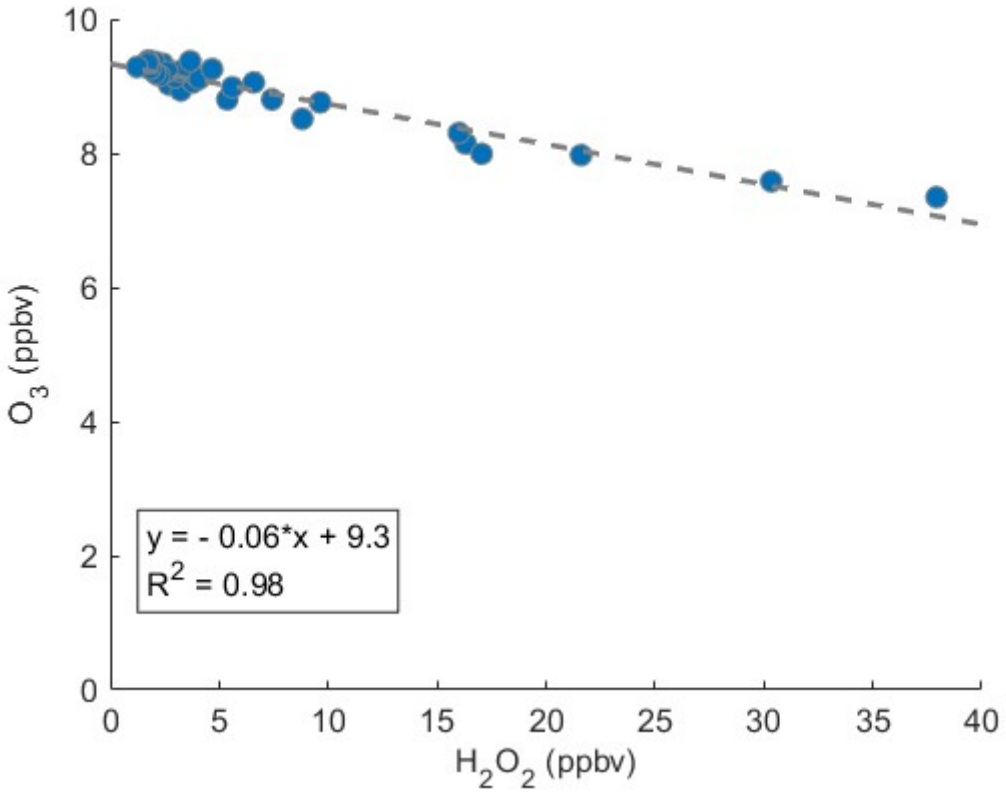

Figure 4.S7. Regression of O_3 signal against H_2O_2 from laboratory sampling of approximately 8 ppbv O_3 with fast introduction of a H_2O_2 source up to 40ppb. Linear regression shows a loss of 0.06 ppbv of the O_3 signal per ppbv H_2O_2 added. H_2O_2 is detected as an adduct with $\boldsymbol{O_2^-}$ the parent ion $\mathbf{H_2O_2^-}$ at —m/Q 66. The $\mathbf{CO_3}\ (\mathbf{H_2O_2})^-$ adduct at —94 m/Q is observed respond with increase with H_2O_2 introduction but has a persistent high signal which is attributed to a ubiquitous $\mathbf{O_2(CO_2)}\ (\mathbf{H_2O})^-$ adduct.

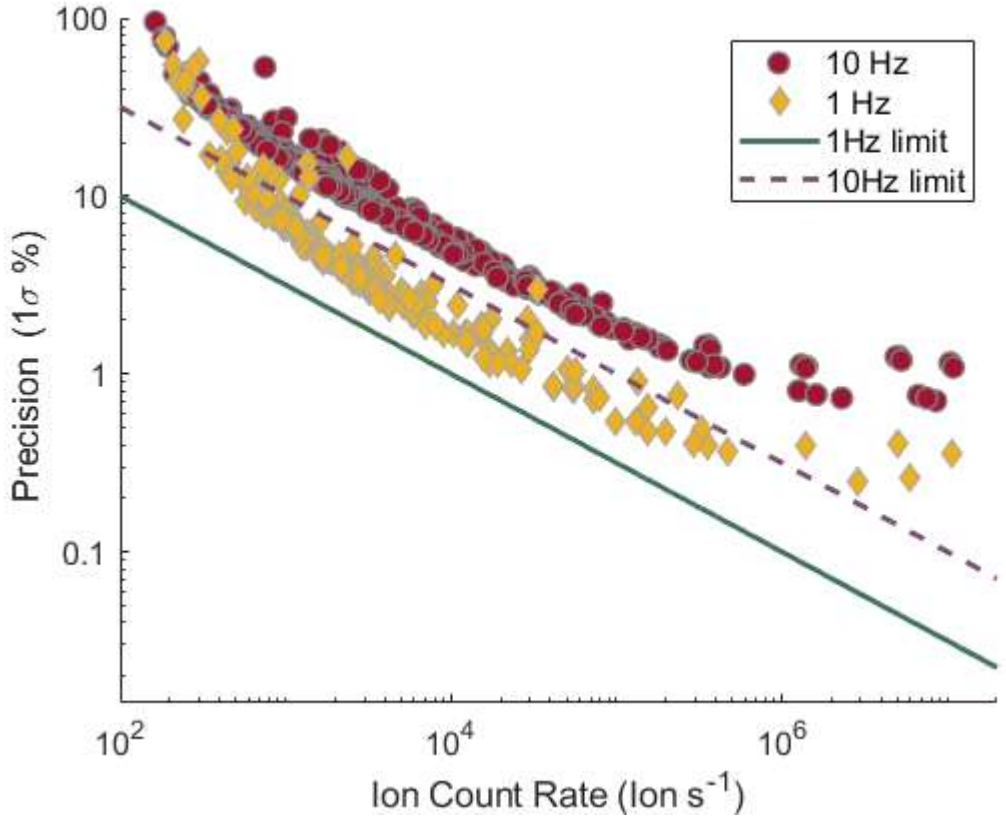

Figure 4.S8. Short-term instrument precision from distribution of normalized adjacent differences against ion count rate for 10 Hz and 1 Hz data averaging. Normalized adjacent differences were calculated for all masses -30 to -250 m/Q for a 27-minute ambient sampling period. Precision is reported as 1σ of the NAD distribution for each mass. Ion count rates are the mean unnormalized count rate over the 27-minute sampling period.

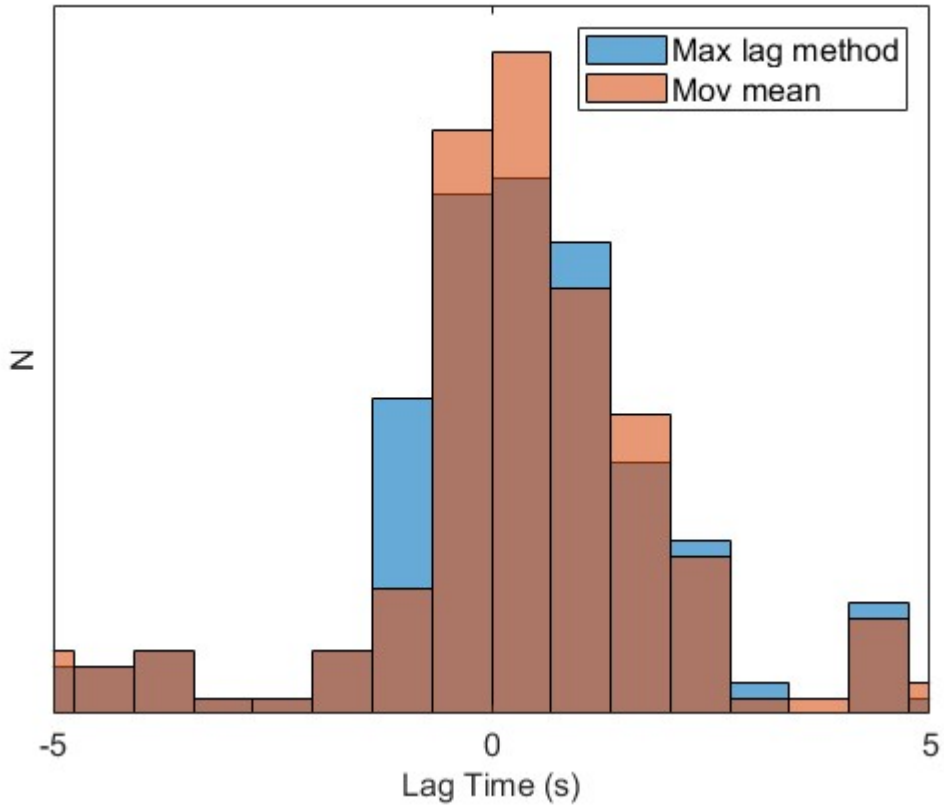

Figure 4.S9. Histogram of determined lag times determined as the maximum (MAX) absolute magnitude of the autocovariance and from the maximum absolute magnitude of a 10 point moving median (AVG) of the autocovariance over a ±5 s lag window.

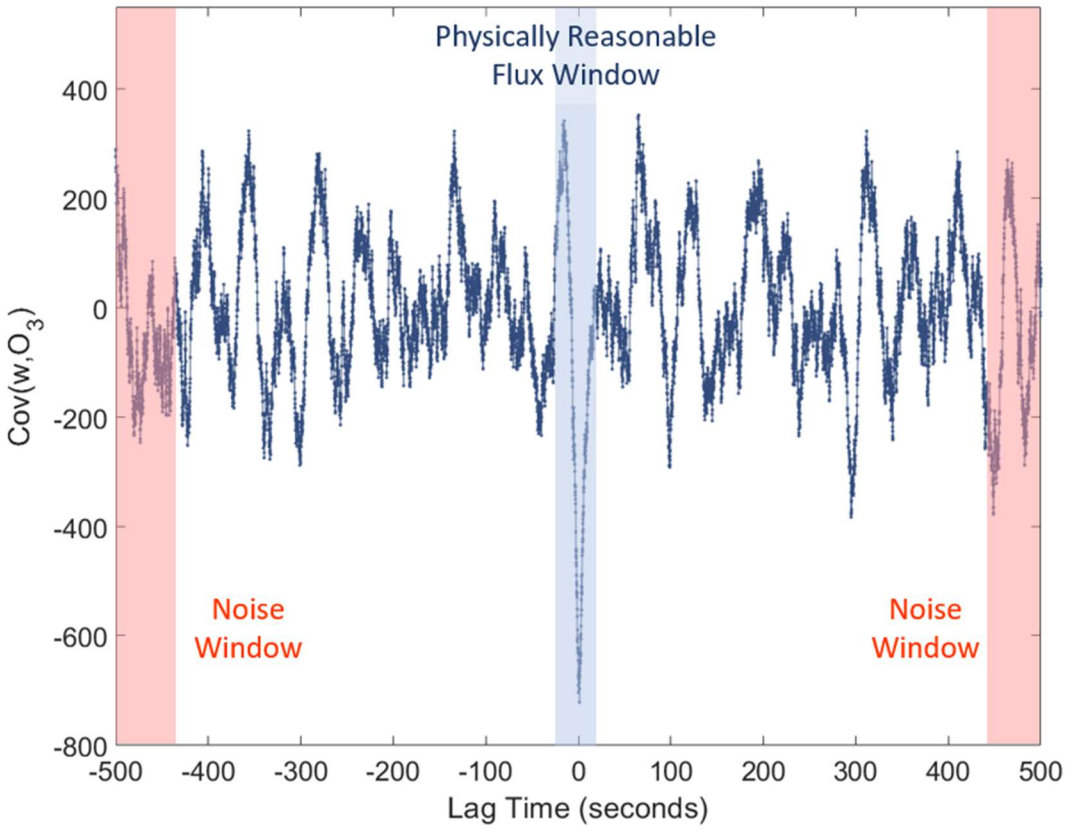

Figure 4.S10. Calculation of cross-covariance at very long lag times (-500 to -485 & 485-500 s) used to determine the flux LOD via the LOD_{RMSE} and LODσ methods. Covariance in the physically reasonable flux window of lag times (-3 to 3 s) is well resolved from the covariance magnitude at long lag times driven by noise.

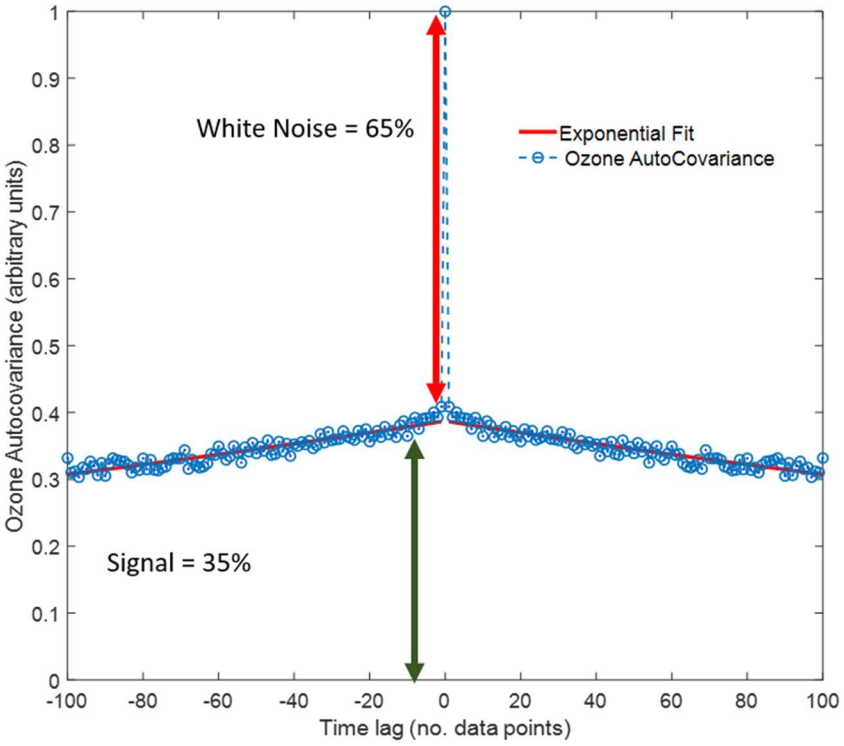

Figure 4.S11. Ozone auto-covariance for 10 Hz O_3 signal for a single flux averaging period. White noise only contributes to the auto-covariance at a lag of 0 points. Auto-covariance at other lag times is from real long-term coherence in the signal, either from atmospheric variability or instrument drift.

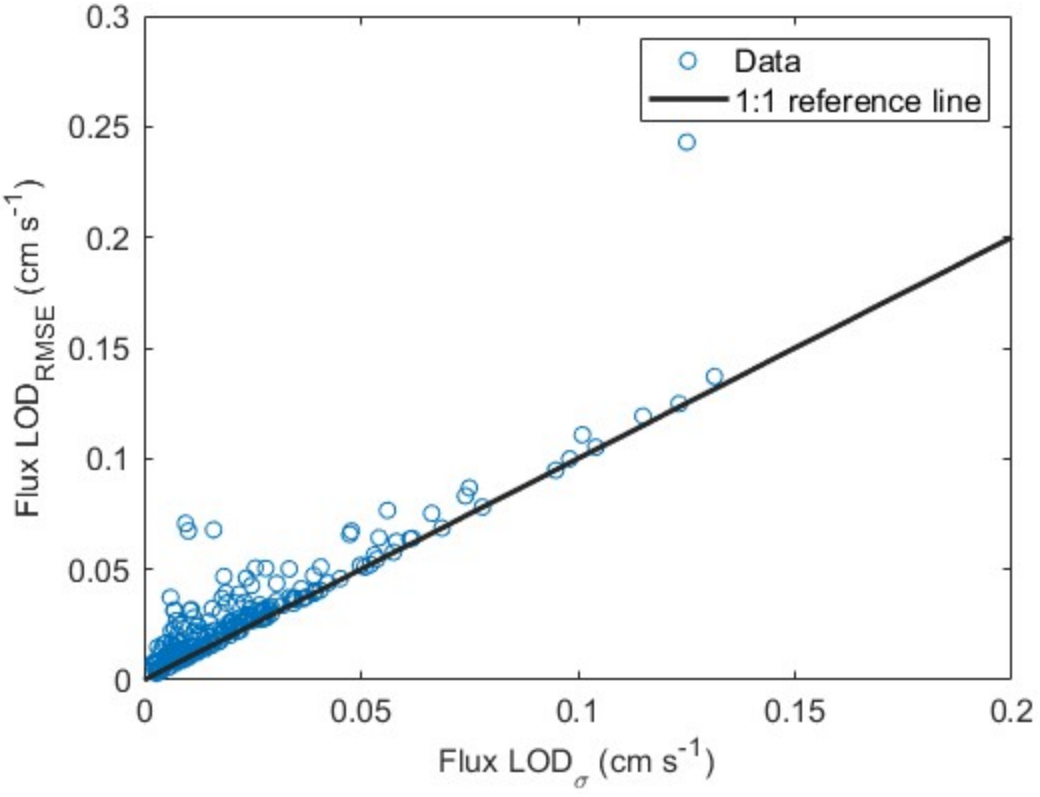

Figure 4.S 12. Ozone flux limit of detection from for 27-minute flux periods determined by the LOD_{RMSE} and LODσ methods.

Chapter 5. The sensitivity of benzene cluster cation chemical ionization mass spectrometry to select biogenic terpenes

Abstract

Benzene cluster cations are a sensitive and selective reagent ion for chemical ionization of select biogenic volatile organic compounds. We have previously reported the sensitivity of a field deployable chemical ionization time-of-flight mass spectrometer (CI-ToFMS), using benzene cluster cation ion chemistry, for detection of dimethyl sulfide, isoprene and α-pinene. Here, we present laboratory measurements of the sensitivity of the same instrument to a series of terpenes, including isoprene, α-pinene, β-pinene, D-limonene, ocimene, β-myrcene, farnesene, α-humulene, βcaryophyllene, and isolongifolene at atmospherically relevant mixing ratios (< 100 pptv). In addition, we determine the dependence of CI-ToFMS sensitivity on the reagent ion neutral delivery concentration and water vapor concentration. We show that isoprene is primarily detected as an adduct ($C_5H_8 \cdot C_6H_6^+$) with a sensitivity ranging between 4 and 10 ncps ppt^{-1}, which depends strongly on the reagent ion precursor concentration, de-clustering voltages, and specific humidity (SH). Monoterpenes are detected primarily as the molecular ion ($C_{10}H_{16}^+$) with an average sensitivity, across the five measured compounds, of 14 ± 3 ncps ppt^{-1} for SH between 7 and 14 g kg^{-1}, typical of the boreal forest during summer. Sesquiterpenes are detected primarily as the molecular ion (C15H + 24) with an average sensitivity, across the four measured compounds, of 9.6 ± 2.3 ncps ppt^{-1}, that is also independent of specific humidity. Comparable sensitivities across broad classes of terpenes (e.g., monoterpenes and sesquiterpenes), coupled to the limited dependence on specific humidity, suggest that benzene cluster cation CIToFMS is suitable for field studies of biosphere–atmosphere interactions.

5.1 Introduction

The annual global emission of biogenic volatile organic compounds (BVOCs) is estimated at 1000 Tg C yr^{-1} and exceeds the total VOC emissions from anthropogenic activities.[1,2] Foliage emissions account for 90% of global BVOC emissions, of which isoprene (C_5H_8), monoterpenes (MTs; $C_{10}H_{16}$), and sesquiterpenes (SQTs; $C_{15}H_{24}$) are the primary constituents.[3] The emission rate and the chemical composition of emitted BVOCs is a complex function of the vegetation species and the wide array of stress factors that it is exposed to.[4–6] Atmospheric oxidation of BVOCs results in the formation of low-volatility compounds that can lead to new particle formation[7,8] and particle growth through secondary organic aerosol formation.[9,10] Both of these processes impact Earth's radiative budget by scattering solar radiation and/or altering cloud formation and precipitation.[11] The contribution of different types of BVOCs (e.g., isoprene, MTs and SQTs) to secondary organic aerosols (SOA) differ significantly.[6] Therefore, uncertainties in BVOCs emissions present significant issues in estimating net climate forcing.[12,13] Identification of the chemical composition of the emitted BVOCs and quantification of the surface exchange rates of these compounds are essential for understanding complex and nonlinear biosphere–atmosphere interactions. Chemical ionization mass spectrometry (CIMS) is a commonly utilized selective and sensitive method for in situ detection of trace gases.[14] The sensitivity and selectivity towards a specific compound or class of compounds having similar functional groups rely on the selection of an appropriate ion (i.e., reagent ion) that reacts with and ionizes the analyte via an ion–molecule reaction. For example, iodide ions have been used to measure reactive nitrogen compounds, halogen-containing species, and oxygenated VOCs;[15–17] $CF3O^-$ has been used for the detection of peroxides and organic nitrates;[18] NO^+ has been used for the selective detection of primary alcohols and alkenes;[19–23] $H3O^+$ has been used for VOCs and their oxygenated products;[24] and benzene cluster cations have been

used for dimethyl sulfide (DMS), isoprene, and terpenes.[25,26] The benzene cation clusters spontaneously with neutral benzene via attractive, non-covalent interactions.[27,28] Leibrock and Huey (2000)[26] and recently Kim et al. (2016)[25] demonstrated that select VOCs including isoprene, MTs, SQTs and aromatic compounds can be ionized by benzene cation clusters. Kim et al. studied the parameters that control the benzene cation cluster distribution $(C_6H_6)^+ \cdot (C_6H_6)_n$ at the operational conditions of the CI-ToFMS, concluding that, for the specific operating conditions used, the reagent ion within the ion–molecule reaction chamber was primarily in the form of the benzene dimer or larger clusters.[25] This conclusion is in agreement with studies showing that the dissociation energy of the benzene cation dimer is significantly higher than that of the trimer or larger benzene cation clusters,[29] suggesting that ionization in the CI-ToFMS by benzene cluster cations proceeds primarily through clusters that are at least the size of the benzene cation dimer. The ionization mechanism for a given analyte (M) with the benzene cation dimer depends on the ionization energy (IE) of the analyte. Charge transfer (R1) is expected to be the dominant reaction for analytes having ionization energies smaller than the benzene dimer (8.69 eV) .[28] In cases when the analyte IE is higher than that of benzene cation dimer, charge transfer is thermodynamically unfavored and adduct formation (R2) or ligand exchange (R3) are the sole modes of ionization. The ligand exchange product (R3) was previously reported for isoprene, dimethyl sulfide and select alkenes; however, the reaction pathway is not known.[25,26]

$$(C_6H_6)_2^+ + M \rightarrow M^+ + 2C_6H_6 \quad \text{(R1)}$$

$$(C_6H_6)_2^+ + M \rightarrow M^+ \cdot (C_6H_6)_2 \quad \text{(R2)}$$

$$(C_6H_6)_2^+ + M \rightarrow M^+ \cdot (C_6H_6) + C_6H_6 \quad \text{(R3)}$$

The low IE of benzene clusters (8.69 eV for the dimer and even smaller for larger benzene cation clusters)[28,30] is a major advantage in the quantification of monoterpenes or larger volatile organic compounds such as sesquiterpenes. The IE of these compounds is slightly smaller than that of the benzene dimer (e.g., 8.3 eV for β-caryophyllene)[31] and the minimal excess energy in charge transfer reactions results in limited fragmentation. For example, approximately 60 % of β-caryophyllene was detected in its molecular ionic form (M+) in comparison to significant fragmentation observed by proton transfer reaction mass spectrometry (PTRMS).[32] The field-deployable CIMS that utilizes a time-of-flight mass analyzer (ToFMS), previously described by Kim et al., combines the efficient production and transmission of ions at high pressure (e.g., 75 mbar) with the high ion duty cycle of orthogonal extraction ToFMS.[25,33] This instrument configuration is highly sensitive and capable of measuring and logging mass spectra (10–800 m/Q) at rates higher than 10 Hz.[33] These benefits make CI-ToFMS highly applicable for studying atmospheric exchange processes of trace gases at the air–ocean interface that require fast response rates.[34] However, at these pressures, the distribution of benzene clusters and their associated ion–molecule reactions times are not well constrained. Unlike PTR-MS, it is not possible to directly derive the analyte mixing ratio from laboratory studies of the ion–molecule kinetics (reaction rates) that are conducted at lower pressure in which both the reaction times and cluster distribution have been previously determined. As such, quantitative analysis of atmospheric trace gases using high pressure CIMS necessitates either a direct or empirical calibration for each analyte as a function of the atmospheric conditions (e.g., humidity or temperature). In what follows, we build on earlier studies in our group,[25] which described the use of benzene cluster cations as a reagent ion for the detection and quantification of dimethyl sulfide, isoprene, and α-pinene. At the time of Kim et al. (2016), it was not known if benzene ion chemistry was equally sensitive to all monoterpene

compounds, to what extent CI-ToFMS sensitivity was dependent on ambient specific humidity for a broad range of monoterpenes and sesquiterpenes, and the source of organic impurities in the reagent ion delivery. Here, we address each of these topics. In this paper, we describe a high-purity liquid benzene source, which permits operation of the CI-ToFMS at higher reagent ion concentrations. We discuss the sensitivity of benzene cluster cation chemistry to a select number of terpenes (**Fig. 5.1**) at atmospherically relevant mixing ratios (< 500 pptv). We report on the effect of atmospheric water vapor and the neutral benzene reagent ion precursor concentration on CI-ToFMS sensitivity to select terpenes (isoprene, α- and β-pinene, D-limonene, β-myrcene, ocimene, farnesene, isolongifolene, α-humulene, and β-caryophyllene). We also examine the de-clustering power of the radio frequency (RF)-only quadrupole to better determine the cluster distribution present in the ion molecule reaction chamber.

5.2 Experimental

5.2.1 Materials

The following analytes were purchased from Sigma-Aldrich and used with no further purification: isoprene, α-pinene, βpinene, D-limonene (≥ 99 %), β-myrcene (96.2 %), ocimene (97.0 %, as a mixture of isomers), farnesene (> 90.0 %, as a mixture of isomers) α-humulene (> 96.5 %), βcaryophyllene (≥ 98.5 %), isolongifolene (≥ 98.0 %, as a mixture of isomers), benzene (≥ 99.5 %), and chloroform-d (99.8 at. % D). A compressed gas cylinder of 0.184 ppm of DMS-d3 in N_2 was purchased from Praxair, USA. Water was supplied from a Milli-Q system at 18.2 MΩ. Nitrogen was used from a UHP liquid N_2 dewar (Airgas). UHP (99.999 %) oxygen cylinders were purchased from Airgas.

5.2.2 Chemical Ionization Mass Spectrometer

The detailed description of the CI-ToFMS (Tofwerk AG, Switzerland, and Aerodyne Research Inc., USA) and its performance are discussed in Bertram et al. (2011). In brief, reagent ions are generated by passing 10 sccm of UHP N_2 over the headspace of a liquid benzene reservoir contained in a stainless steel bottle. Benzene vapor is diluted with 2.2 slpm of N_2, prior to delivery to the ^{210}Po source. The benzene vapor mixing ratio is estimated from the dilution ratio and benzene vapor pressure. In the experiments discussed here, we varied the benzene concentration between 60 and 360 ppm. A combination of stainless steel and Teflon tubing was used to transfer benzene vapors to minimize extraction of organic compounds from the tubing. Following dilution, benzene vapor flows through a 10 mCi α emitting radioactive ^{210}Po source (NRD 2021–1000). The collision of α-particles with N_2 results in the formation of N^+_2 ions that ionize the benzene clusters.[35] The analyte sample is mixed with the formed benzene cluster cations at the ion–molecule reactor (IMR) held at 75 mbar. At this pressure, the estimated analyte residence time in the IMR is 100 ms. The reagent and product ions are transmitted from the IMR chamber into a collisional dissociation chamber (CDC, P = 2 mbar) equipped with a RF-only ion-guide quadrupole, followed by a subsequent chamber ($P = 1.4 \times 10^{-2}$ mbar) in which a second RF-only quadrupole is used to focus the ion beam. The ion beam is then guided by a further set of ion optics to the entrance point of the extraction region of the compact time of-flight mass analyzer (Tofwerk AG, Switzerland).

5.2.3 Liquid Calibration Unit

A custom liquid calibration system was developed to deliver known, atmospherically relevant mixing ratios (< 500 pptv) of gas-phase terpenes to the CI-ToFMS. The liquid calibration system uses a syringe pump to continuously evaporate known quantities of solution into a heated carrier

gas flow, generating known mixing ratios of select terpenes. To produce trace concentrations of each analyte, the standard liquid material was diluted in series with chloroform-d using a set of calibrated auto pipettes. Chloroform-d was chosen due to its solvent properties and low boiling point (61 ˚C) that enhances the evaporation of the analyte. Due to its ionization energy (IE > 11 eV),[36] higher than that of benzene cation clusters, it was expected that chloroform would not be ionized and would have negligible impact on the benzene cluster cation ionization mechanisms. To assess this, mass spectra were recorded for solutions containing solely deuterated chloroform for a variety of different pump flows from 0 to 5 μL min^{-1}. We did not observe the molecular cation of chloroform-d ($CDCl_3^+$, 120 *m/Q*) and only very small signatures of the fragments (at 48, 84, or 86 *m/Q*) were observed (**Fig. 5.2**), consistent with the IE of chloroform-d being higher than that of the reagent ions (11.37 ± 0.02 eV compared with 8.69 eV).[28,37] It was also determined that concentration of deuterated chloroform did not interfere with reagent ion or water cluster signal intensities. To evaporate the analyte solution, a controlled amount (0– 5 μL min^{-1}) of the analyte solution was delivered by a syringe pump (Harvard Apparatus, model 11) via PEEK tubing (Upchurch Scientific) into a heated carrier stream resulting in CDCl3 mixing ratios from 60 to 300 ppmv. A synthetic 80:20 N_2:O_2 mixture was used as zero air and heated by an in-line gas heater (Omega, AHP-3741). The temperature of the zero air flow at the point of intersection with the PEEK tubing was kept at 80 ˚C via a PID temperature controller (Omega, CN9300). Excess zero air flow was used to ensure an overflow of the CIMS inlet. The trace concentration of the evaporated analytes and the elevated temperature in front of the inlet (ca. 50 ˚C) helped to prevent re-condensation of the analyte on the inlet tubing. Humidified zero air was generated by passing a fraction of the total flow through the head space of a water reservoir. The relative humidity (RH) of the total air flow was measured using a relative humidity sensor (Vaisala, HMP110), calibrated

using the procedure described in.[38] The sensitivities reported in this paper are presented in normalized counts per second per pptv (ncps $pptv^{-1}$). We normalized the analyte ion count rates by the sum of the benzene cation monomer (78 *m/Q*) and dimer (156 *m/Q*) count rates to a reference of 1×10^6 counts per second of total reagent ion signal in order to account for changes in ion transmission and generation over time. Sensitivities are calculated as the slope of the linear fit of each calibration curve of 5–7 steps (**Fig. 5.3**). Error bars are the standard deviation of repeated triplicate measurements. The performance of the liquid evaporation technique was validated by comparing the sensitivity to dimethyl-1,1,1-d3 sulfide (Praxair certified compressed gas standard, 0.184 ppm ± 10 %) diluted by zero air to a desired mixing ratio, with that of a diluted nebulized solution of DMS. The slope of the linear fit for calibration measurements from the pressurized cylinder (DMS-d3, 65 *m/Q*) and the solution (DMS, 62 *m/Q*) agreed to better than 10 %.

5.3 Results and Discussion

5.3.1 Benzene cluster cation mass spectra

The CI-ToFMS mass spectra, obtained while overflowing the inlet with nominally dry zero air, are shown in **Fig. 5.4a**. To maximize the transmission of weakly bound ion–molecule adducts, we operated the instrument in all of the experiments described here with a minimal applied electric field between the instrument inlet and the entrance of the second RF-only quadrupole ion guide. The two primary peaks in the mass spectrum correspond to the benzene cation ($C_6H_6^+$; 78 *m/Q*) and the benzene cation clustered to a single, neutral benzene ($C_6H_6^+ \cdot (C_6H_6)$; 156 *m/Q*), where $C_6H_6^+$ and $C_6H_6^+ \cdot (C_6H_6)$ combined account over 90 % of the total ion current (TIC) for a benzene neutral concentration of 300 ppm. Benzene cation clusters larger than the dimer were not observed, as expected from their dissociation enthalpy, which is significantly smaller than that of the benzene cation clustered with a single neutral benzene molecule.[29] The observed mass spectrum indicates

significant ion intensity at 39, 50, 51, and 52 *m/Q* that are attributed to the dissociation of the molecular ($C_6H_6^+$) ion into its fragments $C_3H_3^+$, $C_4H_2^+$, $C_4H_3^+$, and $C_4H_4^+$, accounting for ca. 5 % of TIC. The fragmentation may result from the interaction of N^{+2}, α-particles, or electrons with benzene clusters in the ion molecule reaction region.[39,40] For comparison, a similar spectrum is shown in **Fig. 5.4b**, using the same benzene neutral concentration and operating voltages, but without the RF and voltage bias applied to the first quadrupole ion guide. In this mode of operation, the total ion current is reduced by over 95 %, and $C_6H_6^+$ and $C_6H_6^+\cdot(C_6H_6)$ are nearly equal in intensity, highlighting that benzene cluster collisional dissociation is occurring within this region. Even with the first RF-only quadrupole electronics turned off, the n = 2 cluster ($C_6H_6^+\cdot(C_6H_6)_2$; 234 *m/Q*) was not observed. Of notable absence (< 1 % TIC) in both **Fig. 5.4a** and b are the organic contaminants (92, 106, and 120 *m/Q*) previously attributed to alkyl substituted benzene and protonated water clusters (($H_3O^+\cdot(H_2O)_n$; 19, 37, 55, and 73 *m/Q*) that were present at high abundance (> 10 % of TIC) in Kim et al. (2016). It was postulated in Kim et al. (2016) that the source of the organic contaminants was the benzene compressed gas cylinder, as their combined contribution to TIC scaled with the neutral benzene concentration.[25] It was also noted that low benzene neutral concentrations led to elevated water cluster abundance. This resulted in an optimum benzene neutral concentration of 10 ppm to balance the contributions from organic contaminants and water clusters. Here, we eliminate the organic contaminants through the use of a high-purity benzene liquid source permitting operation at higher neutral benzene concentrations (> 300 ppm). As discussed in Sect. 3.2, this has critical advantages for the detection of analytes such as isoprene and effectively eliminates competing ion chemistry stemming from protonated water clusters. In what follows we assess the CI-ToFMS sensitivity to a series of terpenes, including isoprene, α-pinene, β-pinene, D-limonene, ocimene, β-myrcene, farnesene, α-humulene,

β-caryophyllene, and isolongifolene at atmospherically relevant mixing ratios (< 100 pptv) and determine the dependence of CI-ToFMS sensitivity on the reagent ion neutral delivery concentration (Sect. 5.3.2) and water vapor concentration (Sect. 5.3.3).

5.3.2 Impact of benzene neutral concentration on terpene sensitivity

We examined the impact of the benzene reagent ion precursor concentration on terpene sensitivity in nominally dry zero air for benzene neutral concentrations between 60 and 300 ppm. For the selection of monoterpenes and sesquiterpenes studied here, there was no indication that instrument sensitivity was dependent on the neutral benzene reagent ion precursor concentration between 60 and 300 ppm (**Fig. 5.5a–b**). In **Fig. 5.5a–c**, the reported sensitivity for each terpene is normalized to that measured at a benzene neutral concentration of 300 ppm. Unlike MTs and SQTs, the sensitivity of the isoprene–benzene adduct ($C_6H_6^+ \cdot C_5H_8$; 146 *m/Q*) strongly depends on the benzene concentration below 200 ppm (**Fig. 5.5c**) and therefore all the measurements in this study, were conducted at 300 ppm benzene. The cause for this dependence in benzene concentration is unclear as the exact mechanism for $C_6H_6^+ \cdot C_5H_8$ formation is unknown. It should also be noted that the sensitivity to DMS is independent of benzene concentration. Based on these analyses, we suggest that future studies utilizing benzene ion chemistry operate at neutral benzene reagent ion precursor concentrations of 300 ppm, generated from a high-purity liquid source.

5.3.3 Impact of specific humidity on sensitivity

5.3.3.1 Isoprene

In these experiments, the specific humidity (SH) was varied between 0 and 14 g kg^{-1}, equivalent to 0–80 % RH at 23 ˚C, to assess its effect on the sensitivity. Our reported "nominally dry" cases correspond to 0.7 % RH or ca. 0.01 g kg^{-1} SH. As shown in **Fig. 5.6**, the sensitivity of the CI-ToFMS to isoprene ($C_6H_6^+ \cdot C_5H_8$; 146 *m/Q*) displays a strong, nonlinear dependence on SH.

Instrument sensitivity increases with increasing SH, reaching a maximum value of 10 ncps ppt^{-1} at 4 g kg^{-1} (25 % RH at 23 ˚C), then decreases significantly at higher humidity. Surprisingly, we observed a linear correlation ($R^2 > 0.95$) between the protonated water tetramer signal (73 *m/Q*) and the delivered isoprene mixing ratio at constant SH that was not observed for smaller protonated water clusters (**Fig. 5.7**). The apparent sensitivity, derived from the slope of the linear least squares fit of the observed water tetramer signal vs. delivered isoprene concentration, increases with increasing specific humidity above 2 g kg^{-1} (**Fig. 5.6**). We reiterate that **Fig. 5.6** does not show the protonated tetramer signal as a function of SH but the sensitivity of the 73 *m/Q* signal to the delivered isoprene mixing ratio as shown in **Fig. 5.7**. The decreased sensitivity to isoprene adduct and increase in water tetramer signal with isoprene mixing ratio are unlikely the result of the formation of water protonated clusters via charge transfer reaction with benzene cations since the IE of water is significantly higher than that of the benzene dimer (12.62 and 8.69 eV respectively).[28,41] Since the formation of water tetramer clusters increases with isoprene mixing ratio and humidity, it is suggested that the interaction between water clusters and isoprene–benzene adducts in the IMR results in a charge exchange from the isoprene adduct to the water tetramer in a similar way that was previously described between benzene cation and water clusters. For example, Miyazaki et al. (2004)[42] showed that the IR spectra of benzene–water ion clusters, with more than four water molecules, resemble those of protonated water clusters and suggested that the charge is held by the water molecules; such clusters that are likely to be formed in the IMR are expected to be broken apart in the ion optics. It is likely that the observed trends of the humidity-dependent sensitivity of isoprene and water tetramer signal also results from a similar formation and de-clustering in our CI-ToFMS.

5.3.3.2 Monoterpenes

The dependence of monoterpene sensitivity on SH is shown in **Fig. 5.8** for the molecular ion ($C_{10}H_{16}^{+}$; 136 *m/Q*). Instrument sensitivity under nominally dry conditions displays a wide range of sensitivities that are species dependent (4.8 to 21.0 ncps ppt^{-1}). At high specific humidity, sensitivities converge significantly (9.5 to 15.0 ncps ppt^{-1}). The observed dependence in the α-pinene sensitivity on SH reported here is counter to that previously reported by our group in Kim et al. (2016).[25] This is attributed to the different instrument operational configuration used here (e.g., high concentration and purity benzene reagent ion precursor and low electric field strengths). The humidity-dependent sensitivity of D-limonene is anomalous compared with the other monoterpenes studied, where the CI-ToFMS sensitivity to D-limonene decreases by a factor of 4 over the studied humidity range. The gradual and systematic decrease in the sensitivity suggests that the ionization of D-limonene by charge transfer is not the only ionization mechanism and/or that the D-limonene cation is subjected to subsequent reactions which results in the formation of other detectable ions. We calculated the calibration curves of each of the recorded mass-to-charge ratios to identify product ions that showed (1) high correlation with the delivered D-limonene mixing ratio ($R^2 > 0.98$) and (2) the contribution to the total sensitivity (i.e., slope) was higher than 1 ncps ppt^{-1} . A representative normalized calibration curve of the three ions (135, 136, and 168 *m/Q*) that met these criteria is presented in **Fig. 5.9**. The peak at 168 *m/Q* ($C_{10}H_{16}O_2^{+}$) is attributed to either a D–limonene-O2 adduct or a D-limonene oxidation product (e.g., limonene epoxide). The peak at 135 *m/Q* ($C_{10}H_{15}^{+}$) represents the $[M - 1]^{+}$ product. We speculate that this product could be formed following the oxidation of an $[M+1]^{+}$ ion, formed via proton transfer, and the subsequent departure of HOOH (Karlberg et al., 1994). The purity of the primary standard was confirmed via GC-MS, and comparable peak ratios were measured when sampling the standard

directly, ruling out the potential for the nebulization process to alter the MS peak ratios. Finally, the $[M+32]^+$ and $[M-1]^+$ peak intensities are reduced to baseline by sampling the terpene in nitrogen, suggesting that these peaks are a result of secondary ion chemistry involving O_2. The normalized sensitivity of each of these three peaks decreases with increasing SH (**Fig. 5.10**), suggesting that water clusters compete or suppress the charge transfer to the contributing ions. The humidity-dependent sensitivity of all the studied MTs, calculated as the sum of all their contributing ions, shows lower variability, mostly due to the higher sensitivity to D-limonene when all product ions are accounted for (**Fig. 5.11**). The variations in the sensitivities between different monoterpenes is small (14 ± 3 ncps ppt^{-1}) and instrumental response is largely independent on SH from 4 to 14 g kg^{-1}. This range is typical at boreal forests during the summer.[43] The reported sensitivities, product ions, and dependence on ambient water concentrations and neutral benzene concentration for select monoterpenes are shown in **Table 5.1**.

5.3.3.3 Sesquiterpenes

The sensitivities of the CI-ToFMS toward SQTs, detected as the charge transfer product at 204 *m/Q*, show minimal dependence on SH between nominally dry conditions and 14 g kg^{-1} (**Fig. 5.12**). Using the same process discussed in Sect. 3.3.2 for identifying other product ions, it was found that 203 and 236 *m/Q* ($C_{15}H_{23}^+$ and $C_{15}H_{24}O_2^+$) also contributed to product ion intensity. The response of the farnesene and isolongifolene molecular ions and their related contributing ions are presented as examples of SQTs dependence on SH (**Fig. 5.13**). All three major ions were observed at all measured SHs, and in the case of isolongifolene, the normalized response of 203 *m/Q* ($C_{15}H_{23}^+$) was higher than the molecular ion (204 *m/Q*, $C_{15}H_{24}^+$) over the entire SH range, including at nominally dry conditions (**Fig. 5.13**). At present, we do not have a definitive mechanism for the product ion distribution, but the presence of similar products (i.e., $([M-1]^+$ and

($[M+32]^+$) and their humidity dependence suggest that the molecular ions of sesquiterpenes are subjected to similar reactions to MTs which results in a lower signal of the molecular ion. Similar to MTs, the humidity-dependent sensitivities of sesquiterpenes calculated as the sum of all contributing ions lower the variability in calculated sensitivities (**Fig. 5.14**). Since the sensitivity is independent of the humidity, a general sensitivity to all SQTs of 9.6 ± 2.3 ncps $pptv^{-1}$ can be further used for quantification of ambient SQTs. The reported sensitivities product ions, and dependence on ambient water concentrations and neutral benzene concentration for select sesquiterpenes are shown in **Table 5.2**.

5.4 Conclusions

We show that benzene cluster cations are a sensitive reagent ion for chemical ionization of select biogenic volatile organic compounds. We demonstrate that isoprene is primarily detected as an adduct ($C_5H_8 \cdot C_6H_6^+$) with a sensitivity ranging between 4 and 10 ncps ppt^{-1}, which depends strongly on the reagent ion precursor concentration and specific humidity (SH). This highlights the importance of continuous infield calibrations for isoprene concentration measurements. We show that monoterpenes are primarily detected as the molecular ion ($C_{10}H_{16}^+$) with an average sensitivity, across the five measured compounds, of 14 ± 3 ncps ppt^{-1} for SH between 7 and 14 g kg^{-1}, typical of the boreal forest during summer. Sesquiterpenes are detected primarily as the molecular ion ($C_{15}H_{24}^+$) with an average sensitivity, across the four measured compounds, of 9.6 ± 2.3 ncps ppt^{-1} that is also independent of specific humidity. Given that signal intensity was observed at $[M-1]^+$ and $[M+32]^+$ for a few select terpenes (e.g., D-limonene) we recommend that future measurements of total monoterpenes utilize all three product ions. We suggest that future studies that utilize benzene cluster cation chemistry use high-purity liquid reservoirs and benzene neutral concentrations at or above 300 ppmv.

References

(1) Guenther, A. B.; Jiang, X.; Heald, C. L.; Sakulyanontvittaya, T.; Duhl, T.; Emmons, L. K.; Wang, X. The Model of Emissions of Gases and Aerosols from Nature Version 2.1 (MEGAN2.1): An Extended and Updated Framework for Modeling Biogenic Emissions. *Geosci. Model Dev.* **2012**, *5* (6), 1471–1492. https://doi.org/10.5194/gmd-5-1471-2012.

(2) IPCC. *Climate Change 2014: Synthesis Report. Contribution of Working Groups I, II and III to the Fifth Assessment Report of the Intergovernmental Panel on Climate Change*; Geneva, Sqitzerland, 2014.

(3) Guenther, A.; Nicholas, C.; Fall, R.; Klinger, L.; Mckay, W. A.; Scholes, B. A Global Model of Natural Volatile Organic Compound Emissions s Raja the Balance Triangle Changes in the Atmospheric Accumulation Rates of Greenhouse Triangle Several Inventories of Natural and Exposure Assessment Global Scales Have Been Two Classes Fores. *J. Geophys. Res.* **1995**, *100* (94), 8873–8892.

(4) Hallquist, M.; Wenger, J. C.; Baltensperger, U.; Rudich, Y.; Simpson, D.; Claeys, M.; Dommen, J.; Donahue, N. M.; George, C.; Goldstein, a. H.; et al. The Formation, Properties and Impact of Secondary Organic Aerosol: Current and Emerging Issues. *Atmos. Chem. Phys.* **2009**, *9* (14), 5155–5236. https://doi.org/10.5194/acp-9-5155-2009.

(5) Lang-Yona, N.; Rudich, Y.; Mentel, T. F.; Bohne, A.; Buchholz, A.; Kiendler-Scharr, A.; Kleist, E.; Spindler, C.; Tillmann, R.; Wildt, J. The Chemical and Microphysical Properties of Secondary Organic Aerosols from Holm Oak Emissions. *Atmos. Chem. Phys.* **2010**. https://doi.org/10.5194/acp-10-7253-2010.

(6) Zhao, D. F.; Buchholz, A.; Tillmann, R.; Kleist, E.; Wu, C.; Rubach, F.; Kiendler-Scharr, A.; Rudich, Y.; Wildt, J.; Mentel, T. F. Environmental Conditions Regulate the Impact of Plants on Cloud Formation. *Nat. Commun.* **2017**. https://doi.org/10.1038/ncomms14067.

(7) Jokinen, T.; Berndt, T.; Makkonen, R.; Kerminen, V.-M.; Junninen, H.; Paasonen, P.; Stratmann, F.; Herrmann, H.; Guenther, A. B.; Worsnop, D. R.; et al. Production of Extremely Low Volatile Organic Compounds from Biogenic Emissions: Measured Yields and Atmospheric Implications. *Proc. Natl. Acad. Sci.* **2015**, *112* (23), 7123–7128. https://doi.org/10.1073/pnas.1423977112.

(8) Kirkby, J.; Duplissy, J.; Sengupta, K.; Frege, C.; Gordon, H.; Williamson, C.; Heinritzi, M.; Simon, M.; Yan, C.; Almeida, J.; et al. Ion-Induced Nucleation of Pure Biogenic Particles. *Nature* **2016**, *533* (7604), 521–526. https://doi.org/10.1038/nature17953.

(9) Allan, J. D.; Alfarra, M. R.; Bower, K. N.; Coe, H.; Jayne, J. T.; Worsnop, D. R.; Aalto, P. P.; Kulmala, M.; Hyötyläinen, T.; Cavalli, F.; et al. Size and Composition Measurements of Background Aerosol and New Particle Growth in a Finnish Forest during QUEST 2 Using an Aerodyne Aerosol Mass Spectrometer. *Atmos. Chem. Phys.* **2006**.

https://doi.org/10.5194/acp-6-315-2006.

(10) Wiedensohler, A.; Cheng, Y. F.; Nowak, A.; Wehner, B.; Achtelt, P.; Berghof, M.; Birmili, W.; Wu, Z. J.; Hu, M.; Zhu, T.; et al. Rapid Aerosol Particle Growth and Increase of Cloud Condensation Nucleus Activity by Secondary Aerosol Formation and Condensation: A Case Study for Regional Air Pollution in Northeastern China. *J. Geophys. Res. Atmos.* **2009**. https://doi.org/10.1029/2008JD010884.

(11) Chung, C. E.; Ramanathan, V.; Decremer, D. Observationally Constrained Estimates of Carbonaceous Aerosol Radiative Forcing. *Proc. Natl. Acad. Sci. U. S. A.* **2012**. https://doi.org/10.1073/pnas.1203707109.

(12) Kerminen, V. M.; Lihavainen, H.; Komppula, M.; Viisanen, Y.; Kulmala, M. Direct Observational Evidence Linking Atmospheric Aerosol Formation and Cloud Droplet Activation. *Geophys. Res. Lett.* **2005**. https://doi.org/10.1029/2005GL023130.

(13) Kulmala, M.; Suni, T.; Lehtinen, K. E. J.; Dal Maso, M.; Boy, M.; Reissell, A.; Rannik, Ü.; Aalto, P.; Keronen, P.; Hakola, H.; et al. A New Feedback Mechanism Linking Forests, Aerosols, and Climate. *Atmos. Chem. Phys.* **2004**. https://doi.org/10.5194/acp-4-557-2004.

(14) Huey, L. G. Measurement of Trace Atmospheric Species by Chemical Ionization Mass Spectrometry: Speciation of Reactive Nitrogen and Future Directions. *Mass Spectrom Rev* **2007**, *26* (2), 166–184. https://doi.org/10.1002/mas.20118.

(15) Lopez-Hilfiker, F. D.; Mohr, C.; Ehn, M.; Rubach, F.; Kleist, E.; Wildt, J.; Mentel, T. F.; Carrasquillo, A. J.; Daumit, K. E.; Hunter, J. F.; et al. Phase Partitioning and Volatility of Secondary Organic Aerosol Components Formed from α-Pinene Ozonolysis and OH Oxidation: The Importance of Accretion Products and Other Low Volatility Compounds. *Atmos. Chem. Phys.* **2015**. https://doi.org/10.5194/acp-15-7765-2015.

(16) Riedel, T. P.; Bertram, T. H.; Crisp, T. A.; Williams, E. J.; Lerner, B. M.; Vlasenko, A.; Li, S. M.; Gilman, J.; De Gouw, J.; Bon, D. M.; et al. Nitryl Chloride and Molecular Chlorine in the Coastal Marine Boundary Layer. *Environ. Sci. Technol.* **2012**, *46* (19), 10463–10470. https://doi.org/10.1021/es204632r.

(17) Thornton, J. A.; Kercher, J. P.; Riedel, T. P.; Wagner, N. L.; Cozic, J.; Holloway, J. S.; Dube, W. P.; Wolfe, G. M.; Quinn, P. K.; Middlebrook, A. M.; et al. A Large Atomic Chlorine Source Inferred from Mid-Continental Reactive Nitrogen Chemistry. *Nature* **2010**, *464* (7286), 271–274. https://doi.org/10.1038/nature08905.

(18) Crounse, J. D.; McKinney, K. A.; Kwan, A. J.; Wennberg, P. O. Measurement of Gas-Phase Hydroperoxides by Chemical Ionization Mass Spectrometry. *Anal. Chem.* **2006**, *78* (19), 6726–6732. https://doi.org/10.1021/ac0604235.

(19) Hunt, D. F.; Harvey, T. M. Nitric Oxide Chemical Ionization Mass Spectra of Alkanes.

Anal. Chem. **1975**. https://doi.org/10.1021/ac60362a030.

(20) Hunt, D. F.; Harvey, T. M.; Brumley, W. C.; Ryan, J. F.; Russell, J. W. Nitric Oxide Chemical Ionization Mass Spectrometry of Alcohols. *Anal. Chem.* **1982**. https://doi.org/10.1021/ac00240a032.

(21) Karl, T.; Hansel, A.; Cappellin, L.; Kaser, L.; Herdlinger-Blatt, I.; Jud, W. Selective Measurements of Isoprene and 2-Methyl-3-Buten-2-Ol Based on NO^+ Ionization Mass Spectrometry. *Atmos. Chem. Phys.* **2012**, *12* (24), 11877–11884. https://doi.org/10.5194/acp-12-11877-2012.

(22) Koss, A. R.; Warneke, C.; Yuan, B.; Coggon, M. M.; Veres, P. R.; De Gouw, J. A. Evaluation of NO+ Reagent Ion Chemistry for Online Measurements of Atmospheric Volatile Organic Compounds. *Atmos. Meas. Tech.* **2016**. https://doi.org/10.5194/amt-9-2909-2016.

(23) Mochalski, P.; Unterkofler, K.; Španěl, P.; Smith, D.; Amann, A. Product Ion Distributions for the Reactions of NO+ with Some Physiologically Significant Aldehydes Obtained Using a SRI-TOF-MS Instrument. *Int. J. Mass Spectrom.* **2014**. https://doi.org/10.1016/j.ijms.2014.02.016.

(24) Lindinger, W.; Hansel, A.; Jordan, A. On-Line Monitoring of Volatile Organic Compounds at Pptv Levels by Means of Proton-Transfer-Reaction Mass Spectrometry (PTR-MS) Medical Applications, Food Control and Environmental Research. *Int. J. Mass Spectrom. Ion Process.* **1998**, *173* (3), 191–241. https://doi.org/10.1016/S0168-1176(97)00281-4.

(25) Kim, M. J.; Zoerb, M. C.; Campbell, N. R.; Zimmermann, K. J.; Blomquist, B. W.; Huebert, B. J.; Bertram, T. H. Revisiting Benzene Cluster Cations for the Chemical Ionization of Dimethyl Sulfide and Select Volatile Organic Compounds. *Atmos. Meas. Tech.* **2016**, *9* (4), 1473–1484. https://doi.org/10.5194/amt-9-1473-2016.

(26) Leibrock, E.; Huey, L. G. Ion Chemistry for the Detection of Isoprene and Other Volatile Organic Compounds in Ambient Air. *Geophys. Res. Lett.* **2000**, *27* (12), 1719–1722. https://doi.org/10.1029/1999gl010804.

(27) Chipot, C.; Jaffe, R.; Maigret, B.; Pearlman, D. a; Kollman, P. a. Benzene Dimer: A Good Model for p-p Interactions in Proteins? A Comparision between the Benzene and the Toluene Dimers in the Gas Phase and in an Aqueous Solution. *J. Am. Chem. Soc.* **1996**, *118* (19), 11217. https://doi.org/10.1021/ja961379l.

(28) Grover, J. R.; Walters, E. A.; Hui, E. T. Dissociation Energies of the Benzene Dimer and Dimer Cation. *J. Phys. Chem.* **1987**. https://doi.org/10.1021/j100296a026.

(29) Krause, H.; Ernstberger, B.; Neusser, H. J. Binding Energies of Small Benzene Clusters. *Chem. Phys. Lett.* **1991**, *184* (5–6), 411–417. https://doi.org/10.1016/0009-2614(91)80010-

U.

(30) Shinohara, H.; Nishi, N. Excited State Lifetimes and Appearance Potentials of Benzene Dimer and Trimer. *J. Chem. Phys.* **1989**. https://doi.org/10.1063/1.457342.

(31) Novak, I.; Kobač, B.; Kovačević, G. Electronic Structure of Terpenoids. *J. Org. Chem.* **2001**. https://doi.org/10.1021/jo010141z.

(32) Kim, S.; Karl, T.; Helmig, D.; Daly, R.; Rasmussen, R.; Guenther, A. Measurement of Atmospheric Sesquiterpenes by Proton Transfer Reaction-Mass Spectrometry (PTR-MS). *Atmos. Meas. Tech.* **2009**, *2* (1), 99–112. https://doi.org/10.5194/amt-2-99-2009.

(33) Bertram, T. H.; Kimmel, J. R.; Crisp, T. A.; Ryder, O. S.; Yatavelli, R. L. N.; Thornton, J. A.; Cubison, M. J.; Gonin, M.; Worsnop, D. R. A Field-Deployable, Chemical Ionization Time-of-Flight Mass Spectrometer. *Atmos. Meas. Tech.* **2011**, *4* (7), 1471–1479. https://doi.org/10.5194/amt-4-1471-2011.

(34) Kim, M. J.; Farmer, D. K.; Bertram, T. H. A Controlling Role for the Air-Sea Interface in the Chemical Processing of Reactive Nitrogen in the Coastal Marine Boundary Layer. *Proc Natl Acad Sci U S A* **2014**, *111* (11), 3943–3948. https://doi.org/10.1073/pnas.1318694111.

(35) Dondes, S.; Harteck, P.; Kunz, C. A Spectroscopic Study of Alpha-Ray-Induced Luminescence in Gases: Part I. *Radiat. Res.* **1966**. https://doi.org/10.2307/3571909.

(36) Bieri, G.; Åsbrink, L.; Von Niessen, W. 30.4-Nm He(II) Photoelectron Spectra of Organic Molecules. Part IV. Fluoro-Compounds (C, H, F). *J. Electron Spectros. Relat. Phenomena* **1981**. https://doi.org/10.1016/0368-2048(81)80036-9.

(37) Werner, A. S.; Tsai, B. P.; Baer, T. Photoionization Study of the Ionization Potentials and Fragmentation Paths of the Chlorinated Methanes and Carbon Tetrabromide. *J. Chem. Phys.* **1974**. https://doi.org/10.1063/1.1681585.

(38) Greenspan, L. HUMIDITY FIXED POINTS OF BINARY SATURATED AQUEOUS SOLUTIONS. *J Res Natl Bur Stand Sect A Phys Chem* **1977**. https://doi.org/10.6028/jres.081A.011.

(39) Lifshitz, C.; Reuben, B. G. Ion–Molecule Reactions in Aromatic Systems. I. Secondary Ions and Reaction Rates in Benzene. *J. Chem. Phys.* **1969**. https://doi.org/10.1063/1.1671149.

(40) Talebpour, A.; Bandrauk, A. D.; Vijayalakshmi, K.; Chin, S. L. Dissociative Ionization of Benzene in Intense Ultra-Fast Laser Pulses. *J. Phys. B At. Mol. Opt. Phys.* **2000**. https://doi.org/10.1088/0953-4075/33/21/307.

(41) Chan, W. F.; Cooper, G.; Brion, C. E. The Electronic Spectrum of Water in the Discrete and Continuum Regions. Absolute Optical Oscillator Strengths for Photoabsorption (6-200 EV). *Chem. Phys.* **1993**. https://doi.org/10.1016/0301-0104(93)85078-M.

(42) Miyazaki, M.; Fujii, A.; Ebata, T.; Mikami, N. Infrared Spectroscopy of Size-Selected Benzene−Water Cluster Cations [C 6 H 6 −(H 2 O) n] + (n = 1−23): Hydrogen Bond Network Evolution and Microscopic Hydrophobicity. *J. Phys. Chem. A* **2004**, *108* (48), 10656–10660. https://doi.org/10.1021/jp045823f.

(43) Suni, T.; Rinne, J.; Reissell, A.; Altimir, N.; Keronen, P.; Rannik, Ü.; Dal Maso, M.; Kulmala, M.; Vesala, T. Long-Term Measurements of Surface Fluxes above a Scots Pine Forest in Hyytiälä, Southern Finland, 1996-2001. *Boreal Environ. Res.* **2003**.

Figures

Compound	Sensitivity† (ncps pptv^{-1}) (SH = 6.9 g kg^{-1})	M^+:$[M-1]^+$:$[M+32]^+$ (SH = 0 g kg^{-1})	M^+:$[M-1]^+$:$[M+32]^+$ (SH = 6.9 g kg^{-1})	f(H_2O)	f(C_6H_6)
α-pinene	17.9	23.9:0.64:0.35	17.4:0.21:0.25	Y	N
β-pinene	18.4	14.9:0.28:0.33	17.6:0.33:0.39	N	N
D-limonene	13.6	5.4:3.4:8.0	3.7:3.0:6.9	Y	N
β-myrcene	11.5	4.6:0.56:0.94	8.7:1.1:1.7	Y	N
Ocimene	13.2	13.1:1.50:0.29	12.4:0.42:0.36	N	N

†SH = 6.9 g kg^{-1} corresponds to 65 % RH at 15 °C, representative of Boreal regions. The reported sensitivity includes the contributions from the M^+, $M\text{-}1^+$, and $M+32^+$ ions.

Table 5.1. Monoterpene sensitivities and dependence on operating and sampling conditions.

Compound	Sensitivity† (ncps pptv^{-1}) (SH = 6.9 g kg^{-1})	M^+:$[M-1]^+$:$[M+32]^+$ (SH = 0 g kg^{-1})	M^+:$[M-1]^+$:$[M+32]^+$ (SH = 6.9 g kg^{-1})	f(H_2O)	f(C_6H_6)
farnesene	10.4	7.8:1.3:1.6	7.8:1:.1:1.5	Y	N
α-humulene	8.6	5.2:2.6:0.63	1:5.3:2.8:0.54	N	N
β-caryophellene	6.9	4.6:1.4:2.2	4.0:1.1:1.9	Y	N
isolongifolene	12.3	3.1:7.7:1.2	3.4:8.8:0.15	Y	N

†SH = 6.9 g kg^{-1} corresponds to 65 % RH at 15 °C, representative of Boreal region The reported sensitivity includes the contributions from the M^+, $M\text{-}1^+$, and $M+32^+$ ions.

Table 5.2. Sesquiterpene sensitivities and dependence on operating and sampling conditions.

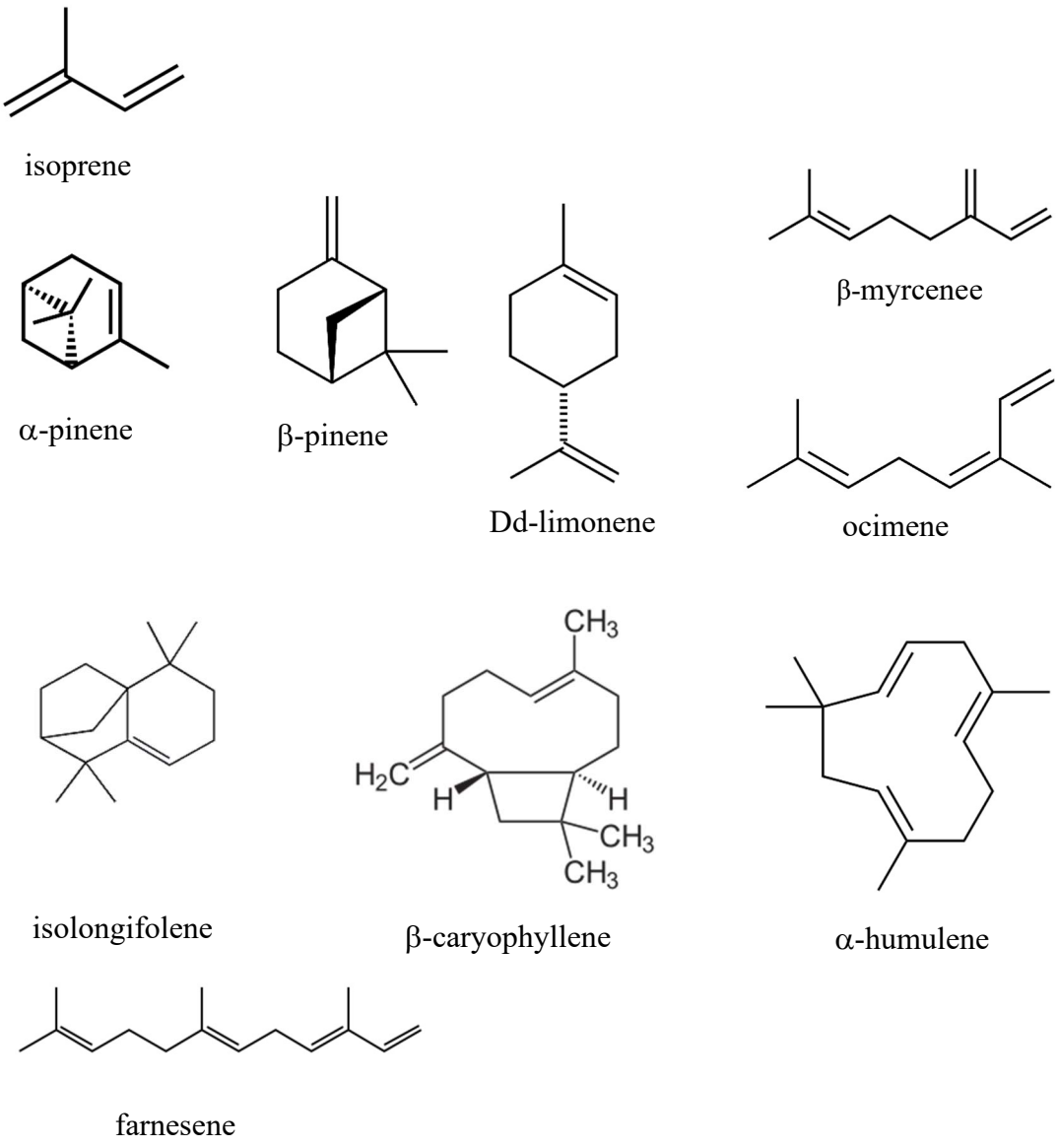

Figure 5.1. Molecular structures for the terpenes characterized in this study.

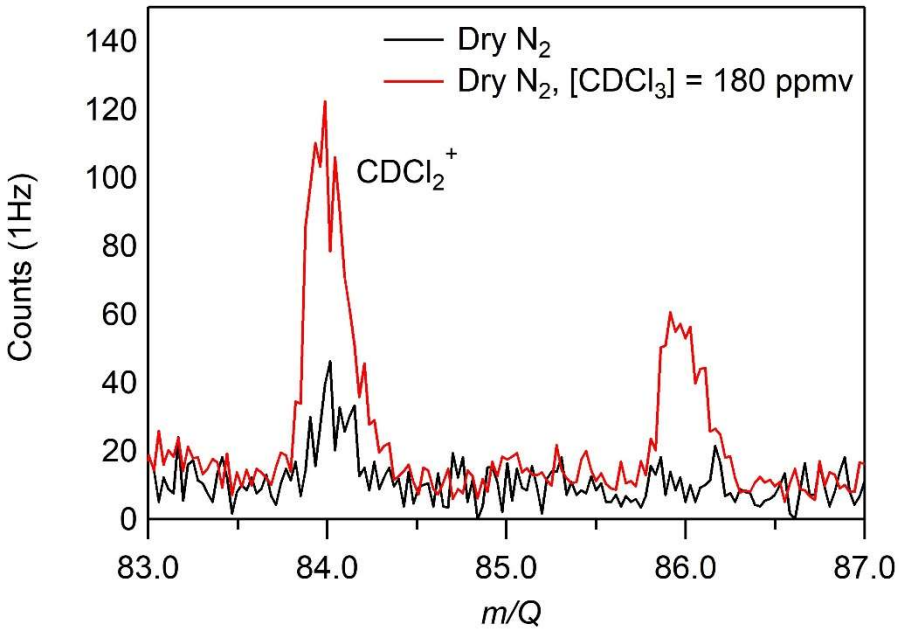

Figure 5.2. CI-ToFMS mass spectrum acquired when overflowing the inlet with excess nitrogen (black) and for a nebulized solution of chloroform-d at a flow rate of 3µl·min^{-1} in a nitrogen carrier gas (red), where the resulting [$CDCl_3$] = 180 ppmv. No signal was observed above the baseline for any other fragments or the parent ($CDCl_3^+$, 120 *m/Q*).

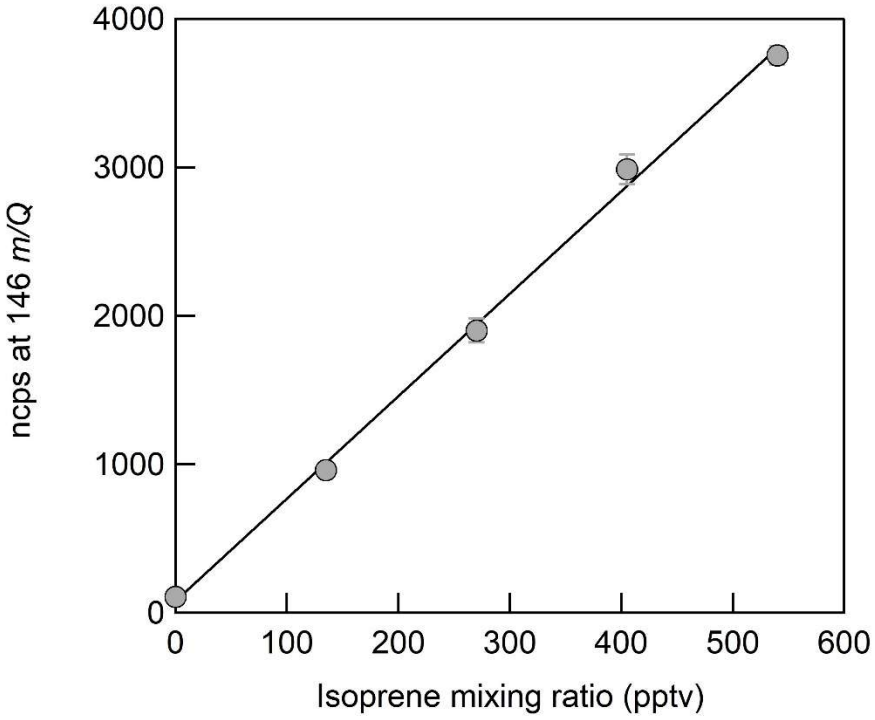

Figure 5.3. CI-ToFMS calibration curve for isoprene, detected as $C_6H_6^+ \cdot C_5H_8$ at 146 *m/Q*. The sensitivity (slope) is 7 ncps, R^2=0.99. Error bars represents the standard deviation of the 1Hz measurements.

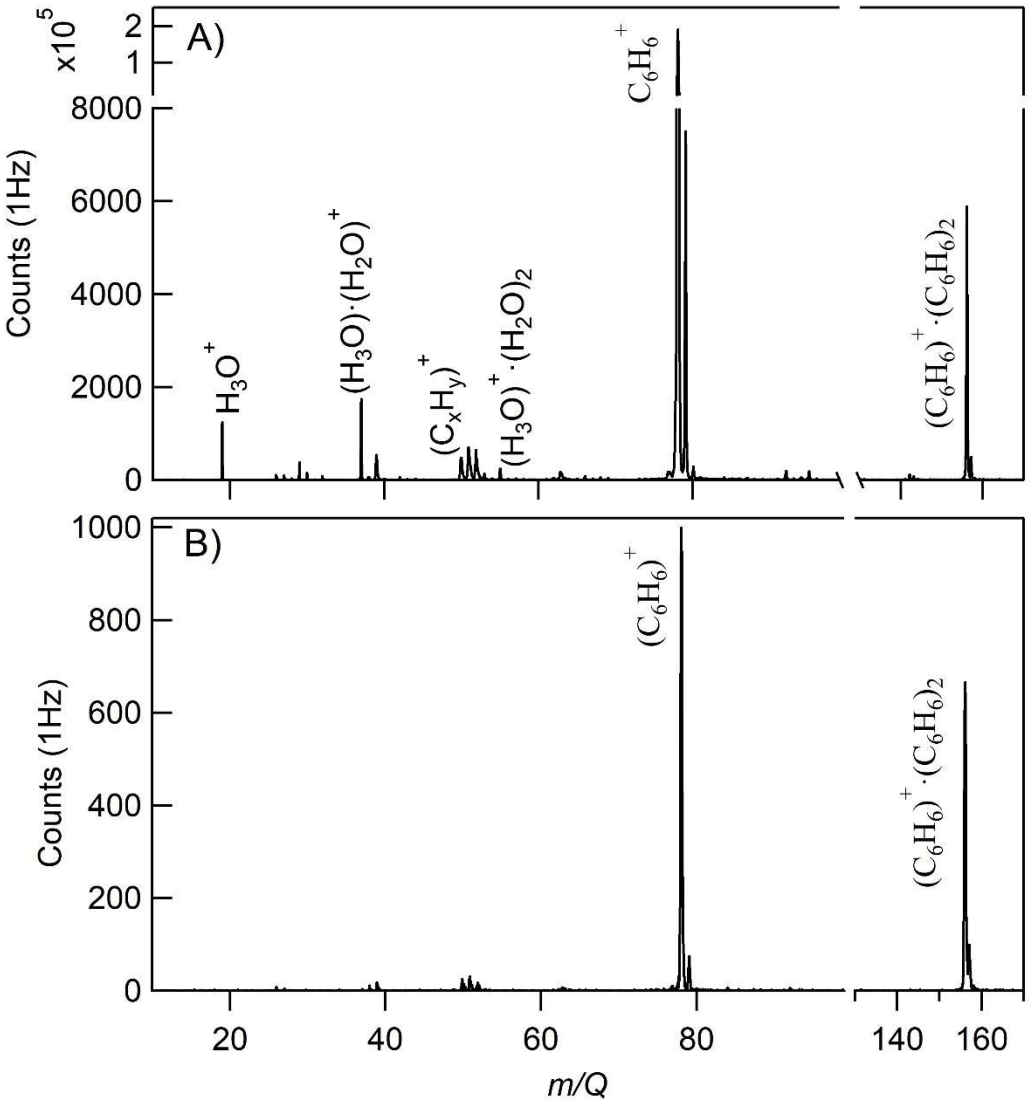

Figure 5.4. (a) CI-ToFMS mass spectrum acquired when overflowing the inlet with nominally dry zero air for a benzene neutral concentration of 300 ppm using a liquid reagent ion delivery and (b) same as in a, but with the first RF-only octupole ion guide turned off, resulting in a much weaker electric field strength.

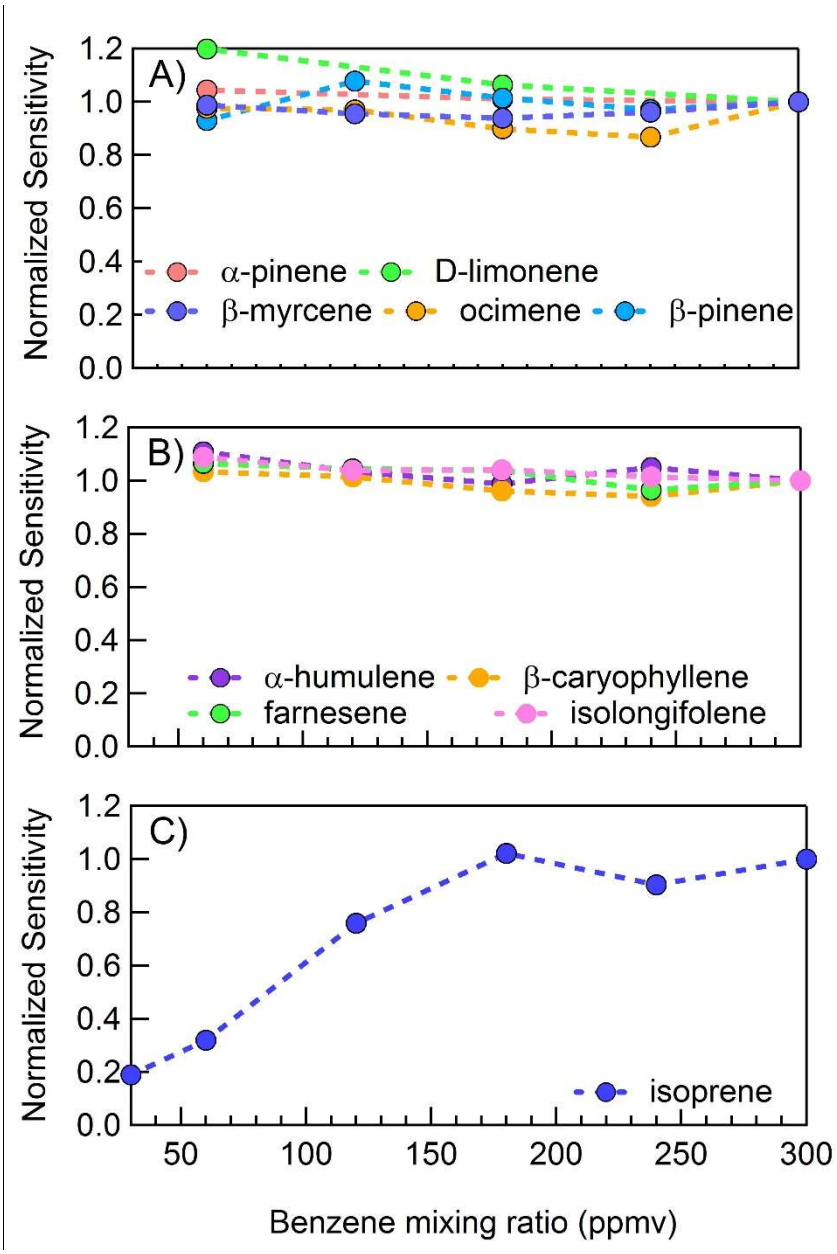

Figure 5.5. CI-ToFMS sensitivity to: a) monoterpenes ($C_{10}H_{15}^+$; 136 *m/Q*), b) sesquiterpenes ($C_{15}H_{24}^+$; 204 *m/Q*), and c) isoprene ($C_6H_6^+ \cdot C_5H_8$; 146 *m/Q*) as a function of benzene neutral concentration normalized to the sensitivity at 300 ppmv neutral benzene. Measurements were conducted in nominally dry zero air.

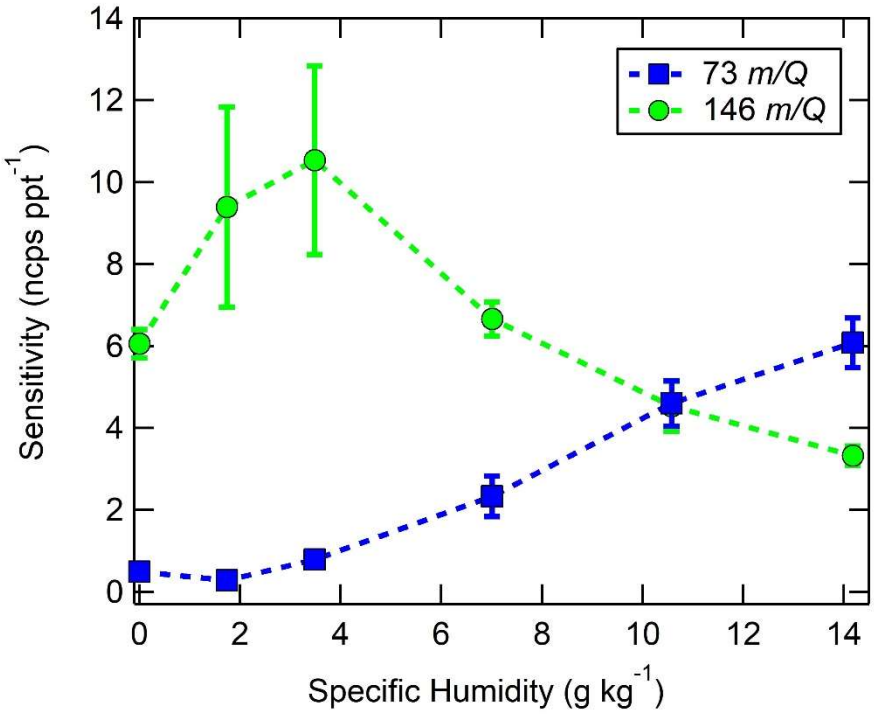

Figure 5.6. Humidity dependent CI-ToFMS sensitivities to isoprene (green circles, $C_6H_6^+ \cdot C_5H_8$, 146 *m/Q*), and the protonated water tetramer (blue squares, $H_3O^+ \cdot (H_2O)_3$, 73 *m/Q*), derived from calibration curves such as those shown in Figure 6. The reported sensitivities are the average of triplicate calibration curves with all linear best fits having $R^2 > 0.98$. Error bars represent the standard deviation of the triplicate calibrations. All calibrations were performed in zero air.

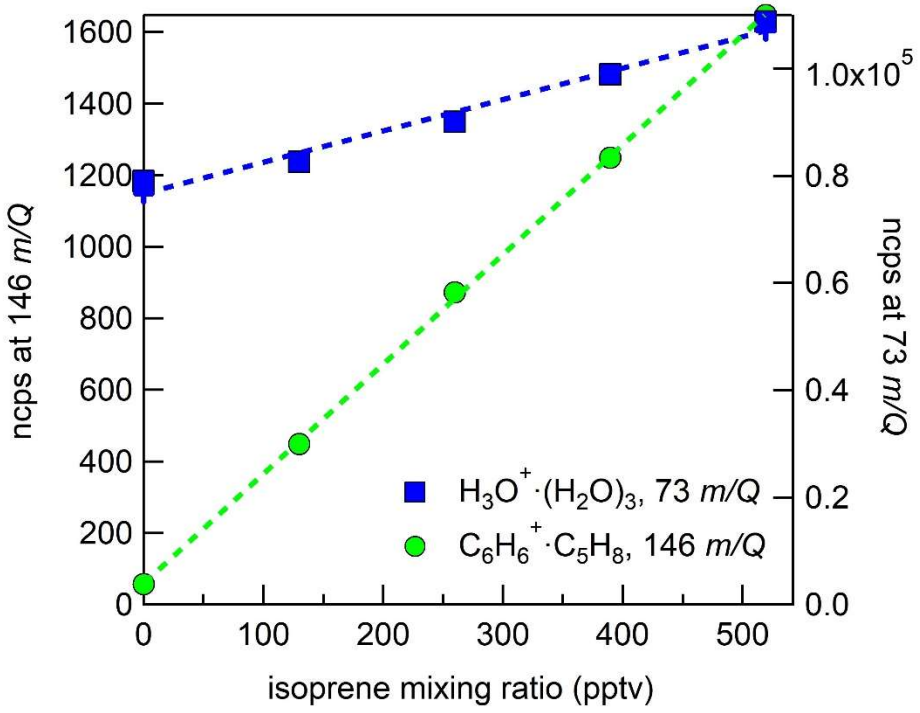

Figure 5.7. CI-ToFMS sensitivity to isoprene, observed as the isoprene-benzene cluster (green circles, $C_6H_6^+ \cdot C_5H_8$, 146 *m/Q*) and water protonated tetramer (blue squares, $H_3O^+ \cdot (H_2O)_3$, 73 *m/Q*). Dashed lines are the least square best fit lines (R^2>0.98). Calibration was performed at SH of 14 g kg^{-1} in zero air.

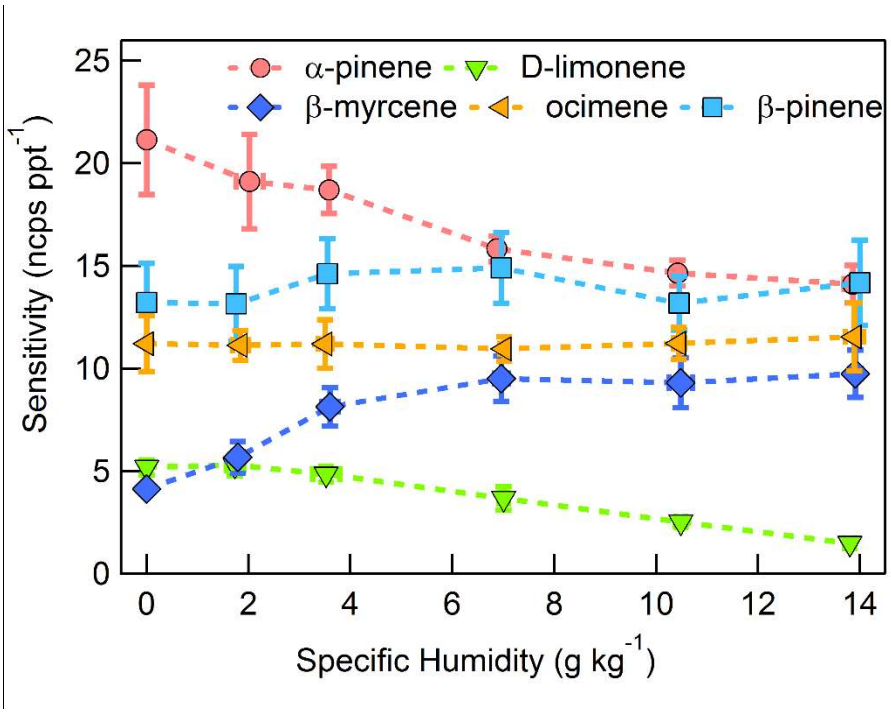

Figure 5.8. Humidity dependent sensitivities to select MTs detected as M^+ ($C_{10}H_{16}^+$, 136 *m/Q*). Error bars indicate the standard deviation of triplicate measurements. All calibrations were conducted in zero air. Error bars represent the standard deviation of the triplicate calibrations. All calibrations were performed in zero air.

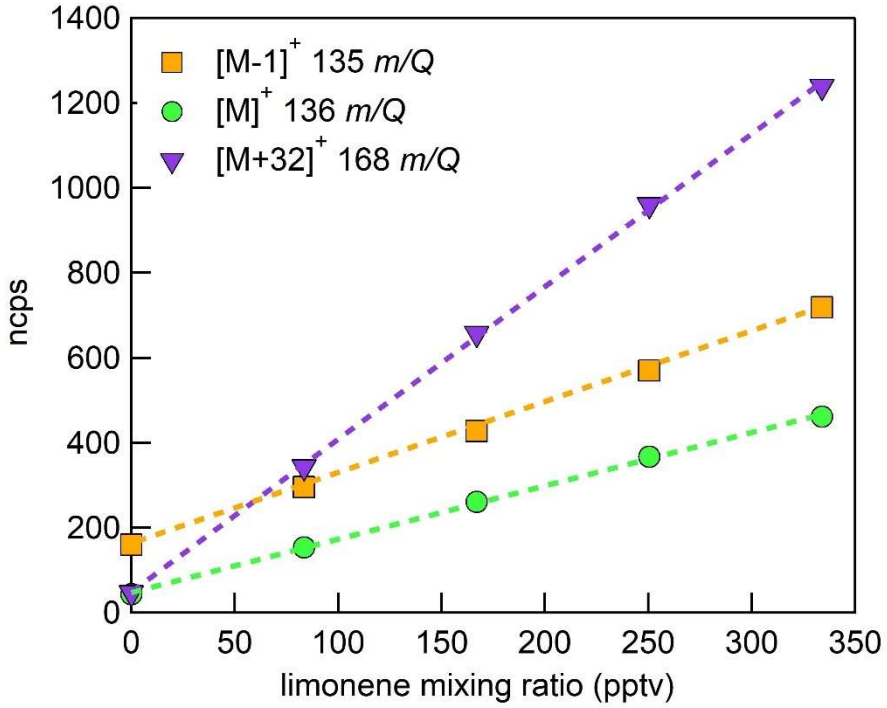

Figure 5.9. Normalized calibration of D-limonene for all major product ions ($C_{10}H_{16}^+$, 136 *m/Q*, green circles), ($C_{10}H_{15}^+$, 135 *m/Q*, orange squares), and ($C_{10}H_{16}O_2^+$, 168 *m/Q*, purple triangles). Calibration was performed in zero air at 14 g kg^{-1} specific humidity (80% RH at 23°C). Dashed lines are least squares best fit lines (all R^2 >0.99).

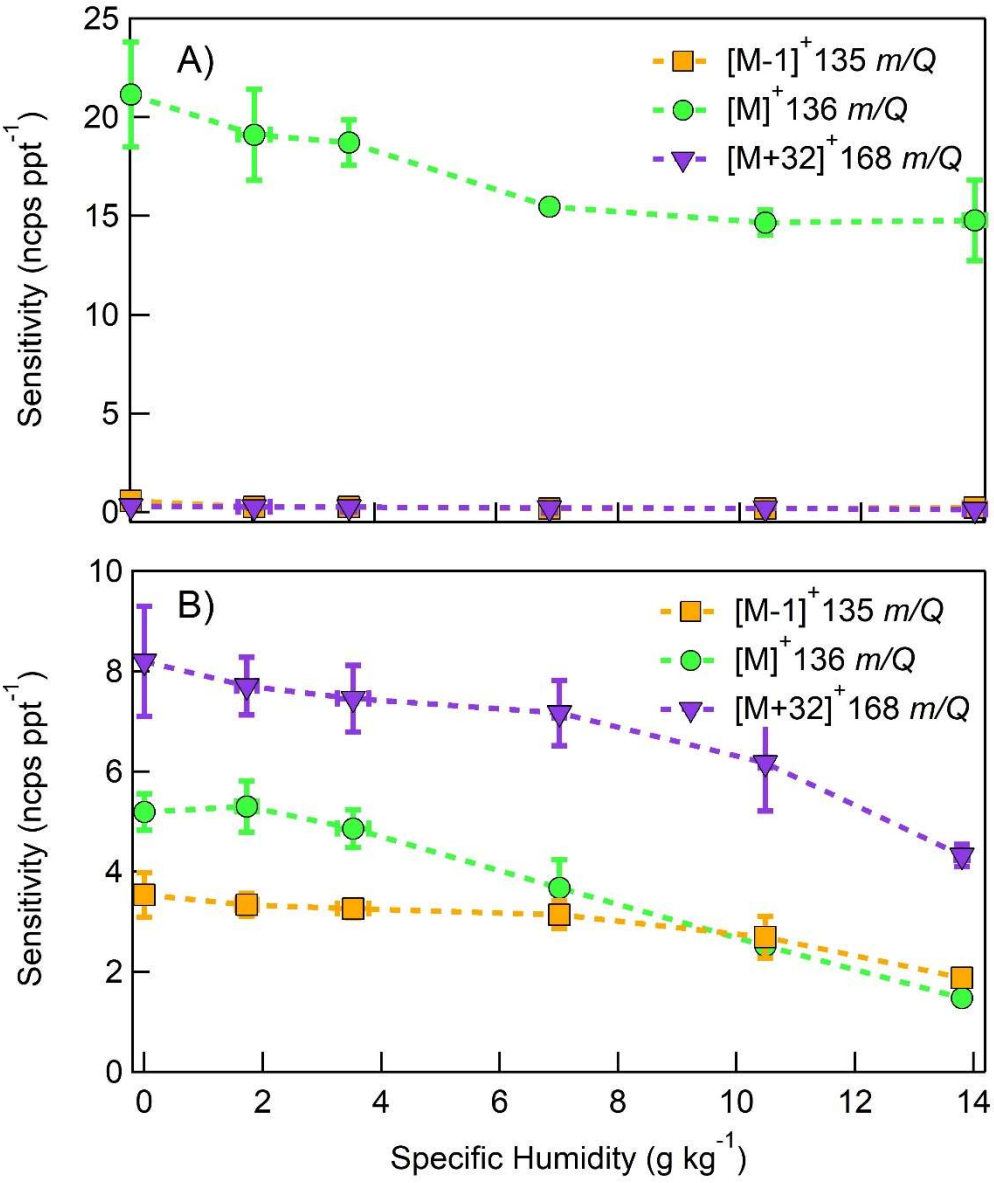

Figure 5.10. Humidity dependent, normalized sensitivities to (a) α-pinene (b) D-limonene for all major product ions ($C_{10}H_{16}^+$, 136 *m/Q*, blue circles), ($C_{10}H_{15}^+$, 135 *m/Q*, green squares), and ($C_{10}H_{16}O_2^+$, 168 *m/Q*, red triangles). Error bars represent the standard deviation of the triplicate calibrations. All calibrations were performed in zero air.

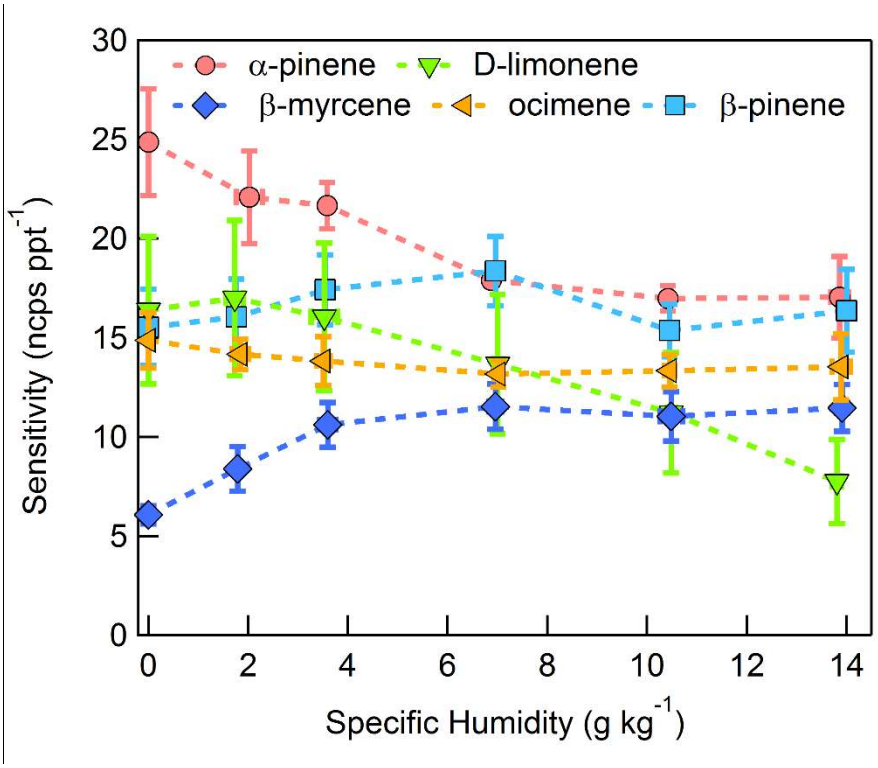

Figure 5.11. Humidity dependent, CI-ToFMS monoterpene sensitivities reported as the sum of all detected masses (135, 136, and 168 *m/Q*). Error bars represent the standard deviation of the triplicate calibrations. All calibrations were performed in zero air.

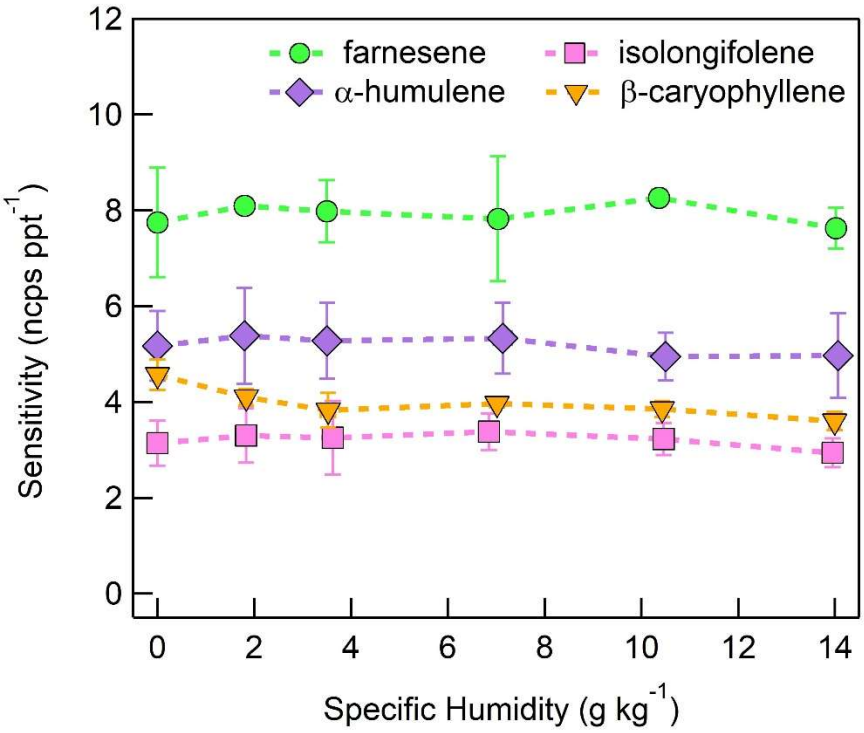

Figure 5.12. Humidity dependent sensitivities of SQTs detected as $C_{15}H_{24}$ (204 *m/Q*). Error bars represent the standard deviation of triplicate measurements. All calibrations were performed in zero air.

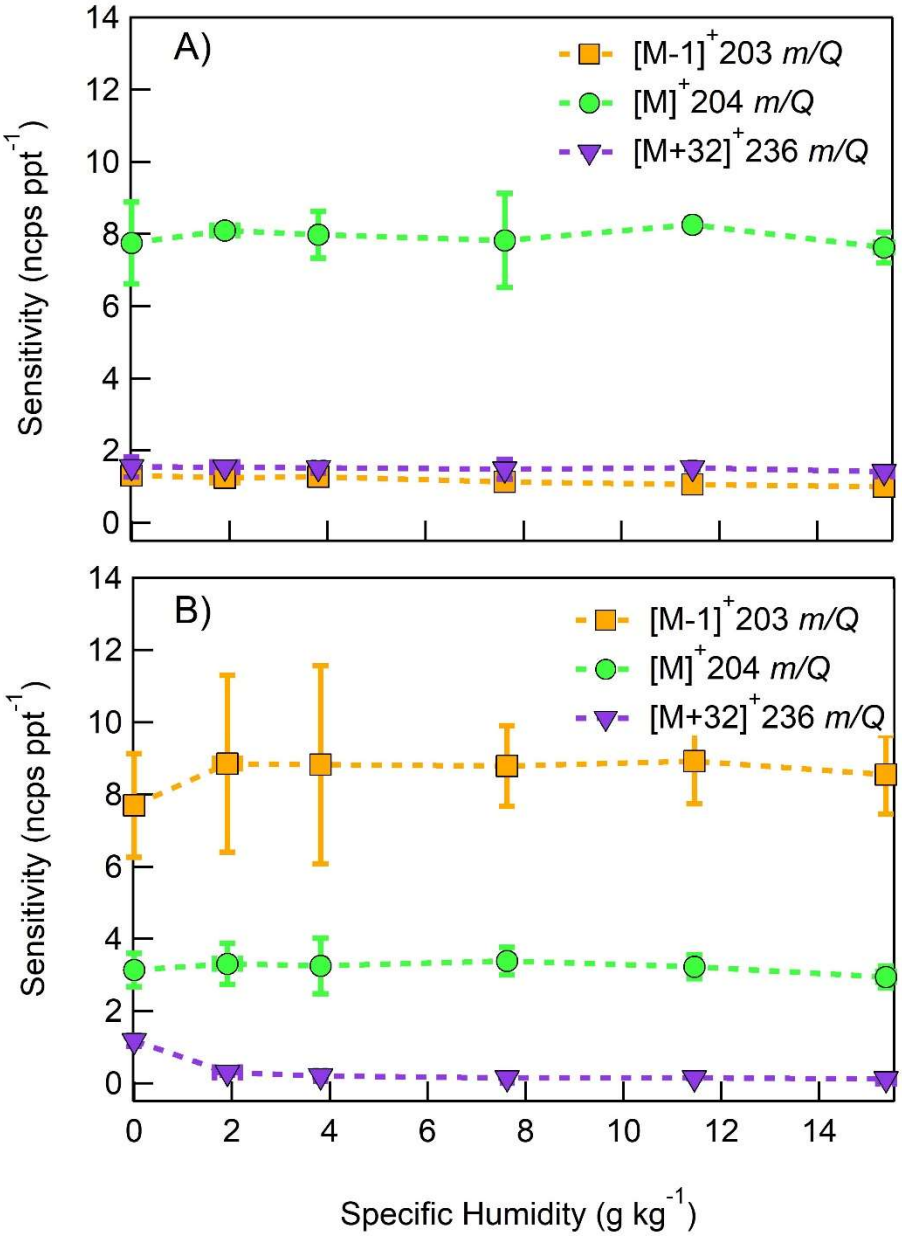

Figure 5.13. Humidity dependent, normalized sensitivities to (a) farnesene and (b) isolongifolene for all major product ions ($C_{15}H_{23}^+$, 203 *m/Q*, blue circles), ($C_{15}H_{24}^+$, 204 *m/Q*, gray squares), and ($C_{15}H_{24}O_2^+$, 236 *m/Q*, red diamonds). Error bars represent the standard deviation of the triplicate measurement.

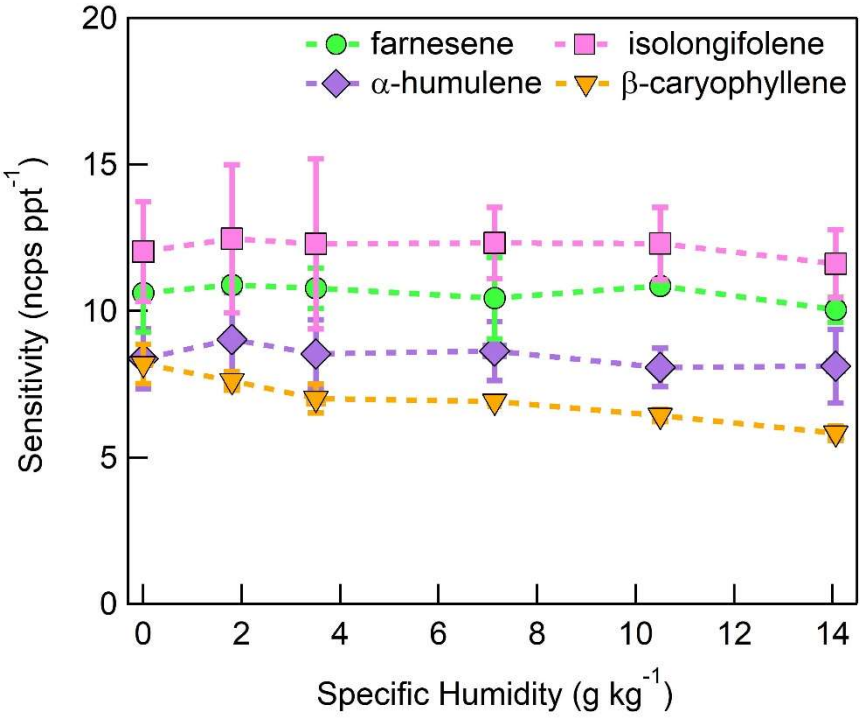

Figure 5.14. Humidity dependent, normalized sensitivities to sesquiterpenes, reported as the sum of the major product ions ($C_{15}H_{23}^+$, 203 *m/Q*), ($C_{15}H_{24}^+$, 204 *m/Q*), and ($C_{15}H_{24}O_2^+$, 236 *m/Q*). Error bars represent the standard deviation of triplicate measurements.